IEKP-KA/2009-23

Electromagnetic measurements with the Katrin pre-spectrometer

Zur Erlangung des akademischen Grades eines
Doktors der Naturwissenschaften
von der Fakultät für Physik der
Universität Karlsruhe (TH) genehmigte

DISSERTATION

von

Dipl. Phys. Florian Habermehl
aus Kleinfischlingen

Tag der mündlichen Prüfung: 24. Juli 2009
Referent: Prof. Dr. G. Drexlin, Institut für Experimentelle Kernphysik
Korreferent: Prof. Dr. T. Müller, Institut für Experimentelle Kernphysik

Abstract

Neutrinos are the only known Standard Model particles for which the absolute mass value has not been identified yet. The next generation direct neutrino mass experiment KATRIN has entered its major construction phase and will soon be ready to investigate the 'electron antineutrino' mass with an unprecedented model-independent sensitivity of $200\,\mathrm{meV/c^2}$ (90% CL). A key to reach this sensitivity is a significant improvement of the MAC-E filter (Magnetic Adiabatic Collimation combined with Electrostatic filter) technology for the high precision energy analysis of β decay electrons, as already successfully employed with less stringent requirements in the Mainz and Troitsk experiments.

The objective of this thesis has been focused on the commissioning of the pre-spectrometer, a novel MAC-E filter with fundamental changes in its vacuum and electromagnetic design. The final role of the pre-spectrometer in the KATRIN set-up is that of a high-pass energy filter limiting the number of β decay electrons which reach the main spectrometer to those of the highest energies, as only these carry information on the neutrino mass. The pre-spectrometer is thus a crucial device for background suppression. It is vital to reach an overall background rate of 10 mHz so that the full physics potential of KATRIN can be reached. Therefore, the pre-spectrometer design is also aimed at achieving a very low background rate. In this context, it is of central importance to reach and maintain stringent ultra high vacuum (UHV) conditions inside the spectrometer section of better than $1 \cdot 10^{-11}\,\mathrm{mbar}$. Furthermore, the KATRIN measurements rely on a novel high voltage scheme to create an ultra precise electrostatic retarding potential. It omits a complicated and massive inner electrode system by elevating the pre-spectrometer vessel itself to a higher electrostatic potential. A lightweight inner electrode system can then be used to stabilise the electric potential and to further help to reduce the background created by cosmic ray induced electron emission from the stainless steel vessel. The verification of both the UHV concept as well as of the novel electromagnetic concept has been a central task of the present work.

Accordingly, a specific test set-up has been conceived, which allows to test the requirements and novel concepts with the pre-spectrometer. To simulate the final KATRIN set-up, a monoenergetic electron emitter was installed to one side of the pre-spectrometer vessel, and a detector system to the other side. Two superconducting magnets with a maximum magnetic field output of 4.5 T were used to guide the

injected electrons to the detector system. An electrostatic potential retarding field was applied to the vessel and the inner electrode set-up. This complete MAC-E filter set-up makes it possible to test the pre-spectrometer functionality with regard to its electromagnetic and UHV properties.

In the framework of this thesis, the following tests were conducted with the objectives:

- verification of the UHV design, including tests of the heating/cooling system,
- implementation and verification of the high voltage design,
- commissioning and characterisation of a segmented silicon PIN diode detector's intrinsic parameters as well as the detector set-up's UHV capabilities,
- commissioning and optimisation of an electron emitter,
- commissioning and characterisation of data acquisition systems, and
- commissioning of a slow control system for experiment control and parameter monitoring.

This scope of work has made the pre-spectrometer test experiment an important testbed in particular for the main spectrometer.

The results of the UHV tests have yielded a result for an excellent outgassing rate of

$$(2.5 \pm 0.5) \cdot 10^{-14}\,\mathrm{mbar{\cdot}l/(s{\cdot}cm^2)}$$

which allows to operate the spectrometers at room temperature. The corresponding end pressure of $p = 4.8 \cdot 10^{-11}\,\mathrm{mbar}$ is close to the required limit but has been limited by the restricted bake-out temperatures. An improved thermo-insulation of the vessel and an increased heating power will allow a further reduction to the required upper limit of $p < 1 \cdot 10^{-11}\,\mathrm{mbar}$. These results have been instrumental in the UHV design of the much larger main spectrometer whose vacuum capabilities subsequently have been proven to be fully compatible with the demands.

The main focus of this thesis has been the characterisation of the various background components resulting from the novel design of the pre-spectrometer by dedicated measurements. One minor background component has been found to be caused by a hot ionization gauge. A major background source was activated as soon as an electric potential was applied to the electrode system and the magnetic field was exceeding a specific threshold value, leading to electric discharges which culminated in a vacuum breakdown. With the help of electromagnetic simulation tools and an extensive measurement effort, it has been possible to identify the background source being a Penning trap located at the entrance and exit region of the spectrometer between the inner electrode and vessel. To eliminate this rather deep Penning trap, a new electrode system has been designed, manufactured, installed and tested in the

framework of this thesis. The results after the modification show that Penning traps are a major source of background with regard to the 10 mHz design specification of KATRIN. However, the measurements have clearly proven that the electromagnetic simulation packages created by the KATRIN member F. Glück provide an excellent tool to predict and prevent potential Penning traps already in the electromagnetic design phase by conducting comprehensive simulation studies.

Having eliminated this major first background component, the characterisation of the remaining background effects in the pre-spectrometer system operating under high electric potential and strong magnetic fields has been continued. A major area of work has been the investigation of small Penning traps, which can be activated and deactivated depending on the chosen potential distribution of the inner electrode parts. This indicates that even small Penning traps can ignite and cause a significant increase in the event rate as measured by the detector system. These Penning traps have been characterised on the one hand with the help of simulations, yielding the depth and the location. On the other hand, the measurements conducted here were able to disclose the dependencies of the trap with regard to magnetic field strength, absolute electric potential value, potential distribution and pressure. The results show the rather complex nature of the processes being involved: In some cases the findings were unexpected and do not fully comply with results published in literature. However, the parameter space of the pre-spectrometer test experiments is different from all the published results, as is the detection method, as solid state detectors are a much more sensitive tool as compared to vacuum gauges.

Having adjusted the parameter space to that of the later operation modus (U≈-18 kV, B_{max}=4.5 T), another major background component has been registered. It features a very distinct ignition behaviour and follows a clear threshold behaviour with regard to the magnetic field strength. The characteristics of this background component have been closely inspected. The results show in some aspects a different behaviour as to that of the small Penning trap investigated earlier. This new component called 'high B-field background' causes a significant rise in event rate in correlation with an increasing magnetic field strength and pressure. It also strongly depends on the electric potential distribution which allows to distinguish interrelated effects for different configurations.

In all measurements the spatial resolution of the silicon PIN detector has been of great value, as it discloses distinct geometrical features such as ring-like structures which assists in the analyzing of the data and helps to devise theories to explain the observed background mechanisms. The experience gained in this work will be of vital importance for the imminent measurements of the main spectrometer, where a silicon PIN diode array with an even higher resolution will allow even greater insights into the MAC-E filter characteristics.

When combining these investigations with an in-depth study of particle storage close to an electron gun one can conclude that stored particles are of major concern for KATRIN. These particles create secondary electrons and negative ions which subsequently increase the background rate. Also in this case the entrance and exit region

where electrostatic and magnetic gradients are the steepest have been identified as the location of the background source. A closer inspection of this region has revealed several possible traps for ions and electrons resulting in a further final change of the inner electrode set-up with the aim to completely eliminate all possible traps present in the novel spectrometer design of KATRIN.

Erklärung

Hiermit versichere ich, daß die vorliegende Arbeit selbständig und nur unter Verwendung der angegebenen Hilfsmittel und Quellen verfaßt wurde.

Florian Habermehl
Kleinfischlingen, den 24.7.2009

Contents

1 Introduction **1**

1.1 Neutrino sources 2

1.2 Massive neutrinos 5

1.2.1 Neutrino oscillation 6

1.3 Determination of the neutrino masses 8

1.3.1 Indirect searches 8

1.3.1.1 Cosmological methods 9

1.3.1.2 Neutrinoless double beta decay 10

1.3.2 Direct search methods 11

1.3.2.1 Time of flight studies 11

1.3.2.2 Kinematics of weak decays 12

1.4 Outline 13

2 Measuring the neutrino mass - the KATRIN experiment **15**

2.1 Tritium β decay 16

2.2 The KATRIN set-up 18

2.2.1 Source section 19

2.2.1.1 Tritium circulation and retention system 20

2.2.2 Transport section 22

2.2.2.1 Differential pumping section 22

2.2.2.2 Cryogenic pumping section 23

2.2.3 Electrostatic spectrometers 23

2.2.3.1 MAC-E filter 25

2.2.3.2 Tandem spectrometer 29
2.2.4 Detector 30
2.2.5 Calibration monitoring system 32
2.2.5.1 Rear wall system 32
2.2.5.2 Monitor spectrometer 32
2.2.5.3 Forward Monitor detector 33
2.3 Aim and sensitivity 33

3 The KATRIN pre-spectrometer test experiment 35

3.1 The pre-spectrometer vessel 36
3.1.1 The vacuum concept 39
3.1.1.1 Verification of the vacuum design 46
3.1.2 Electrode system 50
3.1.2.1 Components on elevated potential 52
3.1.3 High voltage supply 55
3.1.3.1 Improvements of the high voltage stability 58
3.2 Slow control system 61
3.3 Superconducting magnet system 66
3.4 Mono energetic electron emitter 68
3.4.1 Electron emitter set-up 69
3.4.2 Commissioning of the electron emitter 72
3.5 Detector system 75
3.5.1 Detector vacuum chamber 78
3.5.2 Micro channel plate 83
3.5.2.1 Set-up and characteristics 84
3.5.3 Segmented PIN Diode 87
3.5.3.1 Design of the detector system 88
3.5.3.2 Characteristics of the segmented PIN diode 96
3.5.3.3 Conclusion 99
3.5.4 Data acquisition 99
3.5.4.1 UW-DAQ 100

3.5.4.2 IPE-DAQ v3 . . . 105
3.5.4.3 ORCA - Object oriented Real-time Control and Acquisition . . . 108
3.5.5 Conclusion . . . 110

4 Investigation and mitigation of background effects 113
4.1 Discharge mechanisms . . . 113
4.1.1 Townsend discharge . . . 114
4.1.2 Vacuum breakdown . . . 115
4.1.3 Penning discharge . . . 116
4.2 Pre-spectrometer Penning trap . . . 120
4.2.1 EMD simulation tools . . . 120
4.2.1.1 Magnetic field calculation . . . 121
4.2.1.2 Electric field calculation . . . 122
4.2.1.3 Trajectory calculation for charged particles in electromagnetic fields . . . 123
4.2.2 Penning trap characterisation . . . 123
4.2.2.1 Measurements . . . 125
4.2.3 Design for a shielding electrode . . . 132
4.2.4 Conclusion . . . 136

5 Background investigations at the pre-spectrometer II set-up 137
5.1 Background investigation without active Penning trap at magnetic fields smaller than 2 T . . . 138
5.1.1 Potential dependence . . . 138
5.1.2 Magnetic field dependence . . . 140
5.1.3 Production mechanism for U_0-peak . . . 141
5.1.4 Negative ion peak . . . 144
5.1.4.1 Characteristics of the ion peak . . . 145
5.1.5 Conclusion . . . 147
5.2 Characterisation of the residual Penning trap . . . 149
5.2.1 Time dependency of the Penning trap ignition . . . 150

5.2.2 Magnetic and potential dependence 151
5.2.3 Spatial distribution of the rate in the detector segments . . . 151
5.2.4 Energy U_0-peak shift 153
5.2.5 Pressure dependence 156
5.2.5.1 Influences of the electrostatic potential at pressures of 10^{-8} mbar 157
5.2.6 Investigation of the activation mechanism 160
5.2.7 Discussion of the production and transport mechanisms . . . 161
5.2.8 Conclusion 162
5.3 Characterisation of background generating processes at magnetic fields larger than 2 T 162
5.3.1 Event rate dependence on magnetic field strength 163
5.3.2 Ignition characteristics 165
5.3.3 Electrode potential dependencies 168
5.3.3.1 Dipole mode test 169
5.3.4 Variation of potential distribution 171
5.3.4.1 Investigation of potential variations at asymmetric magnetic fields 179
5.3.5 Pressure dependence 183
5.3.6 Special effects of the high B-field background 184
5.3.6.1 Pixel islands 185
5.3.6.2 High-energy tail 188
5.3.7 High B-field background conclusion 191
5.4 Background processes at the e-gun system 192
5.4.1 Investigation of removing trapped particles in the e-gun chamber using a wire scanner 195
5.4.2 Probing the potential limit of the high B-field background . . 198
5.4.3 Conclusion 199
5.5 Conclusion & outlook 199

A Ultra High Vacuum **203**

A.1 Vacuum sealing techniques used at the KATRIN experiment 204

A.1.1 Dimension designation 204

A.1.2 Klein flanges and seals 204

A.1.3 ISO-K seals 204

A.1.4 ConFlat® flanges and seals 205

A.1.5 Swagelok® components and seals 205

A.1.6 O-ring sealing technique 205

A.2 Vacuum leaks 206

A.2.1 Leak detection 207

A.3 Vacuum pumps 209

A.3.1 Turbomolecular pumps 210

A.3.1.1 TMP characteristics 212

A.3.2 Fore vacuum pumps 213

A.3.3 Gas binding vacuum pumps 214

A.3.3.1 Sorption pumps 214

A.3.3.2 Cryopumps 217

A.4 Treatment of UHV-components 218

A.4.1 UHV pre-cleaning 218

A.4.2 Baking procedure 219

A.5 Vacuum gauges 220

A.5.1 Ionisation vacuum gauges 221

A.5.1.1 Cold cathode gauges 221

A.5.1.2 Hot cathode gauges 222

A.6 Residual Gas Analysis 224

B Calibration of FuG power supplies **227**

C Tables **233**

C.1 Americium source 233

C.2 UW-DAQ threshold values 234

D Pre-spectrometer heating/cooling system **235**

List of Figures

1.1 Solar neutrino fluxes 2
1.2 Constituents of the energy density of the universe 4
1.3 Neutrino mass pattern 9

2.1 Theoretical β decay spectrum 17
2.2 Experimental set-up of the KATRIN experiment 19
2.3 Tritium flow rate in KATRIN 21
2.4 Tritium circulation and retention 21
2.5 Forward section of the Differential Pumping Section 23
2.6 Cryogenic Pumping Section 24
2.7 History of m_ν measurements 25
2.8 MAC-E filter 26
2.9 Cyclotron motion of electron 27
2.10 Focal plane detector 32
2.11 KATRIN discovery potential 33

3.1 Pre-spectrometer test set-up 36
3.2 Pre-spectrometer vessel 37
3.3 Pre-spectrometer with inner electrode system 38
3.4 O-ring sealing technique for DN500+ 40
3.5 Electropolishing of vacuum surface 41
3.6 Pumping scheme for the pre-spectrometer test experiment 43
3.7 EBARA turbomolecular pump 43
3.8 Non-evaporable getter cartridge for the pre-spectrometer 44

3.9 Activation of the non-evaporable getter 45
3.10 Pressure rise measurement of the pre-spectrometer and e-gun chamber 48
3.11 Measurement of outgassing coefficient 49
3.12 Inner electrode system of the pre-spectrometer 51
3.13 Isolators of the heating/cooling circuit 52
3.14 Isolators of the pre-spectrometer vessel 53
3.15 Photograph of inner electrode system 55
3.16 High voltage system diagram 56
3.17 High voltage patch box 58
3.18 Longtime high voltage stability 60
3.19 ZEUS graphical user interface 61
3.20 Pre-spectrometer data flow schematics 64
3.21 Magnetic field strength along z-axis 66
3.22 Cryogen free magnet system 67
3.23 Set-up of the electron emitter 69
3.24 Deuterium lamp wavelength spectrum 70
3.25 3D model of shutter plate 71
3.26 Angular distribution of e-gun electrons 72
3.27 Damaged e-gun tip 73
3.28 Simulation of electron tracks for different e-gun cap geometries . . . 74
3.29 Pictures of electrostatic blind and mounted e-gun tip with cap . . . 76
3.30 Detector UHV chamber 79
3.31 Segmented PIN diode coverage 80
3.32 Schematics of the detector cooling system 81
3.33 Corrosion in the detector lance 83
3.34 Scheme and working principal of micro channel plate 85
3.35 MCP circuit schematic 85
3.36 Influence of magnetic field strength on MCP performance 86
3.37 Photographs of the installed MCP 87
3.38 Damaged MCP 88

3.39 Working principle of segmented PIN diode 88
3.40 Backside of SPD ceramics plate 90
3.41 Schematic of SPD set-up 91
3.42 Orientation of the SPD in the x-y plane 92
3.43 Photographs of mounted SPD set-up 93
3.44 RGAs of the detector chamber at different temperatures with SPD installed 95
3.45 The relative energy resolution of the 64 pixel SPD 98
3.46 Trigger circuit of the UW-DAQ 101
3.47 Time distribution of different signals measured by DAQ system . . . 102
3.48 Efficiency of the UW-DAQ 104
3.49 Efficiency of the IPE-DAQ 106
3.50 Time separation of the IPE-DAQ 106
3.51 ADC traces taken with the IPE-DAQ 107
3.52 The KATRIN FLT card 108
3.53 ORCA pre-spectrometer control panel 110
3.54 ADC traces taken with the IPE-DAQ 111

4.1 Breakdown characteristic curves for different pressure values 116
4.2 Electron movement in coaxial cylindrical electrode 117
4.3 Breakdown characteristics 118
4.4 Penning trap schematic 119
4.5 Particle motion inside Penning trap 120
4.6 Continuous discharge 124
4.7 Potential distribution revealing Penning trap in PSI set-up 126
4.8 Ignition curve for fixed potential 128
4.9 Leakage currents and pressure as a function of the electric potential 129
4.10 Rate increase dependence according to Penning trap depth 131
4.11 Start of breakdown with fixed magnetic field 131
4.12 Picture of mounted Anti-Penning and earth electrode 132
4.13 Penning trap in the pre-spectrometer II set-up 134

4.14 Longitudinal kinetic energy of electrons in the pre-spectrometer . . . 135

5.1 Background energy spectra comparison . . . 139
5.2 Spatial asymmetric distribution of the rate for more negative inner electrode . . . 140
5.3 Spatial distribution of the rate for magnetic fields $\lesssim$0.29 T . . . 142
5.4 Background comparison with and without activated hot ionisation gauge . . . 143
5.5 Spatial background distribution of the rate for different energy regions 144
5.6 Negative ion peak . . . 145
5.7 Simulation of ionisation energy loss for H^- ions in silicon . . . 146
5.8 Ion peak height comparison . . . 147
5.9 Z-position dependence of background rate . . . 148
5.10 Penning rap ignition time and increase in background rate . . . 150
5.11 Asymmetric distribution of the rate for quenched Penning trap . . . 152
5.12 Spatial distribution of the background rate for active Penning trap at different B-field strengths . . . 153
5.13 Energy peak shift during active Penning trap . . . 154
5.14 Penning trap secondary electron production place . . . 155
5.15 Background rate as a function of time during a pressure rise test . . . 156
5.16 Influences of the potential at high pressures . . . 158
5.17 Increase of low-energy events at magnetic fields <0.8 T . . . 159
5.18 High B-field background ignition . . . 163
5.19 Background rate as function of monotonically decreasing B-field . . . 165
5.20 HBB ignition characteristics for symmetric magnetic fields . . . 166
5.21 HBB ignition characteristics for asymmetric magnetic fields . . . 167
5.22 The background rate as a function of the potential at B=4.5 T . . . 169
5.23 Dipole modus test . . . 170
5.24 Energy peak shift for different detector B-fields . . . 172
5.25 Detector translation in x and y . . . 173
5.26 Spatial distribution of the rate for inner electrode more negative . . . 175
5.27 Spatial distribution of the rate for wire electrode more negative . . . 176

5.28 Magnetic field lines and Penning traps for asymmetric magnetic field 178
5.29 Spatial distribution of the rate for asymmetric magnetic fields 181
5.30 Ignited Penning trap in asymmetric magnetic field set-up 183
5.31 Event rate and pressure as a function of time for a pressure rise test 184
5.32 Spot-like increase in rate 185
5.33 HBB ignition characteristics comparison 187
5.34 High-energy tails 190
5.35 E-gun background energy spectrum 193
5.36 HBB induced e-gun background at different e-gun positions 194
5.37 Photograph of the wire scanner 195
5.38 Rate modulation by wire scanner use 196
5.39 Investigation of the Penning trap between spectrometer and e-gun . 197
5.40 High B-field background for low potential values up to -10 kV 198
5.41 Remaining particle traps in PSII 200

A.1 Swagelok® connectors 205
A.2 O-ring sealing technique for DN500+ 206
A.3 Leak testing with pressure rise method 209
A.4 Turbomolecular pump working principle 211
A.5 Turbomolecular pump characteristics 212
A.6 Rotary positive-displacement pump 215
A.7 Manufacturing of a getter pump 216
A.8 Temperature distribution during baking of the pre-spectrometer . . . 220
A.9 Hot cathode vacuum gauge set-up 223
A.10 Quadrupole mass spectrometer 224
A.11 Residual gas analysis after getter activation 225

B.1 Deviation of fit values for FUG calibration 229
B.2 Output voltage measurement of FUG3 230
B.3 Output voltage measurement of FUG4 231

D.1 Pre-spectrometer heating/cooling system diagram 236

List of Tables

3.1 Ramping speeds for the superconducting magnets 67
3.2 Blind diameters of the PBSS 70
3.3 Comparison of FPD and SPD requirements 89
3.4 Voltages and devices used for the operation of the SPD 93
3.5 Averaged energy resolutions ΔE of the SPD at $T = -56°C$ 98
3.6 Dead time of the UW-DAQ 104

5.1 Pre-spectrometer background rate potential dependence 138
5.2 Potential dependence for constant ΔU 140
5.3 Magnetic field strength dependence of pre-spectrometer background rate 141
5.4 Negative ion peak location 146
5.5 Event rates as a function of the potential distribution at high pressures 159
5.6 Magnetic field dependence of the background rate for B>2 T 164
5.7 High B-field background longtime stability 166
5.8 Background rate as a function of the potential at B=3.44 T 168
5.9 Background rate as a function of the potential at B=4.5 T 169
5.10 U_0-peak location as a function of the potential 173
5.11 Rate dependence with wire electrode more negative 177
5.12 Rate dependence on west cone electrode potential 179

B.1 Fit-values for the calibration of FUG3 and FUG4 229

List of Abbreviations

ADC	Analog to Digital Converter
APE	Anti-Penning Electrode
BEM	Boundary Element Method
CC	Charged Current
CDM	Cold Dark Matter
CF	ConFlat®
CMBR	Cosmic Microwave Background Radiation
CPS	Cryogenic Pumping Section
DAQ	Data AcQuisition
DIN	Deutsche Industrie Norm
DPS	Differential Pumping Section
E/A	European/Asien
EMD	ElectroMagnetic Design
EMI	ElectroMagnetic Interference
ES	Elastic Scattering
FDM	Finite Difference Method
FEM	Finite Element Method
FPD	Focal Plane Detector
FPGA	Field Programmable Gate Array
FUGx	Name for power supply with descriptor x
FWHM	Full Width Half Maximum
GALLEX	GALLium EXperiment
GERDA	GERmanium Detector Array
HBB	High B-field Background
HDM	Hot Dark Matter
HV	High Voltage
HV	High Vacuum
IPE	Institute of Data Processing and Electronics
JFET	Junction gate Field-Effect Transistor
KATRIN	KArslruhe TRItium Neutrino
KF	Klein Flange

LSM	Laboratoire Souterrain de Modane
lN_2	liquid Nitrogen
LoI	Letter of Intent
LV	Low Vacuum
MAC-E	Magnetic Adiabatic Collimation combined with Electrostatic
MARE	Microcalorimeters for A Rhenium Experiment
MCC	Magnetron Cut-off Criterion
MV	Medium Vacuum
NC	Neutral Current
NEG	Non Evaporable Getter
NI cFP	National Instruments compact FieldPoint
ORCA	Object oriented Real-time Control and Acquisition
PAC	programmable automation controllers
PBSS	Pneumatic Blind and Shutter System
PID	Process and Instrumentation Diagram
PSI	Pre-Spectrometer I set-up
PSII	Pre-Spectrometer II set-up
PSIII	Pre-Spectrometer III set-up
PT	Penning Trap
QMS	Quadrupol Mass Spectrometer
R&D	Research and Development
RGA	Residual Gas Analysis
ROI	Region Of Interest
SAGE	Soviet-American Gallium Experiment
SCS	Slow Control System
SEM	Secondary Electron Multiplier
SK	Super-Kamiokande
SM	Standard Model
SNIIa	SuperNova IIa
SNO	Sudbury Neutrino Observatory
SPD	Segmented PIN Detector
SRIM	Stopping and Range of Ions in Matter
TLK	Tritium Laboratory Karlsruhe
TMP	TurboMolecular Pump
UHV	Ultra High Vacuum
UV	Ultra Violet
UW	University of Washington
VME	Virtual Machine Environment
WGTS	Windowless Gaseous Tritium Source
WMAP	Wilkinson Microwave Anisotropy Probe

Chapter 1

Introduction

In 1930 Wolfgang Pauli postulated the existence of a new particle, thereby creating single-handedly a new field of research, which today thrives more than ever. While Pauli's idea saved the concept of energy and momentum conservation in the light of a continuous β spectrum, it was Enrico Fermi who was giving the particle its name by calling it the neutrino[1].

Today, the neutrino is an integral part of the Standard Model (SM) of particle physics. The SM comprises 12 fermions of spin-1/2 divided into two subgroups of six quarks (up u, down d, charm c, strange s, top t, bottom b) and six leptons (electron e^-, electron neutrino ν_e, muon μ^-, muon neutrino ν_μ, tauon τ^-, tau neutrino ν_τ) each arranged in three families or generations. Together with the antiparticles of opposite charge, these are the constituents of matter as it is known today.

The experimental detection of Pauli's postulate resulted from the work of F. Reines and C. Cowan taking place in 1956 [Cow56, Rei56]. The experiment detected positrons and neutrons created via the process of electron antineutrino capture by a proton (inverse β decay):

$$p + \bar{\nu}_e \rightarrow n + e^+ \tag{1.1}$$

With the second neutrino, the ν_μ being detected at BNL in 1962, it took another 38 years until with the tau-neutrino ν_τ the last particle of the SM was found in 2000 [Kod08].

All the fundamental particle masses are now known with an accuracy which has been significantly improved upon in the last decades. The only exception are the electrically neutral neutrinos, which were massless fermions according to the SM. New discoveries of the last decade, however, have proven that neutrinos do possess mass thereby implying that the Standard Model description of elementary fermions is not complete and that physics beyond the SM exists, which can be investigated.

[1] In Pauli's first famous letter to his friends in the scientific community, he introduced the particle under the name of 'neutron'. Fermi changed the name to 'neutrino' in 1933 as one year earlier James Chadwick had discovered the neutron [Cha32] and claimed the name before Pauli went public.

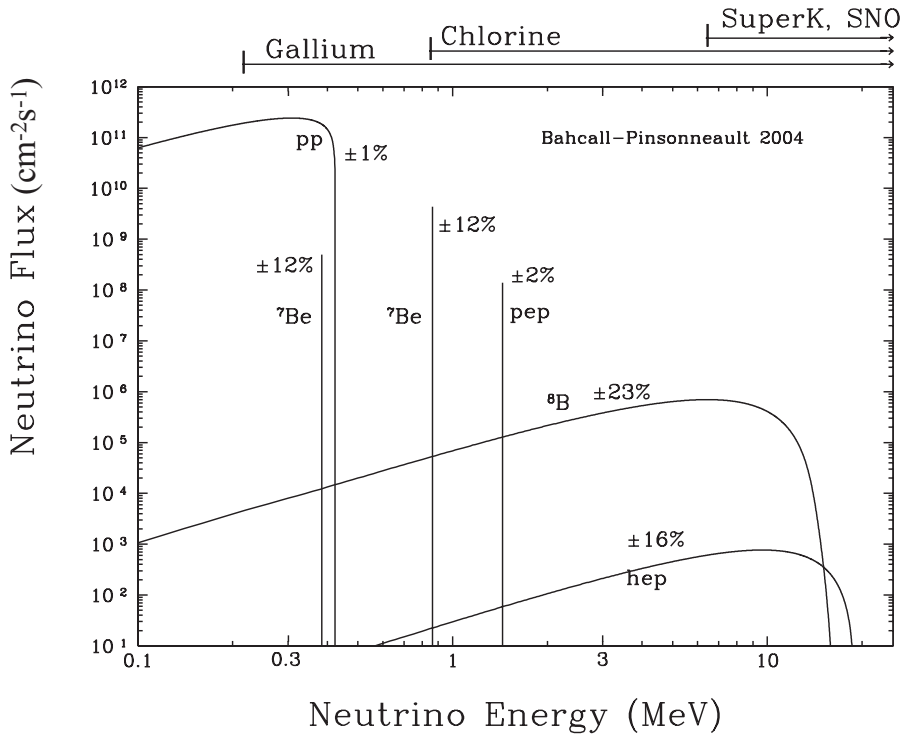

Figure 1.1: The solar neutrino fluxes from the different fusion reactions inside the core of the sun. The experimental sensitivity with regard to neutrino energy depends on the detection method used. The bars on top of the graph indicate the detection thresholds and areas of sensitivity for different detection media. Figure taken from [Bah04]

In the following, neutrinos and their weak interaction production mechanisms are discussed before the evidence for massive neutrinos is presented. This is followed by a discussion of the impact of massive neutrinos on different physics disciplines. The chapter is concluded with a concise overview over the different methods to discern the absolute neutrino mass value m_ν, and their mass pattern.

1.1 Neutrino sources

There is a variety of distinct neutrino sources, both of astrophysical origin as well as in the laboratory, which are discussed below.

Solar neutrinos The nuclear fusion reactions inside the sun produce a multitude of neutrinos of different energies. The energy and neutrino production are dominated by the *pp* chain (98.4% of total energy production) with the basic reaction scheme given by eq. 1.2:

$$4p \longrightarrow {}^4He + 2e^+ + 2\nu_e. \tag{1.2}$$

On average, an energy of 26.73 MeV is produced of about 2 to 20 MeV are carried away by the neutrinos on average at the present temperature of the sun [KK97]. The neutrino fluxes, as presented in fig. 1.1, are the result of detailed calculations footing on the properties of the Standard Solar Model (SSM).

Primordial neutrinos After the Big Bang, the hot dense quark-gluon plasma expanded and cooled down. At time $t \sim 10^{-6}$ s the quark confinement started and the gluons and quarks did form hadrons. Due to the further expansion, the plasma temperature dropped steeply and the interaction rate of the neutrinos was falling below the expansion rate $H(t)$. Thus, the neutrinos could not remain in thermal equilibrium with the remaining particles of the plasma. At t$\sim$1 s and $T = 10^{10}$ K, which corresponds to an energy of $\sim$1 MeV[2], the neutrinos did 'freeze' out of the plasma and kept their thermal distribution at freeze-out time due to their ceased interaction with other particles. As a result, these neutrinos are still present in the universe in a number density comparable to the photons of the cosmic microwave background radiation (CMBR). The density of the neutrinos has been calculated to be N_{ν_j}=113 cm^{-3} for each neutrino flavour making them the second most abundant particle in the universe behind the 3 K photons with N$_\gamma$=411 cm^{-3} [Sch06].

After the freeze-out, the neutrinos subsequently cooled down to their present temperature of 1.9 K. An exceedingly small interaction cross-section of $\sigma \approx 10^{-54}\,\mathrm{cm}^2$ and their low energies below meV make their detection, at least in the nearer future, seem rather unrealistic. Nevertheless, the relic neutrinos are an important factor in large scale structure formation scenarios due to their relativistic free-streeming capabilities. For these reasons they are an integral constituent of hot dark matter (HDM) which is counteracting the 'clumping' effects caused by the cold dark matter (CDM) component. The presently assumed energy densities of the cosmological concordance model explaining the energy distribution in the universe is shown for comparison in fig. 1.2

Atmospheric neutrinos When entering the atmosphere, cosmic rays in the form of high energetic protons interact with the atomic nuclei of the molecules of the atmosphere. In these processes, kaons and pions are generated, which are energetic enough to create more secondary particles. After losing their energy they are unable to further create secondary particles and subsequently they decay into lighter particles according to the processes in eq. 1.3 [Sch97]:

$$\begin{aligned} p + N \rightarrow \pi^{\pm}, K^{\pm} + ... & \qquad (1.3) \\ \pi^+, K^+ \rightarrow \; \mu^+\nu_\mu; & \qquad \pi^-, K^- \rightarrow \; \mu^-\overline{\nu}_\mu \\ \hookrightarrow e^+\nu_e\overline{\nu}_\mu & \qquad \hookrightarrow e^-\overline{\nu}_e\nu_\mu \end{aligned}$$

Kaons, pions and their antiparticles decay into the corresponding muons and neutrinos under conservation of flavour and total lepton number L. The muons in turn

[2]Energy and temperature are interchangeable with $k_B T$ having the dimension of an energy. The conversion factor is 1 eV= $1.1605 \cdot 10^4\, k_B$ K [Sch06].

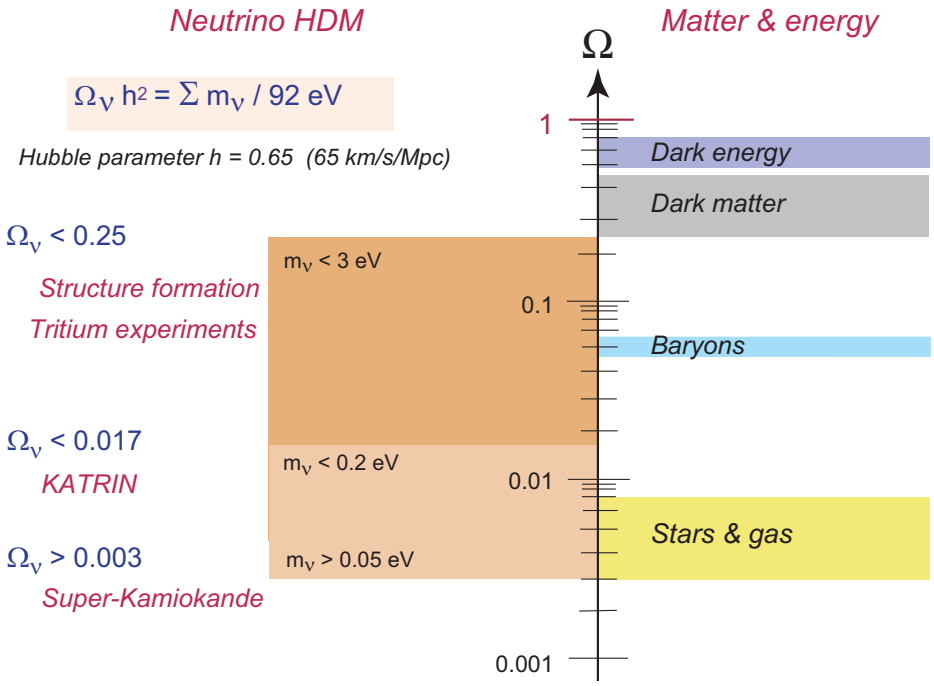

Figure 1.2: Constituents of the energy density of the universe. The energy densities Ω for the different constituents are given with regard to the critical density $\Omega_c = 1$ which is in agreement with a flat universe and the experimental data [Dun09]. The possible parameter space of neutrino mass is large enough so that the neutrino contribution to the energy density as hot dark matter can still be larger than that of the visible baryonic mass [Ang04].

decay into electrons, positrons and the corresponding neutrinos. The ratio of muon neutrinos to electron neutrinos is determined to be 2:1, however a quite different ratio was measured experimentally (see below)

Supernovae neutrinos The final stage in the life of a massive star is called supernova (SNIIa). Neutrinos have been identified to play a major role during the core-collapse of heavy progenitor stars with $M \gtrsim 8\,\mathrm{M}_\odot$. There are many different processes taking place during this last stellar phase. Most importantly, the entire gravitational energy is released when neutrinos are emitted. By observing a supernova's 10 s long neutrino pulse, one gains a deeper insight into the specific stages of the core-collapse and the subsequent explosion in which the outer shell of the star is blown away. Four phases of neutrino emission can be distinguished [APP07]:

core-collapse and initial rebound Electron capture by protons produces neutrons and electron neutrinos (deleptonisation). Most of the neutrinos are trapped by interactions with nucleons due to the huge matter density $>17\,\mathrm{kg/m^3}$.

few ms after core bounce When the supernova shock wave breaks through the

neutrino sphere a second deleptonisation phase starts creating electron neutrinos. A peak is visible in the neutrino flux spectrum.

stalling shockwave 'Neutrino heating' reactivates the explosion mechanism. Neutrinos of all flavours including the antineutrinos are produced by the hot proto-neutron star.

thermal cooling of proto-neutron star During the cooling phase more neutrinos and antineutrinos of all flavours are produced.

A fraction of 99% of the energy of the supernova is carried away by the neutrinos. Interestingly, if the proto-neutron star is too heavy, it collapses and transforms into a black hole a few seconds after the initial collapse. This event is expected to be marked by an abrupt termination of the neutrino signal when the gravitational force of the black hole interacts on the neutrino sphere.

Artificial neutrino sources Neutrinos are also 'artificially' generated by man-made devices. Nuclear fission reactors produce electron antineutrinos as a result of the β^- decay of the neutron rich fission products. An average of 6 neutrinos per fission reaction is generated with energies in the range of 1-10 MeV.

Additionally, neutrinos are produced by using high-energy accelerators to create dedicated neutrino beams tailored with regard to energy distribution or flavour.

Typically, an intense proton beam from a synchrotron is extracted and dumped onto a target of light nuclei which maximises the pion and kaon production rate. These particles are differentiated according to their charge and fed into an evacuated decay tunnel, where they decay into the corresponding muons and muon neutrinos. To prevent a 'contamination' of the muon and muon neutrino beam by other flavours (from muon decay), the hadrons and muons are directed into a 'beam dump' of a dense material like iron or rock. There, they are absorbed by nuclear reactions and lose energy due to ionisation and radiation losses [Sch97].

The set-up typically allows to choose between a neutrino beam with broad energy distribution but high intensity or vice versa, with a distinct neutrino energy but rather low intensity. Another distinction can be made with regard to the neutrino energy. Depending on the proton accelerator energies, the neutrino energy can range from 10-10^2 MeV for low-energy accelerators and 10^3-10^5 MeV for high-energy accelerators, respectively.

1.2 Massive neutrinos

In the framework of the SM, neutrinos were considered to be massless spin-1/2 particles. Early measurements of the solar neutrino flux detected a difference between the SSM predicted flux [Bah06] and the experimental flux. Experiments like

Homestake [Dav94, Cle95], GALLEX[3] [Ans92, GAL99], SAGE[4] [Abd94, Abd96] and Kamiokande[5] [Hir92] observed a factor 2-3 discrepancy from the SSM predicted values. Some authors attributed the discrepancy to astrophysical effects emphasizing uncertainties in the SSM, while others outlined unknown neutrino properties, on the other hand. Already at an early stage, neutrino oscillations[6] were named as a possible solution. In 1998, the Super-Kamiokande [Fuk98, Fuk02, Hos06] water-Cherenkov detector provided unambiguous evidence of the existence of neutrino oscillations with the charged-current (CC) reaction

$$\nu_l + N \to l + N'. \tag{1.4}$$

by observing a top-down asymmetry of muon-like events[7].

The detection of a deficit of muon neutrinos as a function of the atmospheric neutrino's path length is a clear sign for neutrino oscillations. The results show that atmospheric muon neutrinos traversing the earth have undergone a flavour transformation while muon neutrinos created in the atmosphere above the detector have not. This was the first prove that neutrinos do possess a non-vanishing mass, which is a prerequisite for neutrino oscillations, the subject of the following section.

1.2.1 Neutrino oscillation

The fundamental concept of neutrino oscillations is based on the fact that the flavour eigenstates $|\nu_\alpha\rangle$ with $\alpha = e, \mu, \tau$, which are partaking in the weak interaction, do not possess a discrete mass, but are linear combinations of the mass eigenstates $|\nu_j\rangle$ ($j = 1, 2, 3$) with masses m_i [Sch97]. A unitarian mixing matrix U connects flavour and mass eigenstates:

$$\begin{pmatrix} \nu_e \\ \nu_\mu \\ \nu_\tau \end{pmatrix} = \begin{pmatrix} U_{e1} & U_{e2} & U_{e3} \\ U_{\mu 1} & U_{\mu 2} & U_{\mu 3} \\ U_{\tau 1} & U_{\tau 2} & U_{\tau 3} \end{pmatrix} \begin{pmatrix} \nu_1 \\ \nu_2 \\ \nu_3 \end{pmatrix} \tag{1.5}$$

The mixing matrix can be decomposed into the more explicit version [APP07]:

$$U = \begin{pmatrix} 1 & 0 & 0 \\ 0 & c23 & s23 \\ 0 & -s23 & c23 \end{pmatrix} \times \begin{pmatrix} c13 & 0 & s13 \cdot e^{i\delta} \\ 0 & 1 & 0 \\ -s13 \cdot e^{i\delta} & 0 & c13 \end{pmatrix} \times \begin{pmatrix} c12 & -s12 & 0 \\ s12 & c12 & 0 \\ 0 & 0 & 1 \end{pmatrix} \times \begin{pmatrix} 1 & 0 & 0 \\ 0 & e^{-i\phi_2/2} & 0 \\ 0 & 0 & e^{-i(\phi_3/2+\delta)} \end{pmatrix} \tag{1.6}$$

[3] GALLium EXperiment
[4] RuSsian American Gallium Experiment
[5] KAMIOKA Neutrino DEtector
[6] The possibility of neutrino oscillations was first proposed by Pontecorvo [Gri69, Akh93] in 1957.
[7] Super-Kamiokande's detection algorithm is only sensitive to electron and muon events.

with $c_{ij} = cos\theta_{ij}$ and $s_{ij} = sin\theta_{ij}$ being trigonometric representations of the mixing angle θ as well as the phases δ, ϕ_2 and ϕ_3 required for the description of CP violation. The phases ϕ_2 and ϕ_3 are non-zero only in the case of neutrinos being Majorana particles. However, neutrino oscillation experiments are not able to disentangle the Dirac or Majorana nature of the neutrino [Ott08].

Together with the time evolution of the mass eigenstates ν_j

$$|\nu_j(t)\rangle = e^{-iE_j t/\hbar} |\nu_j\rangle \tag{1.7}$$
$$\text{with} \quad E_j = \sqrt{p^2c^2 + m_j^2c^4} \approx pc + \frac{m_j^2c^3}{2p} \quad \text{for} \quad p \gg m_j c$$

(with c the speed of light and p the momentum of the neutrino), the time development of a pure flavour eigenstate $|\nu_\alpha\rangle$ can be written as

$$|\nu(t)\rangle = \sum_j U_{\alpha j} e^{-iE_j t/\hbar} |\nu_j\rangle = \sum_{j,\beta} U_{\alpha j} U^*_{\beta j} e^{-iE_j t/\hbar} |\nu_\beta\rangle \,. \tag{1.8}$$

This formalism shows that the neutrino flavour states change over time. The probability of the change from $|\nu_\alpha\rangle$ into $|\nu_\beta\rangle$ is given by [Sch97]

$$P(\alpha \to \beta; t) = |\sum_j U_{\alpha j} U^*_{\beta j} e^{-iE_j t/\hbar}|^2 \tag{1.9}$$
$$= \sum_{j,l} U_{\alpha j} U^*_{\alpha l} U^*_{\beta j} U_{\beta j} e^{-i(E_j - E_l)t/\hbar} \tag{1.10}$$
$$\text{with} \quad (E_j - E_l)t = \frac{\Delta m^2_{jl}}{2} \cdot \frac{L}{E} \quad \text{and} \quad \Delta m^2_{jl} = |m_j^2 - m_l^2|.$$

where E denotes the kinetic energy of the neutrino in GeV and L corresponds to the distance between source and detector in units of km. Eq. 1.9 thus proves that neutrinos possess a non-vanishing mass and furthermore that the mass eigenstates have to differ. The ratio L/E can be seen as the decisive experimental variable:

$L/E \ll 1/\Delta m^2$ no oscillations can be detected yet as the traveled distance L is too short for a given energy E_ν,

$L/E \sim 1/\Delta m^2$ are the most favourable conditions for the detection of a flavour oscillation,

$L/E \gg 1/\Delta m^2$ the oscillation cycles are too fast and only an average transition probability $P = 1/2$ can be determined.

Although Super-Kamiokande (SK) has given prove for the existence of neutrino oscillations in the case of atmospheric neutrinos, the solar neutrino problem was still not resolved in 1998. This has finally been achieved by the SNO[8] experiment [SNO01, SNO05b, SNO05a]. While SNO shares the basic detector principle

[8] Sudbury Neutrino Observatory

of water-Cherenkov imaging with SK, SNO uses heavy water D_2O instead of light water H_2O as does SK. Using deuterons as target, SNO is sensitive to neutral-current (NC) reactions also besides being able to detect electron-scattering (ES) and charged-current (CC) reactions. SNO can thus identify all neutrino flavours simultaneously:

$$ES: \quad \nu_x + e^- \rightarrow \nu_x + e^-, \qquad \Phi_{ES} = \Phi_e + 0.16\Phi_{\mu,\tau}, \tag{1.11}$$

$$CC: \quad \nu_e + d \rightarrow p + p + e^-, \qquad \Phi_{CC} = \Phi_e, \tag{1.12}$$

$$NC: \quad \nu_x + d \rightarrow p + n + \nu_x, \qquad \Phi_{NC} = \Phi_e + \Phi_{\mu,\tau} \tag{1.13}$$

Measuring for the first time the bolometric neutrino flux from the sun, the results agree with the SSM predictions within the given uncertainties [Bah04].

The latest results with regard to the quadratic mass differences Δm^2_{jl} [Ams08]:

$$\Delta m^2_{21} \approx (7.59^{+0.19}_{-0.21}) \cdot 10^{-5} eV^2/c^4 \tag{1.14}$$

$$\Delta m^2_{32} \approx (2.43 \pm 0.13) \cdot 10^{-3} eV^2/c^4 \tag{1.15}$$

in the solar and atmospheric sector imply very small mass splittings.

1.3 Determination of the neutrino masses

Neutrino oscillation experiments determine the mass differences can be determined but do not fix the absolute mass scale. Therefore, it is still not known whether the neutrino mass eigenstates are following a hierarchical pattern, an inverted hierarchy, or a quasi-degenerate mass distribution, see fig. 1.3. An important benchmark for theory is the orientation of the mass differences. In the case of a normal hierarchy they follow $m_1 \ll m_2 \ll m_3$, in case of an inverted hierarchy the pattern $m_3 \ll m_1 \ll m_2$ are realised. An answer to this question has great impact on the understanding of the theoretical models.

The experimental search for the absolute neutrino mass can be subdivided into indirect and direct methods. In the following, these methods are described in more detail.

1.3.1 Indirect searches

Indirect methods are quite sensitive on even small neutrino mass values, however, they have to rely on model-dependent predictions. As a result, the systematic uncertainties increase considerably, even leading to the point with the measurement method not being sensitive to the neutrino mass ($0\nu\beta\beta$ in the case of Dirac ν's, see below).

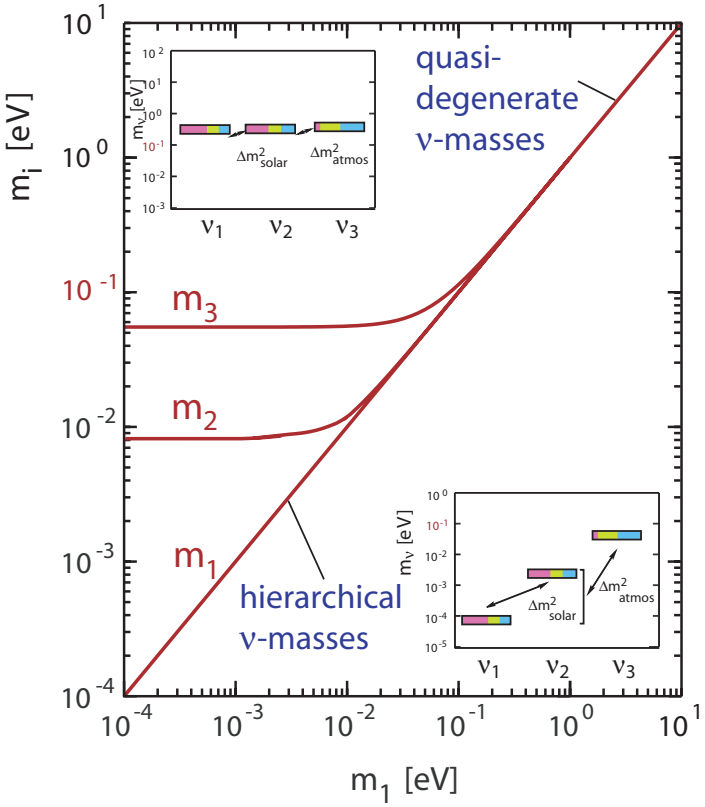

Figure 1.3: Neutrino mass pattern. The mass eigenstates m_j are plotted as a function of the lightest mass eigenstate m_1 in case of a normal hierarchy. The quadratic mass differences are determined by solar (Δm^2_{sol}) and atmospheric (Δm^2_{atmos}) neutrino oscillations with the two possible scenarios of degenerate ($\Delta m \ll m_1$) and hierarchical neutrino masses ($\Delta m \gg m_1$). Figure taken from [Ang04].

1.3.1.1 Cosmological methods

Cosmological studies based on observations of large-scale structures in the Universe and the microwave background radiation allow to infer the contribution of relic neutrinos to the hot dark matter component. With the experimental CMBR results of WMAP[9] [Ben03] alone, it is possible to give an upper limit on the neutrino mass of [Dun09]:

$$\sum_{j=1}^{3} = m_j < 1.3\,\mathrm{eV/c^2} \quad (95\%\,\mathrm{CL}). \tag{1.16}$$

By cross-correlation of different data sets, the limits on the neutrino mass are even

[9] Wilkinson Microwave Anisotropy Probe

more constrained, thus breaching the 1 eV threshold [Goo06]:

$$\sum_{j=1}^{3} = m_j < 0.62\,\mathrm{eV/c^2} \quad (95\%\,\mathrm{CL}). \tag{1.17}$$

In the latter analysis, data of WMAP were combined with large scale structure, supernova Ia and Lyman-α investigations. If the constraints of the analysis, e.g. limiting of the number of neutrinos to $N_\nu = 3$, would yield even lower upper limits of the neutrino mass sum. However, these results crucially rely on assumptions of the nature of dark energy and are only valid if the ΛCDM concordance model is correct.

1.3.1.2 Neutrinoless double beta decay

The second order weak process of double β decay is observable when (a) the daughter nucleus of a single β decay is heavier than the parent nucleus and (b) the second daughter nucleus is lighter than the mother nucleus. This is the case for gg nuclei for which a single β decay would create a uu nucleus with a smaller binding energy. Thus, single β decay is prohibited but double β decay is allowed. The theory of neutrino associated double β decay ($2\nu\beta\beta$) has been successfully confirmed. Here, two electrons and two electron antineutrinos are emitted in the process, indicating that two single β decays happen simultaneously. Another possible decay mechanism was proposed by W.H. Ferry in 1939 [Fur39]. Instead of emitting two neutrinos, one neutrino emitted from the first decay vertex is absorbed at the second. This is only possible if the neutrino is a Majorana particle, which means it is its own antiparticle, and secondly, a helicity flip has to occur, as only a right-handed neutrino can be absorbed at the second vertex. This last prerequisite necessitates a non-vanishing neutrino mass. Thus, the occurrence of a neutrinoless double β decay ($0\nu\beta\beta$) would signify the existence of physics beyond the Standard Model.

In the case of light Majorana neutrinos mediating the $0\nu\beta\beta$ process, a decay rate of [Aal04]

$$[T^{0\nu}_{1/2}(0^+ \to 0^+)]^{-1} = G^{0\nu}(E_0, Z)\,|M^{0\nu}_{GT} - \frac{g_V^2}{g_A^2} M^{0\nu}_F|^2\,\langle m_{\beta\beta}\rangle^2 \tag{1.18}$$

can be expected, with $G^{0\nu}$ denoting the phase space integral, $\langle m_{\beta\beta}\rangle$ the effective neutrino mass and $M^{0\nu}_{GT}$, $M^{0\nu}_F$ the nuclear matrix elements. With the knowledge of the nuclear matrix elements the effective Majorana mass $\langle m_{\beta\beta}\rangle$ can be deduced, which is a coherent sum over all the m_j decay amplitudes:

$$\langle m_{\beta\beta}\rangle = |\sum_j |U_{ej}|^2\, m_{\nu_j} e^{i\alpha_j}|. \tag{1.19}$$

Thus, information regarding the absolute neutrino mass can be won. However, the effective Majorana mass $\langle m_{\beta\beta}\rangle$ carrying complex neutrino phases can be subject to

annihilations when the decay amplitudes are summed up. Therefore, $\langle m_{\beta\beta} \rangle$ may be significantly smaller than the mass eigenstates $|\nu_j\rangle$.

At present, several next generation $0\nu\beta\beta$ experiments, such as GERDA[10] [GER05] and Majorana [Gui08], are in their final stages of development. With these experiments, the present upper limit set by the Heidelberg-Moscow experiment by investigating the decay of enriched ^{76}Ge of [Kla01]

$$\langle m_{\beta\beta} \rangle < 0.35\,\mathrm{eV/c^2} \tag{1.20}$$

will be further reduced if no positive signal is detected. They will also verify or refute the positive detection claim of

$$\langle m_{\beta\beta} \rangle = 0.32 \pm 0.03\,\mathrm{eV/c^2} \tag{1.21}$$

published by a subgroup of the Heidelberg-Moscow Collaboration [KK06].

The potential impact of these experiments is high, however, they remain completely model-dependent. The uncertainty of the nuclear matrix introduces large systematic effects up to a factor. Nevertheless, these experiments aim at breaching the $0.1\,\mathrm{eV/c^2}$ threshold by increasing the source material and by strongly improving the background reduction techniques.

1.3.2 Direct search methods

Direct methods to determine the neutrino mass rely on the relativistic energy momentum relation

$$E^2 = p^2c^2 + m^2c^4 \tag{1.22}$$

in combination with energy and momentum conservation.

1.3.2.1 Time of flight studies

Neutrinos from supernovae are of great interest to astrophysicists. First, the neutrinos released during the last phases in the life of a heavy star may reveal information with regard to the development of the core-collapse, see above. Secondly, massive neutrinos do not propagate with the speed of light but only close to it. The discrepancy in speed is directly correlated to the neutrino energy. Thus, neutrinos of different energies E_1 and E_2 will arrive at different times t_1 and t_2 in the neutrino detector at a distance L to the supernova location specified in units of km. The time difference Δt is given as [Sch97]

$$\Delta t = t_2 - t_1 = \Delta t_0 + \frac{Lm_\nu^2}{2c}\left(\frac{1}{E_2^2} - \frac{1}{E_1^2}\right). \tag{1.23}$$

[10] GERmanium Detector Array

While Δt, L, E_1, E_2 are measured, Δt_0 depends on model predictions. An upper limit for the supernova SN1987A was derived for the electron neutrino mass [Ams08]:

$$m_{\nu_e} < 5.7\,\mathrm{eV/c^2}. \tag{1.24}$$

This limit is already in the range of the best laboratory experiments. Neutrino detection capabilities have vastly improved in the last two decades so that a nearby galactic supernova would yield a massive gain in information for neutrino and supernova physics.

1.3.2.2 Kinematics of weak decays

Investigation of weak decays as for example the β decay allows to deduce the neutrino mass without use of model-dependent predictions. This is possible by measuring the β spectrum near the endpoint energy E_0 as will be explained in more detail in section 2.1. The experimental observable here is the effective neutrino mass m_{ν_e}

$$m_{\nu_e}^2 = \sum_{j=1}^{3} |U_{ej}|^2 \cdot m_j^2, \tag{1.25}$$

which can be deduced from the spectral distortion near the endpoint and which depends on the neutrino's rest mass. Contrary to the effective Majorana mass $\langle m_{\beta\beta} \rangle$ of eq. 1.19, m_{ν_e} is an incoherent sum over the electron neutrino mass eigenstates so that no cancelation processes can occur. This can be considered as the biggest advantage, as the measurement results are thus completely independent from predictions of theoretical models.

The experiments to directly measure the β spectrum either use calorimetric methods with bolometers as a combined source/detector set-up or electromagnetic spectrometers which analyze only the decay-electrons at the highest energy. Both experimental methods have different advantages and drawbacks. The spectrometer configuration recently employed by the Mainz and Troitsk groups have achieved the best upper limit by using tritium as β emitter of $m_\nu < 2\,\mathrm{eV/c^2}$ (95%C.L.) [Yao06] (see section 2.1.

The MARE collaboration [Mon06, And07], which is following the bolometer approach, has chosen ^{187}Re as beta-emitting element. Rhenium is distinguished as the β emitter with the lowest endpoint energy, a fact which has a beneficial influence on the event rate in the endpoint region. The MARE collaboration is building on the success of the Milano and Genoa experiments which achieved an upper limit on the electron neutrino mass of [Sis04]

$$m_{\nu_e} < 15\,\mathrm{eV/c^2} \quad 90\%\,\mathrm{CL}. \tag{1.26}$$

thus proving that the calorimetric method can be considered as a viable method, albeit with still limited sensitivity. At present, this method needs time to mature. A

ten year period of R&D efforts is expected to be competitive with the next generation electromagnetic spectrometer mass sensitivity of $0.2\,\mathrm{eV/c^2}$ (90% CL), as featured by the experiment KATRIN.

Considering the importance of neutrino mass searches, it is evident that an experiment like KATRIN is an essential cornerstone to elucidate the intrinsic properties of neutrinos. With its unmatched model-independent sensibility to neutrino masses it will investigate the sub-eV mass region with high sensitivity. Even an upper limit in the range of KATRIN's sensitivity would represent a huge gain in information and indicate a hierarchical pattern or inverted hierarchy of neutrino mass eigenstates. Following recent results from double β decay and cosmological studies, KATRIN may very well be ideally suited to determine the absolute electron antineutrino mass, which would in turn have great implications on cosmology as well as particle and astrophysics.

1.4 Outline

In the framework of this thesis a first step in direction of the commissioning of the KATRIN experiment has been done by investigating the vacuum and electromagnetic properties of the pre-spectrometer, a pre-stage to the main spectrometer, which is an essential major component of the KATRIN set-up. Chapter 2 first introduces the KATRIN experimentith the focus on the MAC-E filter properties which are key for KATRIN's sensitivity. In chapter 3, the pre-spectrometer's integration into a test set-up which allows to investigate the spectrometer's MAC-E filter qualities as well as the ultra high vacuum performance is described in detail. Also included in this description are the subsystems to generate monoenergetic electrons and the detector system comprised of a segmented silicon PIN diode and a VME-based data acquisition system. The description is completed by detailing the controlling and monitoring system which allows operation of the test set-up by remote control and continuous data storage of the set-up parameters. Following the set-up description, initial measurements of the electromagnetic properties resulting in the discovery of a background source are discussed in chapter 4. The solution for the mitigation of this background source are presented as well. Chapter 5 is comprised of a detailed investigation of the improved pre-spectrometer set-up which now allows a closer inspection of the present background components. The description of the background observations lead to a proposal for a second improvement of pre-spectrometer's electromagnetic properties which aim at reducing the background of the pre-spectrometer system into the mHz range.

Chapter 2

Measuring the neutrino mass - the KATRIN experiment

Ever since Pauli postulated the neutrino in 1930, the interest in this particle did not wane but increase. Even after solving the solar neutrino problem by proving the existence of neutrino oscillations [cite sno sk], the intrinsic properties of the neutrino are not completely understood.

The continued existence of the research subject *neutrino physics* most vividly shows that this particle must have several interesting properties to warrant the ongoing interest. In fact, the neutrino is the only known existing elementary particle for whom the exact mass value has not been determined. This fact alone is in itself an excellent reason to justify the huge interest in this particle. Additionally, this interest is not limited to particle physics – other disciplines like astrophysics and cosmology also show a strong interest in the particles's characteristics as presented in chapter 1.2.

The means to investigate the mass of the neutrino are quite diverse. The best upper limit to date has been found in direct measurements – the kinematic investigation of tritium β decay performed by the Mainz and Troitsk collaborations yielding $m_\nu < 2\,\mathrm{eV/c^2}$ (95%C.L.) [Yao06]. Indirect searches already proclaim lower limits in the sub-eV region [Han07, Han08, KK06]. These methods are highly model dependent. Thus further evidence is needed, preferably coming from measurements with a model independent approach, to scrutinise these results. Therefore, a next generation tritium β decay experiment investigating the sub-eV mass region in parallel to indirect searches is the ideal partner in determining the neutrino mass.

The KArlsruhe TRItium Neutrino experiment (KATRIN) is the next generation experiment to investigate the mass of the electron anti-neutrino directly and model-independently. The improved design of KATRIN allows for an increase in sensitivity which is defined by the systematic and statistic uncertainties on m_ν^2.

After three years of data taking these are expected to be of the same size resulting in a mass sensitivity of $0.2\,\mathrm{eV/c^2}$ (90% C.L.) if KATRIN does not detect a positive

signal after these three years. Thus, the experimental sensitivity for the electron neutrino mass will be lowered by an order of magnitude. The discovery potential for a $0.35\,\mathrm{eV/c^2}$ neutrino mass is $5\,\sigma$. With this level of sensitivity KATRIN will have strong influences on cosmological models by limiting or defining the role of neutrinos as part of the Hot Dark Matter.

The KATRIN Collaboration consists of 14 European and American institutions, also incorporating the groups of Mainz and Troitsk. Thus excellent expertise in tritium β decay research has been assembled. The experiment is set up at Forschungszentrum Karlsruhe (FZK). The decision regarding the location was strongly influenced by the then already existing Tritium Laboratory Karlsruhe (TLK). It is the only European non-military institute granted the license for tritium handling on large scales which are needed to operate KATRIN.

The next chapter will properly motivate the use of tritium as a source routinely deployed in β decay experiments by presenting the necessary prerequisites and describe the KATRIN set-up in detail. It will focus on the design of the spectrometer used for the energy analysis of the β decay electrons and close with a discussion of the objectives and sensitivity of the KATRIN experiment.

2.1 Tritium β decay

The advantages of a kinematic investigation of the single β decay (direct measurement, model independent) have been discussed earlier (see chapter 1.3.2.2). A suitable source-candidate for β decay has to provide a high signal rate in the endpoint region of the β decay spectrum.

In the tritium β decay a tritium atom decays into a $^3He^+$ ion, an electron e^- as well as an electron anti-neutrino $\overrightarrow{\nu}_e$:

$$^3H \rightarrow {}^3He^+ + e^- + \bar{\nu}_e \tag{2.1}$$

In a first approximation the helium ion is considered to be too heavy to carry away kinetic energy from the decay. As a result the total energy is bestowed both to the electron and the anti-neutrino. For the electron, the resulting energy spectrum is shown in fig. 2.1.

The calculation of the β spectrum is based on Fermi's Golden Rule

$$\frac{d^2N}{dt\,dE} = \frac{2\pi}{\hbar}\,|\mathcal{M}|^2\,\rho(E). \tag{2.2}$$

The transition matrix element $\mathcal{M}$ together with the density of final states $\rho(E)$ determines the number of electrons in an energy interval [E,E+ΔE]. The density

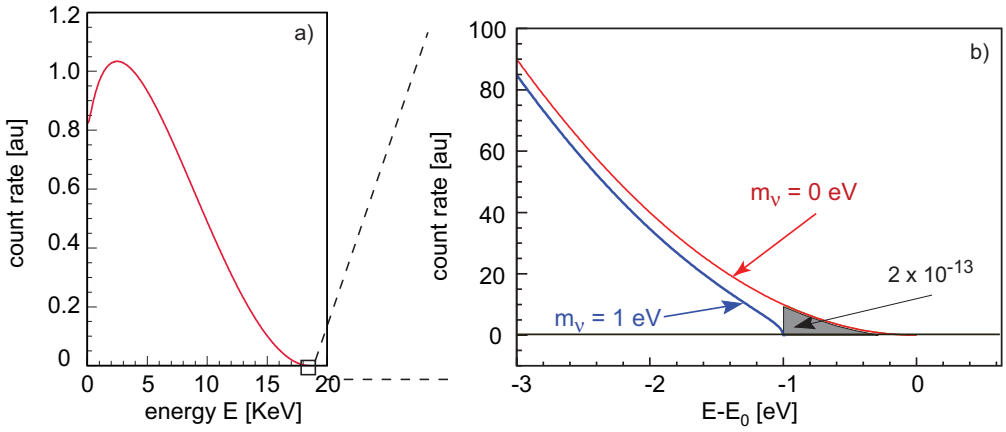

Figure 2.1: The theoretical β decay spectrum of tritium.
a) complete energy spectrum of β decay electrons.
b) endpoint region around 18.575 keV enlarged. Only in this region the influence of a non-zero neutrino mass is visible. The red line symbolises the a β decay spectrum with a vanishing neutrino mass and is compared to the spectrum for a neutrino mass of $1\,\mathrm{eV/c^2}$ (blue line). The blue line features lower count rates overall and reaches an endpoint energy 1 eV earlier than the red line. The decay-rate in the endpoint region is exceedingly small as illustrated by the grey area. Graph taken from [Ang04]

and the nuclear matrix the β spectrum can be written [Alt03]:

$$\frac{d^2N}{dt\,dE} = A(E)\,\sqrt{(E_0-E)^2 - m^2(\overline{\nu}_e)\,c^4}\;\Theta(E_0-E-m(\overline{\nu}_e)\,c^2) \tag{2.3}$$

$$\text{with } A(E) = \frac{G_F^2\,cos^2\theta_C}{2\pi^2\hbar^7}\,\left|\mathcal{M}^2\right|\;F(E,Z+1)\,p_e\,(E+m_ec^2)\,(E_0-E) \tag{2.4}$$

G_F:	Fermi constant	Θ_C:	Cabibbo angle
M:	nuclear matrix element	E_0:	endpoint energy for $m_\nu = 0$
p_e:	electron momentum	m_e:	mass of electron
$F(E,Z+1)$:	Fermi function		

Fig. 2.1(b) illustrates the signature of a non-zero neutrino mass compared to the expected shape and endpoint energy of neutrino with mass zero. Only a small energy interval $E_0 - E$ close to the β-endpoint carries information on the neutrino mass. However, the count rate in this endpoint region drops according to a factor $1/E_0^3$ (this can be derived by integrating equation 2.4). Therefore, the following favourable qualities are required for β decay sources:

1. high activity, corresponding to a short half life $t_{1/2}$
2. low endpoint energy

Only by combining these two properties, the signal rate in the critical area close

to the endpoint region will be sufficiently high to be used in a next generation experiment for exploration of the sub-eV region of neutrino masses.

The β-unstable element with the lowest endpoint energy of $E_0 = 2.47\,\mathrm{keV}$ is $^{187}\mathrm{Re}$ [Arn03]. With a half lifetime of $t_{1/2} = 43.2\,\mathrm{Gy}$ [Arn03], the signal rate is limited and the active bolometers used in this are not yet competitive with the spectrometer method employed by the Mainz and Troitsk experiments [Sis07]. Both experiments used molecular tritium as a source material with the following advantageous properties as a β emitter [Ang04]:

1. **Second lowest endpoint energy $\mathbf{E_0}$=18.6 keV.** This low endpoint energy maximises the rate close to the endpoint region. It also reduces the complexity of the experimental set-ups by requiring a retarding potential of less than 20 kV. The new KATRIN concept of using the vacuum vessel as guard electrode elevated to a potential equivalent to the endpoint energy $\mathrm{E_0}$ includes the challenge of reaching high voltage stability at 20 kV not only in vacuum but also in ambient pressure regimes.

2. **Short half lifetime $t_{1/2} = 12.3\,\mathbf{y}$** of the source material increases the β decay rate and thus the source strength. Only a high source strength allows KATRIN to investigate the endpoint region with enough statistics in an adequate running time of three to five years.

3. **Simple electron shell configuration** of the tritium isotope and $^3\mathrm{He}^+$ ion makes it possible to reliably calculate the necessary corrections for the atom or molecule and the corresponding interaction of the outgoing β electrons with the source material.

4. **Small probability for inelastic scattering.** The β electrons leaving the source do not suffer energy losses as the small nuclear charge minimises the probability of inelastic scattering of 20 keV β electrons leaving the molecular source.

5. **Pure phase space spectrum.** The nuclear transition of tritium β decay is super-allowed (^{3}H and ^{3}He are mirror nuclei); therefore there are no corrections of the nuclear transition matrix elements.

Tritium thus successfully meets all those requirements necessary as a β emitter source for the KATRIN experiment, making it the ideal isotope for a high sensitivity neutrino mass experiment.

2.2 The KATRIN set-up

Advances in neutrino mass sensitivity via kinematic investigations are not possible without changing key parameters of the predecessor experiments' design. Following

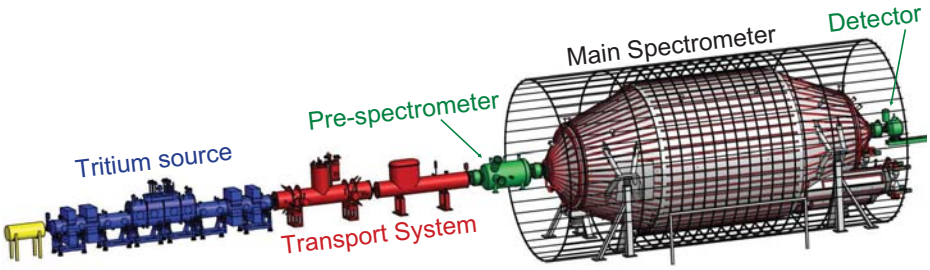

Figure 2.2: The experimental set-up of the Katrin experiment. Tritium gas which is injected into the windowless source tube is diffusing to both ends. The resulting β electrons are transported adiabatically along magnetic field lines, generated by superconducting solenoids. Before reaching the tandem spectrometer set-up tritium is completely retained by differential pumping and b cryosorption onto an argon frost layer. Following the energy analysis in the main spectrometer, electrons with sufficient energy to pass the electrostatic retarding potential are counted in the detector.

fig. 2.1 key requirements for tritium β decay experiments can be defined: a high signal rate in the kinematic endpoint region with a low background rate at the same time. Furthermore, a high energy resolution is necessary to reach the projected sensitivity.

The KATRIN set-up has been designed b optimising the following criteria:

- high signal rate S
- low background rate B
- high energy resolution $E/\Delta E$

The 70 m long experimental set-up is shown in fig. 2.2. The tritium β decay source is closed off on one side by a rear wall section with the purpose of calibration and monitoring. The other side opens to a transport section.

Here, electrons and other charged particles are guided along magnetic field lines while nearly all tritium molecules are extracted. Thus, only the β decay electrons reach two electrostatic spectrometers, a smaller one acting as a pre-filter for lower energy electrons, and a large main spectrometer for the final energy analysis. As the last part of the KATRIN set-up, a detector system will be installed for counting the transmitted electrons. Set apart from the main beam line, a third spectrometer will be utilised for calibration and monitoring purposes.

2.2.1 Source section

The two main requirements for the KATRIN source are high luminosity and small systematic uncertainties. Therefore, a molecular **w**indowless **g**aseous **t**ritium **s**ource (WGTS) design has been chosen. The WGTS consists of a 10 m long tube with an

inner diameter of $d_s = 90\,\text{mm}$ cooled down to 27 K by two phase neon. Molecular tritium gas of high purity ($> 95\,\%$) is continuously injected in the middle of the tube, creating a column density of $5 \cdot 10^{17}$ tritium molecules/cm^2. The free streaming molecules reach both ends of the tube by diffusion. It is of paramount importance to keep the column density stable at the 0.1% level. Only then systematic errors are kept on a level comparable to the statistical errors. Therefore, the demand on temperature stability is high: $\pm 30\,\text{mK}$ is the maximum allowed deviation during individual measurement phases. Furthermore, the gas injection rate (4.7 Ci/s)[1] has to be kept stable, too, at the 0.1% stability level. Thus the monitoring of the temperature values and of other source parameters will be crucial to the success of KATRIN. This is a challenging task, making the WGTS cryostat one of the most complex cryostats presently in development.

Electrons generated by tritium β decay are guided adiabatically by superconducting solenoids with a field strength of 3.6 T. Together with the field strength of the pinch magnet of 6 T (the strongest magnetic field in the beamline which is located in front of the detector chamber) a maximum accepted starting angle of $\theta_{max} = 51°$ is reached according to [Ang04]

$$\sin\theta_{max} = \sqrt{\frac{B_S}{B_{max}}}. \tag{2.5}$$

Thus electrons with a large starting angle and long path lengths in the WGTS will be suppressed. These values are the optimised results of design studies aiming at minimising the fraction of accepted electrons undergoing inelastic collisions inside the source. Electrons with starting angles lower than θ_{max} have a rather low probability of inelastic scattering. Correspondingly, the luminosity is only slightly reduced [Ang04]. With an effective source area of $A_S = 53\,\text{cm}^2$ and following equation 2.6

$$\Phi = \int BdA = B_S \cdot A_S = B_{max} \cdot A_{S,eff} = B_A \cdot A_A \tag{2.6}$$

the magnetic flux is calculated to 191 Tcm^2, injecting $9.5{\cdot}10^{10}$ electrons per second into the transport section.

2.2.1.1 Tritium circulation and retention system

The daily throughput of tritium through the WGTS of the KATRIN experiment is as high as the overall handling license granted to Tritium Laboratory Karlsruhe (TLK). Therefore, tritium pumped out of the beam line in the DPS stages is retained, purified, and sent back into the source via a closed loop. The main fraction (99%) of Tritium circulates in the Inner Loop while a small fraction of 1% is sidelined into an Outer Loop, see fig. 2.4, responsible for impurity processing and tritium enrichment. This ensures a purity of the tritium gas of more than 95%. All tritium regained by the DPS is directly fed into the Outer Loop. The CPS requires a regeneration

[1] this corresponds to 40 g tritium throughput per day.

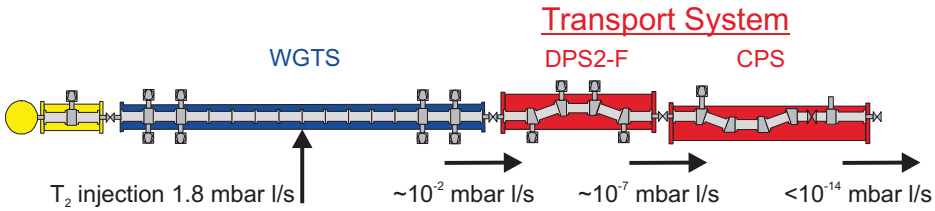

Figure 2.3: Schematic overview of source and transport section detailing the tritium flow rate suppression. Tritium is not allowed to enter the spectrometers. Therefore, a tritium retention system is build to reduce the tritium flow rate below 10^{-14} mbar·l/s. Turbomolecular pumps are reducing the amount of tritium starting at the Windowless Gaseous Tritium Source (WGTS) and over the course of the Differential Pumping Section (DPS) by a factor of 10^7. The Cryogenic Pumping Section (CPS) freezes tritium out on an Argon frost layer, thus further reducing the tritium flow by another factor 10^7 (picture based on [Eic09]).

process of warming up and extracting the frozen on tritium every 60 days. This fraction of tritium is partly injected into the Outer Loop section and to some part retained in the laboratory's retention system.

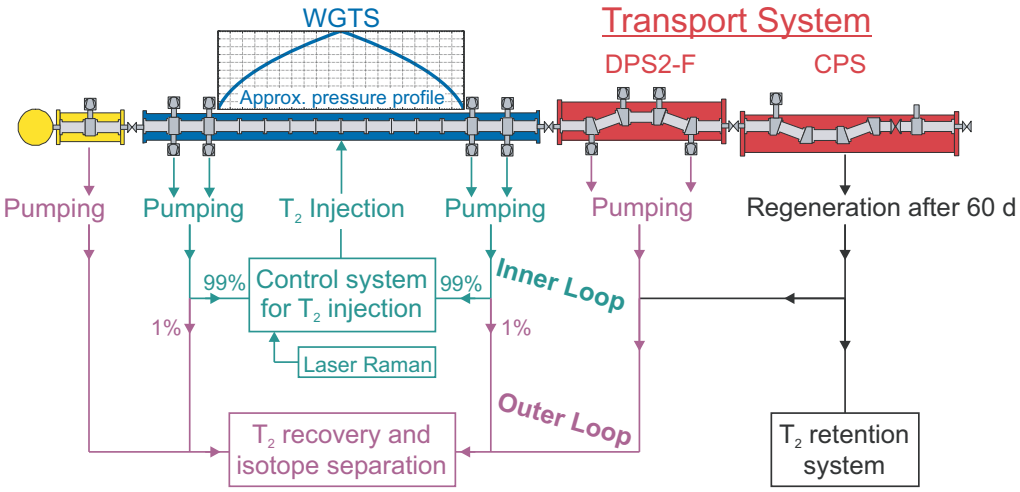

Figure 2.4: Tritium circulation and retention. To achieve a column density of $5 \cdot 10^{17}$ tritium molecules per cm^2 all of the tritium inventory of the TLK (40 g) would be needed every day if no circulation of the process gas would be realised. However, recirculation of the tritium also requires purification to ensure high purity of the gas. Furthermore, the stability of the column density is of utmost importance. The tritium pumped out at the end of the WGTS is re-injected into the WGTS (99%) via an Inner Loop, the other 1% together with the tritium recovered in the transport section is transferred into an Outer Loop responsible for purification of and enrichment with tritium. A small fraction of tritium from the CPS which is not qualifying for re-processing is held back in the TLK's retention system. Figure taken from [Eic09].

2.2.2 Transport section

The transport section has two main tasks to fulfill:

1. adiabatical guidance of β decay electrons
2. final retention of tritium

By deploying superconducting solenoids with a magnetic field strength of 5.6 T the necessary diameter of the beamtube decreases to 66 mm. The transport section is divided into two parts, a Differential Pumping Section (DPS) and the Cryogenic Pumping Section (CPS). While electrons are guided adiabatically to the spectrometer section, tritium molecules have to be filtered out. Starting from a tritium flow of 1.8 mbar·l/s, DPS and CPS reduce the amount down to an upper limit of 10^{-14} mbar·l/s which corresponds to a rate of 10^{-3} counts/s of β electrons originating from tritium decay inside the spectrometer section, see fig. 2.3. A higher background rate would limit KATRIN's sensitivity projection. Both DPS and CPS consist of several tubes tilted to each other by 20° (see fig. 2.5) thus prohibiting a direct line of sight of the WGTS into the spectrometers which could lead to molecular beaming effects [Ang04].

2.2.2.1 Differential pumping section

The DPS itself is also divided into two parts with DPS1-F[2] being integrated into the cryostat of the WGTS source tube and reducing the tritium flow by a factor of 10^2. DPS2-F further increases the reduction factor to a combined value of 10^7. This large factor can be achieved by differential pumping (four turbomolecular pumps (TMP) in every DPS stage (fig. 2.5). In the DPS2-F, the different beamtube elements are, as outline above, tilted by 20° against each other, thus increasing the differential pumping efficiency and preventing direct line of sight from inside the WGTS to the spectrometer and detector section. Thus, neutral particles not guided by magnetic field lines cannot be subject to beaming effects. The DPS is kept at liquid nitrogen temperatures of 77 K. This reduces the outgassing of hydrogen out of the stainless steel which would otherwise have a detrimental effect on the tritium pumping efficiency. Additionally, due to the strong magnetic field of the superconducting solenoids of 5.6 T, the geometry of the pump ports has been optimised as to define a magnetic field strength at this point of >0.5 T. Higher magnetic fields increase the operating temperature of the turbomolecular pumps by inducing eddy currents inside the pumps turbine [Ker07], thereby reducing the device's life expectancy. However, on the other hand, to avoid any substantial contributions to the systematic errors a field strength larger than 0.3 T at the pump port has to be ensured to guarantee adiabatic guiding of the electrons.

[2]The letter F denotes the position of the part in the beamline direction according to the tritium feed-in: F≡ front, R≡ rear

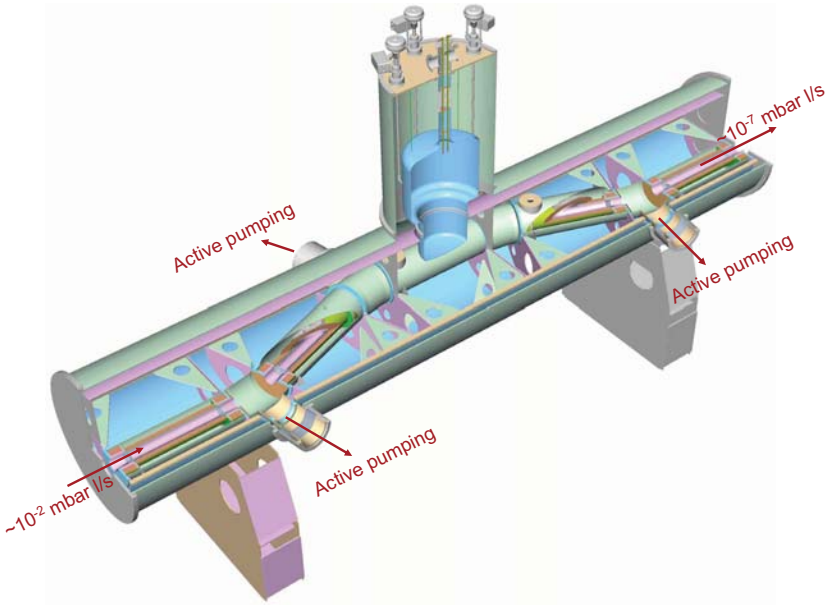

Figure 2.5: Forward section of the Differential Pumping Section (DPS2-F). The tritium flow is reduced by differential pumping with turbomolecular pumps. Each pump has a pumping speed of 2000 l/s for H_2. The beamtubes, kept at a temperature of 77 K, are tilted against each other to reduce beaming effects and to increase the pumping efficiency. The overall reduction factor of the DPS is 10^{-7}. Figure taken from [Ang04].

2.2.2.2 Cryogenic pumping section

The CPS section (see fig. 2.6) will retain the remaining tritium by means of cryo-pumping. On the inner tube surface, which is cooled down to liquid helium temperatures, a pre-condensed argon layer is frozen on. Tritium molecules will stick to the argon snow while electrons will pass the cryo-trap unhindered. A dedicated experiment to investigate the reduction factor of a cryo-trap of this design has been carried out. The results show that the required reduction factor of 10^7 can be achieved [Eic09].

2.2.3 Electrostatic spectrometers

Electrons generated in the WGTS and transported through the tritium retention systems DPS and CPS have to be analysed with regard to their kinetic energy. This information makes it possible to plot the β-spectrum and to fit the data with theoretical curves to deduce the neutrino mass. In a next generation experiment which aims to successfully probe the sub-eV region, an appropriate tool for high precision energy analysis, like bolometers or an electrostatic spectrometer, has to be utilised. The KATRIN experiment is based on an electrostatic filter system which combines an excellent energy resolution of the order of 1 eV for a high luminosity source with a low background contribution.

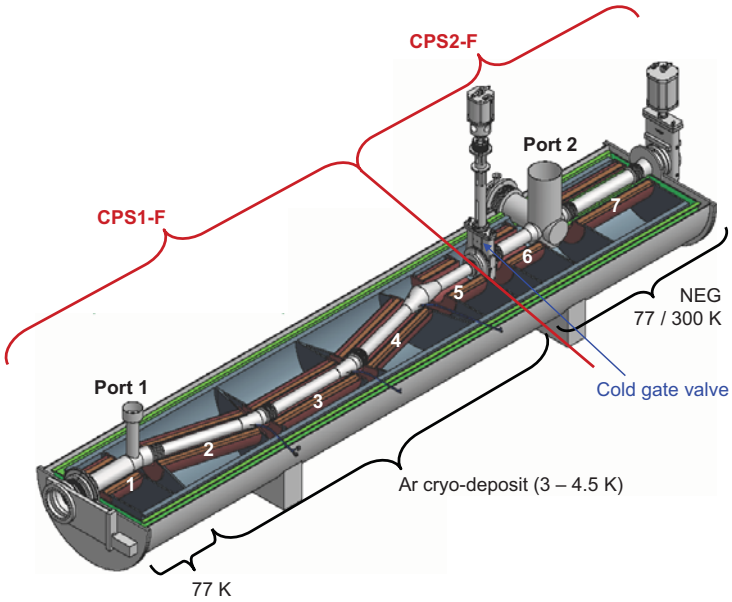

Figure 2.6: Cryogenic Pumping Section (CPS). The CPS consists of two parts: the first part utilising cryo-sorption on an Argon frost layer at approx. 3 K and a second part using non evaporable getter (NEG) strips at room temperature. The combined reduction factor for the tritium flow is 10^7. Figure taken from [KAT08]

In the beginning stage of tritium β decay experiments magnetic spectrometers were used successfully. In 1970 Bergkvist and colleagues obtained an upper limit on the neutrino mass of $55\,\mathrm{eV/c^2}$ [Ber72]. In 1980 however, the design of a new type of spectrometer was presented [Bea80], superimposing an electrostatic retardation potential on a magnetic guiding field for the electrons. This design proposal proved to be superior in energy resolution as well as accepted solid angle Ω. Two groups at Mainz and Troitsk adopted this design for neutrino mass measurements independently of each other. In the first phase of data taking both experiments experienced the problem of obtaining results with an unphysical negative $m^2_{\nu_e}$ value, which was reported in earlier experiments as well [Wil87], see also fig. 2.7. The answer to this problem could only be found with the high resolution of the new electrostatic spectrometers now commonly called **MAC-E** filters (**M**agnetic **A**diabatic **C**ollimation combined with an **E**lectrostatic filter). The negative values of $m^2_{\nu_e}$ disappeared as soon as energy loss processes were taken fully into account [Alt03]. The results of both Mainz and Troitsk yielded the best upper limits for the electron anti-neutrino mass to date which are compatible with zero.

The Mainz result [Kra05]:

$$m^2(\nu_e) = -0.6 \pm 2.2 \pm 2.1\; eV^2/c^4 \tag{2.7}$$

$$m(\nu_e) < 2.3\; eV/c^2 (95\%\mathrm{C.L.}) \tag{2.8}$$

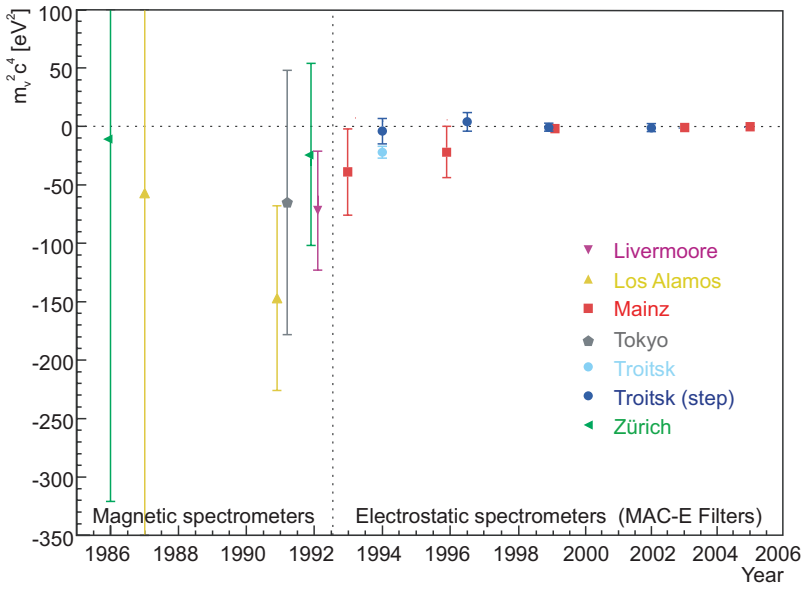

Figure 2.7: History of m_ν measurements. Results of past experiments to measure the neutrino mass are shown. Earlier experiments encountered considerable problems with regard to negative neutrino mass-squares which could be identified as caused by systematic uncertainties. The recent experiments in Mainz and Troitsk do not show this problem anymore. Figure taken from [Eic09].

and the Troitsk result [Lob01]:

$$m^2(\nu_e) = -1.0 \pm 3.0 \pm 2.1\, eV^2/c^4 \tag{2.9}$$

$$m(\nu_e) < 2.5\, eV/c^2 (95\%\text{C.L.}) \tag{2.10}$$

cannot be improved further due to the limited source intensity and spectrometer size. The following chapters will give a detailed description of the operation characteristics of this electrostatic filter system and explain the adaption for the MAC-E filter technique for the KATRIN experiment.

2.2.3.1 MAC-E filter

The main features of a MAC-E filter are illustrated in figure 2.8. Two superconducting solenoids encompassing a spectrometer vessel generate a symmetric magnetic guiding field. Electrons from the source entering the spectrometer propagate along the magnetic field lines on a cyclotron motion. While entering the spectrometer and passing through the first half the magnetic field strength drops by several orders of magnitude. Due to the cyclotron motion electrons possess both transversal and longitudinal energy components. As a result of the inhomogeneous B-field, a magnetic gradient force

$$\vec{F} = (\vec{\mu}\vec{\nabla}) \cdot \vec{B} \tag{2.11}$$

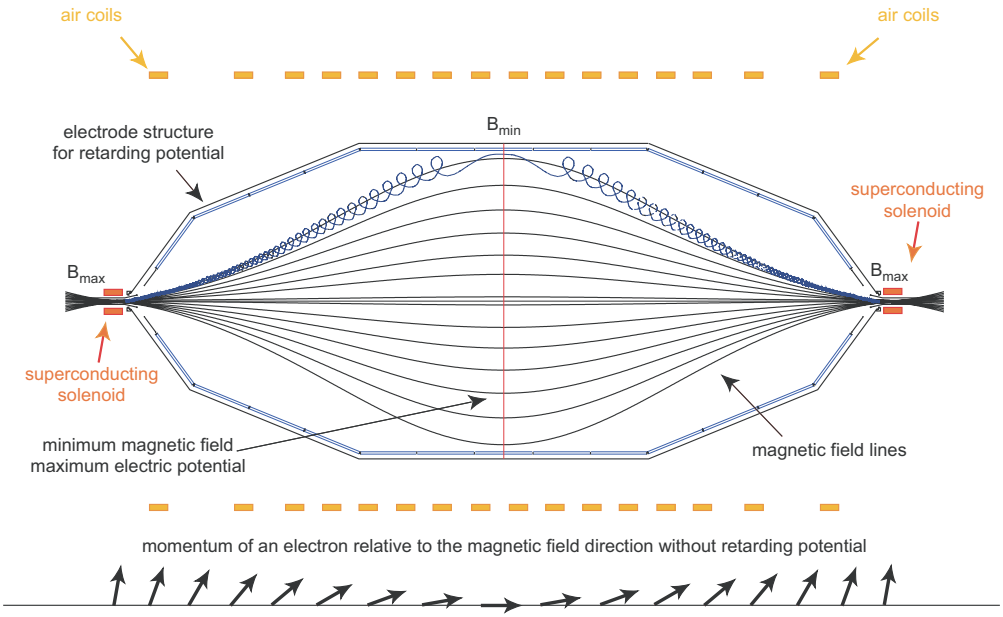

Figure 2.8: Spectrometer using the MAC-E filter technique. Two superconducting solenoids generate a magnetic field. Electrons starting from the source are guided on a cyclotron motion along the magnetic field lines. Air coils around the spectrometer are compensating the earth magnetic field and other magnetic disturbances. The tank itself and an inner quasi weightless electrode system can be put on high voltage thus creating an electrostatic retarding potential. The gradient force of the changing magnetic field transforms the transversal energy component, illustrated by vector-arrows at the bottom of the picture, adiabatically into longitudinal energy. The retarding potential reflects all electrons with insufficient energy - all other electrons are accelerated again and projected onto a detector. Thus it is possible to analyse the energy of β decay electrons with sub-eV precision. Picture taken from [Hug08c]

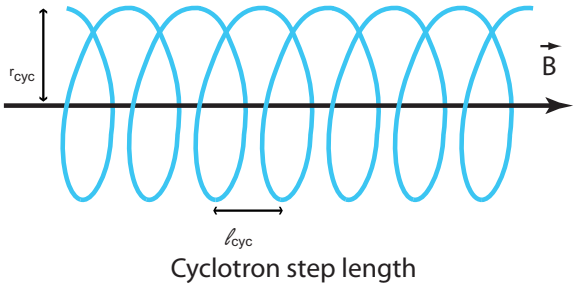

Figure 2.9: Cyclotron motion of electrons guided along magnetic field lines. The step length l_{cyc} and the cyclotron radius r_{cyc} are marked. As long as the magnetic field change is small during a step length the energy transformation is done adiabatically.

acts on the electrons which are guided along the magnetic field lines to the point of the minimal field strength. If the change of the magnetic field strength $\Delta B/B$ is small during one revolution of the cyclotron motion, see fig. 2.9, the momentum transforms adiabatically and the magnetic moment μ keeps constant (non-relativistic approximation)[3]:

$$\mu = \frac{E_\perp}{B} = const. \tag{2.12}$$

With the total energy being conserved, the increase in longitudinal energy $E_\parallel$ causes an equivalent reduction in transversal energy $E_\perp$.

Furthermore, by applying an electrostatic retarding potential U_0 to a set of cylindrical electrodes (see fig. 2.8) all electrons will be decelerated. The plane of maximum potential coincides with the plane of lowest magnetic field in the middle of the spectrometer called *analysing plane*[4]. Here, electrons with longitudinal energy $E_\parallel$

$$E_\parallel > qU_0 \tag{2.13}$$

will pass the potential barrier, re-accelerate and be projected onto a detector counting the single electrons. All other electrons do not pass the analysing plane but are reflected back into the source - even electrons with a higher total kinetic energy but insufficient momentum transformation will be rejected. The rest-momentum which is still in the $E_\perp$ component (illustrated in fig. 2.8 with the help of vector-arrows at the bottom of the picture) cannot be analysed by the retarding potential and therefore, constitutes the energy resolution of the transmission function. Taking advantage of equation 2.12 one can derive an expression for the energy resolution

[3] In the case of tritium β decay electrons the approximation is valid - the Lorentz factor γ peaks at 1.04. In general, the conserved quantity is $\gamma\mu$

[4] While this is true for the general concept of a MAC-E filter, the potential maximum is not necessarily located at the middle of the spectrometer. More information on the electric potential field distribution and the implication with regard to adiabatic guidance of the β electrons is given in reference [Val09]

of a MAC-E filter consisting only of starting energy and the ratio of the magnetic field change. The magnetic moment is conserved, therefore, the ratio of transversal energy $E_\perp$ and magnetic field strength keeps constant in every point of the track, e.g. the point of maximum and minimum magnetic field:

$$\frac{E_\perp^{max}}{B_{max}} = \frac{E_\perp^{min}}{B_{min}} \tag{2.14}$$

The energy resolution is identical to the transversal energy component which is left in the analysing plane where the magnetic field is lowest. With a starting energy E_0 completely stored in the perpendicular component, this yields

$$\Delta E = E_0 \cdot \frac{B_A}{B_{max}} \tag{2.15}$$

The variation of the electrostatic retarding potential applied to the electrodes[5] allows to scan the β spectrum in an integrating mode. MAC-E filters are therefore, high-pass energy filters.

In the following paragraph an analytical function describing the transmission characteristics of a MAC-E filter will be derived.

The solid angle acceptance of a MAC-E filter is excellent – all electrons with forward momentum will be analysed in the spectrometer. However, accepting all electrons with starting angles up to $\theta_{start} < 90°$ increases the possibility of energy losses due to the long path length electrons with high starting angles have to travel through the source. Instead of positioning the source at the point of maximum magnetic field it can be placed in front of the maximum field position thus reflecting unwanted electrons of large starting angles θ_{start} by the magnetic mirror effect. The following equation holds true for electrons of energy E_0 starting under an angle θ_{start} at a point with the magnetic field B_{start}:

$$E_{start}^\perp = E_0 \cdot \sin^2 \theta_{start}. \tag{2.16}$$

With a constant magnetic moment due to adiabatic momentum transformation (eq. 2.12) and taking into account the condition for reflecting electrons $E_{start}^\parallel = E_0 - E_{max}^\perp$ this yields the reflection angle

$$\theta_{max} = \arcsin(\sqrt{\frac{B_{start}}{B_{max}}}). \tag{2.17}$$

Electrons starting with an angle bigger than θ_{max} will be reflected before reaching the spectrometer. Defining the magnetic field at the source point permits to control the maximum starting angle[6].

[5] Alternatively, it is possible to drive a potential applied to the source itself and keep the retarding potential of the spectrometer constant.

[6] The KATRIN experiment has chosen to place the pinch magnet with the highest magnetic field strength in front of the detector section. Therefore, the final selection of the starting angles takes place after the energy selection in pre- and main spectrometer.

Under the assumption that the angles under which electrons are emitted in the source region are isotropically distributed, a transmission function can be derived. Beginning with eq. 2.16 once again taking into account adiabatic momentum transformation (eq. 2.12) and the transmission condition for an applied retarding potential $q \cdot U_0$ (eq. 2.13), the transmission of an electron depending on the starting angle θ_{start} thus reads:

$$E_{min}^{\parallel} = E_0 - E_{max}^{\perp} - eU_0 > 0 \tag{2.18}$$

$$= E_0 - E_0 \cdot \frac{B_{min}}{B_{start}} \cdot \sin^2 \theta_{start} - eU_0 > 0 \tag{2.19}$$

Consequently, electrons with a starting angle

$$\theta \leq \theta_{start} = \arcsin\left(\sqrt{\frac{E_0 - qU_0}{E_0} \frac{B_{start}}{B_{min}}}\right) \tag{2.20}$$

will be transmitted. Together with the relation for the accepted solid angle

$$\frac{\Delta\Omega}{2\pi} = 1 - \cos\theta \tag{2.21}$$

and eq. 2.22 for a limited starting angle θ_{max} an analytical ideal transmission function $T(E_0, U_0)$ can be derived:

$$T(E_0, U_0) = \begin{cases} 0, & E - qU < 0 \\ \frac{1-\sqrt{1-\frac{E-qU}{E} \cdot \frac{B_{start}}{B_A}}}{1-\sqrt{1-\frac{\Delta E}{E} \cdot \frac{B_{start}}{B_A}}}, & 0 \leq E - qU \leq \Delta E \\ 1, & E - qU > \Delta E \end{cases} \tag{2.22}$$

2.2.3.2 Tandem spectrometer

To achieve the high sensitivity and high count rate associated with a MAC-E filter adequate for the KATRIN experiment many aspects have to be considered. The high energy resolution directly affects the dimensions of the spectrometer vessel. Equally important are considerations regarding background suppression and reduction - affecting not only the count rate but also ensuring that the sensitivity goal can be reached. Therefore, the choice of material, shape of the tank geometry as well as the vacuum, high voltage and electrode system design have to be taken into account. To reach all these objectives, the electrostatic filter system of KATRIN is comprised of two separate spectrometers using the MAC-E-filter technique. A smaller *pre-spectrometer* (Ø=1.7 m, l=3.4 m, V=8.5 m^3, A=25 m^2) is placed in front of a much larger *main spectrometer* (Ø=10 m, l=23.3 m, V=1250 m^3, A=690 m^2), as shown in figure 2.2.

The vacuum inside the spectrometer vessels is specified not to exceed the stringent 10^{-11} mbar limit[7]. As a result, stainless steel with a low outgassing is used. To

[7] This pressure regime is referred to as **U**ltra **H**igh **V**acuum (UHV).

exclude any magnetic field distortions the steel is also required to be non magnetic. More detailed information regarding the vacuum design and performance will be presented in chapter 3.1.1.

A major difference in design compared to the MAC-E filters used in previous experiments is the use of the spectrometer vessel itself as part of the electrode system for the retardation potential. An inner electrode system will be installed, focussing on background reduction (e.g. cosmic ray muons) as well as fine-tuning and stabilisation of the potential (see chapter 3.1.2) rather than forming the retardation potential as the main objective.

Employing a pre-spectrometer in a tandem set-up limits the number of electrons reaching the main spectrometer to those of the highest energies only. A high precision energy analysis is thus performed only for those electrons which carry sufficient information to deduce the neutrino mass. Such limiting the number of electrons also minimises the scatter probabilities of electrons on residual gas molecules with subsequent energy loss. This is important considering that electrons losing energy but still pertaining enough to pass the potential barrier are still counted in the detector and thus cause a distortion of the spectrum. KATRIN will keep this uncertainty factor to a minimum. A pre-spectrometer with a moderate energy resolution of about 70 eV already decreases the number of electrons entering the main spectrometer substantially. The difference in energy resolution explains the discrepancy in size. Driven at a fixed potential of 18.3 keV, the stream of $10^{11}\,\mathrm{e}^-/\mathrm{s}$ is reduced to $1000\,\mathrm{e}^-/\mathrm{s}$ entering the main spectrometer for energy analysis.

The required energy resolution directly defines the main spectrometer's dimensions. With the help of eq. 2.15 for a given endpoint energy of the β-spectrum of 18.575 keV and a projected energy resolution $\Delta E < 1\,\mathrm{eV}$ one deduces:

$$\frac{\Delta E}{E_0} = \frac{1}{20000}. \tag{2.23}$$

With a reference flux tube of $191\,\mathrm{Tcm}^2$ and the maximum magnetic field of 6 T the magnetic field has to drop to $3{\cdot}10^{-4}\,\mathrm{T}$ at the centre of the spectrometer, corresponding to a minimum radius of 4.5 m. Leaving some space for the installation of the inner electrode the vessel is required to have a maximum inner diameter of 9.8 m. Unlike the pre-spectrometer, the shape of the main spectrometer is the result of extensive electromagnetic design studies [Val04, Mer09b] carried out to ensure adiabatic energy transformation, field homogeneity, and preventing areas where charged particles are stored in Penning traps. An air coil system around the tank corrects the influence of the earth magnetic field and the inhomogeneities resulting from the detector pinch magnet.

2.2.4 Detector

Finally, a position sensitive detector is needed to count the electrons passing the potential. The detector set-up has to meet several requirements [Ang04]:

High e^--detection efficiency In order not to lose too many signal electrons close to the endpoint, an overall detection efficiency of $\epsilon > 0.9$ is required.

Good energy resolution To discern background events of similar energies as the retarding potential, an energy resolution of $\Delta E < 1\,\mathrm{keV}$ is required.

Spatial resolution allows the investigation of inhomogeneities of the retarding potential in the analysing plane and of systematic effects of the radial source potential

Detector size The sensitive area has to correspond to the electrons' flux tube.

Low intrinsic background and background suppression A detector made of low Z material like silicon helps in reducing the sensitivity to γ background radiation. Furthermore, an active and passive shielding will be implemented to shield against muons.

High event rates The detector and data acquisition system is required to handle high data rates on the MHz scale during calibration runs.

Good time resolution To investigate systematics and to prevent pile-up during high-intensity e-gun runs a time resolution of $\delta t < 500\,\mathrm{ns}$ is needed.

A detector technique which meets the requirements for the KATRIN focal plane detector (FPD) is represented by a monolithic PIN[8] diode array. This choice was due to the versatility of possible detector geometries and the maximum sizes which can be produced by several industrial manufacturers without extensive R&D required. The final design is based on 148 pixels arranged in 12 rings consisting of 12 segments each, plus 4 pixels forming the 'bull's eye' resulting in a detector chip of 90 mm in diameter. The radii of the pixel-rings have been chosen so that each pixel has the same sensitive area of $42\,\mathrm{mm}^2$ (see fig. 2.10). The detector will sit off-centre inside a 3.6 T warm bore magnet limiting the maximum angle of impact to 45°. This is a result of adjusting a value for the magnetic field of the detector region versus the detector size: the smaller the magnetic field, the smaller the percentage of backscattered electrons. On the other hand, the wider the magnetic flux, the larger the size of the detector array and the smaller the background reduction due to magnetic shielding. Compared to other detector techniques the energy resolution is moderate but still sufficient: $\Delta E = 600\,\mathrm{eV}$ FWHM[9] is the design requirement for the FPD.

The detector has to be UHV compliant. This results in a complete separation of the detector wafer from the electronics. The silicon wafer will be in direct contact with the UHV of the main spectrometer. The signal taken by the detector chip will have to be sent via feed-through pins to the first stage amplifiers which themselves are positioned completely isolated in a high vacuum area.

[8] Positive Intrinsic Negative
[9] Full Width Half Maximum

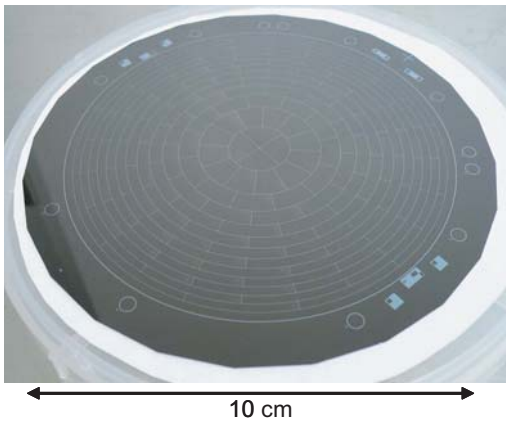

Figure 2.10: Wafer of the focal plane detector (FPD) design. 148 pixels in a radial set-up consisting of 12 rings made up of 12 segments plus 4 pixels for the bulls eye. Each pixel is designed to encompass the same area. The segmentation with the resultant position sensitivity makes it possible to investigate inhomogeneities of the retarding potential in the source and the analysing plane (Picture taken from [Doe08]).

The design of the detector has been finalised and three detector wafers have been produced and shipped to the US collaborators at University of Washington, Seattle. The complete detector set-up will be tested in Seattle and then shipped to Karlsruhe where the commissioning will take place in mid-2010.

2.2.5 Calibration monitoring system

To reduce the systematic uncertainties it is necessary to continuously calibrate and accurately monitor many of the experimental parameters. Therefore, the KATRIN experiment will feature a wide range of calibration sources and monitoring equipment in several places along the beamline.

2.2.5.1 Rear wall system

On the backward side of the WGTS is the rear section. There, tritium gas not pumped down by the DPS1-R will be pumped out into the Outer Loop of the tritium retention and regeneration system also. The rear section will allow to control the WGTS potential as well as to make use of monoenergetic electrons from an electron gun.

2.2.5.2 Monitor spectrometer

Apart from the main beam line a second one will be installed. This beam line includes a fully functional spectrometer (the former Mainz spectrometer) also using

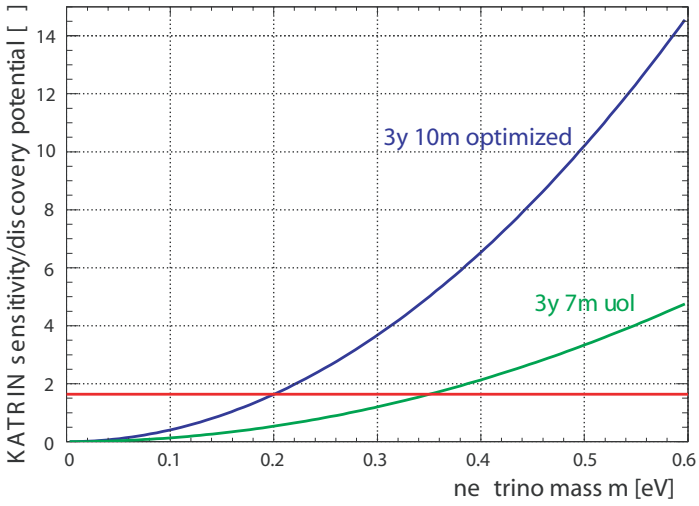

Figure 2.11: Comparison of the discovery potential published in the Letter of Intent (LoI) and after improving the experiment set-up and optimising the measurement time (optimised) [Ang04].

the MAC-E filter principle, a silicon PIN detector and a range of sources providing monoenergetic electrons in the energy range of 17.8-32 keV. The monitor spectrometer is electrically connected to the main spectrometer, thus permitting an online monitoring of the retarding voltage. For this task the spectrometer's energy resolution has to be competitive with the main spectrometer's. By lowering the magnetic field strength in the analysis plane of the monitor spectrometer[10] it is possible to increase the energy resolution to 1 eV at the expense of luminosity. However, this is of minor importance taking into account sufficiently strong monoenergetic sources.

2.2.5.3 Forward Monitor detector

A silicon detector installed into the CPS will permanently monitor the flux of β electrons. The detector will be positioned inside the halo of the electron beam as not to reduce the amount of electrons reaching the spectrometers [Sch08].

2.3 Aim and sensitivity

An estimation of the different systematical and statistical errors results in a total uncertainty of $\sigma_{tot} \approx 0.025\,\mathrm{eV}^2/\mathrm{c}^4$ with equal statistical and systematic errors contributing. If no positive signal is observed, an upper limit of

$$m(\nu_e) < 0.2\,eV/c^2 (90\%\ \mathrm{C.L.}) \tag{2.24}$$

[10] The Mainz spectrometer will act as the KATRIN monitor spectrometer. 3.5 m length, 1 m diameter, $\Delta E = 5\,eV$

will be deduced. Figure 2.11 shows the discovery potential of KATRIN after three years of continuous data taking for two set-ups: the initial Letter of Intent's [Osi01] set-up has been optimised resulting in a lower upper limit of the neutrino mass and higher discovery potential of 5σ for a neutrino mass signal of $0.35\,eV$.

Chapter 3

The KATRIN pre-spectrometer test experiment

The first major component of the final KATRIN set-up has been the pre-spectrometer vacuum vessel, which arrived on-site of Forschungszentrum Karlsruhe in autumn of 2003. Taking advantage of the early arrival, extensive tests with regard to the optimised design of the KATRIN MAC-E filters and to prototype devices were carried out. The research and development (R&D) efforts were of particular importance for the project. As a result, methods were developed to reach UHV standards of 10^{-11} mbar and a new electrode design were implemented which is split up into a guard electrode, the spectrometer vessel itself, and a lightweight segmented inner electrode. To be able to test all aspects of the pre-spectrometer's functionality a test experiment has been devised which simulates the operation of a MAC-E filter (see fig. 3.1). A photoelectron emitter[1], which can be positioned in a plane with fixed radius with regard to the centre of movement, creates electrons of uniform energy selectable between 0 and -30 keV. Two superconducting solenoids with a maximum B-field of 4.5T on axis, positioned at both sides of the spectrometer vessel, guide the electrons along the magnetic field lines through the vessel. A detector system opposite the e-gun detects electrons and other charged particles as well as photons exiting the spectrometer. Vessel and inner wire electrode can be put on high voltage to create a retardation field for charged particles.

In summary the tasks of the pre-spectrometer system are:

1. verification and optimisation of UHV vacuum design
2. verification of the novel electromagnetic design with the vessel being on high potential
3. test of new electrode design: vacuum vessel acting as guard electrode plus lightweight inner electrode system

[1] Due to its function colloquially called 'e-gun'.

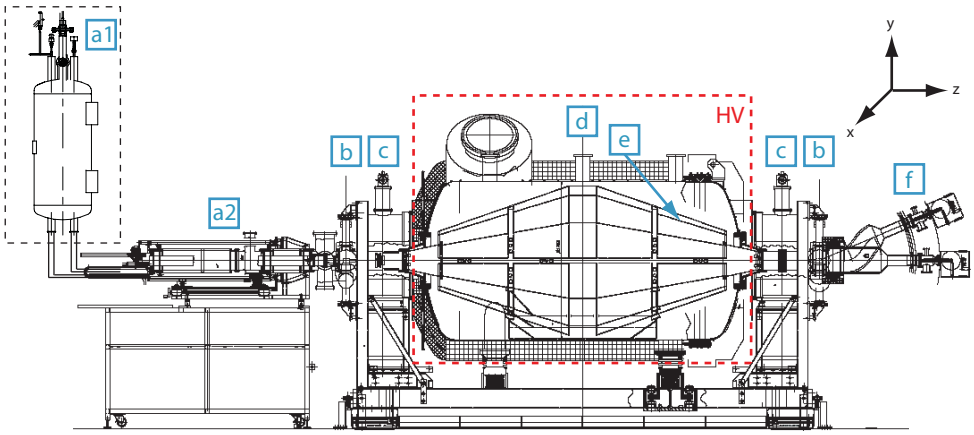

Figure 3.1: The pre-spectrometer test set-up is mimicking the final set-up with an electron emitter as a source of monoenergetic electrons and a detector for particle detection. Combined with two superconducting solenoids and the possibility to create a retarding potential by elevating vessel and inner electrode on high potential, the full characteristics of a MAC-E filter can be explored. (**a**) detector chamber and liquid nitrogen storage vessel (**b**) full metal gate valve (**c**) superconducting solenoid (**d**) pre-spectrometer vessel (**e**) inner wire electrode (**f**) electron emitter

4. test of monoenergetic electron emitter with isotrope angular distribution
5. testbed for a prototype segmented silicon PIN diode detector
6. test of data acquisition software ORCA[2] with pre-existing and new hardware
7. test of process controlling hard- and software

In the following chapters the test experiment will be described in detail. In particular, a review of the vacuum design together with the data responsible for verifications of the UHV-concept will be given. Following a discussion of the high voltage design, the slow control system to operate the experiment as well as to record the data and environment variables will be detailed. Furthermore, the magnet system will be shortly summarised and finally the characteristics of the e-gun and the different detector and data acquisition systems being deployed will be described.

3.1 The pre-spectrometer vessel

The majority of electrons emitted from the WGTS carry no information on the neutrino mass and can contribute to background: ionisation processes with residual gas molecules could possibly influence KATRIN's design sensitivity. The pre-spectrometer working will act as a barrier against these electrons by filtering out

[2]Object oriented Real-time Control and Acquisition

Figure 3.2: Pre-spectrometer setup without satellite systems of detector and e-gun. The left picture shows the pre-spectrometer vessel with the cylindrical main body already equipped with thermal insulation. Attached to the horizontal pump port is the pump system. Magnets are in place to the left and right of the vessel. Right picture: dry air cabin enclosing the spectrometer vessel. The dry air cabin has two functions, a) prevention of air exchange to allow dehumidifying of air to lower the dew point, b) access restriction during high voltage operation.

all electrons with energies lower than a pre-defined threshold energy. Therefore, the pre-spectrometer will be driven with a constant potential at approximately -18.3 kV effectively decreasing the electron flux by a factor of 10^6 . Although this will be the pre-spectrometer's main task it also serves another important purpose during the R&D phase of the experiment, in particular with regard to the increase in the flux tube dimensions of the large main spectrometer vessel by more than a factor of six. It should be emphasised that an ultra high vacuum of less than 10^{-11} mbar in a volume of 1250 m^3 hasn't been achieved before, neither the Troitsk nor Mainz experiments elevated the whole vessel and attached devices to a higher potential. For these reasons the KATRIN Collaboration decided to operate the pre-spectrometer at an early stage of the experiment. Working as a prototype MAC-E filter, it is possible to gather important information on other components still in R&D phase. The findings of over four years of experiments will be presented in the corresponding chapters.

The pre-spectrometer vessel (see fig. 3.3) was manufactured by SDMS, France. It is of cylindrical shape with a diameter of 1.68 m, a length of 3.38 m and 10 mm thick walls and is made of stainless steel of the type DIN1.4429[3], being non magnetic and possessing favourable outgassing properties. Three chimneys, 160 mm in diameter, are welded onto the vessel's top side. They are closed with a DN160 CF[4] flange equipped with three DN40 flanges, one of them housing a sapphire crystal viewport,

[3]DIN type: X2CrNiMoN7133, DIN number: 17440/41/55/56/57/58, DIN standing for *Deutsche Industrie Norm*. In the North American area this type of steel is known under the designation 316LN introduced by the American National Standards Institute.

[4]DN: nominal size of the inner diameter followed by the inner diameter in mm. CF (ConFlat): describing a sexless sealing technique. More information is given in appendix A.1. From now on flanges are considered to be of CF type if not expressly specified otherwise.

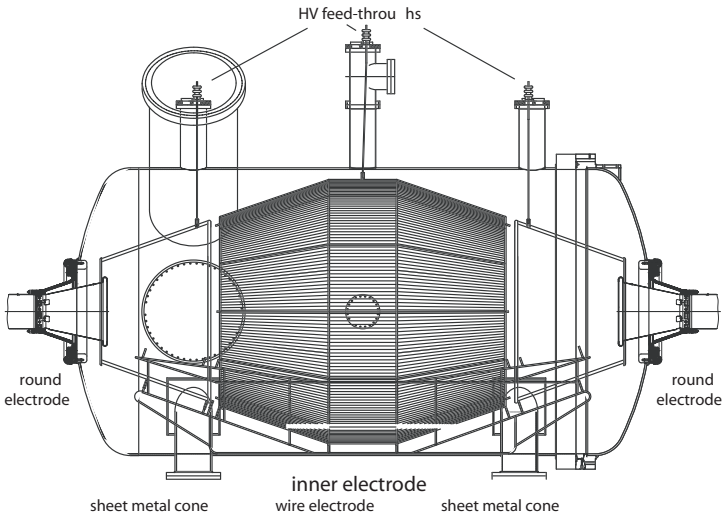

Figure 3.3: Drawing of pre-spectrometer vessel. Shown are the pre-spectrometer vessel including two pump ports, three chimneys with high voltage feedthroughs, a side-flange, the installed inner electrode system and the ground electrodes on both sides.

the other two a high voltage feed-through (GSD 1065-1) connecting the six parts of the inner electrode to the power supplies (see 3.1.2). The chimney in the middle is elongated by an attached t-piece. The free side port is equipped with a rupture disc. In case of an overpressure exceeding 0.5 bar, e.g. a bursting liquid nitrogen line of the detector cooling, the rupture disc bursts open preventing any edge welded bellows to be destroyed. The sides of the cylindrical section are closed by a DN500 flange on one side and a DN1680 flange combined with a DN500 flange on the other. Flanges exceeding an inner diameter of 320 mm are needed for the insertion of the inner electrode system as these cannot be sealed by standard CF technique. A different sealing technique is needed which is described in App. A.1. This technique has to be thoroughly tested with regard to the main spectrometer, where staff members need access to the inside for the mounting of the inner electrode. The following chapter 3.1.1, detailing the vacuum design, contains a concise explanation of the employed sealing technique for DN500+ flanges.

At a distance of 75 cm off the middle axis of the vessel two tubes acting as pump ports, 1 m long and 50 cm in diameter, are welded to the vessel. Both DN500 closing flanges are equipped with four outlets, two DN200 and two DN40 flanges. One pump port, pointing upwards in a 45° angle, houses the non evaporable getter (NEG) pump and two vacuum gauges, a Leybold[5] Extraktor hot cathode gauge (IE 514 sensor, Ionovac IM 540 controller) directly attached to a DN200 reduction flange and an

[5]Oerlikon Leybold Vacuum, Switzerland

MKS[6] inverted magnetron (I-Mag®) cold cathode gauge connected to a DN200-160 reduction flange via a bend tube ('knee') so that both gauges don't affect each other. The other pump port is positioned horizontally. One of the two DN40 flanges houses a second Leybold Extraktor gauge. Attached to the DN200 flanges are VAT[7] DN200 all-metal gate valves (series 48) with an edge welded bellow in-between, necessary to allow for a minimum of expansion of the vessel during bake-out cycles. Connected to the valves' opposite flanges is the pumping system. Right next to the horizontal pump port in the centre axis of the vessel is a 30 cm long side-port with a DN160 flange welded in. Here an MKS residual gas analyzer (MicrovisionIP LM92) is installed.

3.1.1 The vacuum concept

The KATRIN spectrometers have to adhere to very stringent vacuum requirements, approximately one to two orders of magnitude better than the predecessor experiments[8]. In combination with an increase in volume of a factor 500, an extensive research and development phase is mandatory. Following this reasoning a cylindrical test recipient with a diameter of 0.5 m, a length of 1.5 m, a surface of 2.5 m^2 and a volume of 0.3 m^3 was built in advance. With the help of this test recipient it was possible to test the basic concepts of UHV vacuum. Building on this experience, the design and the manufacture of the pre-spectrometer vessel were optimised. The aim was to secure a vacuum of less than 10^{-11} mbar in the tandem spectrometer setup. This requires

- a careful choice of materials used,
- a clean experiment set-up and
- an efficient pumping system.

UHV compliant materials As starting point, only materials not limiting the desired end-pressure by inherent outgassing can be used. This choice includes certain types of stainless steel of high purity and homogeneity and oxygen-free copper. Ceramics and glasses possess a good outgassing behaviour and are easy to clean, however, they are also radioactive but on a low level. Nonetheless, these materials are indispensable when used as insulators; when integrated into a detector system, it is possible to use low-level ceramics to reduce background effects.

To satisfy the above requirements the pre-spectrometer vessel is made of 316-LN ESR[9] stainless steel encompassing a surface of 25 m^2. The inner electrode system is

[6] MKS Instruments, Inc., UK

[7] VAT Vakuumventile AG, Switzerland

[8] A detailed discussion of the UHV standard and the techniques used can be found in the appendix A, more specific references will be given when appropriate.

[9] ESR: electroslag refined

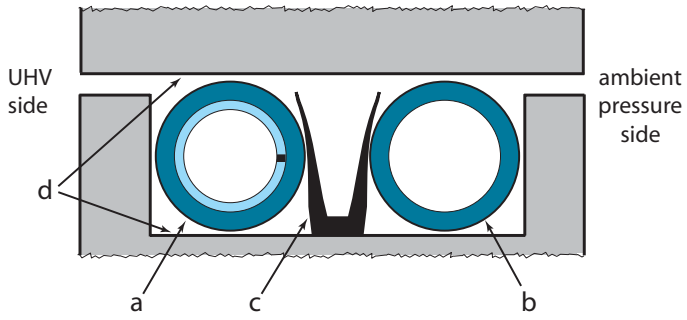

Figure 3.4: Differentially pumped double O-ring sealing technique.
a) spring energised metal O-ring **b)** metal O-ring **c)** spacer **d)** plane surface with defined surface roughness. When compressed the metal O-rings will push against the plane surface of the flange, thus sealing off the vacuum region. This method has proven successful for DN500 flanges and larger.

also made of stainless steel with glass spacers in-between the six parts of the electrode system (see section 3.1.2). Ceramic components are used at the DN500 flanges on both sides, electrically isolating the pre-spectrometer from the detector chamber and the e-gun system which are on ground potential. Six feedthrough flanges containing ceramics parts are installed in the three upper chimneys making contact between power supplies and inner electrode. No other materials have been used in this setup.

Sealing technique for DN500+ The vessel features eight ports, four DN160 ports are closed by ordinary CF flange components, four DN500 ports use a special sealing technique as illustrated in figure 3.4: instead of solid copper gaskets two O-ring gaskets are fitted into a groove. A placement holder also acting as a spacer keeps the rings inside the groove. The flange housing groove and O-rings is fitted onto the plane surface of the vessel flange. The surface has to be free of scratches and completely lint-free but with a defined surface roughness. When the flanges are pressed together the all-metal O-rings deform elastically. As a result of the deformation energy, the O-ring presses itself onto the plane surfaces, featuring a defined surface roughness, on both sides and seals off the vacuum region. The O-ring on the vacuum side is spring loaded, which means a spring inside the ring increases the pressure acting onto the sealing surface when compressed. The volume in-between the two rings can be pumped if the leakage rate exceeds a critical limit. The pre-spectrometer employs four DN500 O-ring seals and also one DN1680 seal connecting the end cap to the vessel[10]. Even without pumping the intermediate space the leakage rate is uncritical. The O-rings are procured from the HTMS company[11], Belgium.

[10] The DN500 flanges are fastened with 75 Nm, the DN1680 with 180 Nm.
[11] High Tech Metal Seals, Belgium

Figure 3.5: Electropolished inner surface of the pre-spectrometer. During the electropolishing process the surface is deburred, effectively reducing the surface area and improving high voltage stability as well as cleanliness performance. Visible are the openings to the two pump ports, the western chimney and the side-port.

Treatment of inner vessel surface The inner surface of the pre-spectrometer vessel is electropolished (see fig. 3.5). This polishing and deburring process reduces the surface unevenness to a value of less than $0.6\,\mu$m, directly affecting and thus reducing the outgassing rate which is proportional to the surface area.

The electropolishing has two more positive effects. Besides an improvement with regard to high voltage stability (see section 3.1.2), cleaning procedures are also more effective. Before assembly every UHV component has to undergo a special cleaning procedure including ultrasonic cleaning. This is necessary to remove any substances contaminating the component during manufacture or storage. With hydrocarbons, which are contained in greases for example, being the most dangerous contaminants it is paramount during assembly to prevent any contact with unclean surroundings or tools. Section A.4 of the appendix gives more detailed information on cleaning procedures and the corresponding precautionary measures to prevent any contamination of vacuum components.

Bake-out process Ultra high vacuum techniques always include a baking procedure after closure and initial pump down of the vacuum recipient. With this post-treatment procedure water and other contaminants introduced into the system during assembly are removed (see also appendix A.4). In this regard, the temperature of the pre-spectrometer is controlled by a Lauda[12] Kryoheater KH 350L system via thermal oil of the type Marlotherm® LH (Dibenzyltoluol) which is circulated in tubes welded directly onto the vessel, see fig. D.1 for a process and instrumentation diagram of the thermal oil circulation. Marlotherm® LH is stable in the temperature region of -70°C to +350°C, the Lauda system's power output of 28 kW correspondingly suffices to cool down the pre-spectrometer to -20°C and to heat it

[12]LAUDA DR. R. WOBSER GMBH & CO. KG, Germany

up to +220°C, on conditio that adequate insulation of the vessel is provided. The main body of the vessel is covered by 20 cm of glass wool covered by a stainless steel casing. This proved to be insufficient after initial bake-out wherefore another 10 cm layer of Armaflex®, a foam based insulator, was installed. The side caps of the spectrometer are insulated with customised cushions filled with glass wool, which are held in place by tension belts. Several problems with the cushion system have been identified: the seam of the outer ring cushions is made of a conductive material which poses a problem with high voltage stability as discussed in chapter 3.1.3.1. Therefore, the cushions have to be removed for measurements with high voltage applied to the spectrometer vessel. After several cycles of attaching and removing the cushions they now have lost their initial form thereby reducing the insulation effectiveness due to air circulation. This problem can be mitigated by applying another layer of glass wool insulation onto the critical spots. A new method to insulate the end caps, preferably a one-piece solution, will be designed in the forthcoming months and be installed when the pre-spectrometer is commissioned at its final location close to the main spectrometer.

Specific parts of the pre-spectrometer not covered by thermal oil heating are equipped with electrical heating bands and customised heating cushions. This includes in particular the satellite systems of e-gun and detector chamber, the beamtubes inside the magnets and the connecting components between pump port and TMP (edge welded bellow, DN200 all-metal valve and DN200 ceramic insulator tube). These electrical heating devices are controlled by altogether 21 thermocontrollers of the type GEFRAN[13] 9400 in connection with PT100 resistivity temperature sensors. The GEFRAN controllers allow different operation modi, e.g. ramping of temperature in units of K/h. The latter is important in connection with ceramics components, where a sudden temperature change or a high temperature gradient can cause damage to the component. The PT100 sensors are to be screwed tightly onto threaded rods which are spot welded onto the stainless steel vacuum component. This secures a good heat transfer from component to sensor. Sensors not tightly fastened to the stainless steel would have an insulating layer of air in-between which would prevent a correct temperature readout. As a result, the heating cables would be powered continuously and the vacuum component could be over-heated and possibly damaged. It is thus strongly advised to place a second temperature sensor next to the one used for temperature regulation. The second sensor is read out passively by the slow control system (see section 3.2). Here, a threshold value can be set, causing a shut-down of the heating procedure when predefined threshold temperature is reached.

Pumping scheme After the bake-out process the pressure is not limited by the partial pressure of water anymore. Now, the pumping system can reach its full potential. The KATRIN pre-spectrometer uses a cascaded two-stage TMP system (see fig. 3.6) consisting of two EBARA[14] ET801H turbomolecular pumps. Each TMP

[13] GEFRAN S.p.A., Italy
[14] EBARA Pumps Europe S.p.A., EBARA Corporation, Japan

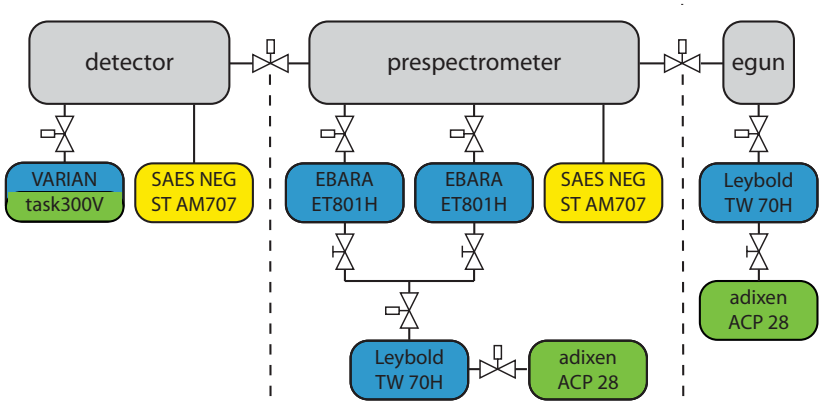

Figure 3.6: The pumping scheme for the pre-spectrometer test experiment. Shown are the three vacuum recipients (grey) with their respective pumping schemes comprising turbomolecular pumps (orange), getter pumps (yellow) and dry fore pumps (green). Also shown are the valves divided into manually operated valves and valves operated via a slow control system.

uses five-axis magnetic suspension, has a nominal pumping speed of 800 l/s (N_2) and is attached to the horizontal pump port in parallel via a DN200 flange. The exhaust flanges are connected to an intermediate vacuum stage in the 10^{-7} mbar region which is pumped down by the second stage TMP (Leybold TW290). The compressed gas stream is taken over by a high performance Adixen[15] ACP28 fore pump operating in the 10^{-3} mbar region which is the final connection to ambient pressure. With an intermediate pressure in the low UHV range, back-diffusion through the EBARA

[15] Alcatel Vacuum Technology corporate

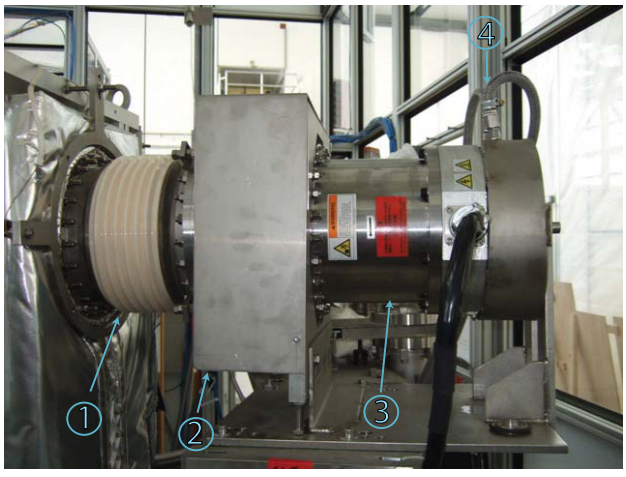

Figure 3.7: Picture of the EBARA TMP. (1) Frialit DN200 isolator tube (shatter protection off during high voltage operation) (2) edge welded bellow covered by shatter protection (3) EBARA ET801H with (4) water cooling

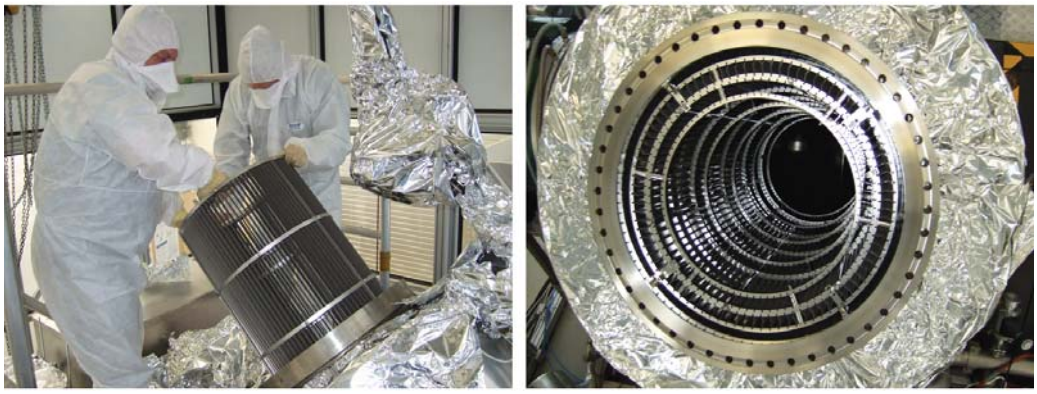

Figure 3.8: Non-evaporable getter cartridge for the pre-spectrometer. Left: installation into 45°-pump port. Right: getter cartridge in place. The 90 strips arranged circular shape in proximity to the walls.

pumps is negligible. The pump ports are each 1 m in length, followed by an edge welded bellow placed before an all-metal gate valve. The valve, being elevated on high potential whenever the vessel is elevated, is followed by a ceramics DN200 tube (fig. 3.7), thus electrically isolating the pumping system with regard to the vessel. To protect the ceramics from vibrations another edge welded bellow is placed between the TMP's intake flange and the ceramics tube. Adding the length of these components, the TMPs, using magnetic suspension of the rotor blades, are dislocated by approximately 2.8 m from the centre axis of the superconducting solenoids and thus not affected by the stray magnetic field, even at routine operation value of 4.5 T on axis. More information on vacuum pumps are presented in appendix A.3.

All subsystems and the different vacuum stages can be separated from each other by all-metal gate valves. These valves are pneumatically driven and controlled by the slow control system. This allows to automatically operate the valves to prevent a possible vacuum breakdown or damage to system components (see section 3.2).

Non-evaporable getter pump The end-pressure achievable with turbomolecular pumps is limited to the 10^{-10} mbar region. Here, molecule transport out of the UHV recipient is compensated by outgassing of the vessel surface and back-diffusion through the pump. In this pressure regime, however, outgassing of hydrogen from the stainless steel is dominating the gas distribution. Thermal velocities of light gas molecules are high, that of hydrogen around 1700 m/s, while rotor speeds are limited (EBARA ET801H: 38.000 rpm). This explains why TMPs are pumping light gas molecules like helium and hydrogen less effectively. To reach the required pressure of 10^{-11} mbar and better, another pumping method has to be used. The pre-spectrometer test-experiment opted for the use of non-evaporable getter material (NEG, see appendix A.3.3). Getter strips of the type SAES® ST707[16] (Zirconium

[16]SAES Getters S.p.A., Italy

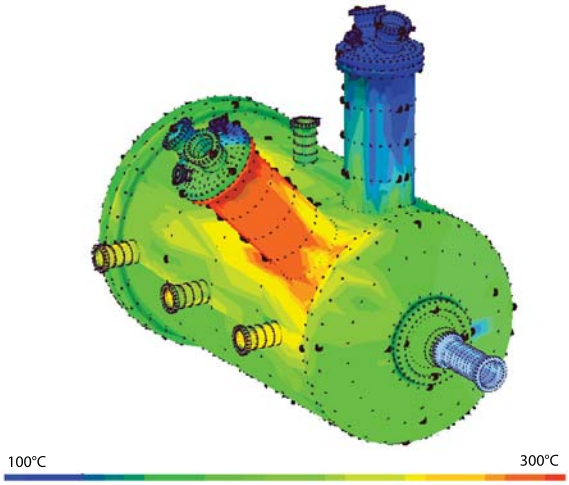

Figure 3.9: Activation of the non-evaporable getter. The temperature in the 45° pump port is increased to the maximum allowed 350°C. The temperature of the getter is read out with a thermocouple sensor showing 250°C. The pump port is on much lower temperature level to protect the turbomolecular pumps. For activation time 48 hours have been chosen. The picture displays the pre-spectrometer vessel rotated by 90°, the horizontal pump port is now pointing upwards.

70%, Vanadium 24.6%, Iron 5.4% [SAE]) are arranged in circular geometry in a tailor-made cartridge, carrying 90 strips with 1 m length each (fig. 3.8).

The NEG cartridge is installed in the 45° pump port. After the installation and subsequent pump down of the vacuum system the getter material has to be activated. This activation process, during which the saturated top layer of the getter material is freed from the adsorbed argon[17] requires temperatures larger than 250°C. The heating power of the pre-spectrometer system does not suffice to reach temperatures in the getter material of more than 150°C. This stems from the fact that with radiation being the sole transport process, temperature losses are too great. Electrical heating cables wrapped around the pump therefore ports allow to heat up the thermal oil to 350°C and more. During this procedure, the circulation of the thermal oil in the pump port is stopped, the oil reaches its maximum temperature of 350°C and the getter a value of 250°C after two days of heating. These rather low temperatures are sufficient, compared to standard bake-out temperatures of 450°C. However, the activation time increases from 10 minutes to 8 hours. An increase in time does not increase the efficiency of the activation, only an increase in temperature can achieve that [Alt08]. Fig. 3.9 shows the temperature distribution of the pre-spectrometer during the getter activation. Higher activation temperatures cannot be used, Marlotherm® LH starts to burn at temperatures exceeding the limit of 350°C. Beyond this regime black flakes are falling out of the thermal oil which can clog filters and even interrupt the circulation lines necessitating a time-consuming cleaning procedure.

Vacuum gauges The pre-spectrometer and the subsystems are housing a wide range of pressure gauges. Due to the fact that no measurement principle is working over the whole pressure range most pressure gauges combine multiple measure-

[17] Argon is used as a shielding gas during the handling of the getter strips.

ment principles. This includes VACOM[18] Atmion® pressure gauges (Pirani, Bayard Alpert) and MKS 999 Quattro^{TM} (hot cathode ionisation, microPirani^{TM} and piezo sensor with differential and absolute pressure reading capabilities).

Two vacuum sensors are installed to monitor the pump stages: an MKS 901P (MicroPirani^{TM} and Piezo sensor) reads the fore vacuum pressure, an MKS 999 Quattro^{TM} is used for the intermediate vacuum pressure. The satellite systems are monitored by Atmion gauges with the detector system switching over to an MKS 999 Quattro^{TM} since January 2009. The lower read-out limit of these gauges is 10^{-10} mbar. For the pressure readout of the pre-spectrometer two vacuum gauges are used: an MKS I-Mag® cold cathode gauge using the inverted magnetron technique (sensitivity limit 10^{-11} mbar) and two Leybold Extraktor (IE 514) gauges sensitive down to 10^{-12} mbar, see App. A.5.1). These gauges have not been calibrated, errors of a factor 2 in the readout value have to be expected at pressure levels below 10^{-10} mbar.

Cooling of pre-spectrometer vessel The end-pressure of the pre-spectrometer is limited by the outgassing rate of the vessel wall with hydrogen as the dominating fraction ($>95\%$). The hydrogen is pumped by the NEG very effectively, reducing the hydrogen fraction to an extent so that water and hydrogen cause the same contribution to the residual gas distribution. A means of further reducing the outgassing rate is to lower the temperature of the stainless steel walls of the entire pre-spectrometer. The thermal oil system has the ability to cool down the vessel to -20°C. To prevent any condensation of water on the outside surface of the vessel the pre-spectrometer and e-gun system is housed in a dry air cabin which is sufficiently closed off from the surrounding area (fig. 3.3). The cabin has a closed ventilation circuit combined with dehumidifying capabilities (A+H[19] DA 2400-S) allowing to lower the dew point down to $T_d = -20\,^{\circ}\mathrm{C}$ for safe spectrometer operation on high potential at those temperatures.

3.1.1.1 Verification of the vacuum design

The first task of the pre-spectrometer set-up was to verify the UHV vacuum concept as described above. To this end, measurements were carried out in 2004 testing the key characteristics of the ultra high vacuum concept. The results of 2004 are summarised below and a more detailed comparison of data ranging from 2007-2009 is presented, focusing on the UHV upgrade and modifications made after 2004.

In 2004 the satellite systems, i.e. the detector chamber and the e-gun chamber, were not available implying that the vessel was blind-flanged on both sides. The east-side DN500 flange was equipped with a Leybold Extraktor gauge, an MKS IMAG® gauge and a Pfeiffer[20] Prisma200 RGA. Another set of vacuum gauges was installed at the

[18] Vakuum Komponenten & Messtechnik GmbH, Germany
[19] A+H GmbH & Co KG, Germany
[20] Pfeiffer Vacuum GmbH, Germany

45° pump port (Extraktor & IMAG®). All vacuum gauges have been installed using DN100 knees to prevent a direct line of sight to other gauges preventing a streaming effect of particles from the hot filament gauges (Extraktor and RGA).

After baking the system at 230°C, an end pressure of $2.9{\cdot}10^{-10}$ mbar has been reached for conventional pumping using only the TMP system described above[21]. RGA data showed a strong hydrogen dominated mass spectrum with only a negligible fraction of water. Corresponding outgassing measurements according to the pressure rise method (see appendix A.2.1) exhibited a strong correlation between outgassing rate and vessel temperature. A first important milestone was reached by the measured outgassing rate of $1.2 \cdot 10^{-12}$ mbar·l/(s·cm^2) at room temperature (H_2 gas correction factor applied, gas load from hot filament vacuum gauges subtracted) [Ang04, Wol06]. This means that the designated outgassing limit of 10^{-12} mbar·l/(s·cm^2) was reached without the need to actively cool down the spectrometer vessel. As a result, the design concept for the large main spectrometer does not include cooling by default, thereby considerably reducing the technical infrastructure. Nevertheless, active cooling of the spectrometers is kept as an option, making it possible to reduce the outgassing rate by a further factor 8 when lowering the temperature to -20°C [Ang04].

After getter pump installation, the IMAG®'s, featuring a sensitivity limit of $1{\cdot}10^{-11}$ mbar, could not determine the pressure value. Also, an Extractor gauge with a sensitivity down to $1{\cdot}10^{-12}$ mbar could not be used due to outgassing of the hot filament leading to a local increase in vacuum of $7{\cdot}10^{-11}$ mbar. Assuming a conservative pressure value of $1{\cdot}10^{-11}$ mbar a pumping speed of 25,000 l has been calculated [Wol06]. These values have been the basis for simulations investigating the sticking probability of ST707 getter also taking into account the geometry of the getter pump. The results indicate a 2% sticking probability for ST707 getter material [Luo07].

After these measurements, modifications of the pre-spectrometer set-up required that the vacuum had to be broken several times, either for installing upgrades, e.g. inner electrode installation, or to carry out maintenance (e.g. change of defective HV feedthrough flange). After getter reactivation in October 2007 the end pressure of the pre-spectrometer vacuum including all subsystems could be measured to be $4.8{\cdot}10^{-11}$ mbar with the Extraktor gauge and $3{\cdot}10^{-11}$ mbar using the IMAG. The location of the Extraktor gauge, now installed at the DN200 flange looking into the 45° pump port, has been changed to limit the effects of a local pressure increase. Switching off the Extraktor gauge has no influence on the IMAG®'s pressure reading. Several pressure rise measurements were carried out to determine the outgassing rate with activated getter pump. Figure 3.10 shows the corresponding pressure rise curves with fit curves according to function A.6. Here, it has been distinguished between measurements with the Extraktor gauge on and off to check for an influence of an increased gas load from the hot filament, as well as for periods with and without open valve to the e-gun chamber. The detector chamber valve is periodically closed for reasons discussed in section 3.5.3.1. The calculated corresponding

[21] pressure values are given as nitrogen equivalent, no gas correction factors applied.

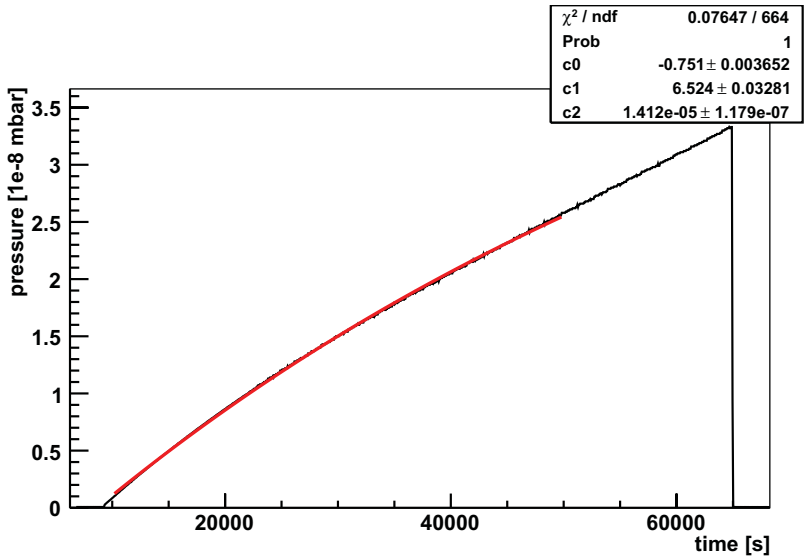

(a) RGA Leybold Extraktor

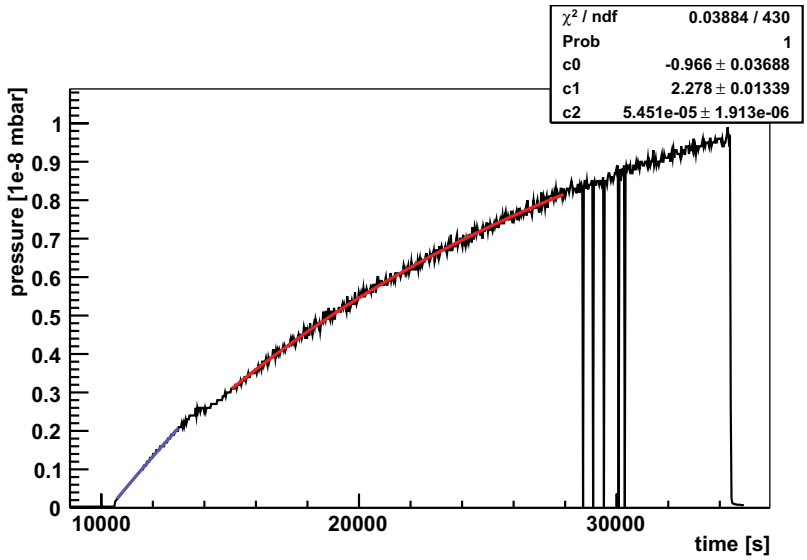

(b) RGA MKS IMAG

Figure 3.10: Pressure rise measurement of pre-spectrometer and e-gun chamber to determine outgassing rate.
(a) Leybold Extraktor data yield $2.8 \cdot 10^{-14}$ mbar·l/(s·cm^2)
(b) MKS IMAG®. The pressure rise is not strictly monotone, two parts have to be distinguished yielding slightly different values of $2.4 \cdot 10^{-14}$ mbar·l/(s·cm^2) (blue) and $2.8 \cdot 10^{-14}$ mbar·l/(s·cm^2) (red)

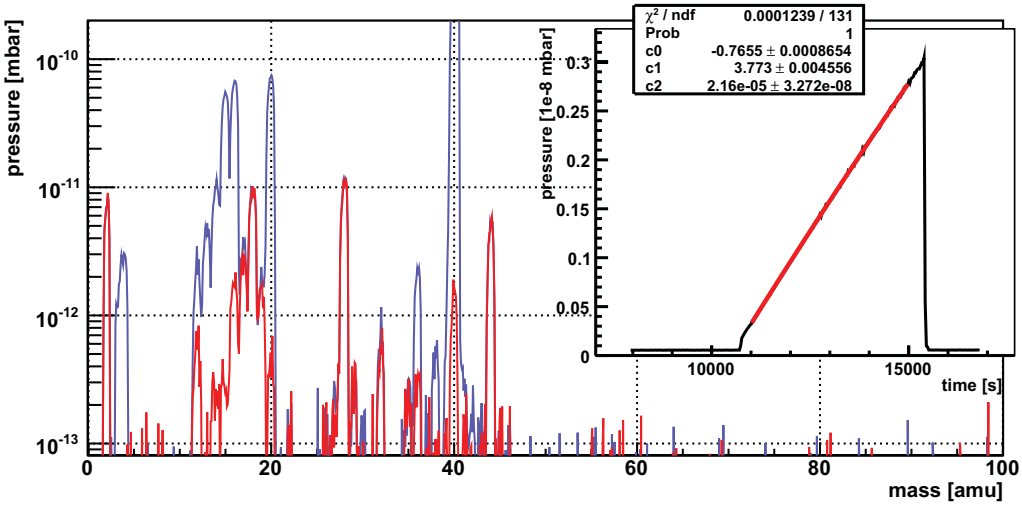

Figure 3.11: Pressure rise measurement to determine outgassing coefficients. All valves to the pre-spectrometer are closed. The pressure increase over time characterises the outgassing from the bulk stainless steel.

outgassing rates vary in the range from 2.2-2.8·10^{-14} mbar·l/(s·cm^2). Considering the relative uncertainties of the pressure measurement in the range of 20% to 50% in the 10^{-11} mbar regime and the uncertain gas distribution which affect the ionisation probabilities, the discrepancies in values are small and an average value of (2.5±0.5)·10^{-14} mbar·l/(s·cm^2) can be quoted. The outgassing rate is well below the designated threshold value, however, as has been stated in [Wol06], the end-pressure and outgassing rate do not directly correlate as can bee seen by the end-pressure reading given.

Investigating the pressure rise with an RGA additional information can be gathered regarding getter efficiency and outgassing properties. In figure 3.11 two RGA spectra are overlaid representing the normal mass spectrum during active TMP pumping and the maximum pressure during a pressure rise measurement. It is clearly visible that all gas contributions to the spectrum remain stable (H_2, H_2O, CO, CO_2) with the exception of argon and methane. Both argon and methane have only negligible contributions to the gas distribution during TMP pumping. However, as soon as the valves are closed, the fraction for these two gases increases rapidly, dominating the gas distribution with fraction of 81% and 15%, respectively. This shows that the pumping speed of the getter for the other gases is not at its limit. Argon, on the other hand, is being adsorbed on the getter surface during the numerous venting procedures and as a result of the storage using argon as shield gas. It desorbs easily considering the low pumping speeds of getter material for noble gases. Hydrocarbons like methane are mostly inert with regard to getter material, therefore, a large increase in methane can be expected.

In the outgassing values given above no gas correction factors have been included.

Taking into account the gas distribution before and during pressure rise, it is obvious that a single gas correction factor cannot be applied. Instead, the gas correction during pressure rise is rather a non-linear function in time. Calculating average gas correction factors $\overline{c}$ for the two spectra presented in fig. 3.11 ($\overline{c}_{red} = 0.92$, $\overline{c}_{blue} = 1.17$), the change in outgassing rate smaller than 17%, an effect which is small compared to the uncertainty of absolute pressure reading using uncalibrated pressure gauges.

In conclusion it can be stated that the upgrade of the pre-spectrometer system (including the installation of the inner electrode system as well as the beam line tubes with edge welded bellows establishing a connection with the satellite systems) has lead to an increase in gas load and correspondingly limits the final pressure to $p_{Extraktor} = 4.8 \cdot 10^{-11}$ mbar. It has been demonstrated that NEG getter material stays operational even after a year long storage under an argon environment and after several activation/passivation cycles. Another important result for large UHV systems is the demonstration that temperatures of 250°C applied for a minimum of two days are sufficient to fully activate ST707 getter material. Finally, the outgassing rate of the system with activated getter pump has been determined to be $2.5 \pm 0.5) \cdot 10^{-14}$ mbar·l/(s·cm^2), a factor 50 lower than without getter pump installed.

As an outlook to the deployment of the pre-spectrometer system in the final set-up it should be aimed at an increase in average bake-out temperatures, necessitating an improvement of the removable spectrometer insulation (sec. 3.1.1) as well as an overall increase in heating power. Thus, a further decrease in pressure should easily be achieved.

3.1.2 Electrode system

A high resolution MAC-E filter requires an electrode system to create a well defined retarding field. In the past, experiments were using a set of cylindrical electrodes placed inside the spectrometer vessel. The KATRIN Collaboration decided to implement the novel concept of connecting the retarding potential directly to the vessel itself. Even though an inner electrode system is still needed, this concept, as illustrated in fig. 3.12, holds several advantages:

Decoupling of retardation potential While the spectrometer vessel is acting as a guard electrode, the inner electrode shields the retarding potential from electric noise resulting from vacuum gauges, gauge controllers and residual gas analyzers, which are directly connected to the vessel, as are the gauge controllers. Uncertainties of the retarding field will thus be dominated only by the stability of the inner electrode potential [Ang04]:

$$\delta U_{inner} = \delta U_{electrode} \cdot (1 - 1/S) + \delta U_{vessel} \cdot (1/S), \tag{3.1}$$

where S is the screening factor, a quantity indicating the decoupling of the vessel potential from the potential inside the inner electrode. For the pre-

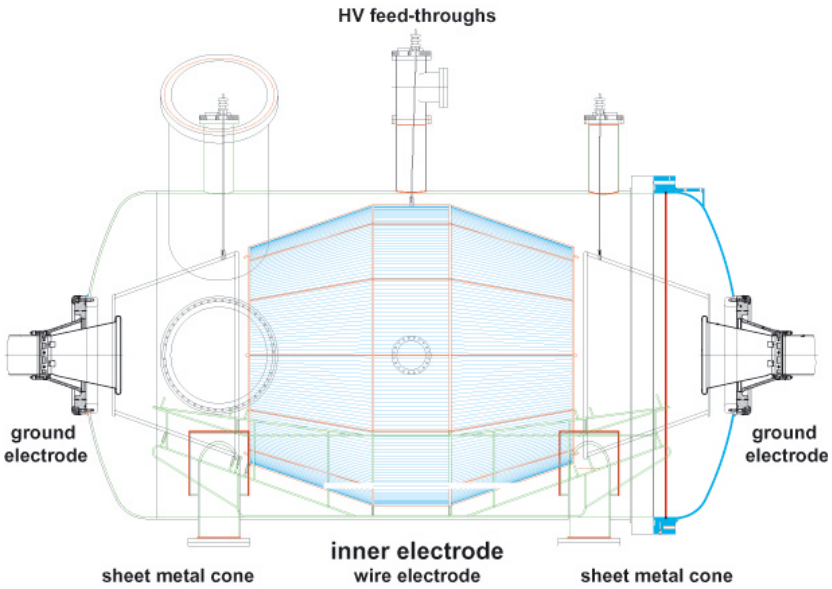

Figure 3.12: Inner electrode system of the pre-spectrometer. The inner electrode consists of 3 groups: wire electrode (blue) and west(left) and east(right) cones. Every group is divided into two halves to enable dipole mode operation. Feedthrough flanges in the chimneys allow HV supply to the six isolated electrode parts. Ground electrodes attached to the DN200 flanges of the conical isolators at the end caps form the potential field to improve the adiabatic transmission of the electrons. The inner electrode is held together by its own weight and only supported by a cradle (green) standing on the vessel bottom.

spectrometer the dimensionless screening factor S has been calculated to be of the order of $S \approx 7$.

Shaping of the electric field The geometry of the pre-spectrometer follows a cylindrical design and has, in contrast to the main spectrometer, not been subject to extensive electromagnetic design studies prior to manufacture. The inner electrodes shape the potential to avoid Penning traps and further optimises adiabatic transmission of multi-keV electrons.

Monopole mode for electrical screening Electrons created in the spectrometer volume through radioactivity or cosmic rays can be dangerous background sources for the neutrino mass investigation: despite electromagnetic shielding a small fraction will reach the detector in the correct energy window mimicking a β decay electron. A source for these background electrons are the elevated components, e.g. the electrode and vessel walls. Therefore it is important to have the inner electrode set on a slightly more negative potential, thus repelling low-energy electrons. The geometrical coverage of the inner electrode is supposed to be small, otherwise the electrode itself will be the source of background electrons.

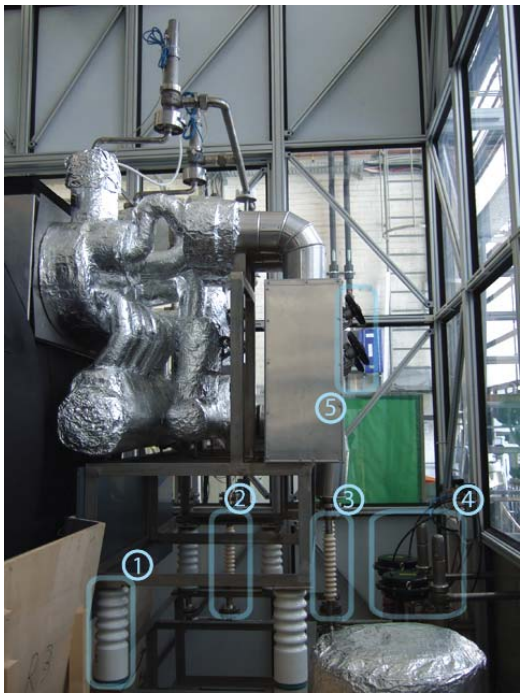

Figure 3.13: Isolators of the heating/cooling circuit.
(1) Argillon J8-125 (2) Frialit isolator (overflow circuit) (3) Frialit isolator (main circuit) (4) in- & outflow main valves of the heating/cooling circuit (5) hand valves for the six heating/cooling cycles.

Dipole mode to remove stored particles Splitting the circular electrodes in two halves along the axis allows to apply different potentials to the sets of electrodes thereby creating an electric dipole field which is perpendicular to the magnetic field. The resulting $\vec{E} \times \vec{B}$ drift removes any stored charged particles.

Over the next sections the different components, which can be elevated in potential, are described in more detail, as well as the high voltage system to power these components.

3.1.2.1 Components on elevated potential

Spectrometer vessel The pre-spectrometer vessel is electrically completely isolated from ground potential. The vessel itself rests on four isolators (Argillon[22] J8-125), while the TMPs are disconnected from the vessel by tailor-made Frialit[23] ceramics tubes with DN200 flanges between valve and first stage TMP. Therefore, the TMP-valves are still connected to the vessel and have to be set on isolators, too. The thermal oil circuit, made of stainless steel, connects the pre-spectrometer to ground potential. For conducting measurements with high voltage applied to the pre-spectrometer, a tailor-made set of Frialit isolators has to be introduced into the thermal oil circuit: these are two isolator tubes for the flow and return and two more for an overflow circuit each. These isolators can only stand temperatures

[22] Argillon GmbH, now Johnson Matthey und Lapp Insulators, Germany
[23] A product of the FRIATEC AG, Germany

Figure 3.14: Electrical isolation of the pre-spectrometer vessel.
Left: DN500 flanges with conical ceramics reduction tube to DN200. The DN200 flange is stainless steel combined with a Vacodil transition piece. Right: four ceramics stands carry the weight of the vessel and establish the electrical isolation to the base frame.

of $T \leq 80°C$ and in the case of the main circuit thus have to be exchanged with stainless steel tubes prior to a bake-out operation, see fig. 3.13.

All electronic devices in direct contact with the vessel have to be powered and controlled by units which are on high potential as well. Hence a controller cabin placed on four isolators and powered by a 50kV DC isolating transformer (FuG[24] HTS 3000-50) is located next to the pre-spectrometer.

Both, detector chamber and e-gun system also have to be isolated from the spectrometer vessel. This is achieved by two DN500 to DN200 reduction flanges with conical ceramic isolators (fig. 3.14) which are connected to the DN500 flange of the DN1680 end caps. These isolator flanges, manufactured by Friatec company, were initially designed with a DN200 flange and contact ring for soldering made of titanium to reduce the forces acting on the ceramics when applying a magnetic field, especially on the ceramics/titanium solder joint. Two isolators were manufactured and both did not pass leak tests. All attempts to fix the leaks were unsuccessful. The problem has been identified to be the soldering of the ceramics to the titanium. An alternative design uses Vacodil, a special nickel/iron alloy, for the solder ring and stainless steel for the DN200 flange. In addition, the solder ring has a height of 1cm which positively affects heat dissipation during soldering. Calculations show that the forces acting on the flange and ceramics are distributed symmetrically in this case. At the maximum magnetic field strength of 4.5 T, they do not exceed 500 N which is still well inside safety limits. All flanges manufactured according to this new design have proven to be leak tight.

Inner electrode system The inner electrode system (see fig. 3.12) consists of two ground electrodes, two cone-shaped full electrodes, and a wire electrode in the

[24] FuG Elektronik GmbH, Germany

middle part of the pre-spectrometer. The conical full electrodes as well as the wire electrode are vertically split in half for dipole mode operation.

The use of titanium was originally motivated by the aim of suppressing a minor source of background known from the former Mainz spectrometer in the form of X-ray photons which are produced by electrons hitting the ground electrode (anode). Secondary photo- or Auger electrons emitted from the central electrode subsequently can reach the detector with energies in the range of or above the expected tritium electron energies. This has been observed in the Mainz experiment in the form of a so-called "trans-U_0 peak". Reducing the X-ray energies by installing a ground electrode made of a lower Z material (e. g., titanium) as compared to that of the central electrode would prohibit the emission of K-shell electrons and thus decrease the number and energy of secondary electrons which are liberated from the central electrode and could find their way to the detector. However, it was argued that the suppression of a minor background component at the pre-spectrometer is of less importance compared to the huge problems caused by the Penning trap.

The ground electrodes, connected to the DN200 part of the isolator flange, are made of titanium to prevent X-ray induced electron background in the energy region of interest[25]. The conical full electrodes are made of stainless steel sheet metal which large electric field gradients near the ground electrodes to prevent field emission. The stainless steel wire electrode is made up by a cylindrical and two conical parts. A frame holds over 240 wires with $d = 0.5\,\mathrm{mm}$ diameter evenly spaced by $s = 2\,\mathrm{cm}$ (measured in the cylindrical part) and yielding a geometrical coverage $f_{gc} = d/s = 2.5\%$ (neglecting the wire frame). The wires are fitted with springs ensuring a safe expansion during bake-out and cool down procedures. All six parts of the inner electrode are electrically isolated versus each other and versus the vessel using glass spacers. They are supported solely by a cradle standing on the bottom half of the vessel connecting the cradle to vessel potential. Every electrode part is equipped with a socket for a connector rod and a connecting electrode with a high voltage feedthrough installed in the three chimneys on top of the vessel. The inner electrode was designed and constructed by the KATRIN Collaborators of the University of Washington, Seattle. The assembly and installation was carried out by personnel from Forschungszentrum Karlsruhe. The left hand picture of fig. 3.15 shows the electrode prior to the insertion through the open DN1680 flange into the pre-spectrometer vessel.

[25] Electrons hitting the ground electrode induce the emission of characteristic X-ray radiation which is in turn able to produce Auger and photoelectrons when hitting the other metal parts of the same material. The released electrons are accelerated by the electric fields and guided along the magnetic field lines present in the MAC-E filter. If the magnetic field lines connect with the detector the electron will be detected with the energy gained through the acceleration plus the surplus energy of the release, e.g. in the region of interest near the endpoint of the β spectrum. A means to prevent this dangerous background component is to use a lower Z material, e.g. titanium or aluminum for the ground electrode. X-rays emitted from these lower Z-materials carry less energy, the number and energy of secondary electrons is removed and the background measured by the detector is moved to lower energies and out of the region of interest.

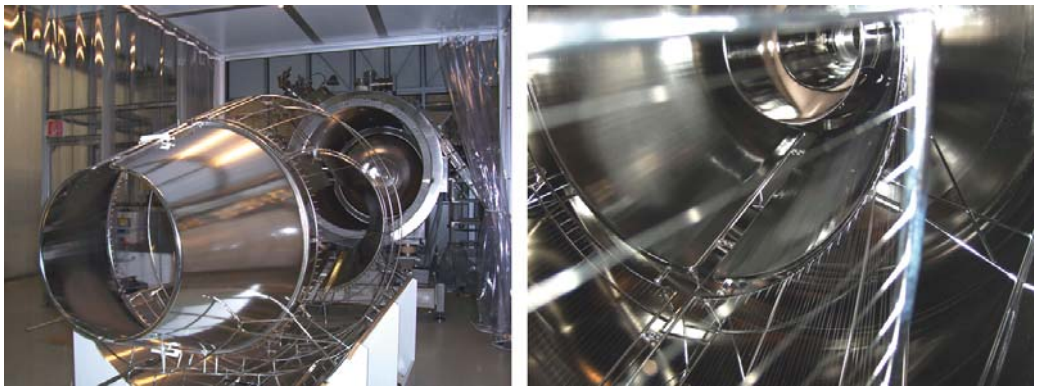

Figure 3.15: Photograph of inner electrode system before insertion into pre-spectrometer and inside the pre-spectrometer as seen from the side-port.

3.1.3 High voltage supply

The supply of the different parts of the high voltage (HV) system with a different set of voltages each requires a high voltage supply system consisting of four different power supplies. A schematic oveview of the HV system is shown in fig. 3.16.

The power supplies are named after the manufacturer FuG with a running number (FUG1-5) or a descriptor (FUG egun).

FUG4 Type designation: HCN 140-35000. Maximum output: -35 kV, 3 mA. Stability: 10 ppm/8 h, 350 mV pp.
Objective: Supply for vessel potential.

FUG3 Type designation: HCN 140M-35000. Maximum output: -35 kV, 3 mA. Stability: 10 ppm/8 h, 350 mV pp.
FUG3 is designed to a) produce an HV output of maximum -35 kV, b) loop through an external voltage (FUG4), c) build a direct connection to two more power supplies via an integrated adapter box. A voltage dependent resistor makes sure that input voltage of FUG4 and output voltage of FUG3 don't differ by more than $|\Delta U| = 5\,\mathrm{kV}$. In the case of a higher input from FUG4, the output of FUG3 will automatically increase to limit the difference in voltage to the set value.

FUG1 & FUG2 Type designation: HCN 35M-5000. Maximum output: 5 kV, 3 mA. Stability: 10 ppm/8 h, 350 mV pp.
FUG1&2 loop through the voltage output of FUG3. Both power supplies can produce an offset of maximum +5 kV onto the output voltage of FUG3.

FUG egun Type designation: HCN 350M-35000mod. Maximum output: -30 kV, 1.5 mA. Stability: 10 ppm/8 h, 350 mV pp.
FUG3 provides the power supply for the e-gun system, see section 3.4.

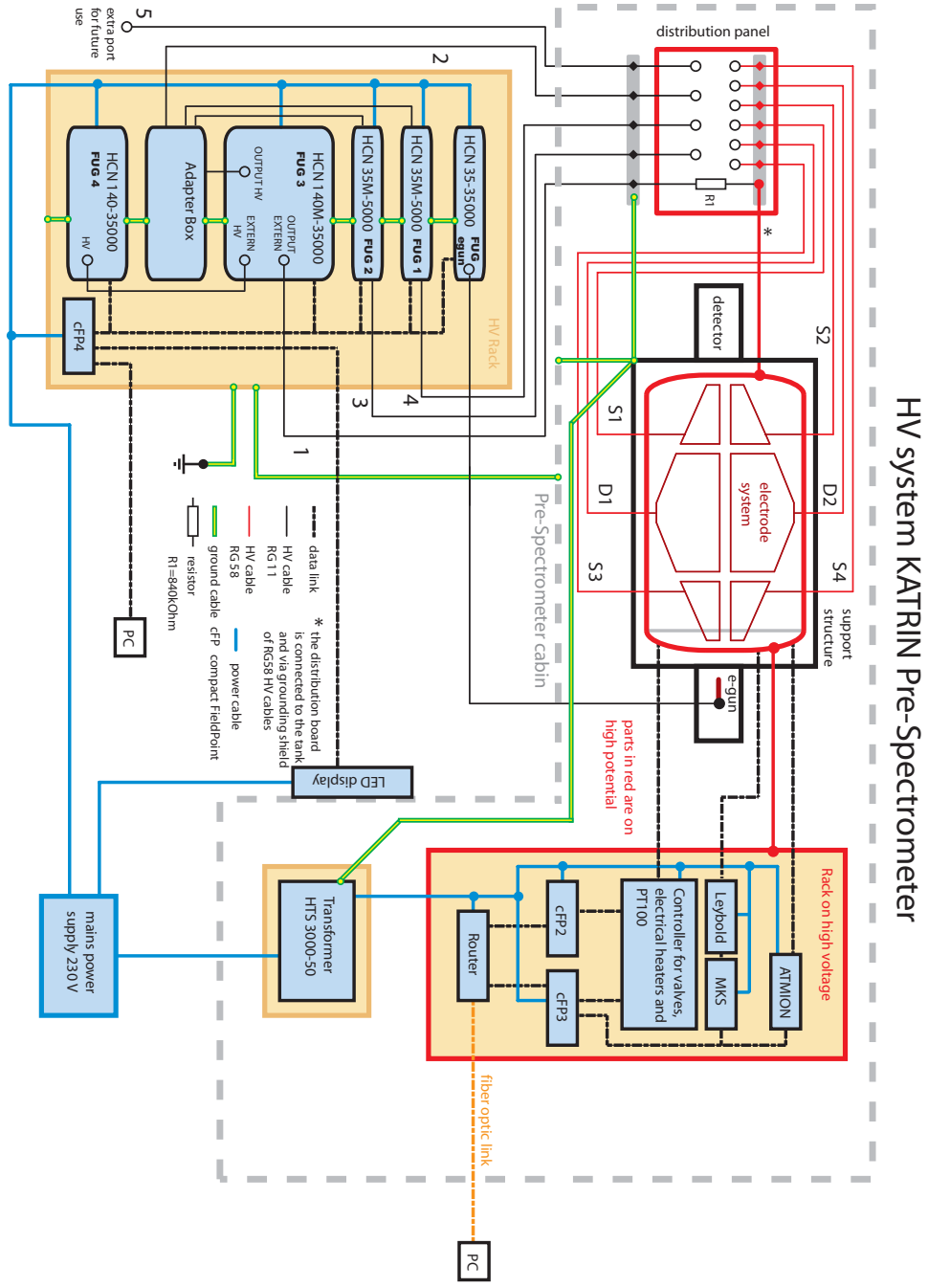

Figure 3.16: Diagram detailing the high voltage system. [Frä07a]

FUG5 Type designation: HCN 140-35000. Maximum output: -35 kV, 3 mA. High precision power supply. Not in use.

The power supplies are equipped with an RS232 interface which allows computer supported remote control and data monitoring (leakage current and voltage). Using a high precision voltage divider read out by a Fluke 45 multimeter a calibration of the voltage output has been carried out. The following conversion formulae have been obtained:

$$U_{set}(FUG3) = (0.99780 \pm 0.00008) \cdot U - (6.2 \pm 1.2)\ [V], \tag{3.2}$$

$$U_{set}(FUG4) = (-2.22977 \pm 0.00001)10^{-7} \cdot U^2 \tag{3.3}$$

$$+ (0.9963 \pm 0.0002) \cdot U - 52.7 \pm 1.8\ [V]. \tag{3.4}$$

More information on the calibration measurement is given in App. B.

The interconnected power supplies make it possible to elevate seven isolated parts of the vessel and inner electrode system to up to four different negative potentials in the range from 0 to -35 kV with a maximum difference of $|\Delta U| = 5$ kV. During the test measurements it has been necessary to change the potential settings. To be able to do this swiftly a so-called 'patch box' has been designed, fig. 3.17. Cables of the type RG11 from FUG1-4 are routed directly from the HV rack, located outside of the dry air cabin, to the ground potential star point which is attached to the base frame of the pre-spectrometer. The base frame in turn is attached to the ground point of the experimental hall. The protective shield of the cables is connected to the star point, the bare inner conductor is guided inside a stainless steel box, with only FUG4's cable being directly connected to the box, while the box itself is connected to the vessel. Inside, the cables are attached to a block of isolating material (Polyoxymethylen). A second block, 15 cm apart, provides the attachment for the inner conductors of six RG58 cables providing connections to the six parts of the inner electrode. With the use of pin plugs, it is possible to create a fully flexible connection of the power supplies with both vessel and electrode This implies that the potentials of vessel and the halves of east cone, west cone and wire electrode can be chosen freely with the constraint of up to four different potential values with a maximum difference of $|\Delta|U = 5$ kV. The restriction of the potential difference is required by the high voltage stability of the glass insulators of the inner electrode and the layout of the patch box, which both are limited to this value. In addition, this limit has also to be guaranteed with regard to the small distance of the wire electrode to the vessel wall: with increasing voltage difference, the electric field increases accordingly and field emission can occur[26]. This is even more apparent at the wire electrode itself. Due to the small wire radii, the electrical field strengths there are much higher and a discharge is more dangerous. A broken wire as a result from a major discharge could possibly necessitate a major maintenance procedure. As mentioned above, looping the FUG4 through FUG3 interconnects FUG1-4. In the case of an output difference

[26] Experiments carried out in Mainz report field emission starting above 0.4MeV/m [Ang04]

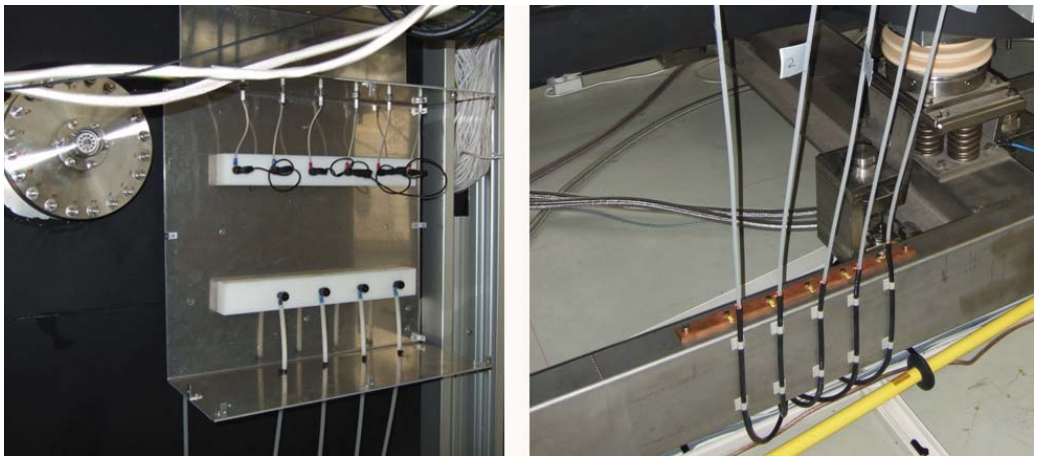

Figure 3.17: Patch box for supplying the vessel and six inner electrode parts with high voltage.
Left: the box layout accommodates supply lines from five high voltage supplies. One is directly connected to the box which in turn is connected with the vessel. An 850Ω resistor, not shown in the picture, is interconnected in-between to restrict potential damages to the electrical devices in the case of a discharge. Up to four supply lines can be connected with the six parts of the inner electrode. The interconnection of the inner electrode parts can be selected freely.
Right: the shielding of the RG11 cables is connected to the ground star point.

of FUG3 and FUG4, a voltage dependent resistor turns conductive and the voltage of FUG3 increases. This voltage increase is supplied by FUG4, therefore, its current increases. The current increase does not exceed 10% of the maximum allowed current of 3 mA which is small enough not to limit the maximum high voltage supply. The patch box has been prepared to accommodate for another power supply designated FUG5. This extra power supply would increase the maximum number of possible potentials to five.

3.1.3.1 Improvements of the high voltage stability

Starting in August 2006, the pre-spectrometer system was ready to be put on high voltage. Over the next months, the high voltage stability was increased steadily from an initial modus with instant discharge after applying high voltage to the final operation with completely stable conditions at -25 kV. Accordingly, in the following, only measures on the spectrometer outside are detailed. A change of the inner electrode set-up is motivated differently and will be discussed in chapter 4.

In the beginning stages of operation, the HV isolation measuring device Metriso 5000 was used. This device applies HV to a recipient and measures the resistance between ground and vessel on elevated potential. This makes it possible to check for unstable conditions without using the FuG HV supplies which, in the case of a discharge, could cause damage to the slow control electronics system. Several

floating structures with no well-defined potential were identified and subsequently connected to the well-defined vessel or ground potential. The glass foam insulation of the heating-cooling system was fixed to the pipes with wires. The wires, however, had no contact with ground or elevated potential which lead to charging effects and subsequent discharges. The insulation has now been completely removed and exchanged for glass wool insulation. A similar effect was caused by the insulator cushions covering the DN1680 end caps of the spectrometer vessel. The inner ring cushions which are in direct contact with the magnet on ground and the vessel on elevated potential have been designed to withstand voltage differences. However, for the outer ring cushions' seam, a metallic wire was used. In addition to the floating effects, potential discharges can occur at the cushion parts next to the magnets. As a result the cushions had to be removed prior to long-term HV measurements.

After identifying the major HV stability problems, high voltage down to -35 kV could be applied but at higher potentials discharges were still recorded. Monitoring of the voltages and leakage currents was then used as a means for discharge recording. The FuG power supplies are limited in broadcasting possibilities, therefore, either leakage current or voltage can be recorded at one time only with a sufficient resolution of 1 Hz. Lower rates already limit the detection efficiency for discharges considerably, while higher rates cannot be handled by the communication interface. By connecting the Julie Research HV divider to the vessel and by reading out the voltage with a Fluke 45 multimeter and transmitting the data via parallel port to a personal computer, the voltage can now be precisely monitored while the FuG power supply logs the leakage current data. These automated data storage measurements allow the precise tagging of the pre-spectrometer system's longtime high voltage stability. The experimental results show the positive effects of conditioning the system, e.g. ramping up the system to the maximum of -35 kV, followed by a subsequent increase of the potential to the desired measurement voltage. In this way, the parts on a more positive potential are bombarded by electrons emitted from vessel and electrode, thereby removing micro-structures on the surface. For the parts on a negative potential, micro-structures can lead to field emission also burning away those structures in the process, thus also removing the source for field emission or discharges. Reversing the polarity also reverses the process of electron bombardment. Now the micro-structures on the electrode surface are eliminated more efficiently. Negative polarity conditioning is carried out every time the system has been connected to ground and the routine operation has ceased for several hours. The positive polarity option is only used after the system has been opened. For the latter, a Heinzinger HNCs 30000 power supply is used to prevent possible damages to the FuG power supplies in case of a severe discharge. The positive effect of the conditioning can be observed in a drop in both rate and amplitude of the logged discharges.

Nevertheless, minor discharges still occurred on the outside. The distribution panel for the high voltage could be identified as the source of the problems. Starting the HV measurements in 2006 the connection of FuG power supplies was following a different strategy: the RG11 cables were guided alongside the roof of the dry air

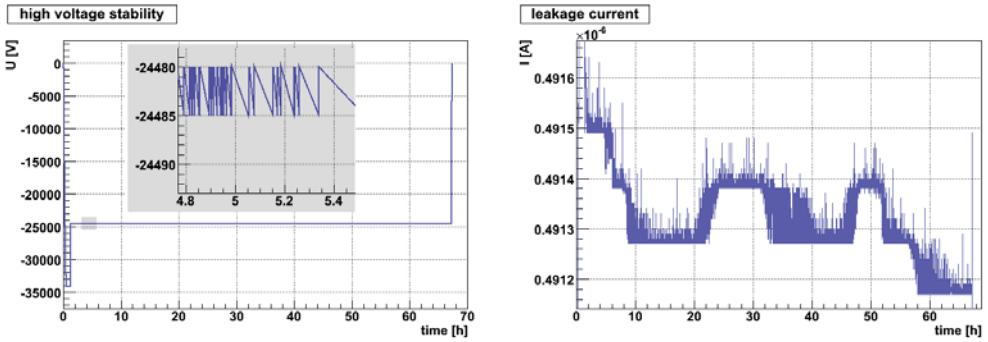

(a) Stability of high voltage

(b) Stability of leakage current

Figure 3.18: High voltage stability. Longtime measurements of the high voltage stability over 64 hours. After a conditioning phase of 30 min no further discharges in the sensitivity limit of 5 V occurred over the whole time. The leakage current shows some drift effects but no abrupt increase as is typical for a discharge. Otherwise it is stable in the sub-μA region.

cabin and connected to a distribution board suspended from the roof as discussed in [Frä06]. After observing and photographing a discharge spark coming from the cabin structure and traveling to the board, a new design was developed. Instead of an open board the new device will have an encapsulated box design with the outside on vessel potential to reduce the differences in potential to a maximum of $|\Delta U| = 5\,\mathrm{kV}$. Secondly, the board location has been removed to a point of small electrical fields; an appropriate place has been identified in a location behind the controller cabinet on elevated potential. Here, the box is attached directly to the spectrometer vessel, see fig. 3.17. Furthermore, the RG11 cables were tailored to the minimum length possible. Finally, a power distribution panel was relocated directly underneath the pre-spectrometer. This power panel, its earth connection being connected to the new ground star point, is supplying also the relocated isolating transformer and the FuG power supplies with 240 V AC. Relocating the FuG cabinet to the inside of the dry air cabin would have further reduced the cable length, however, restricting manual access during measurements is not favourable from a safety point of view.

Additionally, by further altering the inner electrode system as detailed in chapter 4, the stability of the high voltage increased to the point of very good stability. Fig. 3.18 features the monitored leakage current and high voltage over the course of 66 hours, after a conditioning phase of half an hour. During the conditioning discharges can occur, afterwards the voltage stays stable during the stability test within 5 V which is the resolution of the voltmeter used. The leakage current shows drifting effects which again can be attributed to either the Fluke voltmeter, the HV divider or the FuG power supply. At the level of 0.49 μA no discharge was observed.

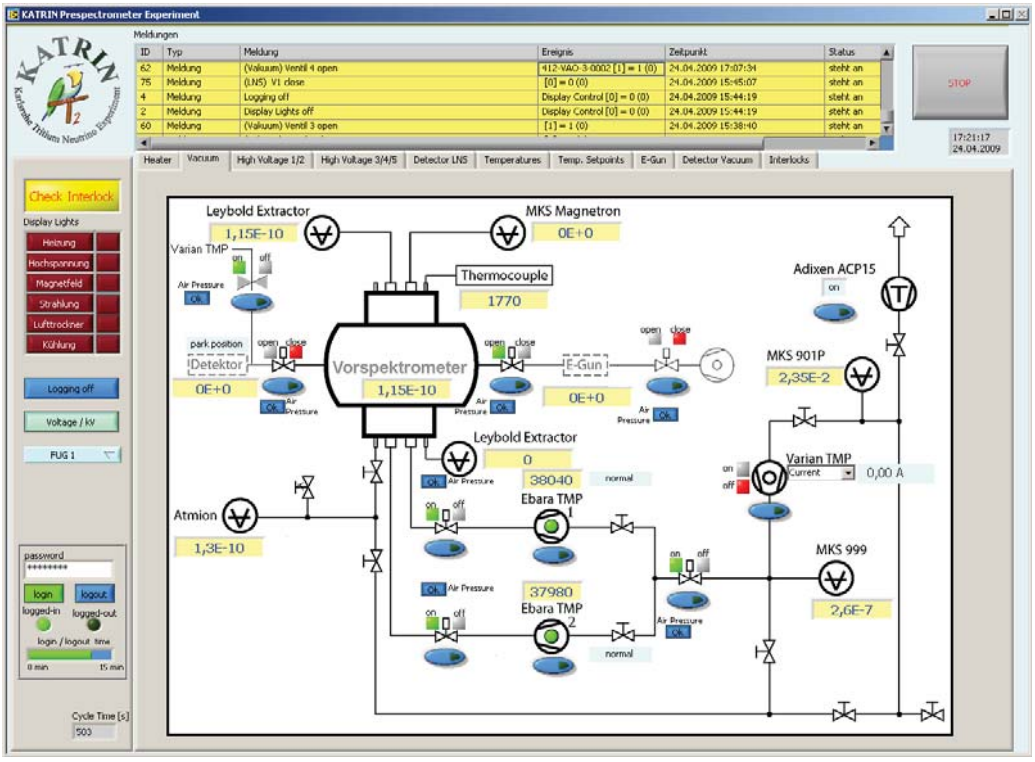

Figure 3.19: The ZEUS graphical user interface. The interface program's main window shows the chosen subsystem mask (e.g. vacuum control). Executed commands are listed in the top table. The column on the left side integrates the status of the interlock system, the warning lights and the buttons are for the logging of the leakage current or voltage applied to the vessel. Only authorised users can change a parameter via the interface, the log-in dialogue can be found on the lower left.

3.2 Slow control system

The many parameters of the KATRIN pre-spectrometer test experiment are monitored and operated via a slow control system (SCS). This system integrates all sensors and devices with digital interfaces like valves, pumps, temperature controllers, high voltage supplies and a multitude of sensors; not integrated into the SCS are the data acquisition (DAQ) and the magnet system. The integrated devices are either passively read-out or actively operated with the help of a user interface, the collected data are transferred to and stored in a database.

The slow control system is made up of five National Instruments Compact FieldPoints (NI cFP). These units are programmable automation controllers (PAC) incorporating a variable and expandable selection of input/output modules combined with TCP/IP[27] communication interfaces. Programs on LabView[28] basis are exe-

[27] Transmission Control Protocol/Internet Protocol

[28] National Instruments LabVIEW, a graphical programming language for measuring and control-

cuted directly on the FieldPoint, the data are internally buffered and after a specified time period collectively broadcasted via TCP/IP to a dedicated data server, thus preventing a possible overload of the network by a constant data stream. The programs running on the FieldPoint can be accessed via TCP/IP from any computer with the LabVIEW software installed when inside the lab network. With LabVIEW version 7 only one program at a time can be accessed. To avoid continuous switching of cFP-programs, an additional graphical interface system ZEUS[29] based on LabVIEW has been developed by the Institute of Data Processing and Electronics (IPE) at Forschungszentrum Karlsruhe. ZEUS monitors and displays all relevant data and in addition enables the user to exert direct control over the hardware by sending the commands to the FieldPoint programs where they are executed.

In 2008 an upgrade from LabVIEW version 7 to 8.5 was carried out. With LabVIEW 8.5 the access restriction to one FieldPoint only at a time has been eliminated. However, only with the ZEUS GUI it is possible to display the subgroups which are spread out over several cFPs consistently. An example is given in fig. 3.19: the complete vacuum system is displayed using an interactive process and instrumentation diagram (PID). The operator is enabled to carry out complex operational and controlling sequences by clear presentation of the parameter values and by granting simultaneous access to several different subsystems.

The ZEUS user interface includes graphical masks for all subsystems. Additional functionalities of ZEUS are a table logging the commands carried out, a status indicator for the interlock system (see below), activation buttons for the warning signals (heating, cooling, high voltage, magnetic field, radiation) and the data logging function (monitoring of leakage currents or high voltage applied to pre-spectrometer vessel).

The subsystems controlled by Zeus are:

Heater Access to 20 GEFRAN 9400 temperature controllers distributed over cFP0, cFP1 and cFP3, allowing the activation of heating and changing of temperature setpoint values.

Vacuum Read out of values of the vacuum gauges, status of pumps including rotor speed of TMPs, valves positions. Location: cFP1.

High Voltage 1-5 The power supplies of the high voltage system can be accessed providing full functionality including leakage current read-out. Location: cFP4.

Detector cooling Activation of cooling for silicon detector and liquid nitrogen fill level indicator. Location: cFP3.

Temperature setpoints Setting of the threshold values for temperature sensors attached to the pre-spectrometer vessel and the detector. Location: cFP2 and cFP3.

ling tasks

[29] German: **Z**entrale Daten**e**rfassung **u**nd **S**teuerung

E-gun Access to electron emitter power supply including shutter system. Location: cFP4.

Interlock system Access to Interlock daisy chain. Needed for a system restart after safety failure. Location: cFP0-4.

The pre-spectrometer SCS and ZEUS systems are test environments for the slow control system of the final experiment. With the pre-spectrometer being a comparably small setup it is still possible to merge multiple data streams in an offline analysis. The DAQ software ORCA (see chapter 3.5.4) is not integrated into the ZEUS system, however, accessing ORCA via ZEUS has been successfully tested, offering the possibility for automated measurement sequences without user supervision. The ORCA raw data are stored on a different data server than the ZEUS data server. The ORCA data are also not transmitted to the database. Another piece of information not being stored in the database are data read-out by the magnet system. Figure 3.20 shows a schematic diagram detailing the data/information and communication flow at the pre-spectrometer test experiment. The final KATRIN set-up will feature a database integrating all information necessary for data analysis. As a first step the ADEI[30] system has been implemented giving browser access to all data stored in the database.

The pre-spectrometer SCS brings about a considerable increase in operation and personnel safety. This is achieved by constant monitoring of vacuum, temperature and positioning sensors employed at the pre-spectrometer. Basic safety procedures encompass ZEUS access restriction to authorised personnel by user log-in as well as command confirmation for the operation of vital devices like valves and TMPs. Moreover, several complex safety measures are defined which are automatically activated if a special trigger mechanism occurs:

Bake-out A table of 128 temperature sensors, which are passively read out, are distributed over the entire pre-spectrometer and its satellite systems combined. For each sensor a threshold value can be set. If any one threshold value is exceeded, the SCS will activate a siren as well as a flashlight and turn off the heating (oil and electrical heating) of the relevant subsystem (detector chamber or pre-spectrometer). In the case of the cryoheater, only the oil heating will be stopped, while the circulation of the oil continues. Thus the temperature distribution stays homogeneous and overheating of a single spot is prevented. The same safety measure is taken when the vessel pressure rises higher than 10^{-5} mbar. At pressures this high, the gas load on the TMPs is nearing its limit.

Detector movement The detector is mounted onto a lance which can be moved horizontally by 43 cm in z-direction into the warm bore of the superconducting magnet. This positions the lance inside the DN200 valve, which is closing off

[30] ***A****dvanced* ***D****ata* ***E****xtraction* ***I****nfrastructure*[Chi08]

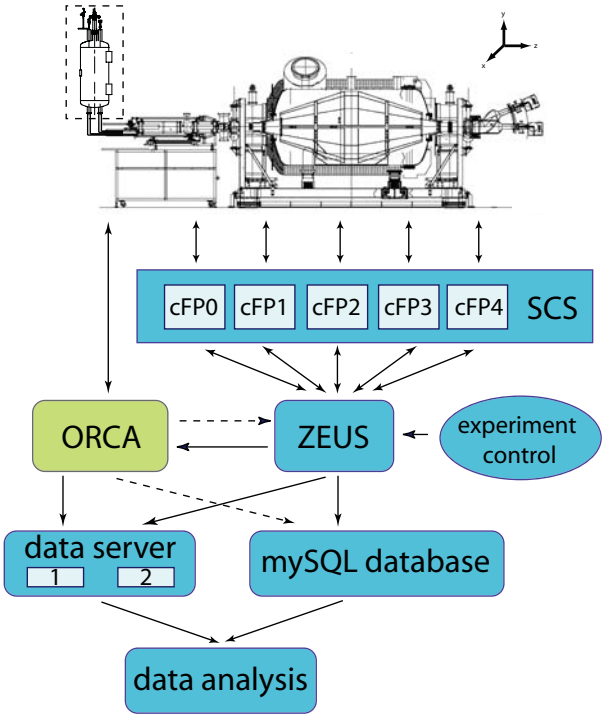

Figure 3.20: Schematic representation of the data flow at the pre-spectrometer test experiment. ZEUS is the central hub handling the data flow coming from the pre-spectrometer's sensors and devices and controlling the communication between software (round symbols) and hardware (angular symbols). Arrows indicate the direction of data/information flow, dashed lines represent projects in development. Components highlighted blue are developments by the Institute of Data Processing and Electronics, Forschungszentrum Karlsruhe, green highlighting refers to the contributions from University of Washington.

the pre-spectrometer from the detector chamber. In the case of a vacuum break-down the normal procedure would be to close all valves to protect the individual subsystems. In the case of this valve this has to be prevented. As soon as the valve is moved out of the maintenance position at z=0 a switch is deactivated preventing the closure of the DN200 detector valve, see sec. 3.5.

Power failure In the case of a power failure all electrically powered units are off including the pumping system, endangering the vacuum integrity. For the pre-spectrometer system safety settings have been worked out which are then activated. Valves will close or stay open according to those settings and also depending on the mode of operation, e.g. during a bake-out the valves of the heating cooling system will stay open (see above) as well as the DN200 valve of the detector system, depending on the detector's z-position.

Vacuum status The vacuum status is permanently monitored. In the case of an increase in vacuum to 10^{-6} mbar or higher the SCS closes all automatic valves of the pumping section, deactivates the TMPs and closes the power-off valve before the fore vacuum pump. This safety measure prevents an inrush of air into the pre-spectrometer, which would contaminate the inner vessel walls, and protects the TMPs from overheating due to a laminar flow of gas molecules.

Personnel safety Several measurement procedures, like high voltage applied to the pre-spectrometer vessel and use of an X-ray emitter, require stringent security measures completely restricting access to the pre-spectrometer vessel. This is achieved by setting up an interlock system: all doors and windows of the dry air cabin are interconnected and the status is monitored. Opening a door or window breaks the loop resulting in the deactivation of any potentially hazards: X-ray emitter and high voltage power supplies are immediately turned off.

The bake-out process also makes use of the interlock system requiring the windows of the dry air cabin to be open so that excess heat can be dissipated.

In conclusion, it can be stated that the SCS and ZEUS systems offer the following advantages:

- central graphical controlling interface
- masking of complex controller system
- easy and simultaneous access to multiple system subgroups
- pre-processing of data and transfer into database
- access limitation for authorised users only
- automated personnel and system safety measures
- automated measurement sequences

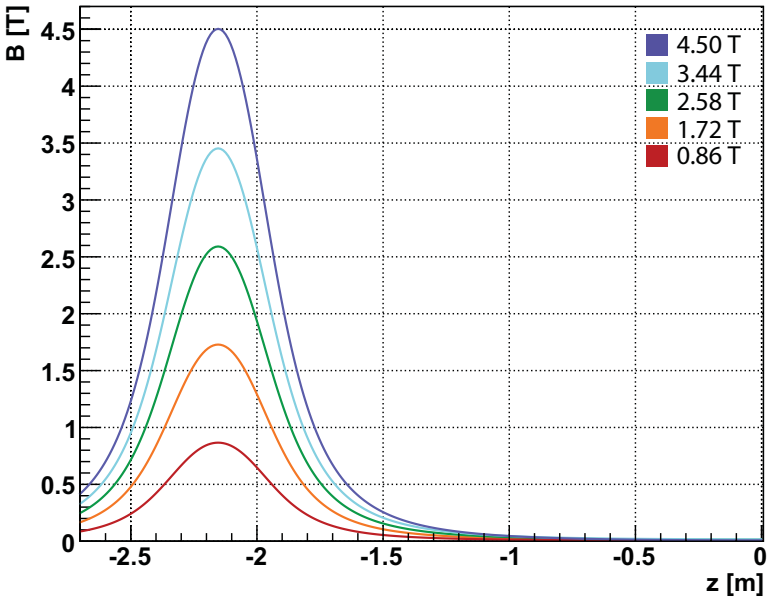

Figure 3.21: Magnetic field along the z-axis for different maximum field strengths.

3.3 Superconducting magnet system

The electrons injected into the pre-spectrometer system are guided on magnetic field lines. The magnetic field is created by two Cryogen Ltd. superconducting solenoids with a horizontal room temperature bore of 40 cm diameter[31]. The solenoids are positioned to both sides of the pre-spectrometer vessel with a distance of 4.3 m from coil centre to coil centre. The maximum magnetic field in the centre of the coils is $B_{max} = 4.5\,\mathrm{T}$, corresponding to a field in the pre-spectrometer's analysing plane of $B_{ana} = 0.016\,\mathrm{T}$. The magnetic field along the pre-spectrometer's z-axis is presented in fig. 3.21 for five different maximum field strengths.

The necessary current of 157 A is provided by the low-voltage-high current power supply FuG NTS 800-5 (see table 3.1 for the allowed ramping speeds). The electrical connection between room temperature and cryostage is realised by High Temperature Superconductor (HTS) current leads reducing heat leaks by a factor 10. The ramping of the magnets is usually done by hand operation of the power supplies but GPIB[32] access is available. A number of RhFe-heat sensors are distributed over the relevant parts of the magnet system monitoring the stability of the temperature distribution and giving information if the system is ready for operation. In the case of a magnet quench, the temperature increase allows to identify the exact time of

[31] Figure 3.22 shows the principle layout of a cryogen free warm bore superconducting magnet system.

[32] General Purpose Interface Bus

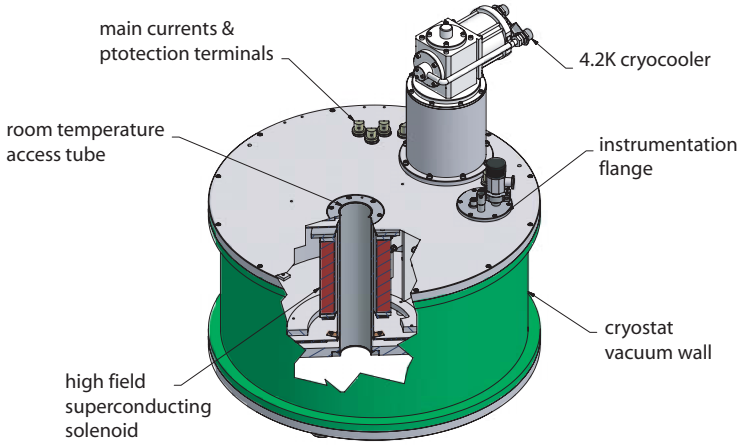

Figure 3.22: Drawing of a cryogen free magnet system. The warm bore of the KATRIN magnets is 40 cm in diameter, and thus considerably larger than shown in the diagram. Diagram taken from [Cry04].

break-down. This information is read out by two dedicated personal computers utilising a LabVIEW monitoring interface showing the different temperature gradients.

The magnet system can be operated in two ways: the power supplies are continuously controlling the current input or switching over to persistent mode. In the latter case, the superconducting coils are short-circuited with a superconducting rod, a superconducting loop is generated which preserves the currents flowing in the windings and hence the magnetic field. In principle, operation of the KATRIN experiment with magnets in persistent mode seems advantageous but measurements show that the stability of the magnetic field deteriorates too fast, thus necessitating continuous operation of the power supplies [Geh08].

To reach superconductivity the cryostat in which the coil is housed has to be cooled

Table 3.1: Ramping speeds for the superconducting magnets. When the magnets are ramped up, a limit is set to the ramping speed according to the injected current as the amount of energy transferred into the magnet coil is $E_{mag} = \frac{1}{2}LI^2$. Too high energy input per unit time can lead to a quench of the superconducting magnet.

current	ramping speed
0A .. 120A	50 mA/s
120A .. 130A	40 mA/s
130A .. 140A	30 mA/s
140A .. 150A	20 mA/s
150A .. 157A	10 mA/s

down to liquid helium temperatures of 4.2 K or better. This is achieved by implementing a cryogen free system in connection with a Sumitomo[33] SRDK-415D (Gifford-McMahon) 4.2 K-cold head: the cold head's second stage is in direct contact with the superconducting coil instead of using a helium bath for cooling while the first stage is cooling the thermal shield to 35-40 K. The cold heads use helium as a process gas which is regenerated by water-cooled Sumitomo CSW-71D compressors. Without the need to refill helium or other process gases the maintenance demands of the system are minimal. The cold heads have to be exchanged once a year causing a downtime of approximately two weeks – one for warm up and one for the cool down – but otherwise allow for continuous operation.

For the cryostat's thermal shields to be effective an insulation vacuum of 10^{-5} mbar is generated by a Pfeiffer Vacuum TSH 071 pumping system which decreases to 10^{-7} mbar when the magnet cooling is activated. The pumping system is equipped with a security valve closing down in case of power loss or pump malfunction. Venting of the system with ambient air has to be prevented, otherwise water would freeze out in-between the superisolation foil, thus possibly causing damage to the magnet system.

3.4 Mono energetic electron emitter

Measurements of the transmission properties of a MAC-E filter require monoenergetic electrons. Employing a radioactive source at the pre-spectrometer test set-up is not feasible. Instead, an electron emitter making use of the photoelectric effect is commissioned. The ideal requirements can be summarised as follows:

1. minimum energy spread (sub-eV region)
2. maximum electron rate of 10^4-10^5 e^-/s
3. total flux tube coverage
4. isotropic emission

For the pre-spectrometer system these requirements can be relaxed slightly with regard to energy spread[34] and to the emission properties.

The Troitsk group of the KATRIN collaboration designed an electron emitter, in the following referred to as 'e-gun'. The assembly and its properties will be presented in the following section.

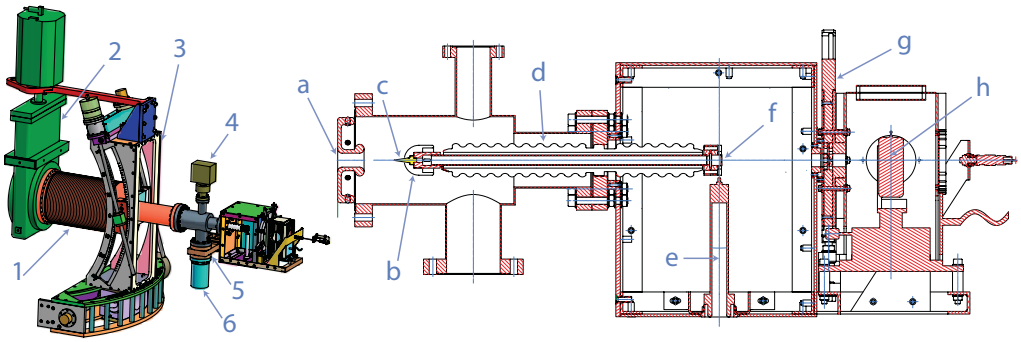

Figure 3.23: Set-up of the electron emitter
Left: 3D model of complete set-up including radial positioning system: **(1)** edge welded bellow **(2)** DN250 VAT valve **(3)** horizontal and vertical axis with $\pm 23°$ freedom of movement **(4)** VACOM Atmion^{TM} multi range pressure gauge **(5)** VAT DN63 gate valve **(6)** Leybold TW70 turbomolecular pump
Right: cut view of e-gun: **(a)** electrostatic focusing lens on ground potential **(b)** removable shielding cap on elevated potential **(c)** gold plated quartz glass tip **(d)** isolator **(e)** HV connection **(f)** entry window for UV light **(g)** pneumatic blind and shutter system **(h)** Hamamatsu L6565 deuterium lamp

3.4.1 Electron emitter set-up

The electron gun as shown in fig. 3.23 utilises the photoelectric effect: light in the range of $400\,\text{nm} > \lambda > 185\,\text{nm}$ is emitted by a deuterium lamp (h) with an intensity maximum at 220 nm[35], see diagram 3.24. The light is passing through a pneumatic driven blind and shutter system (PBSS)(g) and subsequently through a sapphire glass window(f) (DN16 window flange) and onto a quartz glass tip(c). The sapphire and quartz glass show high transmittance of UV light at 200 nm [Som, Ham07] with negligible intensity changes. The quartz glass tip's upper half (see fig. 3.27) is plated with gold. The gold layer is $35\mu\text{g/cm}^2$ on its tip (radius 1 mm) and is much thicker on the cone's side: whereas photons can't penetrate the thick side layers, the tip's head is semi transparent and photons of sufficient energies release electrons via the photoelectric effect. The work function for a gold layer on glass is given as $(4.7 \pm 0.02)\,\text{eV}$ [Riv66]. With ultra violet (UV) light of wavelengths as specified above, photons carry energies of 3.1-6.7 eV resulting in possible excess energies of the created electrons in the range of $0 - 2.0 \pm 0.02\,\text{eV}$.

The quartz glass tip is protruding out of a metal cap by 15 mm. Cap and tip are in contact with a steel tube which is encased by a ceramic isolator. Thus, by applying high voltage to the tube the e-gun cap and tip are elevated to a high negative poten-

[33] Sumitomo (SHI) Cryogenics of America, Inc., USA
[34] To reduce a broadening of the transmission function the energy spread has to be significantly smaller than the energy resolution of the pre-spectrometer which is $\Delta E \approx 70\,\text{eV}$ at 18 kV retarding potential.
[35] Hamamatsu L6565. The wavelength is limited by the exit window's material. The deuterium lamp features small intensity fluctuations in time of 0.005% [Ham07].

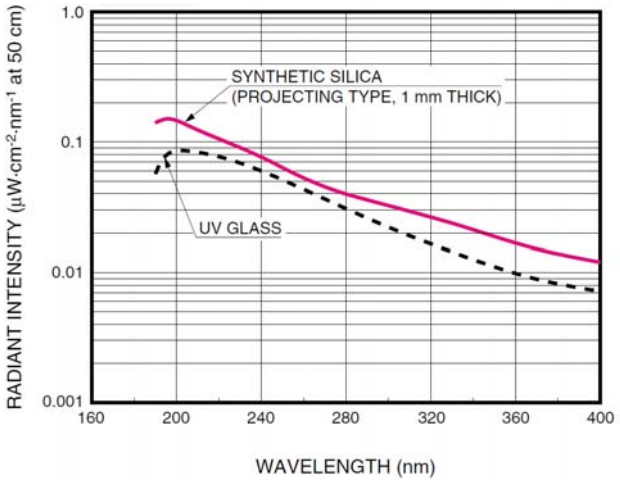

Figure 3.24: Wavelength spectrum of a Hamamatsu L6565 deuterium lamp (UV glass). The wavelength range is dictated by the exit window material [Ham07].

tial while the surrounding structure is connected to ground. The electric potential accelerates the electrons which are then focused onto an electrostatic lens connected to ground. The electrons passing the lens are injected into the pre-spectrometer with the energy gained from the potential difference plus surplus energy transferred by the photon:

$$qU_{egun} < E < qU_{egun} + 2.0\,eV. \tag{3.5}$$

The high voltage is supplied by a FuG HCN 35000 power supply (FUGegun), section 3.1.2. Due to safety regulations this power supply is modified to a maximum output of -30 kV. Therefore, the energy of the electrons can be selected starting from 0 to -30 keV. The number of electrons created depends on the intensity of the UV light hitting the quartz glass tip. Within the scope of this thesis a pneumatic driven and remote controlled blind and shutter system has been developed (fig. 3.25), which allows to control the electron rate by changing the diameter of a blind positioned in front of the lamp's exit window. Table 3.2 gives an overview over the possible blind diameters to choose from. The PBSS is controlled by a LabVIEW program which is integrated into the ZEUS system. Detailed information on the design and operation of the PBSS is provided in reference [Ren07].

Table 3.2: Overview over the possible bore diameters of the PBSS blinds. If all blinds are retracted the opening has a diameter of 10 mm, the minimum diameter is 0.2 mm. The blinds of the shutter system are arranged in two levels allowing to operate it in such a way that during a blind change a shutter will close preventing an unwanted excess in electron production due to an increase in light intensity which in turn could damage the detector.

	Level 1					**Level 2**				
borehole [mm]	0.4	0.6	0.8	1	-	2	4	0.2	0.3	-
channel number	1	2	3	4	9	5	6	7	8	10

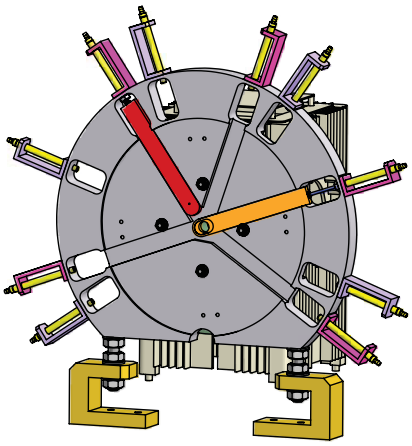

Figure 3.25: 3D model of the pneumatic blind and shutter system (PBSS). Ten pneumatic pistons (yellow) with attached blinds of 0.4-10 mm diameters (red, orange) are arranged in two levels. An automated operation via ZEUS ensures compliance with safety regulations preventing any accidental overexposure with UV light during blind changes.

The pre-spectrometer e-gun system possesses no transversal field dipole magnet. This leads to the possibility of storing charged particles by combined magnetic and electrostatic mirror processes: electrons emitted from the e-gun tip are accelerated in direction of the pre-spectrometer following the magnetic field lines of the entrance side superconducting solenoid. Depending on their starting angle (eq. 2.5) and transversal energy, electrons can be reflected by the retarding potential and subsequently travel back to the e-gun tip. Here, the potential is unmodified but the electrons cannot reenter the gold layer – they do not possess the combined energy of the potential and the work function. Correspondingly, the electrons are trapped between magnet and e-gun. If the trap is efficient and stable enough, negative charged particles accumulate, as a result, the possibility for ionisation of rest gas molecules increases as does the space charge. After passing a critical value, discharges being observed as a voltage break down will occur. To remove trapped electrons, the PBSS system provides an 'empty-trap' mode: trapped electrons are removed from the volume by increasing the negative potential by +24 V allowing them to reenter the gold layer and be absorbed. During this time, the shutter system closes to stop further electron production at a different energy. The time constants can be chosen freely in the range of seconds due to restrictions in remote control and intrinsic reaction time of the pneumatic system.

The complete coverage of the flux tube with the electron beam necessitates a 2-dimensional positioning system. To comply with this requirement the e-gun set-up is integrated into a holding structure which can be rotated along two axes α_x and α_y by $\pm 23^\circ$[36] around a centre-point inside the magnetic bore, see fig. 3.23. The movement along the two axes defines the position of the e-gun tip on a spherical surface which is aligned with the magnetic field (ideally the magnetic field lines meet the surface at a right angle). The location of the tip defines the magnetic field line the electron will follow, thus making it possible to cover the whole magnetic flux

[36] The angle of 23° is the maximum rotation for each axis alone. By operating the e-gun via ZEUS the calculation of the maximum possible movement $\alpha_x + \alpha_y \leq 23^\circ$ is carried out automatically and restricts the movement accordingly.

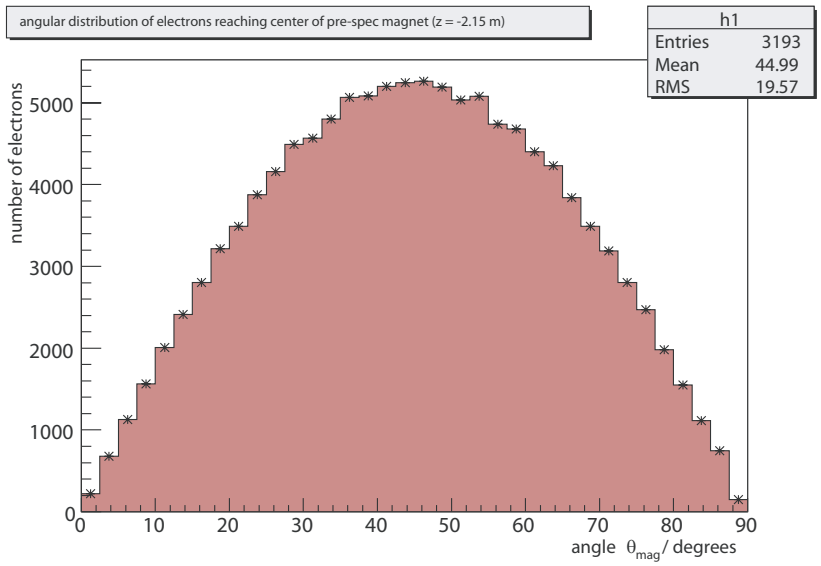

Figure 3.26: Angular distribution of e-gun electrons at the centre of the entrance magnet for B=0.283 T. The diagram shows an isotropic angular distribution for the initial geometry A (tip outside of metal cap). Graph taken from [Hug08c].

tube of 191 T/cm^2. The e-gun movement is achieved by pneumatic driven motors which are still operational in magnetic fields of 0.5 T. The rotation is made possible by a DN250 edge welded bellow which is connected to the DN250 VAT valve closing off the e-gun chamber from the pre-spectrometer.

Furthermore, the e-gun is installed in a vacuum cross to which a VACOM Atmion pressure gauge and a Leybold TW70 TMP, closed off by a VAT DN63 valve, are attached to. The TMP is needed for stand alone bake-out procedures but has to be removed during magnet operation.

Detailed electromagnetic simulations show that the angular distribution of the electron gun is isotropic: electrons of all angles are emitted but large starting angles are strongly suppressed (see fig. 3.26). For the investigation of the transmission properties, especially with regard to the adiabaticity, electrons with large starting angles being close to the border of the flux tube are needed. The electrons are ideal tracemarkers for potential electromagnetic irregularities, which then will be visible most clearly. As a result, R&D for an angular resolved e-gun have started and a first prototype has been manufactured [Hei09].

3.4.2 Commissioning of the electron emitter

During the first tests with the electron gun system, an increase of leakage current up to the limit value of 9 μA occurred as a result of discharges. HV conditioning

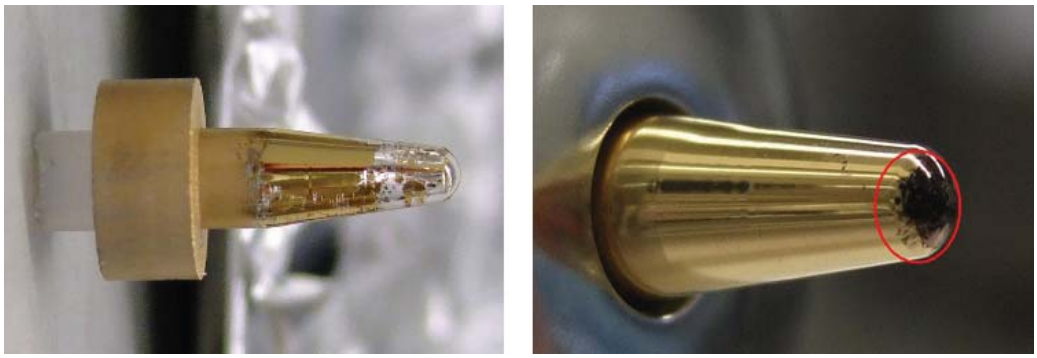

Figure 3.27: Damaged e-gun tip. The tip is protruding out of the metal cap by 1.5 cm. It has been heavily damaged during first commissioning of the e-gun (left) and after a second run despite achieving more stable high voltage conditions (right).

of the system increased the stability but after switching on the UV light discharges frequently occurred in periodic time intervals. An explanation is that the discharge rate goes down when activating the magnets. The electrons created in large numbers are then transported in direction of the spectrometer. In a condition without magnetic field, electrons hit the insulator and charge it up. After a threshold value is reached, a discharge occurs.

But even with magnetic field applied, the HV stability issue is not solved. An inspection of the e-gun tip shows that the gold layer has been heavily damaged to the extent that most of the gold evaporated (fig. 3.27). In the initial design of the e-gun the quartz glass tip is protruding out of the metal cap, as shown in fig. 3.23. Therefore, the tip was unprotected in the case of a discharge. The damaged gold layer featured patches of gold insulated from high voltage connection which results in a further detrimental effect on the HV stability. The chain of events leading to the unstable condition can be explained as follows:

1. an initial discharge develops as the result of an unconditioned e-gun system or a damaged gold layer caused by improper storage[37],

2. further discharges are caused by isolated patches of gold or insufficient distance to electrostatic lens on ground potential,

3. an overall unstable HV condition develops and sustains.

The tips have been replated[38] and three more spare tips have been manufactured. Furthermore, as a precaution, the distance of electrostatic lens and e-gun tip has been increased by 6 mm to a new value of 30 mm.

[37] A second spare tip was showing signs of scratches in the head of the tip, probably due to wrong insertion into the storage vessel.

[38] This work was carried out by the University of Münster

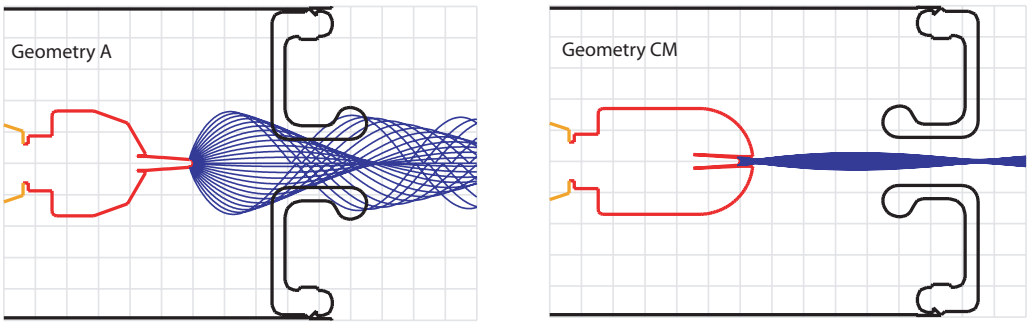

Figure 3.28: Simulation of electron tracks for different e-gun cap geometries. Left: old geometry. The tip is unprotected from discharges, most electrons hit the electrostatic lens or are reflected by a magnetic mirror, for isotropic angular distribution. Right: new geometry. There is a good collimation of the electron beam due to the additional distance between focusing lens and tip yielding an anisotropic angular distribution. [Frä07b]

While the e-gun stability has improved, discharges can still occur. Another theory explaining the discharges is the storage of negative charged particles due to magnetic mirror effect on one side and electrostatic mirror effect on the e-gun side: according to eq. 2.5, electrons with large starting angles will not be able to pass the maximum magnetic field, their transversal energy component increases while the longitudinal energy decreases. When reaching zero longitudinal energy the momentum vector is inverted and the electrons travel back to the e-gun. Here, the electrostatic potential is unchanged but the electron cannot reenter the gold layer due to insufficient energy to surpass the potential barrier and suffice the work function – hence the electron is trapped. If the trap is efficient enough, electrons can accumulate and the possibility for ionisation of rest gas molecules increases as does the space charge. After passing a critical value, discharges will occur. One of the main reasons for implementing the PBSS was the task to empty a possible electron trap and to create stable HV conditions, thereby protecting the e-gun tip. The system has been tested with different voltages and time intervals for swapping between measuring and empty-trap mode. However, no unambiguous evidence supporting the theory of trapped particles as a cause for instabilities could be found. In the course of implementing the PBSS, the electrostatic lens has been polished to remove irregularities in the surface. Wether the increase in HV stability of the e-gun system can be attributed to the polishing of the lens is not decided at the present moment. At present, the high voltage of the e-gun keeps typically stable over the course of about ten hours, yet discharges can still occur.

A study investigating the different cap geometries and electrostatic focusing lens locations has been carried out with the aim to find an overall geometry which increases the HV stability and protects the quartz glass tip from discharges[39] [Frä07b].

[39]Even the good stability, reached after the initial damage of the tip, has not been sufficient as can be seen in figure 3.27. After opening the e-gun system, a burn mark on the tip is clearly visible

The results demonstrate that the initial geometry designated A (tip outside of cap) is rather inefficient with regard to electrons which pass the entrance magnet: most electrons hit the focusing lens (see fig. 3.28), the electrons passing the lens have large angles between momentum and magnetic field lines which leads to reflection of these electrons by the magnetic mirror effect. Geometry C varies from A in the specific form of the metal cap. Instead of leaving the tip in the open for 1.5 cm, the modified cap encloses the tip completely, retracting the tip head by 4 mm to the inside, see figs. 3.28 and 3.29. This leads to a better collimation of the electrons and an increase in small angle electrons resulting in an increase in electron rate as measured in the detector. The drawback of this geometry C is the loss of an isotropic angular distribution. However, by having both geometries at ones disposal, it is possible to choose between geometries according to the planned measurements. Since the pre-spectrometer measurements are mainly concerned with background investigations, the new geometry C has been chosen for the time being. In addition to the change in geometry, the distance between tip and focusing lens has been further increased from 30 mm to approximately 50 mm. As technical reasons require that the focusing lens is mirrored, the descriptor M was added to the geometry, compare fig. 3.28. As can be expected, the changes in the electric fields influence the acceleration of the longitudinal energy according to the actual geometries but do not affect the total energy.

In summary, it can be stated that the new geometry CM increases the safety of the e-gun tip[40] and leads to an increase in electron rate at the expense of isotropy.

In conclusion it can be stated that the installation of the new geometry achieves the desired results: the electron rate has been doubled (0.4 mm blind) from 2.5 kHz (old geometry A) to 5.3 kHz (new geometry CM) as measured with the SPD. Additionally, the tip has not been damaged anymore.

3.5 Detector system

The pre-spectrometer system has several different tasks to fulfil. One of the important tasks is the test of a prototype segmented silicon PIN[41] diode detector (SPD) which is the first step in development of a detector system for the final KATRIN set-up. Additionally, the measurements to validate the novel electromagnetic design (EMD) call for a large-area, multi-pixel detector to be able to monitor a substantial part of the flux tube with good spatial and energy resolution. On the other hand, for the initial commissioning of a MAC-E filter system making use of a novel design with many changes of the high voltage distribution, a robust and rather cheap

showing that all discharges even on micro scale are potentially dangerous.

[40] However, the simulation also reveal that bombardment from positive ions will not be mitigated for ions crated in the electron beam flux tube are guided solely by electric field lines directly onto the tip.

[41] Positive Intrinsic Negative

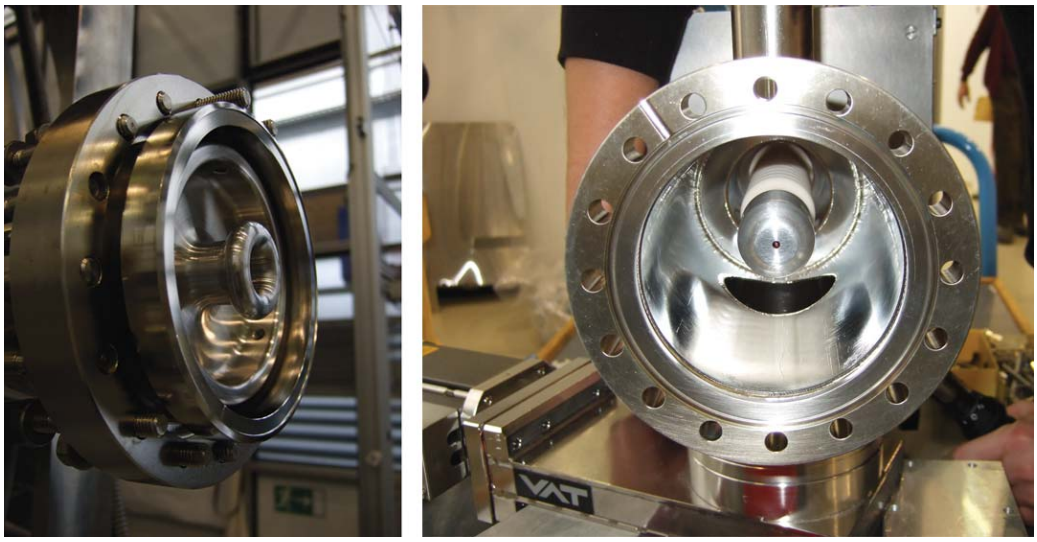

Figure 3.29: Pictures of electrostatic blind and mounted e-gun tip with cap
left: the electrostatic blind on ground potential in mirror configuration.
right: the mounted e-gun with the tip now inside the cap and ceramics isolator.

commercial detector system is needed. Micro channel plates (MCP) fulfil these requirements and provide additional detection possibilities for low energetic electrons and UV-light.

The following lists summarise the combined requirements for the different detector systems:

ultra high vacuum compatibility The vacuum performance of the detector system has to have no significant influence on the pre-spectrometer vessel pressure of $p = 10^{-11}$ mbar.

good spatial resolution A spacial resolution is required to localise the position dependent background (e.g. ignitions of localised Penning traps) as well as to resolve magnetic and electrostatic inhomogeneities in the analysing plane. For the latter, a segmentation of the cross section of the analysing plane into 8×8 pixels is sufficient. In that case (see fig. 3.31) the inhomogeneities for each segment is about 6%, which is comparable to the corresponding pixelisation at the main spectrometer with the Focal Plane detector.

good energy resolution The energy resolution determines both the lower threshold for electrons to be detected as well as the width of the region of interest. Energy resolutions of $\Delta E < 4\,\mathrm{keV}$(FWHM[42]) allow to set the threshold at 10 keV with a signal to noise ratio of about 5:1.

large sensitive area In general, the coverage of the entire flux tube of 226 Tcm^2 is highly desirable.

[42]Full Width Half Maximum

low background rate Simulations [Sch04, Leb09] show that contributions from the ceramics plate onto which the detector is attached and from the mounted electronics both dominate the detector background. Depending on the energy window, this contribution can be as large as 95.6% [Sch04]. Choosing special low-level background materials for the ceramics and the electronics parts has the potential to reduce the total background considerably.

robust and replaceable During first commissioning of a spectrometer system unstable conditions have to be expected. In this regard, a detector system is a an excellent tool for detailed investigation, however, damage to the system is not allowed. Therefore, a commercially available detector is mandatory for the initial site of experiments.

low-energy and light detection In order to investigate the origin of background processes, the possibility to detect also low-energetic ions and UV light is required.

compatible with high magnetic fields The detector has to be operated in a maximum field of 4.5 T, obviating the use of magnetic materials.

In addition, there are the following requirements for the mechanical mounting device:

translation in x,y and z direction Translation into z-direction has to allow the choice of the magnetic field strength at the detector position from 4.5 T (centre of magnet, z=-2.15 m) down to 0.42 T (maintenance position, z=2.7 m). The magnetic field defines the flux density of incoming electrons ($\sim 1/B$) and the maximum angle of the incoming electrons, decreasing from $\theta_{max} = 90°$ (centre of magnet) down to $\theta_{max} = 17°$ (maintenance position).
Translatory movements in x and y direction would not be necessary for a larger customised detector, covering the whole magnetic flux of 226 Tcm^2 tube. However, this takes more effort as compared to a smaller detector with the x,y-translation solution.

stand alone operational capacities This allows the independent opening of the detector chamber for repair, cleaning and maintenance. Furthermore, being decoupled from the pre-spectrometer, the detector does not limit the UHV conditioning of the pre-spectrometer with its bake-out temperatures up to 250°C.

liquid nitrogen (lN_2) cooling capacity Large PIN diodes require cooling for suppression of thermal noise sources in order to achieve a reasonable detection threshold of <10 keV. In fact, present high quality PIN diodes require only moderate cooling, e.g. -60°C, for sufficient suppression of leakage currents. Choosing a lN_2-reservoir as a generic supply method, the cooling resources are also used to improve UHV conditions by cryo-pumping.

multiple connection possibilities for measuring devices Several devices are attached to the detector chamber: electric devices monitoring the pressure and the residual gas distribution as well as getter cartridges to further improve the vacuum conditions.

Signal feedthrough UHV to ambient pressure A stringent UHV compatibility requires the presence of electronic parts with their intrinsic high outgassing rates to be minimised. Especially the amount of standard PCBs[43] for electronic circuits should be minimised – at best by outsourcing the electronics to the ambient pressure side.

over-pressure protection Due to the use of an in-vacuum lN_2 pipe, safety considerations (potential damage to the pipe) require an over-pressure outlet device to protect other devices like edge welded bellows. This means that the signal processing of the detector must be minimal in the UHV region – forbidding any measures to reduce the number of signal lines. Thus, for each detector segment at least one feedthrough from UHV to the ambient pressure side is required. To avoid 'cross-talking' effects, a spatial separation of the feedthrough pins is desired.

In the following section a detailed description of both detector systems, the data acquisition systems and the detector vacuum chamber will be given.

3.5.1 Detector vacuum chamber

The different detector systems used in the pre-spectrometer set-up are housed in a vacuum recipient shown in figure 3.30. The chamber can be operated in stand-alone mode or be connected to the pre-spectrometer's VAT DN200 valve on the west side. The basic design can be derived from the aforementioned requirements. The properties of the detector chamber are:

- construction materials are based solely on stainless steel and other non magnetic UHV compliant materials
- vacuum pump system with UHV capabilities (pumping speed 280 l/s(N_2))
- precision vacuum gauges for pressure monitoring (measuring range: 1 bar to 10^{-10} mbar)
- translation in x,y and z direction is provided by two edge welded bellows
- stand alone operational capacities allowing independent commissioning, repairs and calibration with X-ray sources
- pipe for lN_2 cooling with transition from isolation vacuum to UHV

[43] Printed Circuit Board

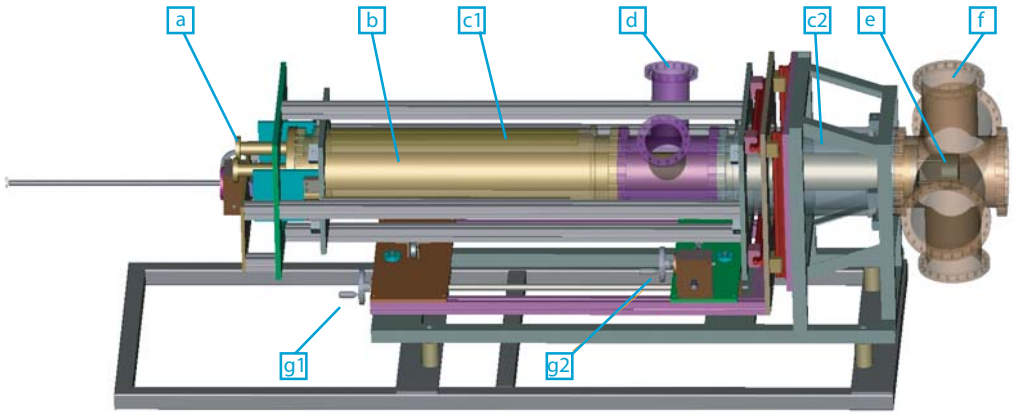

Figure 3.30: Detector UHV chamber.
(a) lN_2 supply line **(b)** movable detector lance **(c)** edge welded bellows **(d)** instrument ports **(e)** detector **(f)** DN200 double vacuum cross **(g)** crank for detector movement. Two edge welded bellows permit the translation of the detector, mounted on a lance, in x,y and z direction. Vacuum gauge, rupture disc and residual gas analyzer can be attached to available ports in the middle of the chamber (2×DN100) and at the DN200 double cross (4×DN200, 2×DN160). A DN40 port closed off with a full metal valve is used for venting the system with dry nitrogen gas. Figure taken from [Zwi09].

- two DN100 ports in the middle of the chamber and a double cross at the front with DN200 ports in beamline and top down direction and two DN160 ports in the horizontal perpendicular to the beamline, DN40 port at the backside used for venting the system
- rupture disc installed at the double cross

The key design feature of the detector chamber lies in its capabilities to move the detector chip. A maximum translation of 43 cm for the SPD (section 3.5.3) and 50 cm for the MCP (section 3.5.2) in z direction (maintenance position z=-2.7 m) allows to move the detector out of the chamber through the valve connecting chamber and spectrometer vessel into the magnet while the x/y translation makes it possible to scan the whole flux tube. As shown in fig. 3.31 for a configuration with maximum magnetic field strength of 4.5 T and a corresponding flux tube of 7.35 cm in diameter, the detector can scan nearly the whole area encircled in green. However, the maximum movement in x/y direction is different depending on the actual direction due to the cooling pipe and the attached connector devices underneath the detector flange. Several maximum positions in x and y coordinates have been inves-

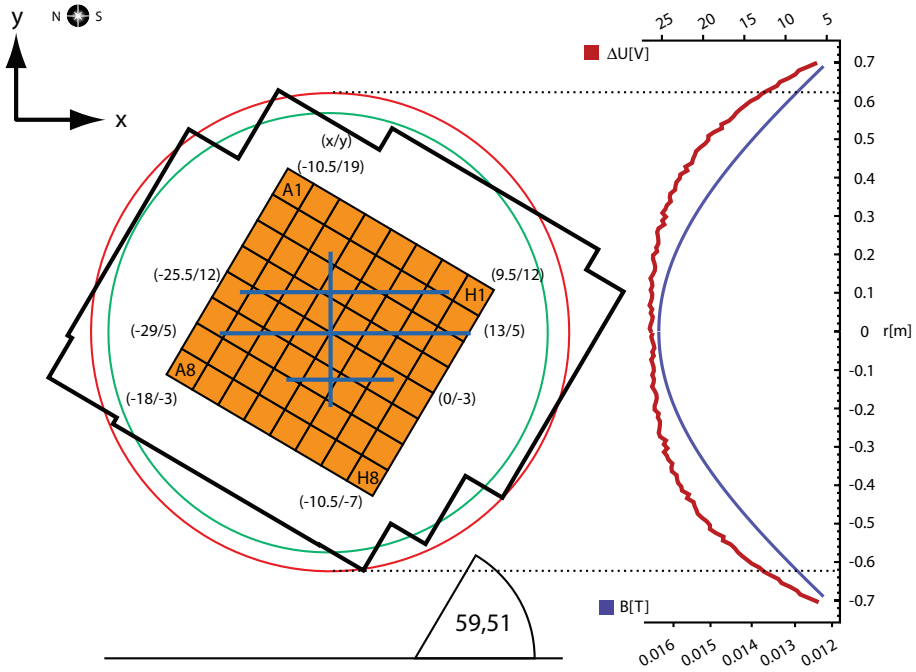

Figure 3.31: Maximum coverage of the SPD in the maximum magnetic field. The sensitive area of the SPD (yellow) with regard to the flux tube of 191 T·cm^2(green, d=7.35 cm), 226 T·cm^2(red, d=8.0 cm) at 4.5 T. The black framed area is the minimum coverage by the SPD's sensitive area according to the positioning test. The x/y coordinates of the measured maximum positions are listed and graphically illustrated. The potential as well as the magnetic field depression in the analysing plane is illustrated in the graph to the right. The potential depression depends on the potential distribution of the pre-spectrometer electrodes. The distribution used is U_{vessel}=18.0 kV, U_{coni}=18.6 kV and U_{wire}=18.7 kV. Attention: this is the view from behind the detector looking into the spectrometer.

tigated from which the minimum flux coverage can be deduced (black framed area in fig. 3.31). As described in section 3.2, the slow control monitors the z-position and prevents the closing of the DN200 valve when the lance is not in maintenance position (z=-2.7 m). To guarantee that the valve won't close during a power failure, it is integrated into the SCS with an inverted logic: the valve opens when no power is applied to the controller. To prevent a vacuum break down in the pre-spectrometer, e.g. in the case the detector chamber is not attached or vented, additional hand valves have been installed in the pressurised air supply tubes. Cutting off the air supply guarantees that the gate valve cannot be moved. The hand valves are also important in the case of a loss in pressurised air supply. Tests have been carried out which show that without applied pressure the valve discs will be sucked into closing position by the pressure difference.

In the case of the SPD the detector electronics for signal processing is situated inside the lance onto which the detector is mounted and which allows the manoeuvrability

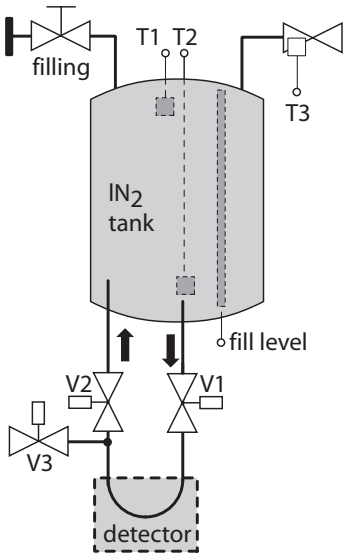

Figure 3.32: Schematics of the detector cooling system. The pressureless liquid nitrogen dewar and the detector are connected by a closed loop in which lN_2 is transported via laminar flow. To start the circulation two valves V1 and V3 are opened and lN_2 is ejected on the outflow side. After an initial cool down phase, V3 is closed and V2 opened, creating a closed loop to decrease the consumption. Fill levels and temperature sensors are monitored and displayed in ZEUS. V3 is equipped with a pressure relief valve to prevent damage caused by overpressure in the cooling pipes.

in z-direction. Although this impedes direct access it is necessary because the operational amplifiers have to be located as near as possible to the silicon wafer. The connection between the detector located in the UHV and the electronics at ambient pressure is achieved by feedthroughs.

To maintain a pressure in the low $10{-}9$ mbar regime in the detector chamber, the amount of material with high outgassing rates must be minimised. This has led to the decision to have only the JFET front end stage in UHV. Any attempts of multiplexing the 64 signals have not been considered, as this would involve additional circuitry, typically mounted on non-vacuum compatible PCB. As a consequence, one has to provide at least one electrical signal feedthrough for each pixel. A special custom DN100 feedthrough flange has been made with a matrix of 10×10 feedthrough pins, separated by 5 mm in a quadratic scheme. The pins, made out of a nickel-iron alloy (Nilo42®), are embedded in a monolithic alumina ceramic body with a diameter of 80 mm and 6 mm thickness. The latter has been brazed onto a stainless steel DN100 flange, whereby a ring made out of a nickel-copper alloy with low magnetic permeability (Ferry®) provides the connection between stainless steel and the alumina ceramic. The choice of Ferry® is to minimise magnetic forces onto the feedthrough body, as well as to avoid distortions of the homogeneous B-field at the detector. In total, 64 pins are used for the signal, 2 pins for provision of the depletion voltage, 16 pins for supply voltages of the JFET stage, 2 pins for heating resistors, 4 pins for PT1000 readout and 3 pins for the photovoltaic test pulse generator.

The cooling pipes of the lN_2 supply are made of stainless steel and are guided along the detector lance with only a few holding devices to minimise cooling losses. Near the detector the stainless steel tubes are interconnected by Swagelok®[44] connectors

[44] See App. A.1.

with a U-bend to create a loop. The U-bend is made of OFHC[45] copper to improve the temperature conductivity and hence the cooling efficiency. At the other end, the cooling pipes are Swagelok®-connected to a flexible cooling pipe. The flexible pipe is needed to compensate for the z-movement of the detector. The cooling pipes in turn are connected with a dewar filled with liquid nitrogen, see fig. 3.32. This dewar is positioned outside of the experimental hall on the roof of a neighbouring building. All parts of the lN_2 pipes are either inside the UHV vessel or under insulation vacuum. The small temperature gradient between in- and outlet inside the dewar causes the start of a circular laminar flow of the liquid nitrogen through the pipes forming a closed loop. An exhaust valve V3 allows to drain the pipe of liquid nitrogen and prevents the build up of an overpressure in the case of closed valves V1 and V2 which could damage the pipes or the seals.

Important to notice is the fact that the lN_2 in- and outflow has a monotone inclination. Any sink in the pipe can be the cause for the formation of a gas cushion immediately interrupting the laminar flow. Furthermore, it is necessary to regularly check the quality of the insulation vacuum, as insufficient insulation vacuum causes problems with the laminar flow. As a temporary solution the lN_2 circulation can be operated with V1 and V3 open while V2 is closed (see fig. 3.32). With this setting the lN_2 circulation is very stable at the cost of increased liquid nitrogen consumption (approximately a factor 1.3). The fill level of the dewar is monitored and displayed by ZEUS.

The vacuum of the detector chamber is generated by a VARIAN task-V301 pumping system (pumping speed: 280 l/s (N_2)). The pump is connected over a bellow to the downside port of the double cross in front of the chamber where the detector is positioned in its maintenance position. A VAT DN160 gate valve attached in-between the TMP and the bellow allows to disconnect the TMP from the detector chamber volume. The pumping efficiency is sufficient to reach pressures of 10^{-9} mbar with a fully baked out system at 200°C. Getter cartridges with ST707 getter have been removed due to photon emission caused by radioactive decay [Wil07]. Especially in the double cross position this could lead to an increase in detector background. The pressure is measured by a VACOM Atmion multirange gauge, and starting in 2009 by an MKS999 multirange gauge covering the pressure range of 1 bar to 10^{-10} mbar.

For the bake-out of the chamber electrical heating bands are used. The bake-out is SCS controlled and temperatures of 200°C and higher can be achieved, depending on the installed detector system (see sections 3.5.2 and 3.5.3 for details).

Corrosion in detector lance After operating both detector systems, MCP and SPD, corrosion of metallic and even stainless steel parts inside the detector lance were detected. Figure 3.33 displays a corroded feedthrough flange and a corroded pre-amplifier board. Both are located inside the lance at the detector flange's ambient pressure side. While the first incident was attributed to corrosion due to

[45] Oxygen Free High Conductivity

Figure 3.33: Corrosion in the detector lance. Corrosion of an MCP feedthrough connector and an SPD pre-amplifier board were caused by air humidity and further intensified by electric currents.

condensation of water intensified by improper surface handling of the flange, the second incident was not anticipated. The SPD electronics inside the lance is cooled by a steady stream of air. However, air humidity is still present and during cooling cycles the temperatures fell under the dew point of water. Parts which are on an electric potential suffer most from corrosion, as was seen in the pre-amplifier and must have also played a role in the corrosion of the MCP's HV feedthrough. The problem was solved by operating an air dryer as a first stage in the air cooling supply. A Seibu Giken Consorb DC-10 dehumidifier, using the adsorption principle, now stabilises the dew point at a safe level. The air stream is intensified by a ventilation system built in as a second stage. The dehumidifying process increases the air temperature by +10°C which is insignificant considering the small heat load from the detector electronics. Repeated inspection of the electronics showed no signs for ongoing corrosion processes.

3.5.2 Micro channel plate

The first detector system which was operated at the pre-spectrometer was a Hamamatsu F2223-21 Circular Micro Channel Plate (MCP). The reasons for using a robust detector which can withstand currents up to the mA range, stem from the undefined conditions of the pre-spectrometer system during initial high voltage and magnet operation. Discharges occurring inside the spectrometer create large numbers of electrons, and the magnetic guiding field will channel these electrons onto the sensitive detector area. There, they could damage or even totally destruct the detector. In this regard, an MCP has many advantages besides availability and cost factors. While a silicon detector is limited to electron detection in the keV energy range, an MCP is able to detect lower energy electrons, in addition to ions, soft X-ray photons, UV light and neutrons, resulting in the possibility to check electromagnetic effects at lower hence safer conditions first.

3.5.2.1 Set-up and characteristics

An MCP is an assembly of several millions of conductive glass capillaries each 4 to 24 μm in diameter. Fusing the glass capillaries together and slicing them into plates creates a two dimensional secondary-electron multiplier (SEM): electrons reaching the inside or created in one of the glass capillaries by photoelectric effect are accelerated by an applied potential gradient. The Lorentz force bends the electron path causing it to collide again with the capillary wall thereby releasing more electrons, see fig. 3.34. At the end of the glass tube, a huge number electrons has been generated; for a 2 keV potential difference a gain factor of 10^6 is typically achieved (fig. 3.35(b)). After leaving, the electrons are collected by an anode, creating a signal which is fed into a pre-amplifier (fig. 3.35(a)).

The F2223-21 is a two stage MCP with a sensitive area of 5.7 cm^2. The 12μm diameter capillaries are each rotated in axial direction by 10° and arranged in two stages which are tilted against each other creating a V-form. These measures prevent electrons from passing the tubes without interaction. The thickness of only 480μm results in excellent time resolutions of some nanoseconds which in the present case is reduced to 100 ns by the DAQ system, see section 3.5.4.

As a drawback, this MCP possesses neither energy resolution nor spatial resolution. The signal pulse height is independent from the impact kinetic energy but correlated with the impact angle; the earlier the electron hits the capillary wall the more electrons are generated. In principal, very low energies of the incident particle in the range of eV suffice to release secondary electrons from the semiconductor material. However, the detection efficiency in this energy will be considerably smaller.

In general, the detection efficiency for electrons and ions is high. Besides from the impact angle, it also depends on a possible electric field at the input face and the intensity of incident electrons. For 1-15 keV electrons a detection efficiency of ∼80% for ideal impact angles can be reached [Kli86].

For the present application it is important to note that the MCP signal shows a clear dependency on the presence of magnetic fields. The z-movement of the detector lance allows to change the magnetic field at the MCP location from 0.4 T to the maximum value of 4.5 T. In figure 3.36 ADC spectra are plotted taken at different magnetic field strengths, illustrating the shifting of the signal peaks. If the B-field is increased to values higher than 2.1 T, the signal peak gradually vanishes due to the threshold value marked by ADC channel 300. A shifting of the signal peak to lower energies corresponds to a decrease in secondary-electron production. This can be explained by a decrease in the number of collisions with the capillary walls due to the parallelisation of the magnetic field lines. In general, this can be compensated by higher supply voltages to achieve high gains (see fig. 3.35(b)). However, to prevent breakdowns across the MCP plate, supply voltages must not exceed 2.1 kV [Ham99].

The geometrical set-up of the MCP is compact and lightweight (figure 3.37 shows photographs of the installed detector). Only three connections have to be fed into the

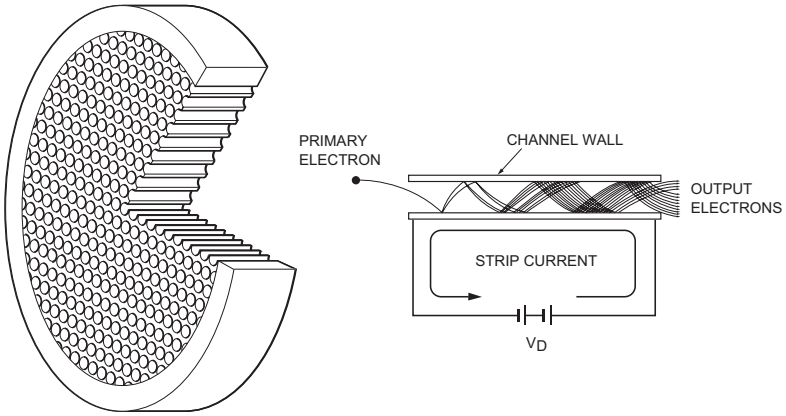

Figure 3.34: Scheme and working principal of a micro channel plate (MCP). Glass capillaries made from semiconductor material are closely packed and electrons hitting the inside of a capillary release several secondary electrons. A potential difference V_d between front face and backside accelerates the electrons which create an avalanche of electrons from multiple hits with the wall resulting in a measurable current. Picture taken from [Ham99]

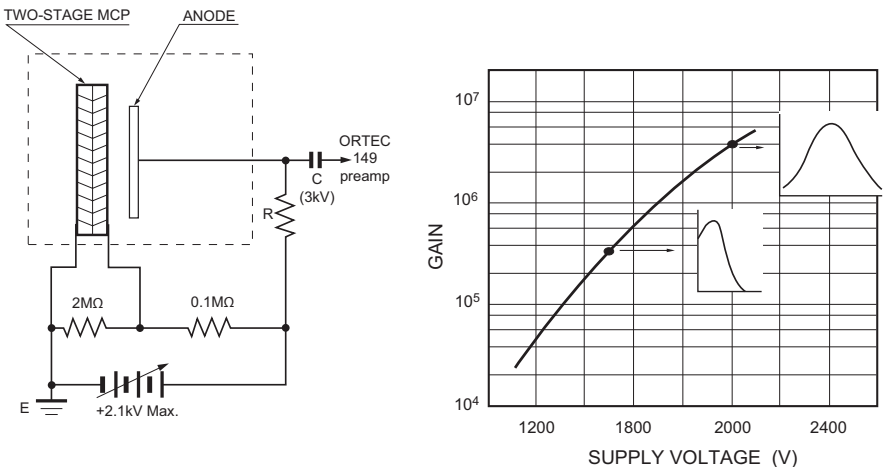

(a) (b)

Figure 3.35: MCP: (a) schematic diagram of the supply circuit (b) diagram of the gain factor showing the functional relationship between the gain factor and the supply voltage.[Ham99]

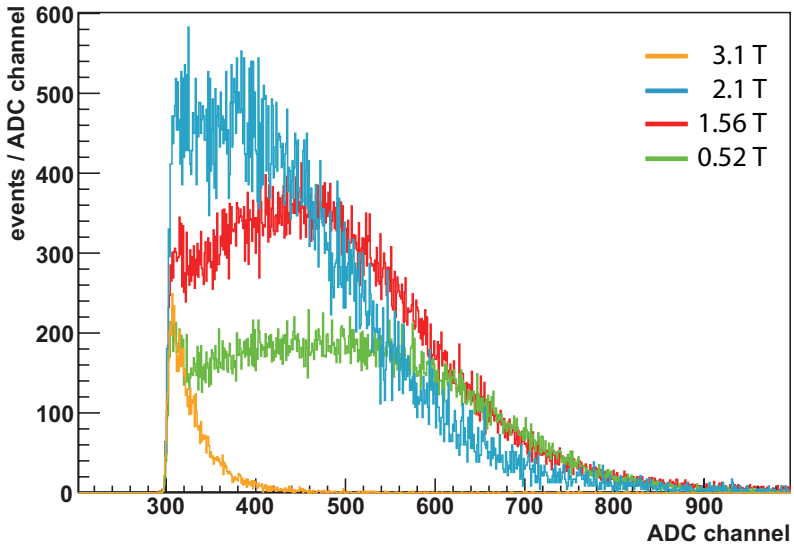

Figure 3.36: ADC spectra of the MCP for different magnetic field strengths. The width of the signal peak enlarges with increasing B-field and the mean value shifts to lower ADC channels.

vacuum chamber, making it possible to rely on commercial products. In the course of this thesis work, the MCP set-up has been made compliant with UHV standards. For this the pre-amplifier had to be relocated from inside the lance in direct vicinity of the HV feedthroughs to the outside to permit proper bake-out procedures. The signal cables inside the length are temperature resistant to a maximum of 200°C while the rest of the MCP set-up can endure temperatures up to 400°C.

During operation, the MCP characteristics are independent from temperature and it can be activated at pressures below $1{\cdot}10^{-5}$ mbar. The potential difference of the MCP capillaries is generated by a standard NIM HV card, the input face is on ground potential while the backside is elevated to +2 kV and the anode to 2.1 kV. The anode signal is fed into a low-noise charge sensitive pre-amplifier[46] from which the amplified signal is read out by the data acquisition system, see fig. 3.35(a).

The MCP was used during the initial investigation and improvement phase to optimise the high voltage stability (section 3.1.3.1), in the first electromagnetic measurements at energies of below 3 kV [Frä06], as well as in measurements to characterise the MAC-E filter background. The latter measurements will be presented in detail in chapter 4. After improving the high voltage stability and gaining better understanding of the background processes in the pre-spectrometer, the MCP was decommissioned and exchanged for the SPD. A visual inspection revealed six lighter spots and one larger burn hole on the sensitive area of the MCP, see fig. 3.38.

[46] Ortec 142B

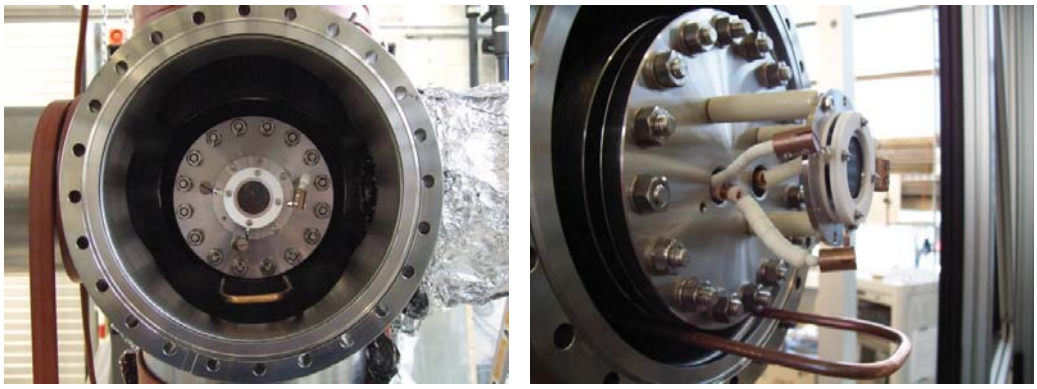

Figure 3.37: Photograph of the installed MCP.
Left: Front view of the MCP (sensitive area: $\varnothing = 27\,\mathrm{mm}$) attached to the DN100 flange at the front of the detector lance.
Right: Three supply lines are connected to the three different MCP stages: input face (ground), backside plate (2.0 kV) and anode (2.1 kV). The MCP itself is isolated from the detector flange by 5 cm long ceramic stands. The complete assembly including the supply lines is UHV compliant using copper wire and connectors as well as Al_2O_3 ceramic beads, isolating the high voltage feed lines from ground potential.

Conclusion The MCP clearly fulfilled the predefined requirements. Despite several damages of the sensitive surface of the MCP, it could still be used for measurements, resulting from the independent glass capillaries construction. The detection of low-energy electrons in the few keV region below the 10 keV detection threshold of a silicon PIN detector allowed an early investigation of the essential electromagnetic properties of the pre-spectrometer MAC-E filter [Frä06]. The complete UHV compatibility as well as the commercial availability make the MCP an ideal detector system for the initial suite of experiments at the main spectrometer taking place in early 2010.

3.5.3 Segmented PIN Diode

The segmented PIN diode prototype detector (SPD) constitutes a first step in the development of the final focal plane detector. The general working principle of a PIN diode is described in fig. 3.39. One major objective of this prototype development was to provide an operational system already after a short amount of R&D time. Therefore, the requirements regarding the prototype were relaxed when compared to that of the final FPD, see table 3.3. The experience gained during commissioning of the prototype detector has proven critical for the design of the final detector. Furthermore, a detector was needed to satisfy one of the key requirements for a detector system during the EMD measurement phase: a large area with a good spatial resolution. While other detector types excel in both energy resolution and spatial resolution, the development of large-area detectors has still not matured as in the case of PIN technology [Ste05]. Medium sized PIN diodes with segmented surface

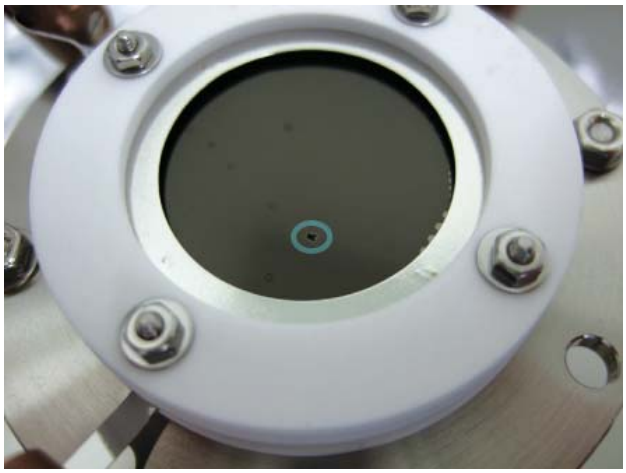

Figure 3.38: Damaged MCP. Removing the MCP after a period of 1 year of measurements, six spots showing minor damages and one major burn hole are visible. The reason for the damages can be found in the electromagnetically unstable conditions of the pre-spectrometer causing discharges. Electrons created in these processes can be guided to the detector by magnetic field lines.

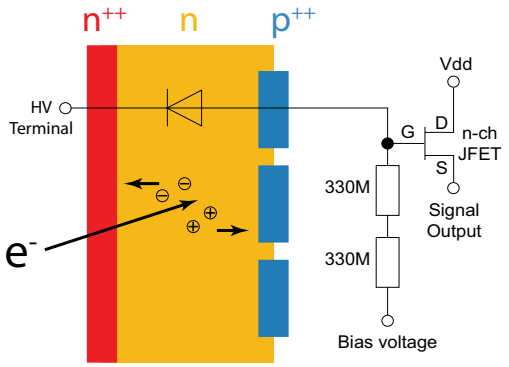

Figure 3.39: Schematic view explaining the working principle of a segmented PIN[47]diode with a JFET stage. Reverse biasing of two joined layers n^{++} and p^{++} creates a depletion layer in-between which is sensitive to ionising particles and UV light. Charge carrier couples which are created by electrons are drawn to the corresponding layer. The voltage difference is registered by the JFET and converted into a signal.

area, however, fulfil the requirements and represent a mature technology reducing the R&D time which has to be invested. In the following, the SPD design including the follow-up electronics as well as the implementation into the pre-spectrometer test set-up are described. Finally, the characteristics are outlined stemming from a set of dedicated measurements.

3.5.3.1 Design of the detector system

The sensitive area of the monolithic silicon PIN diode, which was manufactured by Canberra, Belgium, measures 16 cm^2. he surface is segmented into 8×8 quadratic

[47]The bulk material consists out of slightly n-doped silicon and not intrinsic silicon as the name suggests. N-doped Si is routinely used for silicon detectors to meet the requirements on high resistivity and low leakage currents.

Table 3.3: Comparison of FPD and SPD requirements and detector properties. Translation capabilities and shielding are independent of the detector itself. Pixel distribution, energy resolution and background of the FPD will be considerably improved by the on-going R&D activities at the US partner institutions. Intrinsic background for the FPD is given in the energy range of 15.9-19.4 keV and for the SPD in the interval 15-22 keV.

Parameter	**FPD**	**SPD**
ΔE at 18.6 keV [eV]	600	1400
dead layer [nm]	50	100
thickness [μm]	500	200
geometry	circular	square
sensitive area [cm^2]	64	16
number of pixels	148	64
pixel size [mm^2]	44.1	25
operational B-field [T]	3-5	4.5
intrinsic background [mHz]	1	50
capacity of pixel [pF]	9	16
leakage current [nA/cm^2] at room temp.	0.2	0.2
active/passive shielding	yes	no
translation x,y [cm]	no	$\approx \pm 2$
translation z [cm]	no	50

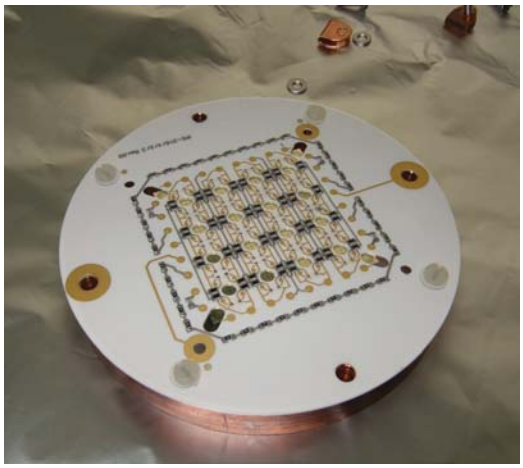

Figure 3.40: Backside of the SPD ceramics plate. Visible are the 40+ heating resistors, the JFET front end stages, which are wire bonded to the p^{++} pixels through laser cut holes in the ceramics plate. The small gold plated circles are the connection areas for the needle pins of the signal feedthroughs.

pixels. The high resistivity wafer ($R > 10\,\mathrm{k\Omega cm}$) has been thinned down to $200\,\mu\mathrm{m}$ thickness, resulting in depletion voltages as low as 10 V. The detector wafer is attached to an Al_2O_3 ceramic plate. On its backside, see fig. 3.40, the ceramics plate carries the JFET[48] front end stage in SMD[49] technology for each pixel. The connection between p^{++} pixels and JFETs is done by wire bonding through laser cut holes in the ceramics. The plate with the wafer is connected to a copper cooling ring with screws made of DuPont VESPEL S3. Also made of VESPEL is the detector holding construction onto which the detector is attached by use of stainless steel screws. A schematics of the detector construction is presented in figure 3.41. VESPEL is used due to its advantageous properties: it is isolating with low thermal conductivity, machinable, temperature resistant below 400°C and possesses low outgassing rates making it UHV compliant. The orientation of the SPD in the x-y-plane and with regard to the beam axis is shown in figure 3.42.

The detector electronics can be subdivided into three different groups [Wüs06]:

- JFET front end stage
- Main circuit board
- Pre-amplifier sub-boards

JFET front end stage The JFETs, one for each pixel, are located close to the detector wafer on the backside of the ceramic plate. The JFET source-follower stage has the following properties:

  - ⊕ no charge feedback line, i.e. reducing the number of UHV feedthroughs
  - ⊕ low output impedance of 60Ω, suppressing electromagnetic interference (EMI) and crosstalk

[48] Junction field effect transistor
[49] Surface-Mount Devices

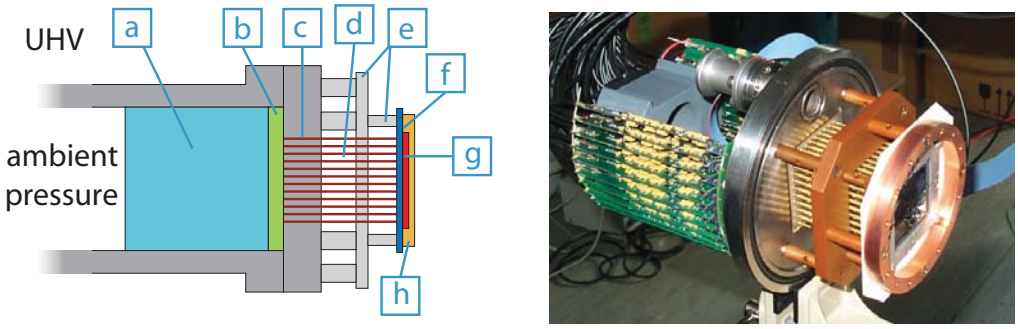

Figure 3.41: Schematics and real set-up of the SPD. (a) 32 custom low noise pre-amplifier boards **(b)** main circuit board **(c)** DN100 flange with 100 signal feedthrough pins **(d)** connector bushings and spring needle cushion **(e)** holding construction made of DuPont VESPEL S3 **(f)** ceramics plate with JFET, PT1000 temperature sensors and heating resistors **(g)** silicon wafer **(h)** copper cooling ring

- ⊕ high signal bandwidth providing sufficient timing accuracy
- ⊖ voltage gain < 1, leading to domination of the amplifier noise by the second stage
- ⊖ periodic re-calibration necessary due to charge-to-voltage conversion factor being dependent on detector junction capacitance and JFET transconductance

Main circuit board provides the signal and power distribution to the pre-amplifier boards. In addition, it features a photovoltaic test-pulser for checking electronics functionality.

Pre-amplifier sub-boards consist of 32 custom design boards with two low noise pre-amplifiers each. The boards are plugged into the main board in a compact radial distribution matching the inner diameter of the detector lance.

This modular design makes it possible to accustom the electronics to different mounting conditions, allows for subsequent design changes of some parts and simplifies the potential repair of a single broken device. The detector signals received in the first stage electronics in the UHV is then channeled via 100 spring-loaded needles and matched connector bushings to the feedthrough pins of the vacuum flange (fig. 3.43) and onto the second stage electronics at ambient pressure. Besides low thermal conductivity and easy assembly the needle connection method manages without soldering, which is important with regard to vacuum and low-level background considerations.

Instead of establishing the detector electronics connection to ground potential via 3 m long LEMO[50] connector signal cables, the ground connection has been realised via

[50]LEMO SA, USA

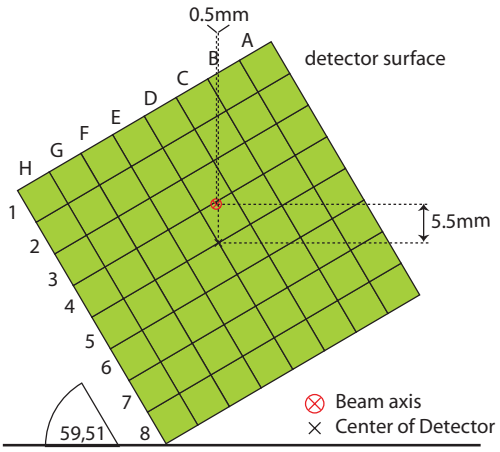

Figure 3.42: Orientation of the SPD in the x-y plane at x=0, y=0. The position, as shown by a scale for each dimension, can be changed in all three dimensions; the tipping is fixed. The diagram represents the front view from the spectrometer.

the CF gasket of the DN100 detector flange. Three soldering lugs are soldered onto the the copper gasket facing to ambient pressure, in this case the inner diameter ring. The soldering lugs are connected via short cables to a thin copper plate wrapped around the preamplifier stage which is in turn soldered to the ground contacts of the 32 pre-amplifier boards. All ground contacts are interconnected to each other thus minimising ground loops. With this method a stable contact to the detector chamber is established and therefore also to the pre-spectrometer framework with the chosen ground star point.

The necessary cooling of the detector is achieved via liquid nitrogen supply already discussed in section 3.5.1. The previously mentioned copper U-bend of the lN_2 pipe is shown in fig. 3.43. Two OFHC copper bands, clamped with copper plates to the U-bend, connect four points of the cooling ring with the lN_2 tube thus establishing the heat transfer. Despite losses in the cooling capacity from heat radiation, the ceramics plate including wafer is cooled down to -101°C. This is measured by four PT1000 temperature sensors included on the ceramics plate. The laminar flow of the lN_2 substantially reduces vibration-induced noise, often called "microphony".

While carrying out initial cooling tests, damages to the test ceramic plates occurred. The reason could be attributed to the rigid connection of the copper cooling ring to the VESPEL holding construction: the contraction of the stainless steel screw during cool down increases the contact pressure of the copper ring. which in turn leads to stress in the ceramics and its eventual breakage. Using bent copper plates instead of conventional washers allows to absorb the pressure increase in the copper plates. Furthermore, the thread of the screws has been removed at the location of the ceramics plate ensuring that no contact between both exists. The optimum operating temperature of the JFETs lies between -100°C and -60°C. The detector temperature can be adjusted to the range of ideal operation conditions with the help of 40 heating resistors (4.7 Ω each) integrated into the ceramics plate reaching a total of 4.8 Watt heating power. As soon as the JFETs are supplied with power the temperature increases and finally stabilises at -57±2°C, close to the desired value. To suppress noise contributions from leakage currents, even a moderate cooling to

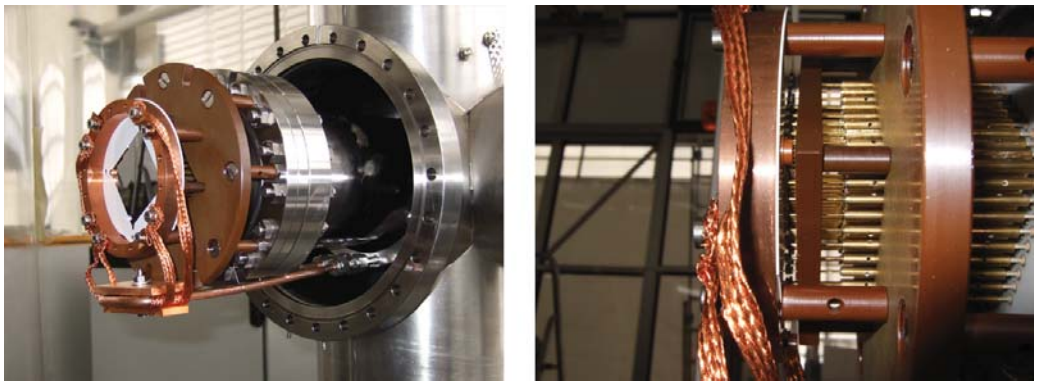

Figure 3.43: Photographs of the mounted SPD set-up.
Left: full set-up with lance moved out of the detector chamber. Visible are the white ceramics plate with reflective silicon wafer, the copper U-bend of the lN_2 supply pipe, the cooling connection using copper bands and the VESPEL holding construction attached to the DN100 flange.
Right: close-up view of the spring loaded needles and the bushings connected to the feedthrough pins.

$\sim -20°C$ would be sufficient.

The supply voltages of the SPD electronics and the devices being used are listed in table 3.4. During operation an increase in supply current from 2.8 A to 4.8 A due to high frequency oscillations can be observed from time to time. The primary source has not been identified yet, with the exception of an operating RGA when the SPD pre-amplifier power supply is switched on. To prevent any damage to the pre-amplifiers, a protection circuit has been developed which shuts down all detector power supplies when a threshold value of 3 A is overstepped. Also included into this safety-off device is the temperature read-out, which activates the safety measures at temperatures exceeding $+10°C$ to protect the JFETs from overheating. The protection circuit is not yet integrated into SCS, however, this is planned for the near future.

To protect the pre-amplifiers and the main circuit board from overheating, an electrically driven blower circulates ambient air inside the detector lance keeping a constant

Table 3.4: Voltages and devices used for the operation of the SPD.

	U [V]	**device**
Detector depletion voltage	10-20	Rhode & Schwarz Typ NGT 20
pre-amplifier supply +	11.6	TOELLNER TOE 8852
pre-amplifier supply -	-6.3	TOELLNER TOE 8852
JFET supply	0.2-0.8	Rhode & Schwarz Typ NGT 20
heating resistors	0-30	Invensys Lambda

temperature of 25°C. In the light of the corrosion problems mentioned earlier in section 3.5.1, a dehumidifier has been connected in-line, thereby successfully preventing further corrosion inside the lance. The dehumidifier also acts as a fail safe device: in the case that the blower stops operation, the air stream being provided by the dehumidifier suffices to prevent a temperature increase beyond the critical threshold of 70°C.

Vacuum considerations The detector chamber has been designed according to stringent ultra high vacuum standards. The SPD, however, compromises these rigid standards, in particular with regard to making use of soldering and to the bake-out properties. The JFETs, heat resistors and temperature sensors are all soldered to the ceramics plate, and the bushings of the needle pins are also soldered on the inside, thereby generating potential sources of outgassing. Another problem comes from the bake-out limit of 120°C for the ceramic plate and 80°C for the detector electronics inside the lance. As a result, it is difficult to remove thin water films, the main contaminant after opening and closing of the system. In addition, a possible contamination of hydrocarbons cannot be removed at all. To analyze the vacuum status of the SPD detector system, a set of RGA spectra is taken prior to any bake-out procedure, see fig. 3.44. The spectrum up to 300 amu reveals no 'heavy' contaminant with mass values above 50 amu, the hydrocarbon fraction (broken hydrocarbon chains occupying amu 35-45) is also small compared to the other gas fractions, namely H, H_2, H_2O, CO, CO_2 and O_2. Extensive bake-out tests reveal that baking the system at moderate temperatures of 120°C while keeping the temperature inside the lance low by activating the air cooling has no significant positive effect. Even going up to 200°C with the SPD removed shows that the main problem lies in the cool surface of the lance. Water and other contaminants which are desorbed from the hot surfaces, particularly the edge welded bellows, are not pumped out by the TMP system but condense on the cool surface of the lance. This effect is amplified by the fact that the lance is reaching through the whole chamber. Shutting off the air cooling and closing off the outlet of the lance[51], the temperature inside the lance adjusts to the surrounding metal parts and baking shows the desired results.

In the case of an installed but not actively cooled SPD, the end pressures are limited to the low 10^{-7} mbar regime. After an extended time of several months of continuous pumping, the system reaches a pressure of $8{\cdot}10^{-8}$ mbar.

A mitigating factor, which improves the vacuum by two decades, is the active cooling of the silicon detector with liquid nitrogen. This has two beneficial effects: first, the outgassing of the cooled down ceramics plate and the attached devices is significantly reduced and secondly, the lN_2 feeding line operating at temperatures of 77 K acts as a cryopump, which is very effective in freezing out the main contaminants water and hydrogen (for more information on cryopumps see App. A.3.3). With active cooling,

[51] The inside of the lance with a diameter of 10 cm houses the SPD electronics necessitating cooling during detector operation. Without electronics installed, the backend of the lance can be closed with a tin foil which interrupts the air circulation and the connected heat dissipation.

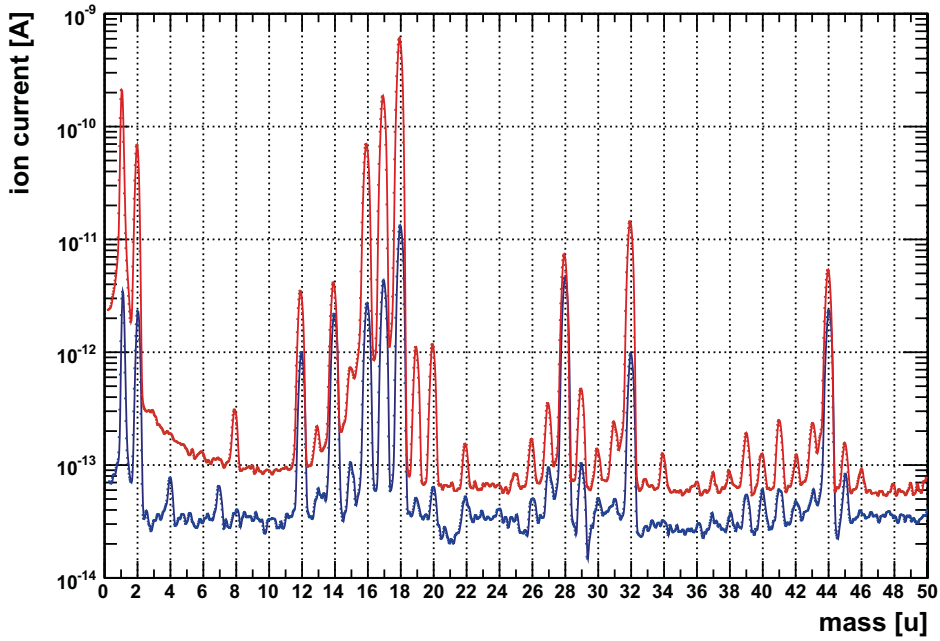

Figure 3.44: RGA spectra of the detector chamber with SPD installed: (red) operation at room temperature (30°C) at pressure $p = 8.3 \times 10^{-8}$ mbar (blue) SPD operation temperature T=-56°C with a pressure of $p = 6 \cdot 10^{-10}$ mbar.

the pressure decreases to $6{\cdot}10^{-10}$ mbar. An RGA taken at operating temperature of -56°C (see fig. 3.44), shows main contributions coming from H(amu 1), H_2(amu 2), H_2O(amu 18,17,16), CO(amu 28) and CO_2(amu 44). The O_2(amu 32) and N(amu 14) contributions are the result of an air leak in a sealing at the TMP. During measurements this leak is sealed off by closing the valve in front of the detector pumping system. At present, the leak has been closed, thus eliminating the nitrogen contribution. The excess in O_2 is still visible, even when the SPD has been removed from the chamber. Therefore, this peak must be the result of outgassing from stainless steel, probably not of the type 316LN. The RGA measurements at room temperature and at operating temperature show that the SPD is UHV compliant and a contamination of the detector chamber or the pre-spectrometer is excluded. An RGA taken in the pre-spectrometer after a cooling failure of the SPD[52] proves that a) the pressure is regenerating over the course of hours after the additional gas load is taken from the system and b) no lasting effect regarding end-pressure or RGA composition can be observed.

During the first measurement phase with the SPD, the pre-spectrometer was operated without getter pump installed. Therefore, with a pre-spectrometer pressure of

[52]The laminar flow of the liquid nitrogen broke down and two hours later the pressure in the pre-spectrometer increased to $5{\cdot}10^{-8}$ mbar.

$3{\cdot}10^{-10}$ mbar, the additional gas load of the detector chamber was negligible. This changed after the re-installation of the getter pump and its activation. With a pressure of $4{\cdot}10^{-11}$ mbar, the gas load of the detector chamber is a dominant observable in a pressure rise over several hours to an equilibrium pressure of $5{\cdot}10^{-10}$ mbar. Therefore, an effort of re-designing the detector vacuum to further decrease the gas load reaching the pre-spectrometer volume has been started. The novel design includes an aperture sitting inside the magnet beamtube, which connects the pre-spectrometer vessel and the detector chamber. The aperture limits the diameter to 10 cm. Also part of the new design is an increase in pumping speed by installing a two-stage TMP system and the addition of a getter cartridge containing 10 m of SAES ST707 getter material. In a first implementation of this design the pumping speed of the first stage Leybold TW290 TMP has been found lacking. Also, the pumping speed is reduced by the new location of the TMP as every bend in-between the vacuum chamber and the TMP entrance flange halves the pumping efficiency. In a second step the V-ports in the middle of the chamber will be used to realise a differential pumping concept. Installing a TMP/getter combination at the V-ports directly pumps the gas load of the long edge welded bellow. Realizing these measures, a decrease in the gas load of the detector chamber might remove the vacuum limit presently set for the pre-spectrometer system.

In conclusion, it can be noted that the SPD is UHV suitable within the vacuum limit of $p_{min} = 5 \cdot 10^{-10}$ mbar at the pre-spectrometer system, which is also confirmed by RGA results. Therefore, the SPD is suited for test operations in the main spectrometer, too, without bearing the risk of a lasting vacuum contamination or a potential damage to the getter material. Alternatively, the SPD can be used to commission the DPS2-F, WGTS and CPS cryostats and to verify their electrooptical properties.

3.5.3.2 Characteristics of the segmented PIN diode

In a series dedicated measurements carried out in the framework of this thesis, the characteristics of the SPD have been investigated in detail. In the following the results of the measurements of the energy resolution are presented, as well as the investigation of a possible temperature and depletion voltage dependence of the energy resolution. Furthermore, exhaustive background studies of the SPD in stand-alone mode have been carried out, and their results will also be discussed here. A more detailed account of the measurements and data analysis with regard to the SPD is given in [Ren07].

The measurement of the energy resolution was done by using X-ray emission lines emitted by an ^{241}Am source with different exit windows. This allowed to use the following isotopes: ^{37}Rb, ^{42}Mo, ^{47}Ag, ^{56}Ba and ^{65}Tb. For every exit window element different fluorescence lines exist. The different fluorescence lines and their energies are listed in appendix C.1. For the calibration curve a weighted average $E_{\overline{X}}$ has been calculated.

The energy resolution ΔE can be determined by fitting the signal peaks with a

Gaussian fit according to

$$f(x) = p_0 e^{-\frac{1}{2}\left(\frac{x-\mu}{\sigma}\right)^2}. \tag{3.6}$$

with the standard deviation σ and the mean value μ. The energy resolution in terms of FWHM can then be calculated via

$$\Delta E = \mathrm{FWHM} = 2\sqrt{2\ln 2}\,\sigma. \tag{3.7}$$

The results of all 64 pixels are shown in fig. 3.45, the averaged values of ΔE together with the relative energy resolution $\Delta E/E_{\overline{X}}$ for a weighted average energy $E_{\overline{X}}$ is presented in table 3.5.

The results show an energy resolution of the order $\Delta E \sim 4\,\mathrm{keV}$, which is a factor 3 larger than the design value of $\Delta E_d = 1.4\,\mathrm{keV}$. The reason offered by the manufacturer is stress in the silicon wafer induced by the gluing process which is used to firmly join the wafer and ceramics plate together to reduce the effects of microphony. An earlier version of the PIN diode was using a clamping system to attach the wafer to the ceramics. While this design showed slightly better energy resolutions ($\Delta E = 3.5\,\mathrm{keV}$ for 20 keV electrons) it was very susceptible to microphonic effects [Wüs06]. A third design has now been realised with a new wafer, which will be available for first tests in August 2009. This design is intended to eliminate the microphony problems and to improve the energy resolution to the design value [Ste09].

Another information that can be deduced from fig. 3.45 is the existence of three inferior pixels (E5, F5, F7) with regard to energy resolution and noise performance.

Further investigations yielded neither temperature nor depletion voltage dependence of the energy resolution within the systematic uncertainties [Ren07]. It has to be added that an increase in depletion voltage above 12 V led to an increase in noise in one pixel (H6), and any further increase in this operation parameter increases the number of affected pixels to 20[53]. Given that the recommended depletion voltage is referenced with 20 V [CAN04], the noise problems might also be the result of the increased stress in the silicon wafer. A depletion voltage of 12 V has been chosen for the SPD operation due to the facts that complete depletion of the diode is already achieved at 10 V and a break down in noise performance is only observable at values >14 V.

The studies measuring the intrinsic detector background rate in the region of interest of 15-22 keV yield the following results:

without pixels E5, F5, F7:	(439.8 ± 2.7)	$\times 10^{-3}$ events/s per pixel
after noise filtering:	(20.3 ± 0.05)	$\times 10^{-3}$ events/s per pixel

The results have been compared to simulation described in [Sch04]. Measurements and simulation differ in the size of the detector and the employment of a passive lead shielding. However, the rate can be normalised to a standard area and the shielding effects can be neglected. The simulation shows that 80% of the background

[53] Affected pixels: F5-F8, G1-G8, H1-H8.

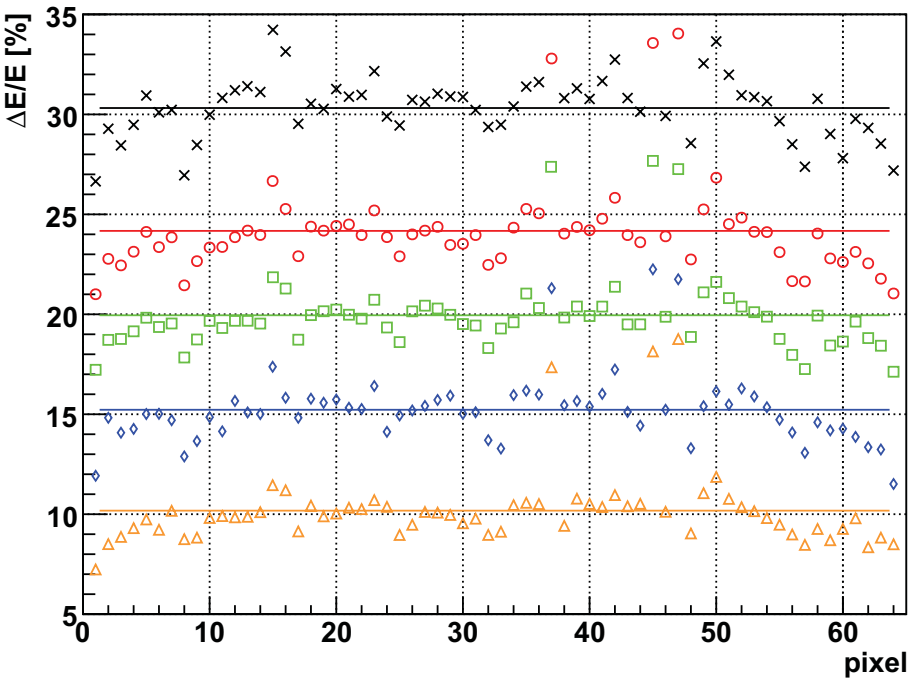

Figure 3.45: The relative energy resolution of the 64 pixels of the SPD for five different energies. ^{37}Rb (black), ^{42}Mo (red), ^{47}Ag (green), ^{56}Ba (blue) und ^{65}Tb (orange). Three pixels E5(#37), F5(#45), F7(#47) show bad results with regard to energy resolution and noise performance, see text.

Table 3.5: Absolute (ΔE) and relative ($\Delta E/E_{\overline{X}}$) energy resolutions averaged over the SPD's 64 pixels at T=-56°C for the reference energies $E_{\overline{X}}$. The X-ray lines used for the calculation of the weighted averaged X-ray energies $E_{\overline{X}}$ are also given.

Element	$E_{\overline{X}}$ [keV]	fluor. lines	ΔE [keV]	$\Delta E/E_{\overline{X}}$ [%]
^{37}Rb	13.585	$K_{\alpha_{1,2}}$,$K_{\beta_{1,2,3}}$	4.10 ± 0.32	30.2 ± 2.4
^{42}Mo	17.765	$K_{\alpha_{1,2}}$,$K_{\beta_{1,2,3}}$	4.23 ± 0.31	23.8 ± 1.8
^{47}Ag	22.565	$K_{\alpha_{1,2}}$,$K_{\beta_{1,2,3}}$	4.46 ± 0.35	19.8 ± 1.6
^{56}Ba	32.061	$K_{\alpha_{1,2}}$	4.81 ± 0.57	15.0 ± 1.8
^{65}Tb	44.216	$K_{\alpha_{1,2}}$	4.33 ± 0.31	9.8 ± 1.7

is produced in the Al_2O_3 ceramics plate. After adaption of the data, measurement and simulation results are in good agreement [Ren07].

In addition to the measurements described above, the KATRIN members from the University of Washington, Seattle, determined the dead layer of the SPD using two different types of measurement. The first method is an angle method measuring the energy loss of monoenergetic electrons for different incident angles. The second is an energy method calculating the energy loss by multiplication of the Bethe-Bloch function with the dead layer thickness t and comparing the results of a number of measurements using different starting energies. The results are [Wal06]:

$$\text{angle method: } 119 \pm 3\,\text{nm}, \tag{3.8}$$

$$\text{energy method: } 109 \pm 3\,\text{nm}. \tag{3.9}$$

The results confirm the design value of the dead layer.

3.5.3.3 Conclusion

The segmented PIN diode has been thoroughly characterised and the results show that the detector is suitable for EMD test measurements under UHV conditions in the pre-spectrometer test set-up. The desired energy resolution could however not be achieved, even in a second attempt reducing microphonics. The cause for this effect has not been identified unambiguously but seems to be related to the fact that a temperature independent leakage current source exists, which scales with depletion voltage. However, it should be emphasised that the energy resolution is sufficient for the pre-spectrometer measurements and the experience gained during the prototype's R&D phase was carried over directly into the design effort for the FPD. For example, the identical wafer processing technologies with p^{++} pixels in n-substrate silicon and homogeneous n^{++} entrance window were chosen [CAN04]. The FDP's manufacturing phase is finished and has now entered its test phase at the University of Washington, Seattle, with the first results already being presented [Bod08].

3.5.4 Data acquisition

In the course of the pre-spectrometer measurements two data acquisition (DAQ) systems have been commissioned. The requirements for the pre-spectrometer system are somewhat relaxed compared to the requirements of the larger final set-up. In this thesis, e-gun measurement rates of several kHz only are expected, while in the final set-up these rates will range from a few mHz during ν-mass measurements to more than 1 MHz during calibration runs. On the other hand, the pre-spectrometer system is the first platform on which single event recorded detector data have to be combined with slow control data from numerous sensors. The two systems used

are based on a VMEbus[54] with the first system being developed by the University of Washington, Seattle, therefore, labeled UW-DAQ. The second system is an in-house production of the Institute of Data Processing and Electronics (IPE) at the Forschungszentrum Karlsruhe, thus labeled IPE-DAQ. Both DAQ systems can handle the signals received from the detectors employed at the pre-spectrometer. Each system's characteristics will be presented below, including the investigation regarding its efficiency and dead time. Independent from these hardware configurations is the software environment ORCA[55] to control the data acquisition and to read out the VME bus. This software system, also being a development of the University of Washington, has already served in other major experiments [Cou99] such as SNO [How04] and is continually expanded and improved to the needs of KATRIN. The features inherent to ORCA will be presented, too, with the focus point on specific changes and adaptations for KATRIN.

3.5.4.1 UW-DAQ

The DAQ hardware developed by the University of Washington consists of a VME crate, a VME controller board, eight VME based shaper cards and one VME trigger card with four channels. With the exception of the controller board, a Digidesign SBS Bit3 VME backplane controller, all devices are custom made.

Eight shaper cards with eight channels each are available to receive the signal pulses of the detector. Each shaper channel is equipped with an 11 bit analog-to-digital converter (ADC), which digitises the pulse signal with shaping times of 2 μs provided that the pulse height exceeds a predefined threshold value. While the shaper card is busy digitising the signal, a TTL[56] signal is given out on a separate *shaper event* output channel. A *shaper inhibit* input channel is also available, causing the shaper card to reject any arriving signals while an inhibit signal is broadcasted.

The trigger card is equipped with four independent circuits to apply a time information to an incoming signal with a precision of 100 ns. The 50 MHz clock provides only a relative and no absolute time information. To be able to provide all available shaper channels with a time information, two shaper cards are addressed to one trigger channel. This is achieved by the FAN-IN/-OUT electronic interconnected between shaper and trigger card, see figure 3.46. The *shaper event* output channels of two boards are linked by a logic `OR` to the trigger card. The trigger card then starts to provide the time information during which time a *shaper inhibit* TTL-signal is sent to the shaper cards, thus locking the 16 channels associated with the trigger channel.

The connection of the VME crate to a personal computer running the DAQ software via fiber optic cable is provided by the Digidesign SBS Bit3 controller board on the VME crate side and by the corresponding PCI interface card installed in an

[54] Virtual Machine Environment
[55] Object oriented Real-time Control and Acquisition [How04]
[56] Transistor-transistor-logic ($U_0 < 0.8\,V$, $U_1 > 2.0\,V$)

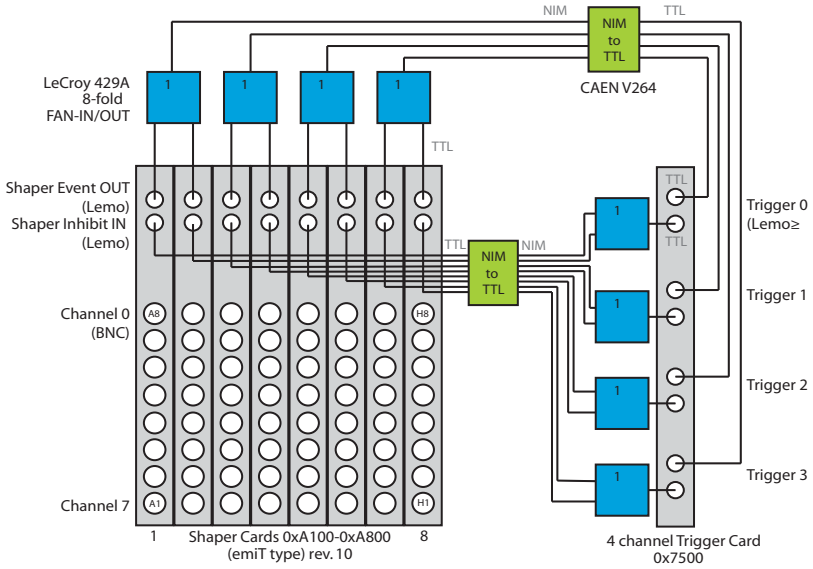

Figure 3.46: Trigger circuit of the UW-DAQ. Two shaper cards are associated with one trigger channel. During generation of the time information, the specific trigger channel does not accept another request and a TTL inhibit signal blocks the corresponding shaper channels. More information is provided in the text.

Apple Macintosh G4 PowerMac. Thus personal computer and DAQ hardware are electrically isolated, thereby preventing the introduction of electrical noise.

Efficiency and dead time The determination of the dead time τ of a DAQ system is of utmost importance. During this time the DAQ is blind for an incoming signal resulting in the loss of an event. Being strongly rate dependent, dead time effects are getting gradually more severe with increasing signal rate. For example, in case of measuring the transmission function of a MAC-E filter the detected electron rate on the silicon detector is the observable. Shooting at first electrons against a retarding potential which is lower than the electron energy will imply that all electrons pass the potential barrier. If the electron energy is kept constant, and the retarding potential is increased, the detected electron rate decreases until no electron is transmitted anymore. If the initial electron rate is too high and thus induces dead time effects, the detection rate and correspondingly the transmission function will be skewed. Only by precisely measuring the dead time it is possible to correct the data rate accordingly, or to avoid these effects altogether by switching to measurements at lower rates.

In a set of dedicated measurements an investigation with regard to the dead time and hence the efficiency of the UW-DAQ has been carried out.

The efficiency ϵ_f of a DAQ system represents the fraction of the measured rate R_m

and signal rate R_s implying a constant average frequency f:

$$\epsilon_f = \frac{R_m}{R_s}. \tag{3.10}$$

Two signals, a reference pulse signal S_R and a noise signal S_N with different pulse heights h and randomly distributed in time, are superimposed and fed into a channel of the DAQ. By choosing the frequency of the reference signal according to $f_R \gg \frac{1}{\tau}$ non-negligible dead time effects will occur. The noise signal, in contrast to the reference signal, is randomly distributed and the pulse height will be set on a lower level making it easy to differentiate between both signals in the ADC spectrum. By measuring with and without noise signal and with different signal rates the efficiency can be determined.

According to the well known Poisson distribution

$$P_f(k) = \frac{f^k}{k!} e^{-f}, \qquad k \in \mathbb{N} \tag{3.11}$$

the number of lost events increases with an increase in the noise rate averaged in time, with f being the event rate. Accordingly, the probability to find n events in a time interval of ΔT can be given as

$$P_n(\Delta T) = \frac{e^{-f\Delta T}(f\Delta T)^n}{n!}. \tag{3.12}$$

A graphical explanation of the distribution in time of signal and noise events is given in fig. 3.47.

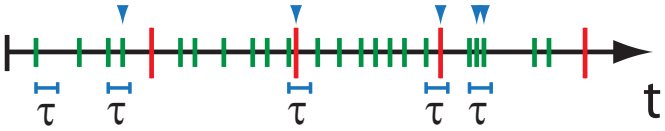

Figure 3.47: Time distribution of the different signals measured by the DAQ system during dead time investigations. Green events are randomly distributed noise signals, the red events are reference signals of constant frequency generated by a pulser. The blue markers indicate events lost due to dead time, also illustrated by the blue interval in time below the affected events.

Supposing that the noise signal is randomly distributed and the frequency is higher compared to the reference signal, it is possible to assume that the sum of the signals is randomly distributed, too. This yields

$$\epsilon_f(R_R) = \epsilon_f(R_N) \tag{3.13}$$

resulting in

$$\frac{R_{Rm}}{R_{Rs}} = \frac{R_{Sm}}{R_{Ss}}. \tag{3.14}$$

Efficiency and dead time τ are linked by equation

$$\epsilon_f = P_0 = e^{-f\tau}. \tag{3.15}$$

Thus, by determining the efficiency the dead time can be deduced allowing to correct a measured rate R_{Sm} to the actual signal rate R_{Ss} using equation 3.14.

For the measurements, a Hamamatsu single PIN diode has been used to generate randomly distributed noise signals and an ORTEC Precision Pulse Generator 419 to create the constant reference signal. The complete measurement set-up is described in detail in [Ren07].

The dead time has been tested for the following different DAQ configurations:

1. Shaper card (histogram mode)
2. Shaper and trigger card without FAN-IN/-OUT
3. Shaper and trigger card with FAN-IN/-OUT
4. Shaper (2×) and trigger card with FAN-IN/-OUT

By removing the link to the trigger card, the event will only carry the energy information, the so-called 'histogram mode' tested in configuration 1. Configuration 2 removes the connecting electronic stage including TTL to NIM[57] signal conversion (fig. 3.46). In configuration 3 the standard measuring set-up is tested. The results presented in table 3.6 show that in histogram mode (1) the dead time after a trigger event is considerably lower with $(21 \pm 1)\,\mu$s, the other configurations (2)-(4) show identical dead time values within the error limits. Configuration 4 proves that an increase in shaper cards does not limit the efficiency due to an increase in ADC operations; each channel commands its own ADC and is therefore, independent from the other channels.

Thus, the source for the dead time can be identified. For the histogram mode the analog-to-digital conversion is the limiting factor, otherwise creating the time information in the trigger card will define the DAQ efficiency. It has to be noted that the dead time created by a trigger channel only affects the 16 channels on two shaper cards assigned to said trigger channel - the subgroups comprised of two shaper cards and one trigger channel are independent from each other.

The results of the DAQ efficiency are illustrated in figure 3.48. Efficiency values above 90% in dependence on the signal rate for histogram mode and normal operation, called event mode of the UW-DAQ are plotted including statistical errors. For the event mode, including all information of up to 64 pixels, the 90% efficiency limit is breached at a rate of 1.5 kHz. In the case that each detector pixel registers the same amount of events a maximum rate of 6 kHz for all trigger channels combined

[57] Nuclear Instrumentation Module

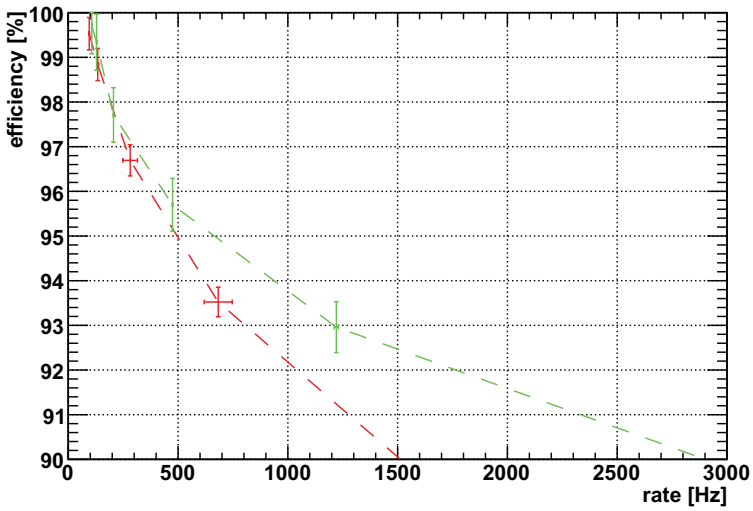

Figure 3.48: Results of the efficiency measurement of the UW-DAQ. Plotted are the efficiency results as a function of the signal rate for the histogram mode (green) and the normal operation mode (red) to a limit of 90% efficiency. The statistical errors shown. The lines indicate the expectation.

can be reached without breaching the efficiency limit. In histogram mode, the limit is given for a single shaper channel and is reached at 3 kHz.

To reduce dead time effects as much as possible, the threshold values for the shaper cards have been set in such a way that the low energetic noise is cut predominantly away but still conservative enough to show the increasing slope. This minimises undesired triggering of background events while still retaining a maximum detection efficiency on signal events. The determined threshold values are listed in appendix C.2.

In [Ren07] time-correlated events in an energy-over-time scatter plot were observed. The source for this effect has now been identified. The noise events are generated by non-matching signal fall times of the SPD pre-amplifiers and the UW-DAQ pole zero

Table 3.6: The measured dead time of the UW-DAQ for different measurement configurations.

measurement configuration	**dead time** [μs]
Shaper card (histogram mode)	21 ± 1
Shaper and trigger card without FAN-IN/-OUT	47 ± 1
Shaper and trigger card with FAN-IN/-OUT	45 ± 1
Shaper (2×) and trigger card with FAN-IN/-OUT	46 ± 1

correction. The pre-amplifier signal has a decay time of 1 ms. During this time the pole zero correction causes the UW-DAQ to trigger more events as long as the signal height is above threshold level. The pole zero correction was implemented into the shaper cards to correct for a return of the pre-amplifier signal to a wrong reference level. The correction time slope applied is 39 μs, which is much shorter than the decay time of the pre-amplifier signal. After removing the pole zero correction on the shaper cards, no artificial events are created anymore and the correlation in time vanishes.

3.5.4.2 IPE-DAQ v3

The final DAQ system for the KATRIN experiment has to accommodate total rates starting from mHz to rates of 1.2 MHz spread out over 148 pixels during energy calibration and 100 kHz in one pixel during e-gun runs to measure the spectrometer response function. For this task a new DAQ system is being designed. The design is based on the Auger observatory's VME DAQ electronics, an in-house production of the IPE which is now being adapted for the use in KATRIN.

A first prototype labeled IPE-DAQ v3 is finished and has been tested by the KATRIN collaborators of the University of Washington and at the pre-spectrometer system. After a commissioning phase, very promising results led to the decision to switch from the UW-DAQ to the new IPE-DAQ v3.

The advantages of the new system are:

- better efficiency
- waveform mode
- FPGA[58] support

IPE-DAQ v3 counting efficiency A circular buffer stores events before sending them on to the DAQ software. With the help of the buffer the efficiency for rates up to 7 kHz in event mode and 50 kHz in histogram mode is still 100% [Leb09], see fig. 3.49. Every channel is independent from each other so the efficiency limit is not valid for a group of pixels as in the UW-DAQ.

Surpassing a value of 7 kHz in event mode, the DAQ efficiency goes down. Due to the buffer design, events then are lost in blocks as shown in fig. 3.50. In this case, the data structure features a periodic appearance of equidistant gaps of missing events. This deficiency due to a limited bandwidth between DAQ and software will be removed in the next generation DAQ system IPE-DAQ v4 and reaching efficiencies extremely close to 100% for rates exceeding 50 kHz seems to be realistic [Wil09].

[58] Field Programmable Gate Array

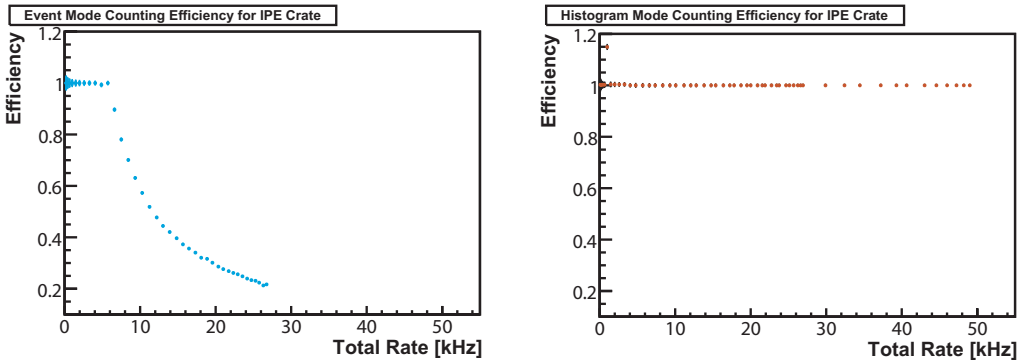

Figure 3.49: Counting efficiency for the IPE-DAQ v3 in event mode (left) and histogram mode (right). 100% efficiency is achieved for rates lower than 7 kHz in event mode and lower 50 kHz in histogram mode. Figure taken from [Leb09]

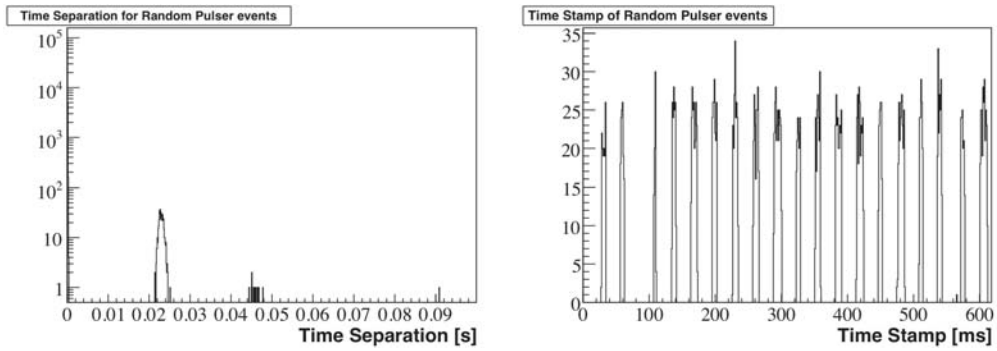

Figure 3.50: Time separation of the IPE-DAQ. If the rate limit for full efficiency is exceeded, events are lost in blocks visible as gaps in the time stamp distribution (right) and as a peak in the time separation plot (left) with the location depending on the signal rate of events. Figure taken from [Leb09]

Waveform mode The IPE-DAQ allows to display and store the ADC traces in a sampling of 100 ns bins over a history of 100 μs around the trigger time (see fig. 3.51(a))

This is a great advantage when dealing with background events which may be caused by noise. However, with activated waveform mode the efficiency decreases. As a result, this mode is considered as a diagnostic tool and is not intended to be used as a standard feature.

FPGA support The IPE-DAQ has a modular layout, where 22 channels are integrated into one board with a set of four FPGAs. With the help of the FPGAs the shaping time can be easily changed, even for the four subgroups associated with the corresponding FPGA. Fig. 3.52 demonstrates the layout of the IPE-crate as visualised by ORCA. In this panel the gain, threshold and shaping time settings can be adjusted. Furthermore, with an FPGA version with addi-

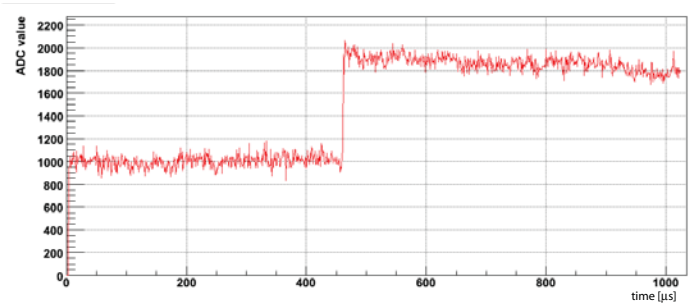

(a) typical event

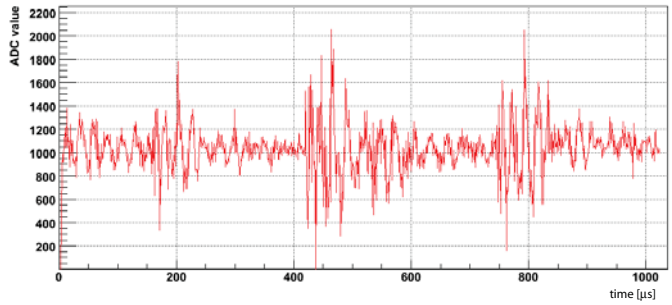

(b) event caused by electrical noise

Figure 3.51: ADC traces taken with the IPE-DAQ (a) typical electron event (b) event caused by switching on the control cabin lights.

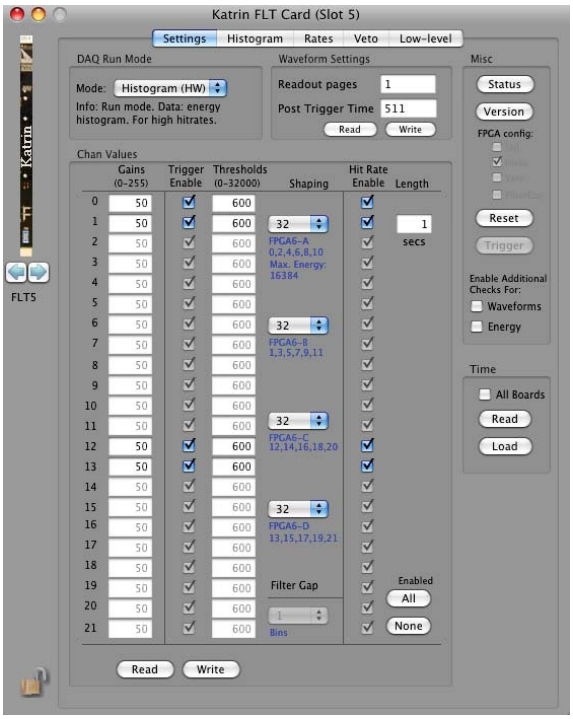

Figure 3.52: Display of the Katrin FLT card as seen in ORCA. One card commands 22 channels and four FPGAs. The panel presented allows changing of gain, threshold and shaping time settings as well as the operation mode.

tional resources (memory), further on-board algorithms can be implemented, e.g. correction of the pole-zero effects.

After switching to the IPE-DAQ the personal computer running the DAQ software has been modernised, too. An Apple Macintosh MacMini system is easily capable of running the software without limiting the counting efficiency of the DAQ. The connection between IPE-DAQ v3 and MacMini is established via FireWire[59] connection removing the need for expensive extra hardware.

The IPE-DAQ v3 hardware is a significant step in direction of the final KATRIN DAQ. However, the requirements stated above are not yet met. In the meantime, the design stage of the successor IPE-DAQ v4 is completed and work on hardware as well as software implementation has started.

3.5.4.3 ORCA - Object oriented Real-time Control and Acquisition

The data acquisition software for the pre-spectrometer test set-up and also for the final KATRIN set-up is ORCA. ORCA is a development of the University of Washington with the purpose of providing a highly modular, object-oriented data acquisition tool which is also capable of controlling DAQ hardware. Furthermore, it is intended

[59] IEEE 1394

to be easy to use, develop and maintain [How08]. To this end it is developed under the MacOS X Cocoa application framework development environment using Objective-C language.

ORCA's main feature directly comes from the object oriented programming approach: software modules correspond either to hardware devices or controlling, tasks and analysis modules which are independent from each other. ORCA provides the framework to connect the modules. Therefore, the term *Object Oriented Software Bus* arises making the legitimate comparison between a hardware bus system like VME and ORCA. This key feature gets apparent when looking at the management of the data stream. Each hardware module is responsible for storing the hardware parameter and the data stream making it possible to reconfigure the read-out scheme at run time - no re-compiling is necessary.

This means for the pre-spectrometer DAQ that it is possible to control hardware parameters like threshold values of the shaper cards and to easily change between operation modes without the need for changing the hardware.

Other features of the ORCA software are that the measurement time can be chosen freely and that a restart option takes data indefinitely but divides the data stream into runs of specified lengths in time reducing the risk of data loss. Acquired data is displayed in histograms as ADC spectra, which are continually updated during measurements. Rates can be viewed for a single channel or the integrated rate over all channels.

The data is either stored locally or, after run stop, is directly broadcasted to another computer. The conversion of the data stream is done by a special application called ORCAroot which directly converts the binaries into ROOT [Bru97] format using tree structure. ORCAroot also has the ability to run as an application, it then receives the raw data from ORCA, converts it in real time for storage in a data base. A more advanced application is the streaming of the ORCA data to another PC. Here, the data is converted via ORCAroot, processed using ROOT and then sent back again to ORCA where it is displayed. This feature allows quasi online analysis capabilities, which are only limited by the amount of data compared to computer time and network speed needed to process the data. The data is not processed on the same computer which is operating the DAQ software to prevent limiting the processing power required for the data acquisition. A second MacMini is used to analyse the data.

As stated above, ORCA is continually being adapted to the KATRIN experiment. For the pre-spectrometer task, a new module has been created acting as run control, see fig. 3.53. The total rate summarised over all pixels, the threshold and gain settings as wells as run start and stop with specified length of time are visible or can be operated from a single window. The most useful feature is to view the rates in colour code for the whole pixel 'chessboard' revealing structures in the pixel distribution. This allows operators to check the uniformity of predefined threshold values or to visualise physics processes. The pixels are numerated according to the numbering scheme as shown in fig. 3.42.

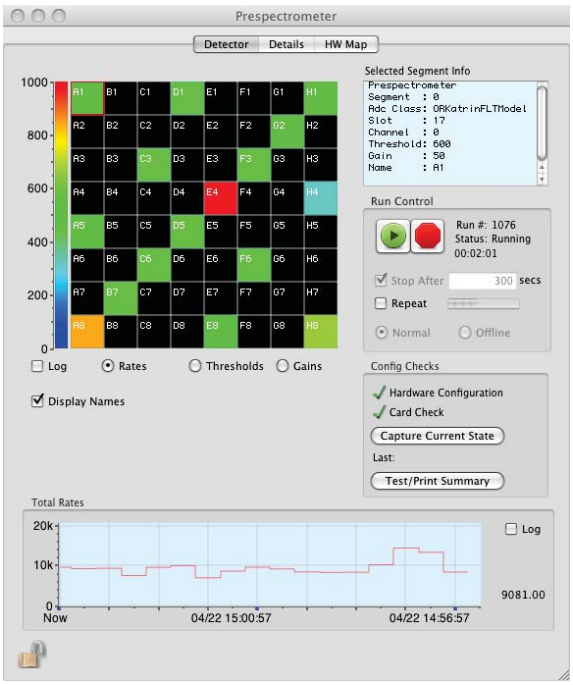

Figure 3.53: The ORCA pre-spectrometer control panel. The customised run control for the pre-spectrometer allows to stop and start runs and to change the duration of the measurement time. The 64 pixels of the SPD detector are visualised online, displaying the individual rate in a colour code. The overall rate is also displayed. The naming scheme inside the pixels is customizable. By clicking onto a pixel the corresponding energy histogram is displayed.

ORCA can be remote controlled via TCP/IP interface. The ZEUS system has been upgraded to accommodate communication with ORCA, allowing automatisation of more complicated measurement tasks to combine ORCA run control with SCS actions.

3.5.5 Conclusion

In the framework of the pre-spectrometer set-up the detector systems were commissioned, one of which is a prototype for the final KATRIN set-up. The detectors are housed in a special vacuum chamber which has been designed to allow freedom of movement in three dimensions, making it possible to scan the whole flux tube at maximum magnetic fields of 4.5 T. MCP and SPD have been successfully operated for long-term measurements. Each system showed its unique performance in its respective application area: the MCP, during the first stages of the spectrometer system's commissioning, and later on the SPD, as soon as stable conditions could be guaranteed.

The SPD has been fully characterised with the main feature being a discrepancy between design and measured energy resolution. The likely causes have presumably been localised and a new prototype will be ready for tests in August 2009. However, the energy resolution has proven to be adequate for measurements regarding background and electromagnetic effects. Background behaviour of the SPD is as good as expected, showing an improvement with regard to microphonics effects as compared to an older model.

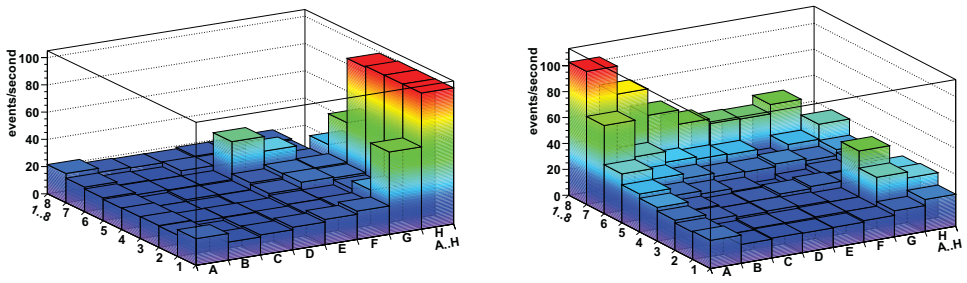

(a) $x = -2.00\,\text{cm}$, $y = -0.35\,\text{cm}$ (b) $x = -0.10\,\text{cm}$, $y = -0.35\,\text{cm}$

Figure 3.54: Spatial effects in the pre-spectrometer recorded with the SPD for different x-values. During measurements a rate excess of a few pixels hints at an active Penning trap. A detector translation of $\Delta x = 2\,\text{cm}$ reveals a ring-like structure. Also visible is the translation of a so-called 'pixel island', EF56 moving to GH23. Detailed information regarding these effects is presented in chapter 5.

The SPD's spatial resolution and its online presentation in ORCA makes it possible to find correlations between background effects and detector response, in particular to allocate the point of origin inside the spectrometer volume. The spatial displacement in the x,y plane allows to investigate effects of the entire flux tube, see fig. 3.54.

The data acquisition has been subject to a significant change in electronics. The IPE-DAQ v3 has been successfully commissioned and is now used as primary DAQ hardware bringing the distinct advantage of better counting efficiency at high rates and new functionalities. Consistency checks are still carried out to further investigate data integrity.

In summary it can be stated that the detector system in all its parts is well suited for the measurements carried out at the pre-spectrometer test set-up.

Chapter 4

Investigation and mitigation of background effects

After finalising the pre-spectrometer set-up, detailed investigations of the electromagnetic properties were started in the framework of this thesis. Already during the first measurements with ramped up magnetic fields and electric potential applied to the vessel, an increase in background events as detected by the MCP detector was observed. After exceeding specific threshold values, this in turn led to a severe vacuum breakdown.

Shortly thereafter, additional measurements were conducted to fully characterise this background behaviour and to discern the source of the problem. In this chapter several possible breakdown mechanisms are discussed, the measurements conducted are summarised and compared to the theoretical assumptions. Both are backed up by comparing them to the results of a set of simulation tools which allows the exploration of the spectrometer's electromagnetic properties. In conclusion, a solution to remove the instabilities in the pre-spectrometer set-up is presented as well as the implementation and the test measurements to verify this solution.

4.1 Discharge mechanisms

The pre-spectrometer design includes a number of parameters which are able to cause electric discharge even leading to electric breakdown. Non-optimum UHV conditions in combination with strong electric fields are known to be a possible source for discharges while operating a set of HV electrodes in vacuum. Here, not only the absolute values are crucial but also the specific geometries of the electrodes and the composition of the residual gas can play a major role. The Townsend discharge and the vacuum breakdown are possible mechanisms for electrical discharges. While the Townsend mechanism is limited to bad vacuum regimes, the vacuum discharge can be generated even at high and ultra high vacua. By adding the magnetic field as

yet another parameter, the combination of electrical and magnetic field gives rise to a third mechanism, the Penning trap [Pen36, Dru40], named after F.M. Penning by H.G. Dehmelt, who was inspired by Penning's work on cold cathode vacuum gauges, which led him to design the first Penning trap as they are known today, earning both physicists a Nobel prize in 1989 [Deh90]. To consider the Penning trap mechanism for creating background or even causing a breakdown in vacuum is of utmost importance – unlike the Townsend discharge, it can also occur at ultra high vacua.

4.1.1 Townsend discharge

This process is named after J.S. Townsend, who in 1903 studied the electrical breakdown mechanisms in vacua [Tow10], and is confined to poor vacuum regimes. To describe the process, a starting number N_0 of electrons is created at the cathode of an electrode system placed in a vacuum recipient. The initial electron production mechanism is of no further concern, possible sources are radioactivity or cosmic ray induced ionisation in the cathode material. The N_0 electrons are then accelerated in direction of the anode. Depending on pressure and electric field strength, the electrons gain sufficient energy sufficient for ionisation of the gas molecules. The average number of electron-ion pairs produced during a specific drift length l is described by the primary Townsend coefficient α. In the simplified case that the energy is gained while traveling the distance of a free path length λ, the connection between the primary Townsend coefficient and the mean free path length can be given as [Dav06]

$$\alpha = \frac{1}{\lambda}. \tag{4.1}$$

In this case, an ionisation cascade is started and the number $N_{e^-}(d)$ of electrons arriving at the anode increases to

$$N_{e^-}(d) = N_0 e^{\alpha d}, \tag{4.2}$$

with d being the distance between cathode and anode. The positive ions, however, travel in direction of the cathode. When hitting the cathode, they produce more electrons which in turn will be accelerated to the anode creating a positive feedback mechanism. This process is taken care of by introducing the secondary Townsend coefficient γ, defined as the average number of electrons liberated by a single ion impact on the cathode. The total number of electrons $N_{e^-,tot}$ increases to

$$N_{e^-,tot} = N_0 \gamma (e^{\alpha d} - 1) \tag{4.3}$$

In the case of $\gamma(e^{\alpha d} - 1) < 1$ the number of electrons produced will decrease after every cycle and the discharge will discontinue after some time. For the reverse condition

$$\gamma(e^{\alpha d} - 1) \geq 1, \tag{4.4}$$

the electron number increases after every cycle and a continuous discharge will be created.

4.1.2 Vacuum breakdown

Electric breakdowns with no magnetic fields present, while good vacuum conditions predominate, are referred to as vacuum breakdown. Because the mean free path length λ between collisions of electrons with residual gas molecules is much larger than the distance d between electrodes, the gas composition plays no role in the process. In this case, the surface character of the electrodes alone is the dominating factor.

One mechanism leading to vacuum breakdown is once again electron emission from the cathode. This process is described by field emission, originally developed by Fowler and Nordheim [Fow28]. Both authors use a quantum mechanical solution to the Schrödinger equation to describe the tunneling of electrons through the potential barrier in the presence of strong electric fields at the cathode surface. The field emission current $I(E_{surf})$ can be expressed as [Bas07]:

$$I(E_{surf}) = \frac{A_{FN}(\beta E_{surf})^2}{\phi} exp(-\frac{B_{FN}\phi^{3/2}}{\beta E_{surf}}). \tag{4.5}$$

given in units of A/m^2. A_{FN} and B_{FN} are constants while ϕ is the electrode material's work function given in eV and E_{surf} denotes the surface electric field in MC/m. The surface characteristics influences the surface's electric field, this is considered by applying a factor β.

The importance of the β factor is shown by comparing theoretical results of a perfectly smooth surface with experimental results. According to eq. 4.5, even for electric fields in the 1 GV/m range, the dark current $I(E_{surf})$ should remain small. Experiments, however, experience discharges starting already at 7 MV/m [Ard59]. This decrease is caused by irregularities in the surface material in form of tips and protrusions in the μm range, which increase the local field considerably as expressed in the factor β of eq. 4.5. Contaminants adsorbed on the surface further influence the field emission by changing the work function.

As a consequence of the heating, created by the field emission, tips or microprotrusions start to melt creating a local pressure increase by the emerging metal vapor resulting in a vacuum breakdown with the possibility of activating ionisation processes [Glü07b].

Apart from electron emission which ultimately can lead to vacuum breakdown, particles of μm-size have a similar effect. Particles in this mass range are accelerated when crossing the anode-cathode gap. The energy gained is sufficient to vaporise the particle itself and part of the electrode surface it is hitting. Once again, the local pressure increase can lead to electric breakdown in the gap. This process seems to be the dominant one for electrode distances above 1 cm, at lower distances, field emission is the primary source for vacuum breakdown [Glü07b].

The effect of micro-particles or ion bombardment is used to condition the electrode set-up. High voltage surpassing the normal operation values are applied to provoke

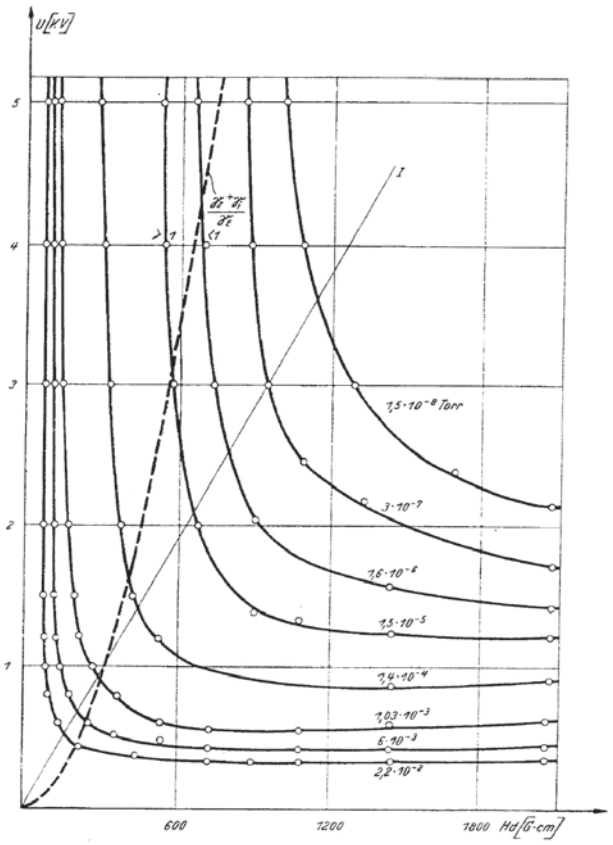

Figure 4.1: Breakdown characteristic curves depending on magnetic and electric fields for different pressure values. Figure taken from [Hae53a].

field emission as well as particle bombardment. Tips and micro-protrusions are eliminated in the process thereby producing a stabilising effect on the electrode operation during normal measurement operations, see section 3.1.3.1.

4.1.3 Penning discharge

Before discussing the mechanism of a Penning discharge, the requirements for Penning trap creation need to be discussed. While Penning traps are also influenced by the pressure in the set-up (see fig. 4.1), the process itself does not require a specific pressure value. The Penning trap requires, however, apart from an electric field, a crossed magnetic field. Looking at a standard electrode system consisting of cathode and anode, it is obvious that a configuration with parallel magnetic and electric fields is identical to the case with no magnetic field: electrons released from the cathode travel directly to the anode. With the mean free path length being longer than the distance between the electrodes (a result of the good vacuum conditions), ionisation processes of the residual gas molecules do not happen. In the case of crossed electric and magnetic fields, the motion of electrons is influenced however by the magnetic field lines.

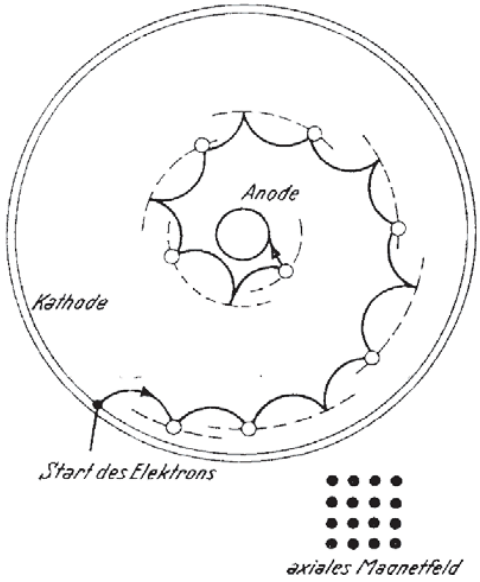

Figure 4.2: Movement of electrons in a coaxial cylindrical electrode set-up with axial magnetic field. An electron emitted from the cathode is bent back to the cathode. Colliding with residual gas molecules prevents the electron from reentering the cathode if the energy loss exceeds the work function. While moving on a hypocycloidal path the electron does not reach the anode if the magnetic field exceeds the magnetron cut-off criterion. However, after each inelastic collision the electron will lose more energy resulting in a smaller radius and in a movement in direction of the anode. The electron's movement is not confined to the plane of projection, collisions with gas molecules provide the electrons also with velocity vectors in axial direction [Hae53b].

In a coaxial cylindrical electrode, as presented in figure 4.2, electrons emitted from the cathode cannot cross the distance d between anode and cathode in a direct line by following the electric field lines but are forced by the Lorentz force on a circular track. With no collision taking place, the electron finally hits the cathode and is absorbed. Irregularities in the surface can however lead to a reflection of the electron [Hae53b] and sooner or later also to inelastic collisions with residual gas molecules. If the lost energy is larger than the work function, a reentry of the electron into the cathode is no longer possible. Another result of the energy loss is the circulation on a hypocycloidal path around the inner anode with a smaller radius. However, with the magnetic field strength exceeding a critical value, called magnetron cut-off criterion(MCC), the electron won't reach the anode [Har89]. Only by colliding numerous times more, the electron can finally reach the anode. By guiding the electrons on cyclotron tracks, the track length surpasses the mean free path length and as such increases the probability for ionisation. The process starting from then on is similar to the Townsend mechanism: secondary electrons are also trapped and cause more ionisation after gaining the required energy from the electric field. The created ions travel to the cathode and there release more electrons, effectively starting an avalanche process creating a large current between the electrodes which

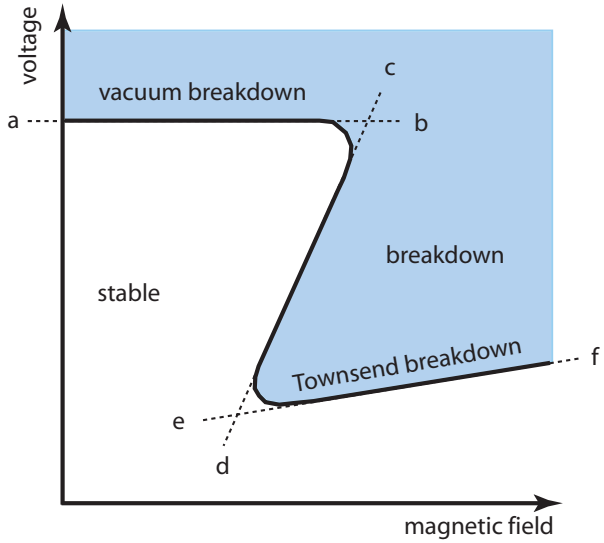

Figure 4.3: Conceptual characteristic of breakdown voltage versus magnetic field. Magnetic fields below the critical value given by the magnetron cut-off criterium don't influence the breakdown characteristics, the breakdown will start as if no B-field is applied according to the vacuum breakdown mechanism (curve a-b). Breakdown characteristics at higher magnetic fields differ according to the starting process. Curve c-d describes the start of breakdown if the electron energy is higher than the ionisation energy, which is influenced by an increase of the electrode potential. Curve e-f describes the region where electrons have to gather energy along their cycloidal path to be able to ionise residual gas molecules [Har89].

ultimately leads to a discharge. Blevin and Haydon [Ble63] introduced the equivalent pressure concept utilising the fact that an increase in path length has the same effect on the number of ionisation collisions as an increase in pressure.

Investigating the breakdown strength of a specific set-up yields a graph similar to fig. 4.3. At magnetic fields below the MCC, electrons moving on cyclotron tracks are not trapped successfully with the mean free path length still exceeding the electron track length. In this region only very strong electric fields will lead to vacuum breakdown. The MCC value is not constant but depends on the electric potential. At values exceeding the MCC, the electrons are guided on small cyclotron tracks around the magnetic field lines which are less susceptible to non-adiabatic motion. If the tracks are stable, the electron path will be larger than the mean free path length and ionisation of gas molecules is possible. At potential values below the threshold limit the depth of the Penning trap is too small leading to unstable trapping conditions. As a result of the hysteresis form of the curve, the potential-magnetic field combination for triggering a breakdown depends on the order of which value is met first.

For the pre-spectrometer a different kind of Penning trap is important. Here, if the magnetic field lines are connecting different parts of the cathode, as shown in

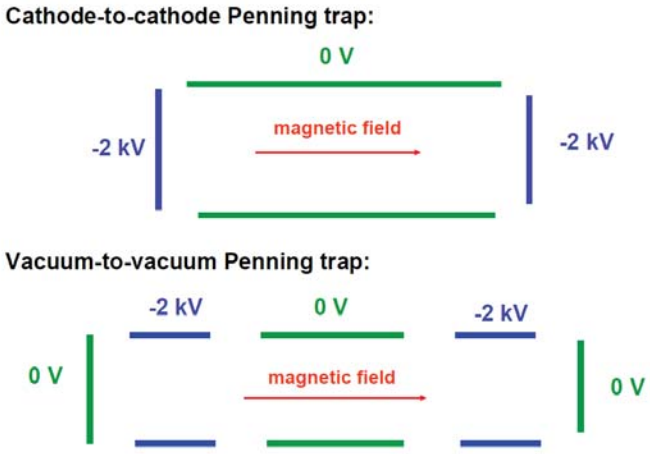

Figure 4.4: Schematics for two different kinds of Penning traps. a) magnetic field lines are connecting two cathode surfaces, and an anode elevates the potential to more positive values in-between. b) while the magnetic field lines are connecting two anode surfaces, two cathode electrodes create a negative potential in-between, so that electrons can be trapped, provided another anode creates a more positive potential in the middle. This is a so-called vacuum-to-vacuum Penning trap. Figure based on [Glü07b]

fig. 4.7(a), it is possible to trap electrons in the space between. The schematics in fig. 4.4 illustrates this case. Electrons at first are released from the cathode with rather small starting energies which are insufficient for ionisation. If the electric field between the two cathode parts is getting more positive due to an influence of the anode potential, the electron is accelerated along the magnetic field line and gains energy. If the electron loses energy along its way by collisions with residual gas molecules it is trapped in the potential well. Here, the path length of the electron increases until it is larger than the mean free path length for ionisation. The ions produced in the ionisation process hit the cathode and release more electrons, creating an avalanche according to the Townsend formalism. It is important that the potential well to which the electrons are confined to is sufficiently deep, see fig. 4.7(b). Only then will the avalanche mechanism produce enough electrons to start a Penning discharge: the number of created secondary electrons is larger and the kinetic energy of the ions increases, resulting in a higher probability of releasing electrons from the cathode. The second schematics provides a different possibility: a second set of negative electrodes creates a vacuum-to-vacuum Penning trap (see fig. 4.4), which is very important with regard to the KATRIN set-up: the combination of the pre- and main spectrometer creates such a Penning trap in the intersection. This is due to the fact that the negative potential barriers of both spectrometers lead to the trapping of electrons with energies smaller than the pre-spectrometer's retarding potential. An investigation regarding this Penning trap has been carried out and the results are presented in [Val09].

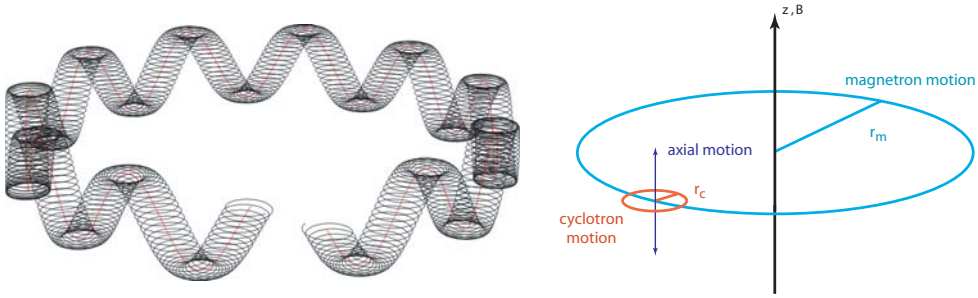

Figure 4.5: Simulation and schematics describing the motion of a charged particle confined in a Penning trap. A magnetic field confines the particle perpendicular to the magnetic field axis. Confinement in the z-axis direction is achieved by high voltage applied to electrodes. The motion is described by three uncoupled harmonic oscillations: cyclotron, axial, and magnetron oscillation. Left picture taken from [Wer].

4.2 Pre-spectrometer Penning trap

Since the arrival of the pre-spectrometer in 2003, a large number of measurements have been carried out to obtain detailed information for different R&D efforts of the KATRIN experiment. After completion of the vacuum tests, the set-up was made readied for the electromagnetic measurements. In 2006, the set-up was finally completed: superconducting magnet, e-gun and detector system were mounted and high voltage stability secured. While the system has been working as expected with either magnetic or electric fields applied, the first time both fields were applied simultaneously, a vacuum breakdown with the pressure increasing rapidly to $1 \cdot 10^{-6}$ mbar was observed. With the help of simulation tools and a dedicated measurement plan, the source for this breakdown could be found. In the following sections the simulation tools, which make it possible to characterise the electromagnetic properties of the spectrometer with excellent precision, together with the measurement results are presented. These works corroborate the hypothesis of a Penning trap in the entrance and exit region of the spectrometer vessel to be the dominant source of background and the cause for vacuum breakdown. This problem could be solved in the framework of this thesis by a modification of the inner electrode system. The design of an additional shielding electrode is motivated before the results of the modification are finally presented.

4.2.1 EMD simulation tools

The optimisation of the KATRIN experiment requires a powerful programme package to simulate the electromagnetic properties of the whole set-up. Commercial programmes and their embedded tools do not offer the numerical precision required. In particularl the need to simulate adiabatic particle motion in large structures like the main spectrometer, which also contains small-scale but important parts such

as the wire electrodes, is beyond the scope of commercial programmes. Thus, for the electromagnetic design studies, several specific programme packages based on C language and developed by F. Glück are used. The tools allow the simulation of

- magnetic fields for user-defined coil configurations
- electrostatic fields for user-defined electrode configurations
- charged particle trajectories in electromagnetic fields.

The simulation tools are shortly summarised. A detailed description of the structure and the working principles is given in references [Val04, Hug08c, Vöc08].

4.2.1.1 Magnetic field calculation

The superconducting solenoids of the KATRIN experiment use inductor coils to generate a magnetic field. Dividing the coils into thin current loops the magnetic field can be calculated applying Biot-Savart's law:

$$d\vec{B} = \frac{\mu_0}{4\pi} \frac{I d\vec{l} \times \vec{r}}{r^3} \tag{4.6}$$

with the magnetic field $d\vec{B}$ being induced by a current I flowing through an infinitesimal conductor element $d\vec{l}$ at a given point $\vec{r}$ in space. The programme tool calculates the components B_r, B_ϕ and B_z of the magnetic field with the help of Legendre polynomials. The Legendre polynomial expansion relies on a set of requirements, e.g. the location of the calculation point $\vec{r}$ is supposed to be inside a convergence zone which is defined by either the remote or central Legendre polynomial expansion. If this requirement is not fulfilled, or the convergence ratio is not favourable, this method, in the worst case, cannot be used or computing is slow. In this case the programme switches automatically to another method – the magnetic field calculation with elliptic integrals. Elliptic integrals allow the calculation of any point, even inside the coil windings, to very high precision at the expense of additional calculation time.

By relying on the Legendre polynomial method first, good and fast results are achieved. A further speed-up of the calculation time can be gained by exploiting symmetries in the coil structure. For the pre-spectrometer the whole set-up shares in first order a single rotational symmetry axis. This simplifies the magnetic field calculation considerably, however, even complex coil structures with different symmetry axes can be simulated as well. The only input needed are coil locations in cartesian coordinates as well as the inner and outer radii and a discretisation parameter, specifying the number of radial segments.

4.2.1.2 Electric field calculation

Computation of electrostatic potentials can be done using the *finite difference method* (FDM) or the *finite element method* (FEM). While these methods yield good results in the calculation of electrostatic potentials they are of disadvantage when the scale of the problem varies, for example the calculation of large structures including small details. Investigations in reference [Val04] show that the methods are not suited for calculations regarding the main spectrometer set-up including the small structures of the inner electrode because the mesh structure's grain size with equidistant spacing defines the accuracy of the method. However, a mesh fine enough to accommodate the wires and the vessel has fatal consequences with regard to calculation time.

An alternative method also discretises the electrode set-up, however, the structures need not to be of the same size. Depending on the problem at hand and the given structure of the electrode it is possible to choose the granularity of the mesh differently for each subgroup of the complete geometry. For each quadrant of the mesh's surface a charge density is calculated which is assumed to be homogeneous in its boundaries'. Therefore, the discretisation has to be chosen accordingly. The *boundary element method* (BEM) thus makes it possible to define large and small structures simultaneously and is only limited by the homogeneity of the structure's potential distribution and not its actual size.

After the discretisation, the structure is made up of N surface parts with a charge density $\sigma_i \, (i = 1, ..., N)$. Each part of surface a_i can be attributed with a charge $q_i = a_i \sigma_i$. Using the BEM the potential distribution in a specific volume can be determined. In a first step the potential of each element i with regard to the element j is calculated [Glü04]:

$$C_{ij} = \frac{1}{4\pi\epsilon_0} \int\limits_{a_j} \frac{d^2 \overrightarrow{r}_j}{\overrightarrow{r}_i - \overrightarrow{r}_j}. \tag{4.7}$$

Multiplying C_{ij} with σ_j, which is assumed constant within the boundary of the corresponding element, and summing up all potential contributions to the subelement i, yields the potential U_i:

$$U_i = \sum_{j=1}^{N} \phi_{ij} = \sum_{j=1}^{N} C_{ij} \sigma_j. \tag{4.8}$$

To calculate the potential for a given field point $\overrightarrow{r}$ the relevant potentials ϕ_{ik} with $k = 1, ..., N$ are added up like in equation 4.8:

$$U(\overrightarrow{r}) = \frac{1}{4\pi\epsilon_0} \sum_{k=1}^{N} \sigma_k \int\limits_{a_k} \frac{d^2 \overrightarrow{r}_k}{\overrightarrow{r} - \overrightarrow{r}_k} \tag{4.9}$$

It is important to notice that electric field calculation close to the electrode surface can be the cause for problems. According to [Hug08c], test calculations with a wire

of 0.1 mm diameter and a 1 kV potential, the distance limit for accurate calculation is approximately $5{\cdot}10^{-5}$ m. A finer discretisation in critical parts of the geometry, like sharp edges or points, can mitigate the inaccuracies to some extent.

Furthermore, utilising geometrical symmetries like mirror and rotational symmetries speeds up the calculation. Axial symmetric objects can be divided into infinitesimal rings of charge which are then calculated according to the method for magnetic field calculation with either complete elliptic integrals of the first kind or, if applicable, Legendre polynomial expansion [Glü04].

4.2.1.3 Trajectory calculation for charged particles in electromagnetic fields

In a space with electric and magnetic fields the motion of a charged particle is given by six first order differential equations:

$$\dot{\vec{x}} = \vec{v}, \tag{4.10}$$

$$\dot{\vec{p}} = \vec{F}_L, \tag{4.11}$$

$\vec{F}_L = q(\vec{E} + \vec{v} \times \vec{B})$ being the Lorentz force, $\vec{x}$ the cartesian coordinates, $\vec{v}$ the velocity and $\vec{p}$ the momentum of the particle.

The fields $\vec{E}$ and $\vec{B}$ for each step of the tracking equations 4.11 are calculated by utilising the Runge-Kutta algorithm of 4th or 8th order. Accuracy increases for the higher order calculation, as does the computing time.

Another factor which impacts the computing time for high degrees of accuracy is the number of calculation steps which are taken. The microscopic tracking follows the cyclotron motion around the magnetic field lines. By sub-dividing the period $T = 2\pi/\omega$ of a cyclotron turn with a constant n_{st} specifying the number of steps, the accuracy of the computation can be adjusted, particularly in areas where the prevailing fields change strongly and more detailed calculations are called for.

4.2.2 Penning trap characterisation

During the first electromagnetic test with the pre-spectrometer, a highly unstable condition was induced. The pre-spectrometer vessel and inner electrode was elevated in steps to -20 kV, as shown in fig. 4.9(a). The system was stable with no discharges, visible as a breakdown in voltage. In this stable condition the magnetic field was ramped up. Before reaching a magnetic field strength of 0.2 T[1] a total breakdown in high voltage occurred, with subsequent stabilisation around -4 kV. Simultaneously with the HV breakdown, the vacuum increased to $1.6 \cdot 10^{-6}$ mbar and stabilised

[1] Magnetic field strengths are normally given with regard to the maximum value in the middle of the warm bore of the magnets if not mentioned otherwise. The conversion factor for the magnetic field value in the analysing plane is $(274.48)^{-1}$.

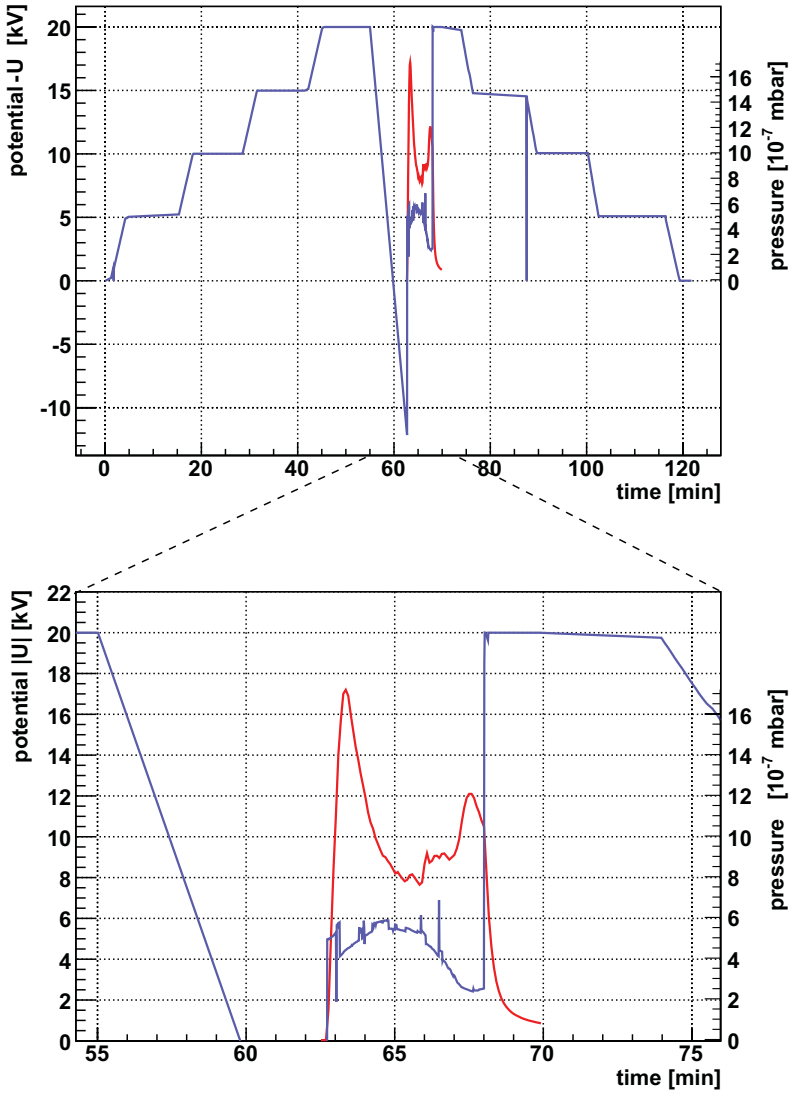

Figure 4.6: Continuous discharge with elevated pre-spectrometer and activated magnetic fields. Ramping up the magnets to 0.2 T while the pre-spectrometer is elevated to -20 kV causes a sudden breakdown in the potential(the slope being an artefact caused by the read-out routine as is the negative voltage reading) with simultaneous pressure increase. As soon as the magnetic field is deactivated the potential and pressure recover to the original values.

around 10^{-6} mbar, see the enlargement of the breakdown interval in fig. 4.9(a). The discharge with vacuum breakdown continues until the magnetic field is ramped down. As soon as the influence of the magnetic field wears off the discharge requirements are gone and the initial stable conditions are reestablished with pressure readings completely recovering in an exponential decline over the course of several minutes.

An explanation for this behaviour is the presence of deep Penning traps in the pre-spectrometer [Glü06]. As explained in section 4.1, the combination of steep gradients of both magnetic and electric fields can lead to the trapping of charged particles. Through further ionisation of residual gas particles this can cause an increase in background or even lead to vacuum breakdown, as experienced in this measurement.

With the help of the simulation tools developed by F. Glück, (see section 4.2.1), it is possible to 'scan' the pre-spectrometer set-up for regions where Penning traps can be formed. Earlier investigations during the R&D phase of the inner electrode system used a different set of software tools and were focused on the inner volume of the flux tube [Fla04]. For this restricted region no harmful Penning trap was found. However, in these investigations all regions 'shadowed' by electrodes (regions with magnetic field lines which are not part of the flux tube) were not included. Motivated by the experimental observation, a dedicated simulation effort[2] was started to detect possible Penning traps [Glü06]. As a result, Penning traps were discovered in the region between ground electrode and the full metal sheet cone of the inner electrode system, see fig. 4.7(a). Here, magnetic field lines connect parts on vessel potential with the coni of the inner electrode. This cathode-to-cathode connection in combination with a more positive potential in-between (caused by the nearby earth electrode) leads to the trapping of electrons. In fig. 4.7(b) the electric potential distribution along the magnetic field lines is displayed. Penning traps are visualised by a depression in the slope. Electrons following the magnetic field lines lose energy by inelastic collisions when inside the dip. Subsequently, they may not possess sufficient energy to leave the potential depression, or in other words they are unable to reenter the cathode material, and are thus trapped. A careful study of the pre-spectrometer geometry, which also considers different potential distributions, yields a maximum depth of the pre-spectrometer Penning trap of 5.2 kV for a potential distribution of $U_{wire} = -18.6\,\text{keV}$ and $U_{cones} = U_{vessel} = -18.5\,\text{kV}$ [Val09].

To validate or refute the hypothesis of Penning traps as the source for vacuum breakdown when electromagnetic fields are applied, a detailed measurement programme was carried out. The corresponding results are presented in the next section.

4.2.2.1 Measurements

The measurements carried out were following two aims: first, to validate the hypothesis of Penning traps as the source of the instabilities and second, to obtain

[2] The EMD simulations have been carried out by Ferenc Glück (University of Karlsruhe), Karen Hugenberg and Kathrin Valerius (University of Münster)

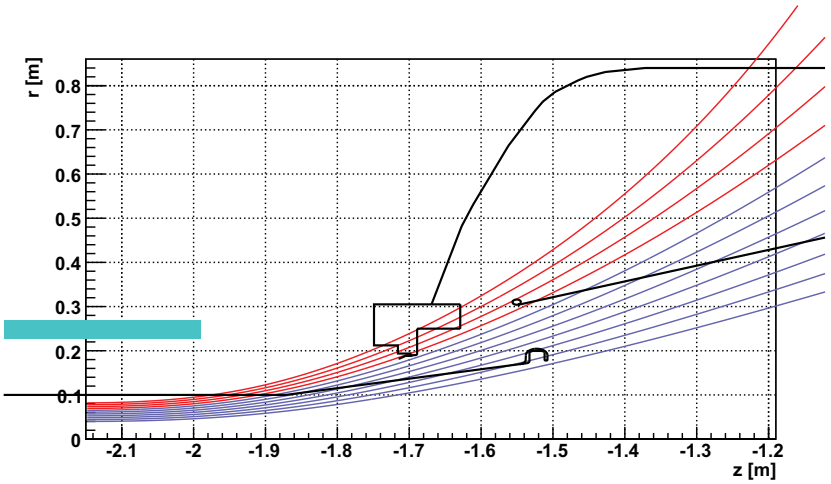

(a) Magnetic field lines

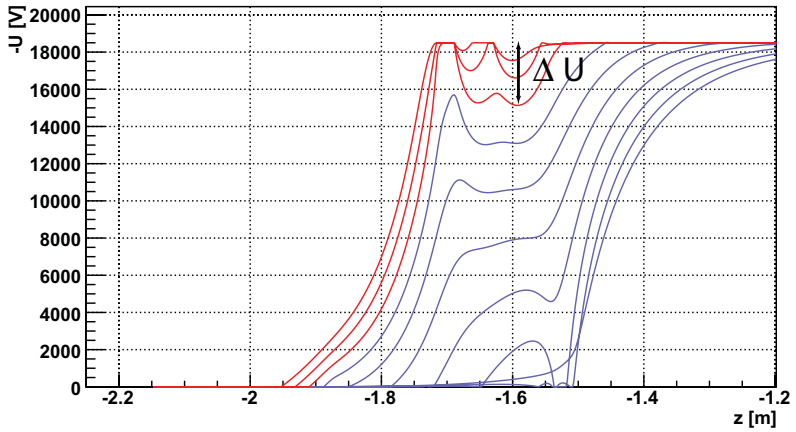

(b) Electric potential along the magnetic field lines

Figure 4.7: Penning trap in the pre-spectrometer I set-up.
(a) Diagram showing the magnetic field lines. Cathode-to-cathode field line connections in red, cathode-to-anode connections are in blue.
(b) Diagram of the electric potential along the magnetic field lines for standard potential distribution $U_{wire} = -18.6\,\mathrm{kV}$, $U_{cones} = U_{vessel} = -18.5\,\mathrm{kV}$. A dip in the field lines indicates a potential well. A potential well with a depth of several hundred eV is sufficient to form a stable Penning trap. The Penning trap depth is indicated by ΔU. A fine-tuning of the starting radii yields a maximum depth of $\Delta U = 5.2\,\mathrm{kV}$ [Val09].

a qualitative characterisation of the behaviour of the activated processes. At first leakage currents and pressure values monitored by SCS were used as observable to define the pre-spectrometer status. After gaining some initial understanding of the mechanisms involved and their parameter, space the MCP is utilised.

Fixed potential When investigating the starting requirements for a breakdown it has to be expected (see fig. 4.3) that ramping up the magnetic field to a designated value prior to increasing the potential will lead to a different result as as opposed to a procedure where the vessel is first elevated and then the ramping of the magnets is started. Fig. 4.8 presents the results from the measurement with fixed potential and variation of the magnetic field until a discharge occurs. These measurements show a clear distinction between a stable parameter space and unstable conditions leading to an abrupt increase in leakage currents which results in a vacuum breakdown as shown in fig. 4.9(a). The sudden onset of the discharge is explained by the requirement for stable conditions of the Penning trap. If this is not fulfilled, secondary electron production is insufficient to produce a discharge.

By applying a current to one magnet only different geometrical traps can be studied, either on the west (detector) or east (e-gun) side trap. Using this method it is possible to study the effects of the trap independently. At voltages more negative than -10 kV no major differences are detectable. The observed changes can be explained by different starting pressures, which have a tangible effects as shown in fig. 4.1. At a potential of -10 kV a large difference in the limit of maximum magnet field before breakdown of a factor 3 between east and west trap were measured. This difference is not understood, particularly as no major discrepancies between east and west trap were detected during other measurements. There may be slight differences due to small deviations in the inner electrode geometry[3]. However, these are not significant to explain a difference of that magnitude. Furthermore, the measurements so far were meant to give a qualitative understanding of the mechanisms. More measurements would be necessary to achieve an accuracy as published in the literature, which is not the aim here. One measurement point in diagram 4.8 has been taken by reversing the order in which magnetic and electric fields are applied, verifying the relation presented in fig. 4.3. The result of tracking simulations yield a minimum value of 0.1 T for stable trapping of electrons [Glü07c]. In spite of the measurements' systematic effects the experimental value of 0.1-0.2 T is in accordance with the simulation results.

Fixed magnetic field For a procedure, where the magnetic field remains fixed while the potential increased, a different behaviour is observed. Instead of a sudden onset of a discharge leakage current, the pressure already starts to rise at a lower potential level until a discharge threshold is reached. An example is presented in fig. 4.9(a). For B=0.86 T the leakage current and pressure are stable up to -4 kV but

[3] A photographic survey yields a maximum deviation from the specified value of 27±2 mm. More information is given in ref. [Frä06].

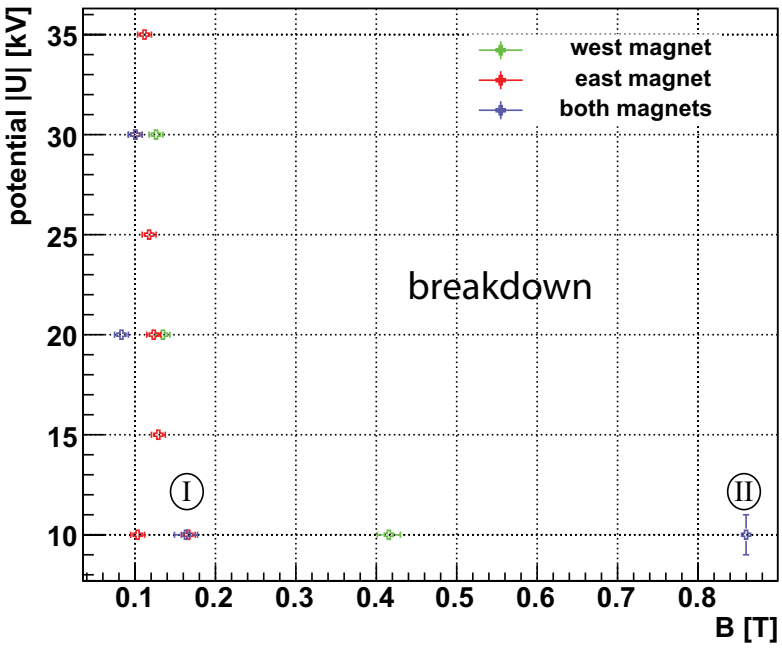

Figure 4.8: Experimental ignition curve for fixed potential and variation of the magnetic field. Increasing the magnetic field leads to a sudden increase in leakage current and pressure. West and east trap have been tested independently and simultaneously, with no detectable difference besides one measurement point at -10 kV. One measurement point has been taken to illustrate the difference in changing the magnetic prior to the electric field and vice versa. Increasing the potential first, results in a lower breakdown value B_{crit} of the magnetic field (I) as compared to ramping the magnetic field first (II), compare fig. 4.3.

start to increase beyond this limit. At -10 kV the resistivity between cathode and anode is diminished sufficiently so that a discharge occurs.

When investigating the dependency of the pressure as a function of the leakage current, a linear increase is observed, fig. 4.9(b). This can be explained by a rise in outgassing of the cathode surface due to stimulated desorption caused by positive ion bombardment [Glü07c]. At some point (90 μA) an equilibrium in the outgassing is achieved and the linear increase goes over into a nearly constant pressure level, while the leakage current is rising further.

Penning trap depth dependence By supplying vessel and both inner electrode cones and wire parts with different potential values, the depth of the Penning trap changes. Measurements show that cone electrodes with a more negative potential compensate for the potential penetration of the more positive earth electrode on ground potential. This results in a decrease of the trap depth and hence in a deteri-

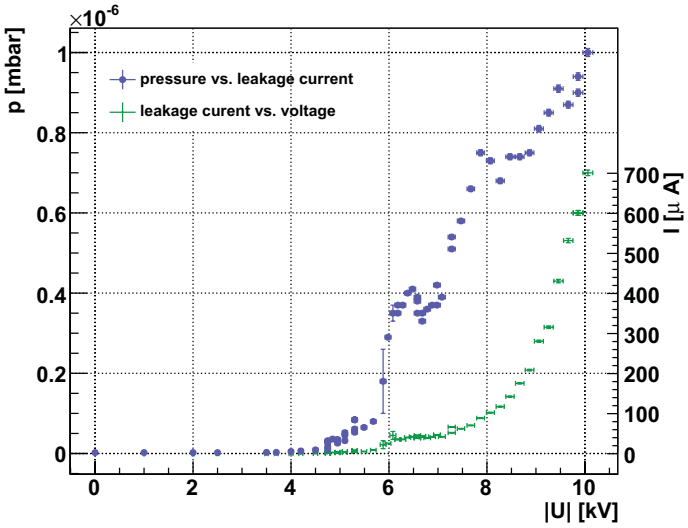

(a) Pressure p and leakage current I over potential |U|

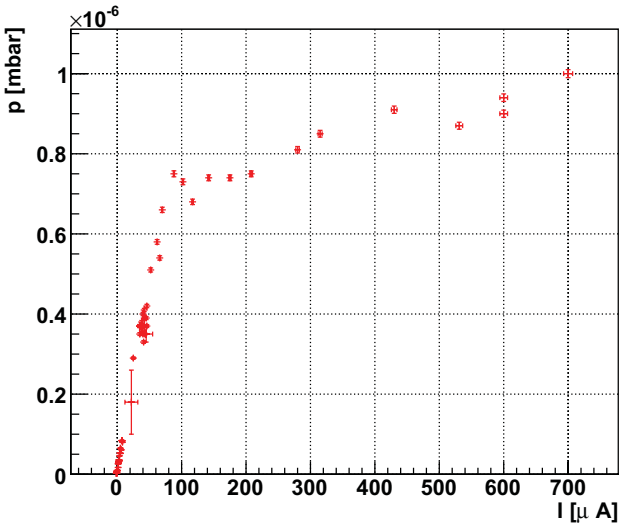

(b) Pressure p over leakage current I

Figure 4.9: Rise of the leakage current and pressure as a function of the electric potential.
(a) Increasing the potential with fixed magnetic fields (B=0.86 T) leads to an increase in pressure and leakage current. The increase is not sudden as with fixed potential and changing B-field but gradual. At -10 kV a discharge takes place (not included in the graph).
(b) Plotting the pressure over the leakage current reveals a linear relationship up to 90 μA, afterwards the pressure stabilises while the leakage current increases further. The pressure increase can be attributed to stimulated desorption triggered by ion impact.

oration of the secondary electron production mechanisms ultimately leading to more restrained discharge effects. The opposite effect is achieved by applying a positive potential to the vessel and inner electrode. In this case a huge Penning trap in the middle of the vessel is formed leading to strong discharges. After changing the magnetic field from a symmetric to an asymmetric distribution by turning off one magnet, the Penning traps vanish and the discharge is quenched.

Tests with the MCP detector The MCP proved to be a very sensitive tool for detecting the start of a discharge. The measurements were mostly done while keeping the magnetic field fixed so that the gradual increase in rate during potential elevation could be controlled and damage to the detector prevented. In particular the pre-amplifier proved to be vulnerable to a sudden increase in amplitude of the signal-current. It showed that the MCP's sensitivity for incoming particles is much higher than the leakage current measurement of the FuG power supplies: the detector rate increases even before a change in pressure or leakage current is visible. The efficiency of the MCP decreases in higher magnetic fields, therefore the MCP was positioned at z=0 which is 500 mm west from the middle of the magnet (B=0.42 T).

Plotting the rate over time reveals an exponential increase in rate prior to the final breakthrough of the discharge. The rise time until discharge breakthrough correlates with the Penning trap depth – the rate increases faster if the Penning trap is deeper, analogous to the observation of discharge severity already discussed in this section.

The rise time as well as the slope can be compared for two measurements with different Penning trap depths. When the coni of the inner electrode are kept on a more negative potential the Penning trap depth is reduced. The rise time is about 70 s, fig. 4.10(a). If the same potential is applied to all electrodes the trap gets deeper, the rise in rate is getting steeper and takes 35 s until discharge. Independent from the slope inclination the transition to the breakthrough starts at a rate of 100-200 Hz.

Additional measurements were conducted where the magnetic field was kept constant and the potential was gradually increased until the MCP rate reached 10 kHz. The results are displayed in fig. 4.11. As expected, the limits are lower compared to measurements using leakage currents and pressure increases as tools. However, the principal course of fig.'s 4.3 ignition curve is once again confirmed.

As stated before, the use of asymmetric magnetic fields allows to study the Penning traps of the east and west side independently. This method is used to clarify the type of particles detected by the MCP. If the east magnet is ramped up (on the opposite end of the detector) the east trap ignites. It is important to note that the electron starting energy is defined by the potential applied to the cones of the inner electrode and vessel. By elevating the wire potential in the middle of the spectrometer to more negative values, electrons created at the cones and the vessel surface are not able to pass the potential barrier. On the other hand, positive ions are blocked by applying a more positive potential to the wire electrode as compared to the vessel or the

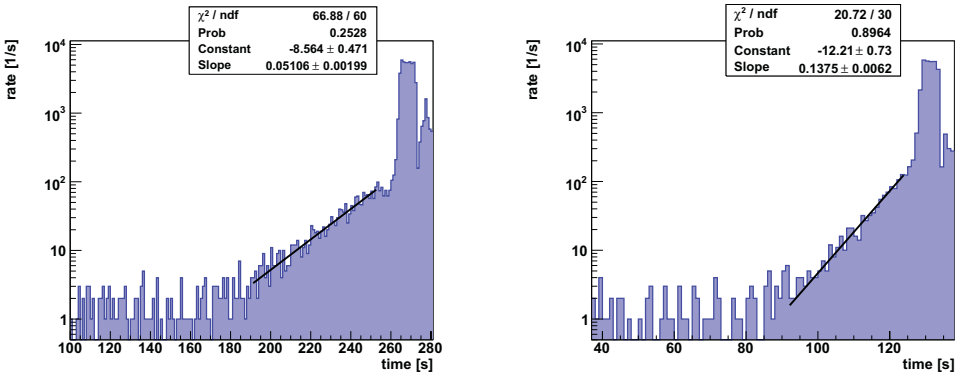

(a) shallow Penning trap (b) deeper Penning trap

Figure 4.10: Dependence of the rate increase and the Penning trap depth in the pre-stage of a discharge. The MCP proves to be more sensitive than the monitoring of leakage currents and pressures. A discharge is preceded by an exponential increase in detection rate. The time scale depends on the depth of the Penning trap. A more negative cone compensates for the influence of the earth electrode's positive potential, thus the trap depth decreases and the discharge is weaker.
(a) $U_{wire,vessel} = -1.3\,\mathrm{kV}$, $U_{cones} = -1.4\,\mathrm{kV}$,
(b) $U_{wire,vessel} = -1.4\,\mathrm{kV}$, $U_{cones} = -1.4\,\mathrm{kV}$.

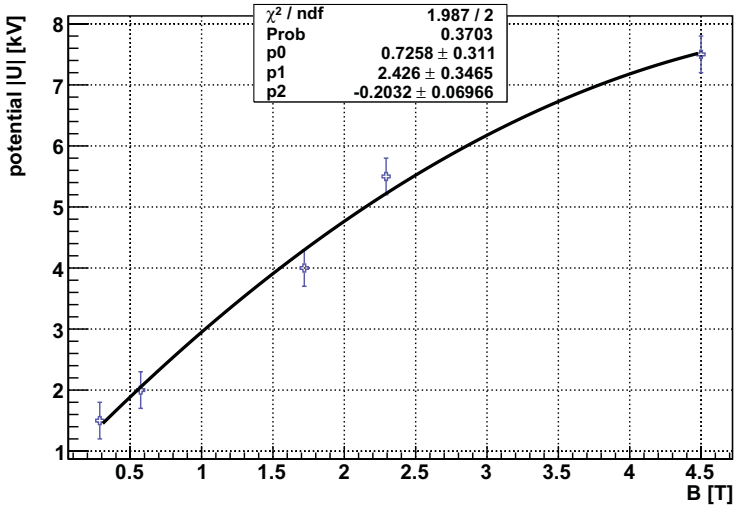

Figure 4.11: Start of the electric breakdown when keeping the magnetic field fixed while increasing the potential. The ignition potential is an increasing function of the magnetic field in concordance with the conceptual breakdown characteristics presented in fig. 4.3. A polynomial fit of second order is in good agreement with the data.

Figure 4.12: Picture showing the novel Anti-Penning electrode (APE) and stainless steel earth electrode mounted together onto the DN500 flange with conical isolator. The APE is attached with screws to the inside of the DN500 flange, the earth electrode is fixed to the DN200 flange of the conical insulator.

coni. Furthermore, by carefully studying the magnetic field lines it seems unlikely for positive ions to reach the detector: the field lines are connecting the Penning trap region with the vessel surface and with opposite coni on negative potential. Thus it his highly improbable that they reach the MCP on ground potential in its retracted position. Also, changes of the wire electrode potential have no influence on the observed rate. This leads to the conclusion that the main contribution to the MCP signal is coming from photons created during the discharge as these are unaffected by magnetic fields as well as by the electric potential distribution.

Conclusion The initial EMD measurements clearly support the hypothesis of Penning traps as generic source for electric breakdowns. It has been shown that

- no discharges appear when Penning traps are absent or are only unstable,
- discharges appear when Penning traps are present,
- the depth of the Penning trap correlates with the strength of the discharge as measured by the leakage current, pressure and rate increase,
- the EMD simulation software developed by F. Glück yields excellent results in the precise localisation of Penning traps and is in good agreement with the experimental results.

4.2.3 Design for a shielding electrode

One elegant way to eliminate the Penning traps is to fill the problematic area with insulator material, which obviates the trapping of particles [Har89]. Another way to solve the specific problem of the pre-spectrometer traps is the insertion of another

conical electrode on vessel potential between earth electrode and the inner electrode coni. This concept shields the area from the influence of the earth electrode's positive potential [Glü07a].

Insertion of an additional electrode was considered to be the easier solution and has been realised successfully. The mechanical design of the electrode was subject to several restrictions superseding the EMD considerations: the installation of the additional electrode is only possible through the DN500 opening of the end-cap flanges. From an EMD point of view an electrode of larger diameter is favoured, the technical solution of such a design, however, is too demanding and bears the risk of damaging the inner electrode set-up during the installation process.

On the basis of these requirements an extensive study of the KATRIN EMD group was carried out with the aim to find a design which

1. eliminates all Penning traps,
2. preserves the adiabatic transmission properties while
3. keeping a safety margin to the flux tube and
4. keeps the electric field strength within safety limits.

The result is shown in fig. 4.12 and 4.13(a),(b), consisting of a conical electrode with a diameter of nearly 500 mm and a length of 250 mm along the z-axis. This so-called Anti-Penning electrode (APE) is attached to the inside of the DN500 flange. The new earth electrode, sitting inside the APE, had to be made shorter as a consequence of the limits to the APE dimensions. When operating the pre-spectrometer with a single potential applied to all electrodes, the Penning traps of this configuration are reduced to a depth of 210 eV only [Val09], see fig. 4.13(b). By choosing a potential distribution with a more negative cone potential the traps are completely eliminated.

The requirements for adiabatic transmission of electrons through the pre-spectrometer in the final KATRIN set-up had to be relaxed at the same time however. The pre-spectrometer's electromagnetic design was carried out with the aim to maximise the adiabatic transmission properties resulting in a separate power supply for the inner electrode coni. Increasing the voltage of the coni to more positive values a too early retardation is prevented [Val09], see also fig. 4.14. While the new design of the APE and new ground electrode deteriorates the transmission properties to some extent in the pre-spectrometer's stand alone mode of operation, it is of no consequence for the final KATRIN set-up if the filter energy of the pre-spectrometer is well below the tritium end-point energy taking into account the pre-spectrometer energy resolution. To be able to measure the pre-spectrometer transmission function, an increase to $U_{coni} = U_{vessel} + 1\,\mathrm{kV} = -17.5\,\mathrm{kV}$ is proposed in ref. [Val09]. This change in the potential distribution has been found to result in a Penning trap of approximately $\Delta U = 750\,\mathrm{V}$ depth. The trap, however, is between vessel and full metal coni and thus shielded from the flux-tube.

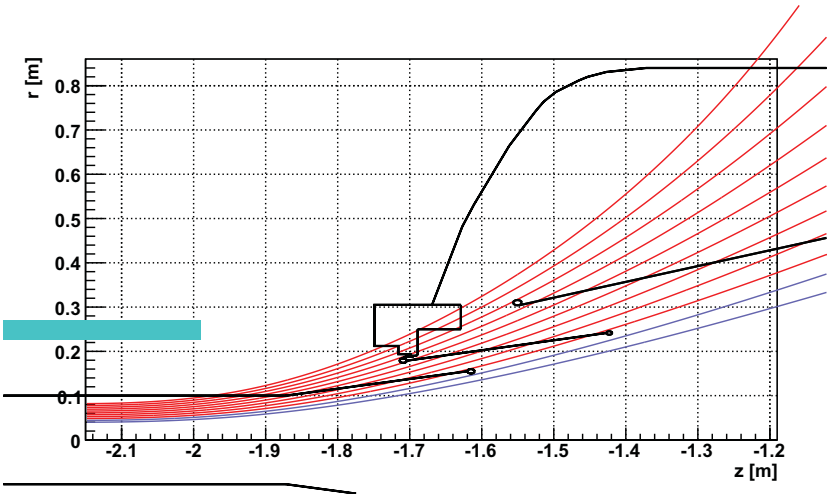

(a) Magnetic field lines

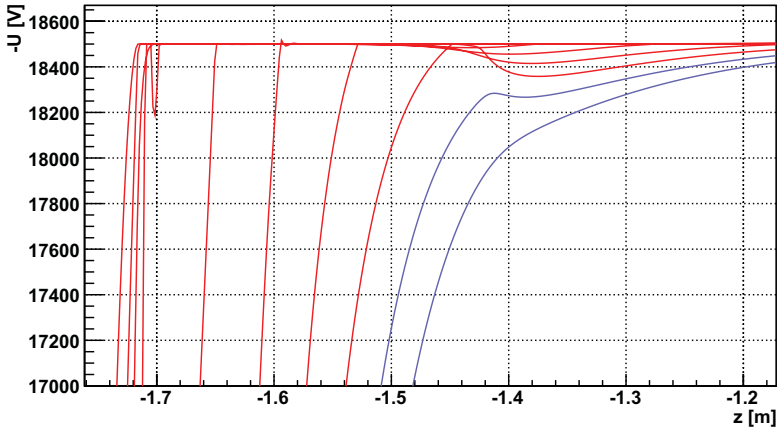

(b) Electric potential along magnetic field lines

Figure 4.13: Consequence of the modification of the inner electrode set-up. In close analogy to figs. 4.7(a),(b) the magnetic field lines and the potential along these lines are shown for the same potential distribution $U_{wire} = -18.6\,\mathrm{kV}$, $U_{cones} = U_{vessel} = -18.5\,\mathrm{kV}$. Cathode-to-cathode connecting field lines are marked in red. A small Penning trap, located at the end of the APE, remains. Changing the potential distribution to more negative cone potentials eliminates this trap.

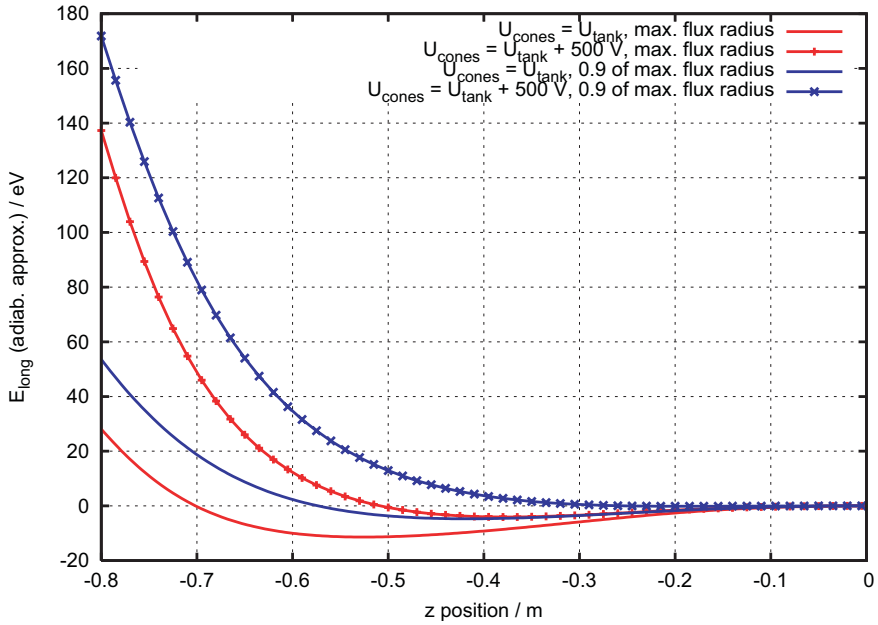

Figure 4.14: Change of the longitudinal energy for electrons entering the pre-spectrometer. A too early retardation for electrons in the outer flux tube with large starting angles can be mitigated by increasing the cone potential by +500V compared to the vessel potential (PSI configuration) [Val09].

The safety margin with regard to the flux tube in the final set-up is 17.4 mm [Val09] which is reached at the pre-spectrometer's exit side. The distance prevents electrons emitted from the electrode via field emission to enter the flux tube and to possibly reach the detector.

The electric field with the new design has been subject to further extensive simulations. To limit the electric field strength, a tube with 10 mm diameter is welded to the end of earth and Anti-Penning electrode. Compared to the old design the electric field strength increases at the anode ring by a factor of 2.5 but stays stable at the cathode [Val09]. The increase on the anode side does not limit the high voltage stability due to field emission originating at the cathode potential.

During the design phase of the new electrodes another point had to be considered. High voltage instabilities of the set-up had been credited to discharges between the DN500 flange and the earth electrode. The cause for these effects can be attributed to bad surface conditions from soldering of the ceramics to the DN500 flange and welding of the earth electrode made of titanium, more information is presented in [Hug08c]. As a result, the APE is designed to cover the solder joint and the earth electrode is remade of non-magnetic stainless steel which is easier to work with. Electro-polishing of both earth electrode as well as of APE guarantees good surface quality diminishing the probability of discharges as described in section 4.1.2.

4.2.4 Conclusion

An extensive ensemble of detailed and specific simulations, measurements and theoretical descriptions of discharge mechanisms are all consistent with the theory that the increase in background leading to vacuum breakdown is caused by electrons confined inside a Penning trap formed in the regions between the DN500 flanges and the cones of the inner electrode. A thorough comparison of corresponding measurements and simulations proves that the EMD simulation package developed by F. Glück provides a highly versatile and precise description the pre-spectrometer electromagnetic properties.

The MCP detector has been found to provide excellent sensitivity to background processes in combination with a generic robustness which allows operation during unstable conditions. With the help of the MCP, the increase in background rate was identified as being caused mainly by photons created during discharge processes.

Using these simulation tools, a design for a shielding electrode was realised which is a compromise between geometrical specifications and electromagnetic requirements. As a major result of the present thesis a novel concept consisting of an Anti-Penning electrode and an earth electrode was designed, manufactured and installed. Initial measurements with this optimised set-up prove that the discharges compromising the vacuum are successfully eliminated.

Chapter 5

Background investigations at the pre-spectrometer II set-up

After completing the installation of the Anti-Penning electrode, measurements are carried out to test possible influences of the residual trap, discussed in section 4.2.3. These measurements have proven that also Penning traps with depths below 200 V can ignite, given the required potential distribution. However, the residual trap, identified to be geometrically located at the end of the APE, can be controlled as will be shown in this chapter. The stability of the pre-spectrometer system with electrostatic potentials and magnetic fields being applied in parallel is investigated in a set of measurements. The results show that, while the system is stable at lower magnetic fields (B<1.72 T), the situation changes with magnetic fields exceeding a critical value: a new background component is generated with characteristics which clearly distinguish this new process from the residual Penning trap at the APE. An extensive measurement programme to further elucidate these processes was carried out. The results are presented starting off with a discussion of the pre-spectrometer background as measured with the silicon PIN detector when no Penning trap ignition has been observed. In a second step, a new background mechanism arising at magnetic field strengths exceeding 2 T is analyzed. This comprises a discussion of its characteristic behaviour with regard to changes in magnetic fields strength, pressure and electric potential values, as well as to changes due to the potential distribution. Included therein is a discussion of a background component originating at the e-gun which is also connected to the background process at high magnetic fields. The chapter is concluded with a review of the analyses results culminating in a recommendation for a second change of the inner electrode set-up.

5.1 Background investigation without active Penning trap at magnetic fields smaller than 2 T

Before taking an in-depth look at the residual Penning trap characteristics, the background behaviour of the pre-spectrometer without ignited Penning trap is presented.

5.1.1 Potential dependence

In a first test, the background of the pre-spectrometer is investigated with active magnetic fields and the result is compared to the detector background as measured in stand-alone mode before attachment of the detector chamber to the pre-spectrometer, see table 5.1. Applying the same cut which removes events with a time difference smaller than 0.3 ms yields the same result as the stand-alone measurement. This clearly shows that the magnetic shielding is working and that secondary electrons which are released from the inner vessel walls by cosmic rays cannot enter the flux tube easily and that ionisation of residual gas molecules is strongly suppressed by the excellent UHV conditions.

Once the pre-spectrometer is elevated to a negative potential, the energy spectrum changes. Apart from low-energy noise, which is not completely cut-off intentionally to not limit the detectable energy range, and higher energy events caused by

[1] Elog 336. For KATRIN-internal use, entries in the pre-spectrometer task's electronic logbook dealing with the subject are referenced.

[2] The potential for the different electrode parts are denoted as follows: pre-spectrometer vessel: U_{vessel}, inner electrode: U_{ie}, west cone electrode: U_{wc}, east cone electrode: U_{ec}, wire electrode: U_{wire}. U_0 is used if several electrode parts are linked together and are supplied by one power supply.

Table 5.1: Potential dependence of the pre-spectrometer background for different values ΔU in the region of interest of 15-22 keV. Applying high voltage to the vessel (U_{vessel}), and the inner electrode (U_{ie}) changes the background rate. The stand-alone set-up denotes a measurement carried out with the detector chamber not attached to the pre-spectrometer. The other measurements have been done with the SPD moved into the magnet at z=-2.28 m position, thus measuring the background of the spectrometer. In the case of equal potentials of inner electrode and spectrometer vessel only one power supply has been used.[1]

Run #	set-up	time	z [m]	B [T]	U_{ie}/U_{vessel} [kV]	R_{ROI} [Hz]
	stand-alone	15 h	-2.28	0	0 / 0	0.0203±0.0006
401ff	pre-spec	12 h	-2.28	1.72	0 / 0	0.0202±0.0006
334f	pre-spec	14 h	-2.28	1.72	-18.0 / -18.0	1.365±0.005
349f	pre-spec	15 h	-2.28	1.72	-18.3 / -18.0	0.951±0.004
48	pre-spec	10 min	-2.29	1.72	-19.0 / -18.6	7.2±0.2
47	pre-spec	10 min	-2.29	1.72	-19.0 /-18.0	15.3±0.2

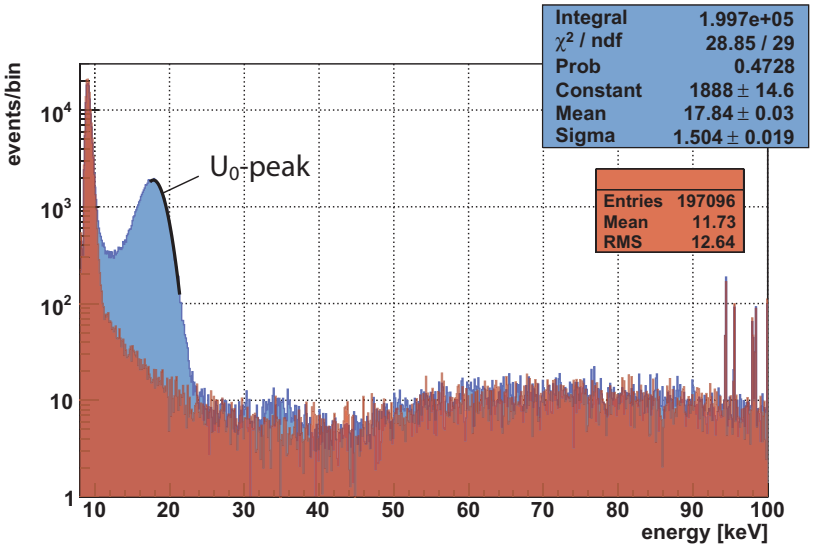

Figure 5.1: Background energy spectra comparison for B=1.72 T and U_0(red)=0 (Run 401ff) and U_0(blue)=-18 kV (Run 334f)[2]. After activation of the electrostatic field a peak at U_0 appears with a small contribution in a second order pile-up peak. The peak location is determined with a Gaussian fit. Only the right slope and the peak tip are taken into account as the left slope includes contributions from backscattered electrons and thus deviates from a pure Gaussian distribution.

minimum ionising particles[3], e.g. muons, a peak at vessel potential, referred to as U_0-peak[4] arises. This is shown in fig. 5.1, where energy spectra with and without electrodes elevated to a negative potential are shown. The background rate in the ROI is increasing by a factor 60 (see table 5.1). After elevating the inner electrode to a more negative potential, the rate decreases somewhat, corresponding to a rise factor 40 as compared to background at zero potential. This implies that the inner electrode's shielding properties take effect. A further increase of the potential difference between vessel and the more negative inner electrode causes the rate to not decrease further but to rise again. Looking at the spatial distribution of the background rate for $|\Delta U| = 1$ kV, fig. 5.2, an increase in pixels H1-4 and multiple pixels in the A, B and C rows appears, resulting in a spot-like pattern.

Investigating the potential dependence, while keeping the potential difference between vessel and inner electrode constant, yields an increase in rate if a more negative potential is applied, see table 5.2, with the exception of the measurement point at $U_{vessel} = -20$ kV. This measurement point features an excess rate which is higher

[3]Simulations of the background from minimum ionising particles carried out in [Sch04] identify the contribution maximum at 100-110 keV for a 300 μm thick silicon detector. With the SPD's wafer of 200 μm thickness, the peak is expected around 70±4 keV which is in good agreement with the measurement, see fig. 5.1

[4]The U_0-peak denotes the Gaussian peak created by electrons accelerated by the potential applied to either the vacuum vessel, the inner electrode or a distinctive part of the latter.

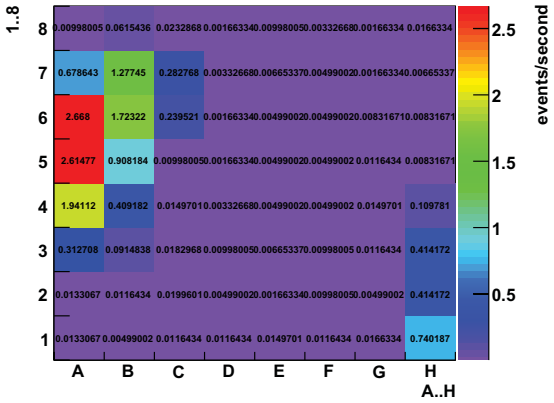

Figure 5.2: Spatially asymmetric distribution of the rate for a configuration with a more negative inner electrode (Run 47). Lowering the potential of the inner electrode creates an asymmetrical distribution of the rate with a hot spot around detector elements A5, A6 and another one located at H1-4. Parameters: U_{vessel}=-18 kV, U_{ie}=-19 kV, B=1.72 T, detector position (x,y,z)=(0,0,-2.29) cm.

than the subsequent measurements with more negative potentials.

5.1.2 Magnetic field dependence

As a next step, the magnetic field dependence of the background rate with constant and uniform potential distribution was tested. Starting at zero magnetic fields[5], the rate is already in the kHz range when the detector is still in maintenance position at z=-2.7 m. Ramping up the magnetic field, the rate is at first falling steeply, but after

[5]To really measure at zero magnetic fields the magnets have to be warmed up for a short time to dissipate the residual magnetic field, which remains present even when the coil current is ramped down to zero.

Table 5.2: Potential dependence for constant ΔU. Measurement parameter: B=1.29 T, z=-2.43 m, time difference cut: 0.3 ms. Elog 342

Run #	U_{wire} [kV]	$U_{vessel\&coni}$ [kV]	R_{all} [Hz]	R_{ROI} [Hz]
9	-13.5	-13	2.7 ± 0.1	-
11	-16.5	-16	3.3 ± 0.1	0.6 ± 0.1
12	-18.5	-18	4.5 ± 0.2	1.0 ± 0.1
14	-20.5	-20	12.3 ± 0.3	3.4 ± 0.1
16	-22.5	-22	8.8 ± 0.2	1.8 ± 0.1
18	-24.5	-24	14.2 ± 0.3	3.2 ± 0.1

exceeding a value B=0.14 T it keeps constant and is independent of the magnetic field even when the field strength is increased further, see table 5.3. Interestingly, the spatial distribution of the rate changes from a distinctive ring structure for low magnetic fields to an asymmetric one starting at B=0.29 T, compare figs. 5.3(a),(b). For a perfect MAC-E filter one would expect the rate to go down to detector background level of ∼20 mHz. This is however not the case. The rate reaches a stable value at B=0.14 T and only by further ramping up the magnetic field to 1.72 T one is able to decrease the rate to 1.1 Hz. The cause for the elevation of the background has been found to originate in the hot ionisation vacuum gauge utilised at the pre-spectrometer. The effect is discussed in the following section 5.1.3. Later measurements determined the remaining background level to be lower by a factor 3, which however is still significantly higher than the intrinsic detector background.

5.1.3 Production mechanism for U_0-peak

The generic processes responsible for the production of the energy peak in the ROI are not completely understood. Electrons released from the vessel walls are repelled by the magnetic shielding effect and thus are not able to enter the flux tube easily. Measurement results presented in table 5.3 at low magnetic fields prove that magnetic fields as low as 0.14 T sufficiently shield the flux tube from charged particles. The excessive rate at 0.03 T is caused by a hot cathode ionisation (Extraktor) gauge installed in the 45° pump port, which produced electrons and positive ions. The electrons cannot enter the flux tube but are repelled by the negative electrode potential. Positive ions, however, are able to traverse the wire mesh and move through the flux tube perpendicularly to the magnetic field lines. A fraction of these ions hits the full metal coni of the inner electrode. Because of the low magnetic field, some of the secondary electrons released by the ion's impact reach the detector. Tracking

Table 5.3: Magnetic field strength dependence of the pre-spectrometer background rate in the region of interest from 15-22 keV. Measurement parameters: B=0.86 T, U_0=-18 kV, z=-2.28 m.

Run #	B [T]	R [Hz]
96	0.03	3181 ± 2
97	0.06	32.1 ± 0.2
98	0.09	2.7 ± 0.07
99	0.14	1.9 ± 0.03
100	0.29	1.9 ± 0.03
101	0.57	1.8 ± 0.02
102	0.86	1.7 ± 0.03
103	1.72	1.1 ± 0.03
104	2.15	1.0 ± 0.03

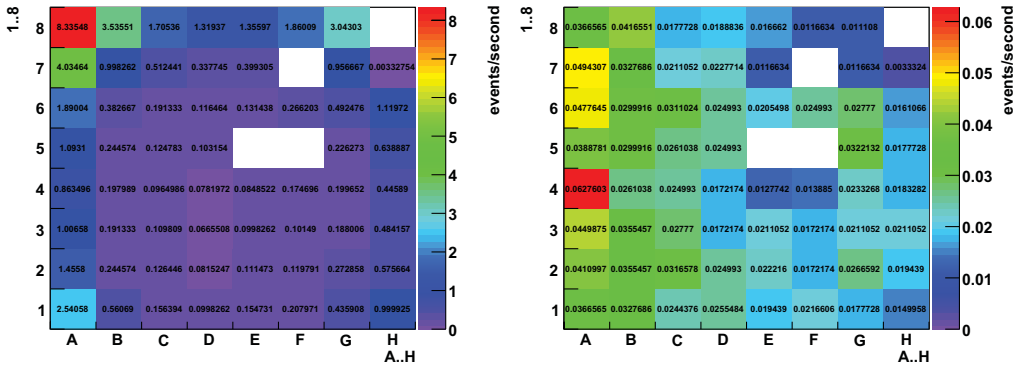

(a) Ring-like distribution: B<0.29 T (Run 97) (b) Asymmetric distribution: B>0.29 T (Run 103)

Figure 5.3: Spatial distribution of the background rate for magnetic fields $\lesssim$0.29 T. The distribution of the rate as shown by the pixel chessboard changes from a ring-like distribution (a) to an asymmetric distribution (b) as soon as the magnetic shielding takes effect.

simulations of the ion trace to prove this assumption are planned for the near future, once more extensive computer infrastructure is available. This explanation gives an ansatz to understand the production mechanism in the case of an effective magnetic shielding being in place. For higher magnetic fields, primary electrons from the hot ionisation vacuum gauge as well as secondary electrons resulting from the ion impact at the electrode coni cannot enter the flux tube and thus are not the source of the U_0-peak. The place of production has to be located inside the flux tube. Another product of the vacuum gauge are UV photons. These photons possess sufficient energy (>15 eV) to ionise residual gas molecules. When this happens inside the flux tube, the electrons produced are accelerated by the electric field and guided along the magnetic field lines to the detector, where they are registered with an energy of approximately $e \cdot U_0$. This explanation is strongly supported by a separate measurement testing the Extraktor gauge influence by turning the gauge off and comparing the energy spectrum with measurements where the vacuum gauge was activated. The energy spectra are presented in figs. 5.4(a),(b), demonstrating that the U_0-peak has disappeared. The only other parameter differing in this specific measurement, besides the status of the vacuum gauge, is the potential distribution. However, this has been shown to not influence the presence of the U_0-peak. This is confirmed in another measurement at B=0.86 T and $U_0 = -18$ kV. In the light of these results, there is no doubt of the Extraktor gauge's strong influence on the energy spectrum.

While the source of the U_0-peak is identified, this is not true for the intrinsic production mechanism creating the secondary particles which are finally counted by the detector.

The geometric distribution for events in the energy region of interest around the U_0-peak as visualised by the pixel chessboard is clearly asymmetric (fig. 5.5(a)). The

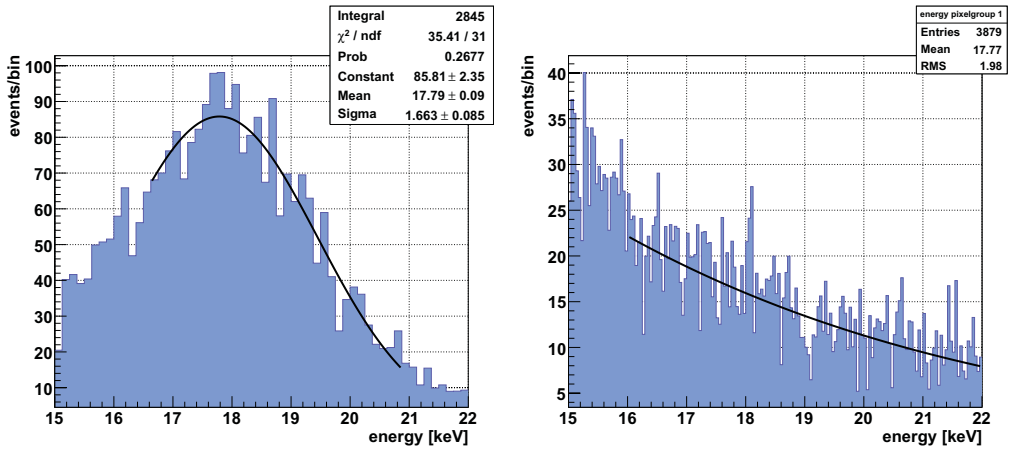

(a) Active hot cathode vacuum gauge (Run 298ff)(b) Inactive hot cathode vacuum gauge (Run 797ff)

Figure 5.4: Background comparison with and without activated hot cathode ionisation vacuum gauge in the ROI of [-15,-22] keV. The influence of the hot ionisation gauge is clearly observed for low magnetic fields, but at higher magnetic fields of 1.72 T and even beyond the effects are detected as an U_0-peak in the energy spectrum. Shutting off the vacuum gauge eliminates the peak at E=e·U_0. Parameters: U_{298}=-18 kV, U_{797}=-18.3/-18 kV, B=1.72 T, detector in maintenance position.

rate is high in the upper right side of the detector as viewed from inside the vessel and decreases to the lower left side (refer to fig. 3.42 for a better understanding of the detector orientation in the x-y-plane). It is important to note that the asymmetric distribution can only be found in the corresponding energy interval from [-15,-22] keV for a U_0-peak at 18 keV. The low-energy noise shows an increase in rate at the beamline with a radius r≈1 cm (z=-2.28 m), while high-energy events are uniformly distributed. This distribution of the rate cannot be explained within the theory of photon induced ionisation inside the flux tube, as in this case a uniform distribution is expected. The higher energy events (>50 keV) can be attributed to the ionisation of residual gas molecules by cosmic rays. Accordingly, the corresponding distribution is uniform with the exception of the corner pixels, which show a rate twice as high (fig. 5.5(b)). This could be hinting at a ring-like increase in rate with a minimum radius in the range of 5.5 cm, see fig. 5.5(b). These results clearly show the importance of covering the entire flux tube at any time.

Electrons released out of the inner vessel hull by minimum ionising particles in general do not penetrate the magnetic shield. Simulation results [Glü05] demonstrate that electrons in symmetric magnetic and electrostatic fields do not have a radial motion component, moreover this fact is independent of non-adiabatic guiding of the electrons. Also diffusion of the electrons into the flux tube via collisions is not possible either. However, under the assumption of a non-axisymmetrical system with regard to magnetic and electrostatic fields, electrons released from the inner vessel wall can enter the flux tube. These asymmetries create a magnetron drift giving the

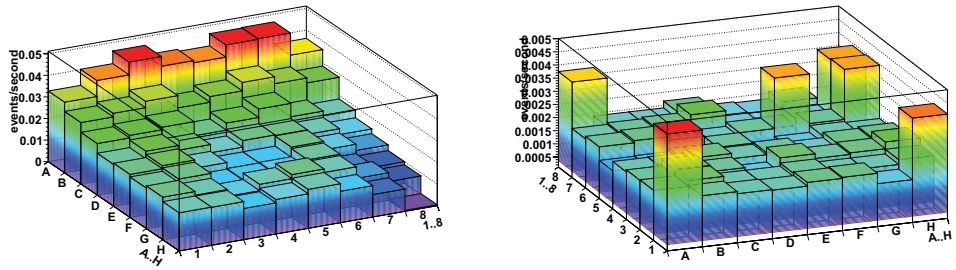

(a) asymmetric distribution at U_0 (15-22 keV)

(b) symmetric distribution for higher energy events (30-100 keV)

Figure 5.5: Spatial distribution of the background rate for different energy intervals (Run 349f). (a) U_0=18 keV (ROI 15-22 keV), asymmetric distribution (b) higher energetic events (30-100 keV), symmetric distribution eventually hinting at a ring-like structure for larger radii. Parameters: U_{vessel}=U_{ie}=-18 kV, B=1.72 T, detector position (x,y,z)=(-1.1,-0.35,-2.28) cm.

electrons a radial component which allows low-energy electrons to penetrate deeply into the flux tube. However, this process cannot generate as many electrons as have been observed in the U_0-peak by cosmic rays alone. It is far more likely that the hot cathode ionisation gauge generates enough electrons that pass the magnetic and electrostatic barrier ultimately causing the increase in rate at energies e·U_0.

A measurement at -18 kV and B=1.29 T intended to test the shielding effects of the wire electrode and of the coni has following supporting results: when the wire electrode is elevated to a 500 V more negative potential this results in a lower event rate (1.37 ± 0.09 Hz, z=-2.43 m) as compared to a 500 V more positive potential (1.57 ± 0.09 Hz, z=-2.43 m). According to this observation, the shielding of the wire electrode seems to be more important (repelling electrons from the hull) than the shielding of the coni (repelling electrons produced in the flux tube at wire electrode potential). This is in agreement with the theory and the explanations presented above.

5.1.4 Negative ion peak

If the threshold values of the DAQ electronic's discriminator are lowered a new background component extending to lower energies is visible. This is only partially due to noise in the electronics or low-energy gammas from cosmic rays. The energy spectra with both magnetic field and potential applied show an increase in low energetic events well below the U_0-peak. This new feature can be either more pronounced or subdued depending on the measurement parameters. In general, it has a much higher event count as can be expected from low-energy noise. In particular, if the U_0-peak is shifted to higher energies, a second peak starts to rise from the low-energy tail, see fig. 5.6. If the potential is varied, the energy difference between U_0-peak

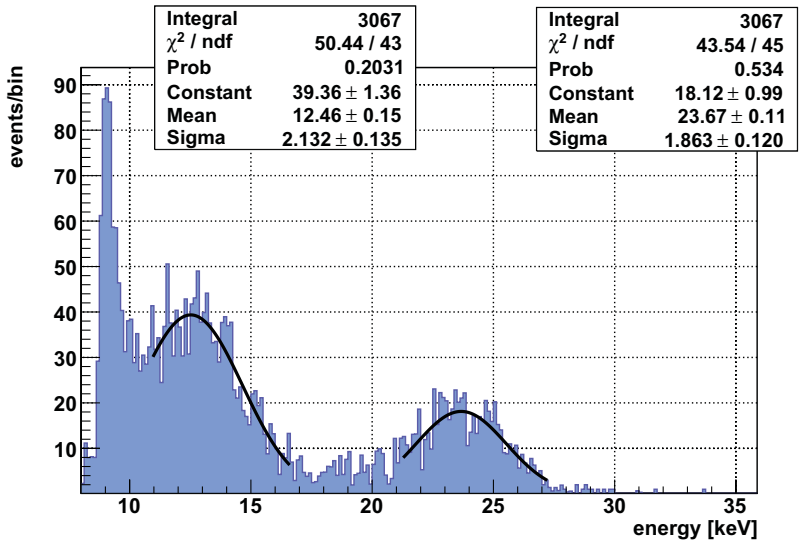

Figure 5.6: Negative ion and U_0-peak (Run 18/071220). The observed increase at lower energies corresponds to a peak consistent with the theory of being created by negative ion detection. Parameters: U_0=-24 kV, U_{wire}=-24.5 kV, B=1.29 T, detector position (x,y,z)=(0,0,-2.43) cm.

and the second peak is always a constant offset of 11 keV for $U_{ie} = -24.5$ keV, which rises slightly to 11.8 keV for $U_{ie} = -30.5$ keV, see table 5.4.

A similar peak has been witnessed in the early stages of the Mainz experiment [Pic90]. Using a small transverse magnet field in front of the Mainz detector, the U_0-peak vanished while the peak at approx. $2/3U_0$ persisted. After installing a thin Kapton film (30 μg/cm^3) in front of the detector, which is transparent for electrons, the U_0-peak was detected but the smaller peak completely vanished. The U_0-peak has been attributed to electrons created in the spectrometer via ionisation of residual gas molecules. The second peak is supposed to be caused by negative ions created by residual gas molecules' accretion of low-energy electrons of ∼0.1-10 eV or by positive ion impact on the electrodes on negative potential. The lower energy of the second peak can be explained by the energy loss of the H^- ion in the detector's dead layer.

Simulations using the software SRIM 2008 [Zie08] support this theory, assigning for a -30 keV ion an energy loss of ∼12 keV for zero impact angle in a 110 nm silicon dead layer (fig. 5.7), which is in good agreement with the experimental results.

5.1.4.1 Characteristics of the ion peak

In contrast to the Mainz experiment, the ion peak observed here is not limited to magnetic fields larger than 2 T but can be observed down to at least B=0.086 T. Similar to the U_0-peak, it has no defined threshold potential where the production mechanism stops or starts. The constant energy offset between the two peaks implies that ion and U_0-peaks are interconnected and created by the same production

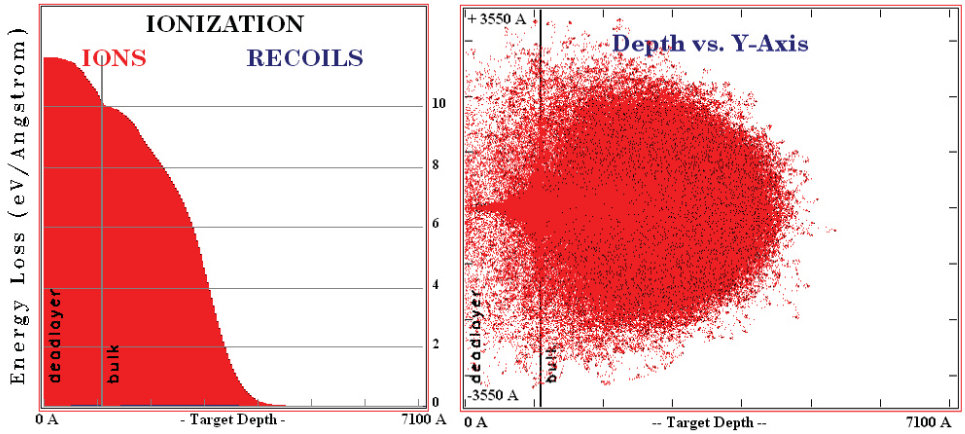

Figure 5.7: Simulation of ionisation energy loss for H^- ions in silicon.
Left: Shown are the energy losses differentiated into a 110 nm dead layer and the detector bulk material. An average energy loss of 12 keV for a -30 keV H^- ion is found for an impact angle of 0°.
Right: Penetration depth and ion tracks in silicon for a -30 keV H^- ion. The Simulation routine and plots are taken from [Zie08].

mechanism. However, the variable amplitude of the peaks in relation to each may be a result of a different transport mechanism for both background classes.

In figure 5.8 for B=0.086 T and z=-2.43 m, U_0 and ion peak are compared for two different potential settings. The run with a more positive potential featured an increase in the ion peak and a decrease in the U_0-peak, as compared to a measurement where the wire electrode is more negative. At higher magnetic fields of B=1.29 T, this is not witnessed anymore. With the wire electrode being more positive than both vessel and coni of the inner electrode, the probability for low-energy electrons passing into the spectrometer volume increases. In this case, some are accreted by residual gas molecules and the resulting negative ion is accelerated by the potential in direction of the detector.

Table 5.4: Negative ion peak energy as compared to U_0-peak energy.

Run #	U_{ie}/U_{vessel} [kV]	ion peak [keV]	U_0-peak [keV]	ΔU [keV]
974	-18.5 / -18		17.66 ± 0.03	
975	-20.5 / -20		19.45 ± 0.03	
976	-22.5 / -22	10.69 ± 0.16	21.29 ± 0.02	10.6
977	-24.5 / -24	12.20 ± 0	23.25 ± 0.02	11.1
978	-26.5 / -26	13.76 ± 0.03	25.08 ± 0.02	11.3
979	-28.5 / -28	15.58 ± 0.02	27.03 ± 0.02	11.5
980	-30.5 / -30	17.24 ± 0.02	29.01 ± 0.01	11.8

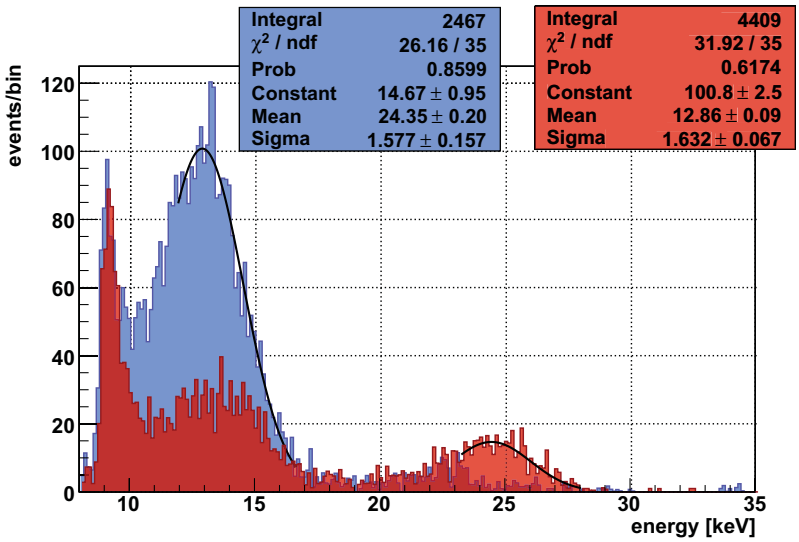

Figure 5.8: Comparison of the ion peak height (Run 27f/071220) for two opposing configurations of the wire electrode potential being more positive (blue) or more negative (red). Parameters: U_0=-24 kV, U_{wire}=U_0±0.5 kV, B=0.086 T, detector position (x,y,z)=(0,0,-2.43) cm.

Another supporting measurement also shows that at low magnetic fields (B<0.86T) the fraction of low-energy events caused by negative ions increases above average. At values B∼0.29 T, the safety device of the detector regularly shuts the SPD electronics down, although the rate has increased only slightly and is well below critical kHz range. This might be connected to an overload caused by negative ions below the detection threshold, affecting the read-out electronics which leads to a higher current consumption and thus to the observed shut-down.

Moreover, a dependence of the detector z-position is observed which is most visible for strong magnetic fields of 4.5 T. In the maintenance position (z=-2.7 m) the ion event fraction visible as low-energy tail is more pronounced as the U_0-peak. By retracting the detector out of the magnet bore, the flux tube part which is observed by the detector is reduced from 27.3% at z=-2.28 m by almost one order of magnitude down to 3.5% at z=-2.7 m. As a result, the outer pixel of the SPD do not detect the ring structure anymore but display only the inner area with a uniform distribution of the rate. While events of energy e·U_0 dominate in the ring structure, the inner area of the flux tube events is predominantly populated by negative ions.

5.1.5 Conclusion

The investigation of the background shows that in case of simultaneous activation of magnetic and electric fields a new background component is started which creates a Gaussian peak at E=e·U_0. Further tests indicate that the shielding capacity of the inner electrode reduces the rate coming from this background process to some

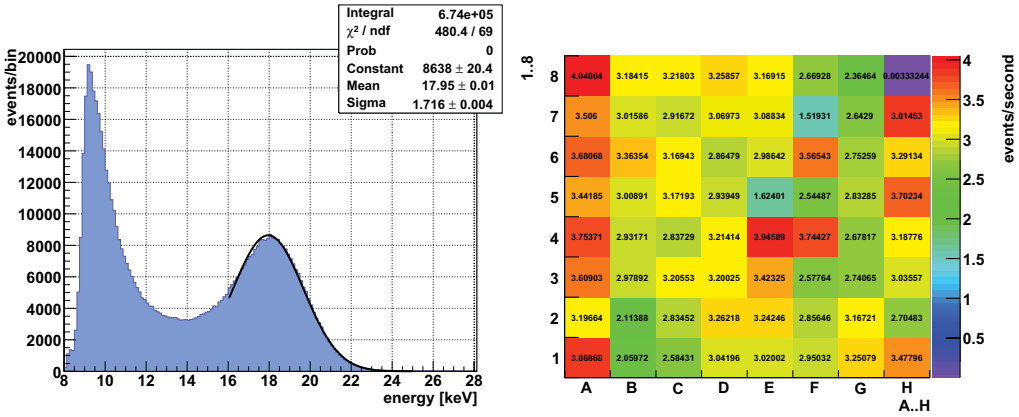

(a) Energy spectrum with large fraction of negative ion events at z=-2.7 m

(b) Symmetric distribution of the rate at z=-2.7 m

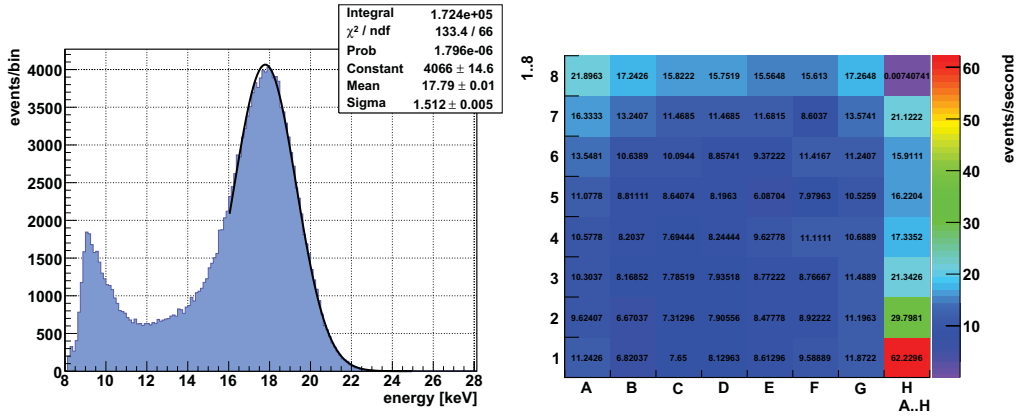

(c) Energy spectrum with dominating U_0-peak at z=-2.28 m

(d) Ring-like distribution of the rate at z=-2.28 m

Figure 5.9: Z-position dependence of background rate (Run 204/206). At z-positions far from the magnet the detector registers events with smaller radius around the centre axis. The spatial distribution of the rate develops a ring-like structure for higher radii. The ring structure is caused by events with energies in the range of e·U_0. In the inner circle, U_0-events are suppressed as compared to negative ion events.

extent but not completely. Switching off the Extraktor vacuum gauge eliminates this U_0-peak, proving that positive ions and maybe also photons coming from the vacuum gauge are the source for the background elevation. In the meantime, the vacuum gauge has been relocated to a different position to prevent UV photons and ions to reach the pre-spectrometer volume.

Elevating the inner electrode to a more negative potential as the vessel with $\Delta U >$ 0.5 kV causes the rate to rise in only some pixels creating two hot spots, a radial distribution is no further visible.

The spatial distribution of the rate, as visualised by the pixels of the segmented PIN diode, changes depending on the settings of the magnetic field, the potential distribution and the energy interval. An asymmetric distribution corresponds to the U_0-peak, contradicting as outlined above the UV-light hypothesis as dominant source for the peak.

The magnetic shielding effect has been found to take effect at B=0.06 T and reaching nearly 100% efficiency at 0.14 T. Increasing the field strength any further has only a limited shielding effect. The background rate is independent of the magnetic field between 0.14 T and 0.86 T, at higher magnetic fields the full shielding effect is achieved.

To summarise the results, several background components have been identified, however, the details of the generic production and transport mechanisms are not completely understood at the present moment due to the limited access to large-scale computing infrastructure.

5.2 Characterisation of the residual Penning trap

According to the information presented in section 4.2.3, a residual Penning trap with a rather shallow depth of ∼200 V is present in the pre-spectrometer located at the end of the APE, for configurations when vessel and inner electrode are elevated to equal potential. As the potential influence of such a trap cannot be predicted from simulations, it was investigated by a set of measurements. Elevating both vessel and electrode to -18 kV by using FUG4 as the only power supply, no increase in rate was registered. However, once the electrode and vessel are supplied with different power supplies to test the electrostatic shielding of the inner electrode, a large exponential increase in rate is measured, see fig. 5.10. To test the hypothesis that this increase was caused by the ignition of the anticipated Penning trap, the inner electrode was lowered to -18.5 kV. According to simulations in reference [Val09], the residual Penning trap should be eliminated completely by this measure. This is verified by the measurement: the rate abruptly decreases back to background level as illustrated in fig. 5.10 at time t=2550 s. This is a clear indication not only for the existence of a Penning trap, but even more so for a Penning trap located in the region between the APE and the coni of the inner electrode.

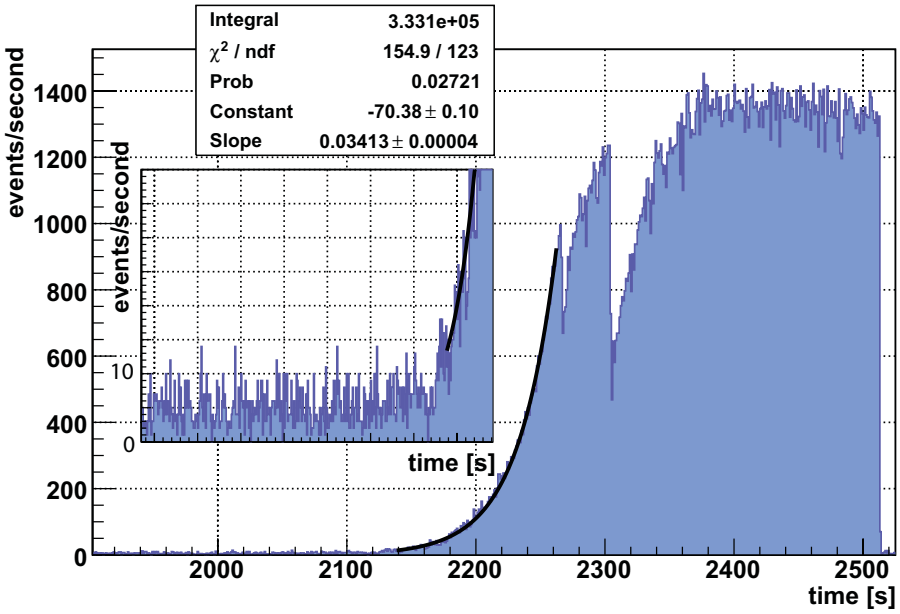

Figure 5.10: Penning rap ignition time and corresponding increase in background rate (Run 150) for B=1.72 T, z=-2.28 m and U_{vessel} =U_{ie} =-18 kV. A 200 V deep Penning trap ignites when the inner electrode and vessel are powered by two different power supplies. After an ignition time interval t_{ig}=6 min, the rate increases exponentially. During the rise time two major breakdowns occurred caused by instabilities in the trapping mechanism. However, the trap is stable enough to reach a constant rate of ∼1350 Hz. Elevating the inner electrode to a more negative potential of -18.5 kV at t=2550 s quenches the trap.

5.2.1 Time dependency of the Penning trap ignition

Additional evidence that the observed behaviour is caused by a Penning trap can be gathered by analysing the time response. The increase of the rate is not instantaneous, the time interval depends on both electric potential and magnetic field strength as well as the prevailing pressure value. The magnetic field strength seems to be the dominant factor: for 1.72 T the rate increases after approx. 4 min, whereas for 0.86 T the increase starts only after 12 min. Furthermore, the ignition time also depends on the measurement history. After quenching the trap by elevating the inner electrode to a more negative potential the trap does not restart immediately when the potentials of the vessel and electrode are matched again. Once again, it takes a finite amount of time t_{ig} until the trap restarts. However, the time is considerably shorter, with a time of 6 min instead of 12 min for B=0.86 T. Due to the complex nature of the dependencies a more detailed investigation of the ignition time is unlikely to reveal additional information and has therefore not been pursued.

During the critical phase of exponential rise in rate one almost always observes one

or several abrupt breakdowns in rate. These drops in rate hint at instabilities in the initial stage of starting a Penning discharge. The positive ions created by the ionisation of the residual gas molecules caused by the trapped electrons are not stored but immediately drawn to the cathode. This leads to the formation of a non-neutral plasma. The electrons with axial, cyclotron and magnetron motion can also gain a radial movement component: small fluctuations in the electric field generate an E×B drift [Glü09a]. If the magnetic field is sufficiently small, the electrons may move out of the trap and are lost for the discharge process. If this happens in increasing numbers the discharge is interrupted, as demonstrated in fig. 5.10. However, the discharge process is stable enough to recover and once it reaches its maximum strength, no further drops in rate are observed anymore. Then, the electron production mechanism is able to balance any potential losses and keeps the rate stable.

5.2.2 Magnetic and potential dependence

The detected rate is also anti-correlated with the magnetic field strength. At B=0.86 T in combination with a potential U_0=-18 kV which is applied to vessel and inner electrode, the maximum rate for a detector position of z=-2.28 m[6] is 2250 Hz. At a higher value B=1.72 T, the rate peaks already at a maximum of 1350 Hz.

If, on the other hand, the magnetic field is kept constant, one registers that the Penning trap also depends on the potential. In this case, the rate is directly influenced by the depth of the Penning trap and thus the potential distribution. Lowering for example for the configuration described above the potential of the inner electrode by 100 V to U_{ie}=-18.1 kV, the rate decreases in the case of B=0.86 T from 2250 Hz to 2100 Hz. At U_{ie}=-18.2 kV a second decrease to 270 Hz is measured. At $U_{ie} \leq$-18.3 kV the trap is finally quenched, normal vacuum conditions of 10^{-10} mbar presumed.

5.2.3 Spatial distribution of the rate in the detector segments

The distribution of the background rate viewed over all 63 pixels[7] deviates from the normal background distribution for both potential distributions. Quenching of the trap by putting the inner electrode to a more negative potential forms an asymmetric distribution of the rate, see fig. 5.11. Pixel H8 and to some extent H7 feature an increased count rate. The energy spectra of all pixels exhibit a peak at the energy

[6] At z=-2.7 m, the maintenance position, the detector is located 55 cm outside of the middle of the superconducting coil at B=0.42 T, at maximum translation z=-2.27 m the magnetic field strength is B=3.78 T, see also fig. 3.21

[7] Pixel H8 has been damaged and is not producing meaningful signals anymore. Exchanging the pre-amplifier board had no positive effect. It seems that the error is connected to the JFET stage or the wafer itself, as the first problem with pixel H8 has been noticed after a large rate over 20 kHz hit the detector. The signal feedthroughs have been tested and can be ruled out as the source of the problem.

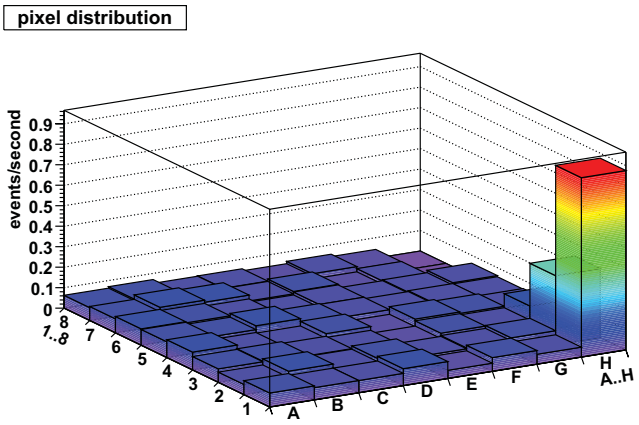

Figure 5.11: Asymmetric distribution of the rate for a quenched Penning trap (Run 150). Parameters: U_{vessel}=-18 kV, U_{ie}=-18.5 kV, B=1.72 T, detector position (x,y,z)=(-1.1,-0.35,-228) cm.

of the inner electrode voltage $U_0=U_{ie}$=-18.5 kV. When comparing the measurement parameters of figs. 5.11 and 5.2 one expects the same kind of spatial distribution. While the excess in the H row pixels is similar in both cases, the excess in the A and B rows is missing. This can be explained with the translation of the detector in negative x and y direction causing an increase in the signal-to-background fraction in the H-row pixels and dislocating the other hot spot away from the pixel chessboard.

On the other hand, while the Penning trap is active, a ring is visible on the detector pixel chessboard, see fig. 5.12(a). The centre of the ring is identified as the middle of the pre-spectrometer, in this case represented by pixel D3. The diameter of the ring strongly depends on the magnetic field strength. Measuring at B=0.86 T, the ring contracts to a diameter of roughly 2 cm at the detector position z=-2.28 m (fig. 5.12(b)). On the inside of the ring, the rate decreases by a factor of four as compared to the ring wall and a factor of three as compared to the outer pixels' rate. The energies of the three different pixel groups vary slightly: ∼16.8 keV for the inner pixels, ∼16.0 keV for the ring-pixels and ∼16.4 keV for the outer pixels, while the electrode potential is U_0=-18 kV. In this case, the magnetic field lines passing the sensitive detector area are only connected to parts on ground potential, e.g. the focussing lens of the e-gun system. Therefore, electrons detected by the SPD have to be created in the vacuum inside the flux tube or some transport mechanism has to move electrons originating from the electrodes on negative potential or from an active Penning trap into the detector flux tube.

Before further discussing the origin of the pixel ring, it is necessary to investigate the corresponding energy spectra in more detail.

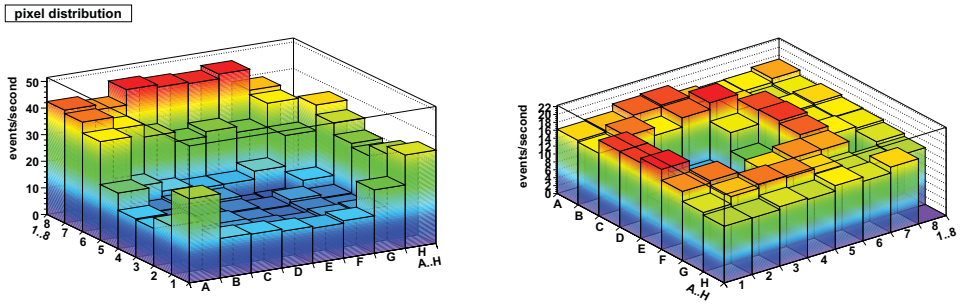

(a) Active Penning trap at B=1.72 T (Run 150)

(b) Active Penning trap at B=0.86 T (Run 177)

Figure 5.12: Spatial distribution of the background rate for an active Penning trap at different B-field strengths. The typical ring structure observed for an activated Penning trap depends in size on the magnetic field strengths. With increasing B-field the diameter of the ring widens. Parameters: U_{vessel}=-18 kV, U_{ie}=-18.5/-18 kV, detector position (x,y,z)=(-1.1,-0.35,-228) cm.

5.2.4 Energy U_0-peak shift

Once the Penning trap is activated, the Gaussian shaped energy peak shifts to lower values as shown in figs. 5.13(a),(b). Moreover, the energy shift is proportional to the magnetic field strength.

Interestingly, the U_0-peaks also feature a small offset with regard to the electrode potential owing to the higher dead layer losses of electrons with larger transversal energy component, see section 5.3.4. On the other hand, the shift of the peak with activated Penning trap is much stronger. This leads to the conclusion that the events have to be generated by secondary electrons. While this does not yield more information with regard to the primary production mechanism, it allows to pin down the place of production of the secondary electrons inside the flux tube. This is made possible by the spatial distribution of the rate with its characteristic ring structure, especially for the B=0.86 T measurements when the ring-pixels are clearly distinguishable from the inner and outer pixels (fig. 5.12(b)). The magnetic field lines pertaining to the maximum and minimum location on the x- or y-axis are plotted in figure 5.14. In a second step, the place of secondary electron production along the z-axis is determined by using the information gained from the peak shift, also taking into account the shift due to the magnetic field at the detector position. From the figure the electric potential along the magnetic field lines connected to the ring can also be determined and thus the z-location of the secondary electron production, as marked in the graph showing the potential as a function of the z-value. Irrespective of the exact energy shift value, the location is confined to a small space on the z-axis as shown by the coloured bars in the pre-spectrometer view. At this z-value, the end of the Anti-Penning electrode is reached and thus the location where the Penning trap is expected to be.

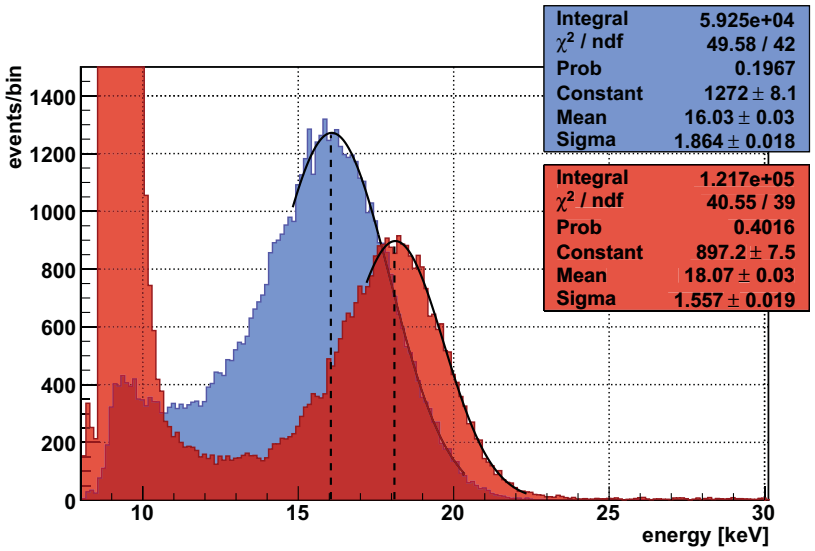

(a) Peak shift for B=1.72 T (Run 186/349)

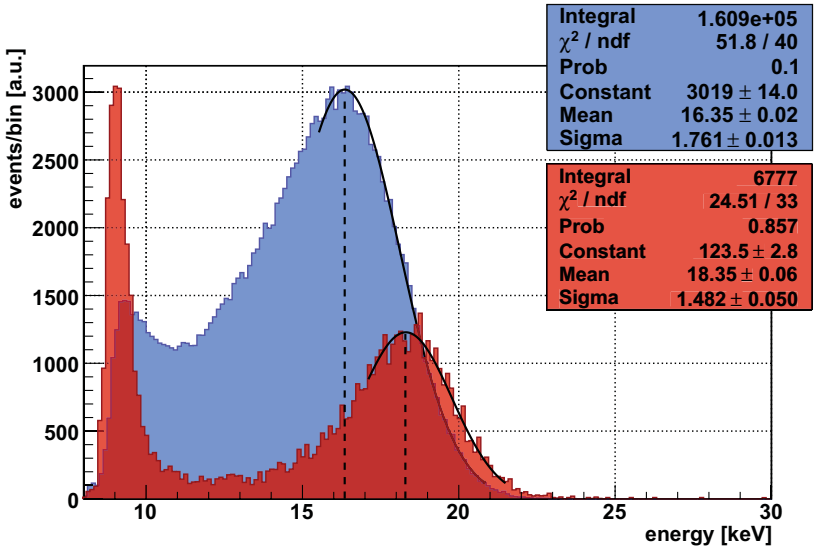

(b) Peak shift for B=0.86 T (Run 177)

Figure 5.13: Energy shift of the background peak after activation of a Penning trap for B=1.72 T and B=0.86 T and vessel potential U_{vessel}=18 kV at z=-2.28 m. The peaks in red are the U_0-peaks when the Penning trap is quenched. A Gaussian fit determines the energy to be in good agreement with the potential (a) $U_{0,off}$=18.3 kV (b) $U_{0,off}$=18.5 kV applied to the inner electrode. The peaks in blue are the shifted energy peaks during the phase of an activated Penning trap. The actual energy shift is not the difference between red and blue peak as $U_{0,on}$ = 18.0 kV.

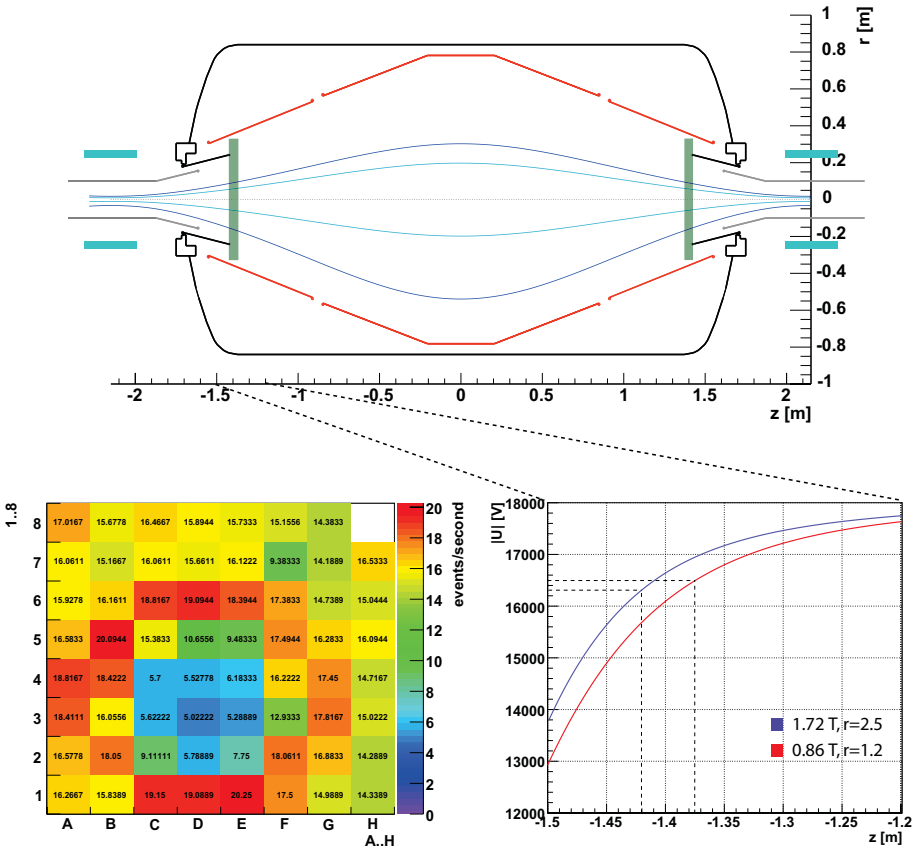

Figure 5.14: Determination of the place of production of secondary electrons by Penning traps. Starting from the observed ring structure as a result of an active Penning trap, the magnetic field lines connecting to the ring pixels are plotted. With the shift of the peak energy from figs. 5.13(a),(b) the z-location of the secondary electron production in the flux tube can be deduced of the potential distribution along the corresponding magnetic field line.
Figure (a): Flux tubes for the detector ($r=^{+2.0}_{-3.4}$ cm around centre axis) and for the ring pixels ($r=\pm 1.2$ cm around centre axis). The latter are symmetrically arranged around the centre field line. The bars at $|z|=[1.38,1.42]$ cm indicate the place of secondary electron production.
Figure (b,left): The spatial distribution of the rate for B=0.86 T is shown exemplarily. A ring diameter of 1.2 cm is used for the calculation.
Figure (b,right): Electric potential along the magnetic field lines connecting to the ring pixel for B=0.86 T and B=1.72 T.

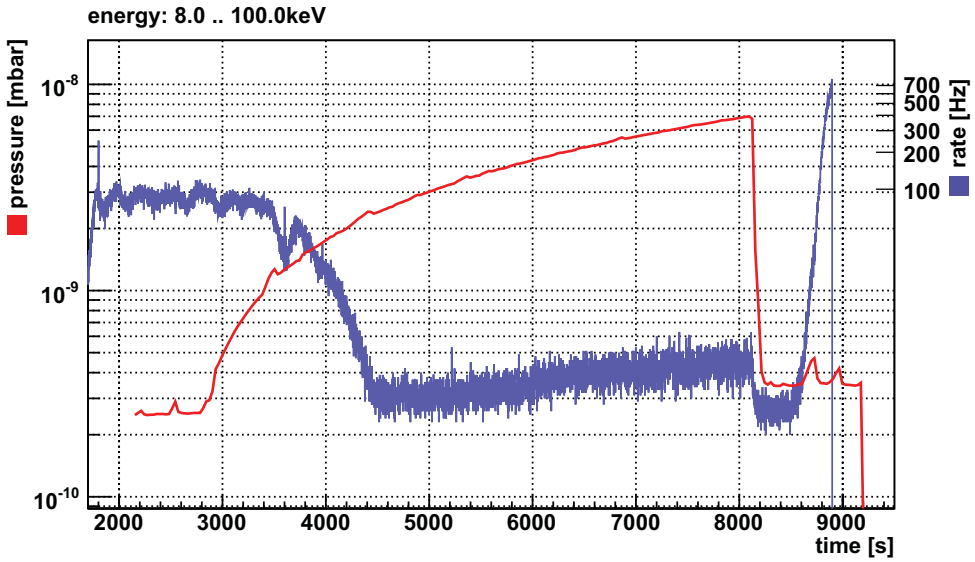

Figure 5.15: Background rate as a function of time during a pressure rise test (Run 178). The rate caused by an active Penning trap is anti-correlated with pressure. A rise in pressure causes a decrease in rate. While the rate approaches the background level the trap is not quenched but still active. Abruptly decreasing the pressure first deactivates the trap (t=8150 s). A restart at t=8600 s after a time span t_{ig} is the result of the once again stable pressure conditions leaving the trapping mechanism undisturbed.

5.2.5 Pressure dependence

Penning traps also depend on the prevailing pressure even when maintaining UHV conditions. To test the pressure dependence of the presumed Penning trap at the APE, the potential was ramped to U_{vessel}=-18 kV and U_{ie}=-18.2 kV with a magnetic field strength B=0.86 T and the detector being moved into the magnet at z=-2.28 m. After several minutes, the rate increased and stabilised at 220 Hz. Now, the valves in front of the pumping system were closed, leading to an increase in pressure caused by the outgassing of the stainless steel[8]. According to the literature, an increase in pressure should lead to a decrease in starting values for a Penning discharge, as illustrated in fig. 4.1. This dependence also gave rise to the equivalent pressure concept as described in section 4.1.3. According to this information, an increase in pressure is expected to lead to a further rise in background rate. Contrary to these expectations, the rate did go down, see fig. 5.15. The observed rate of 9.3 Hz is only slightly above regular background levels. If the potential difference is reduced by increasing U_{ie} the Penning trap is deepened, and the rate slightly increases to 20 Hz (3.6 Hz in the ROI of -15 to -22 keV) at U_{ie}=U_{vessel}=-18.0 kV. At this level, the rate stayed stable for 20 min without increasing further. After the pressure had

[8]Information regarding changes to the residual gas distribution during a pressure rise is given in section 3.1.1.1.

reached $7{\cdot}10^{-9}$ mbar the valves were opened and the pressure instantly recovered to $3.5{\cdot}10^{-10}$ mbar. Simultaneously, the remaining trap was quenched as the rate dropped to background level. Seven minutes later, the trap restarted. This shows that the Penning trap is still active while the pressure increases. However, when the vacuum recovers, the abrupt decrease in pressure affects the trapping mechanism quite effectively and quenches the trap. Subsequently a time t_{ig} is needed for the restart. It can be concluded that the pressure change primarily affects the production mechanism of the Penning trap itself and only to a lesser extent the transport mechanism responsible for the secondary electron production.

The spatial distribution of the rate is also affected by the pressure increase. The ring structure visible at $3{\cdot}10^{-10}$ mbar is much more pronounced than at a pressure regime of $5{\cdot}10^{-9}$ mbar. The fraction of the inner pixels to ring pixels drops from 6:1 to 2:1. The hypothesis of a gas jet caused by a high outgassing rate coming from the detector being the source of the ring-like structure cannot be excluded by this result. As a consequence, the detector vacuum is currently being improved as outlined in section 3.5.3.1.

A final evaluation of the implications of the observed pressure dependence with regard to the Penning trap's production and transport mechanisms is given in section 5.2.7, also including the facts presented in the following sections.

5.2.5.1 Influences of the electrostatic potential at pressures of 10^{-8} mbar

An important cross-check is to investigate the scaling of the background rate with the electrostatic potential at a higher pressure regime of $4.5{\cdot}10^{-8}$ mbar[9,10]. The high voltage of both vessel and inner electrode is supplied by a single power supply (FUG4) which is not causing the ignition of the Penning trap in the 10^{-10} mbar pressure region. A magnetic field of B=1.72 T is applied, and the detector is retracted at z=-2.7 m. A variation of the potential results in a different behaviour as expected. First, applying a negative potential to the vessel and inner electrode causes a sharp increase in rate to several hundred Hertz. Secondly, while the rate increases when going to more negative potentials it decreases abruptly after exceeding a threshold value of approximately -15 kV. The total rates corresponding to specific potential settings are listed in table 5.5, fig. 5.16 shows the rate as a function of time, thus providing a chronological order of the different potential settings. Independent of whether the potential is increased or decreased, the observed differences in rate were significant. One particular value at -15 kV, showing a small rate, does not comply with the observation. It could be argued that -15 kV corresponds to a threshold value so that the direction of the potential change could result in a difference, an observation which is repeated in other measurements, too. Moreover, in this measurement the potential settings have been set by hand and are therefore neither

[9] A pressure this high could only be reached via outgassing in combination with a vacuum leak. As a result, the residual gas distribution also contains oxygen and nitrogen contributions.

[10] Elog 398

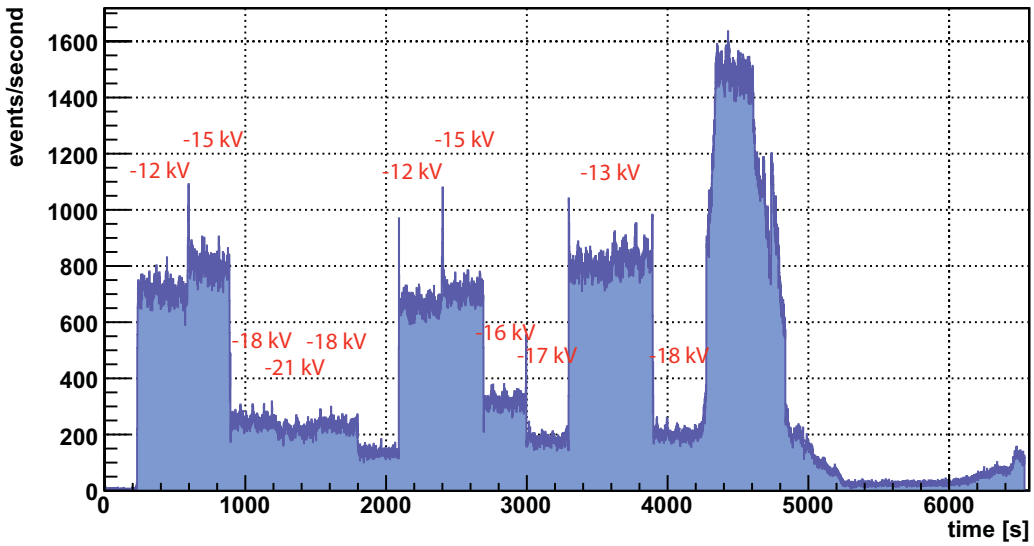

Figure 5.16: Test of the influences of the potential at high pressures of $4.5{\cdot}10^{-8}$ mbar (Run 449f). At high pressures the background rate is lower for more negative potential values than for more positive values. This effect is not necessarily connected to the background starting at B$\gtrsim$2 T, referred to as high B-field background (HBB), as at t=4250 s the magnetic field is ramped up starting from 1.72 T. Reaching 1.9 T, the HBB's threshold value, the rate increases similarly to the characteristic two-step starting behaviour of the HBB. Parameters: B=1.72 T, detector position (x,y,z)=(-1.3,-0.5,-270) cm.

exact, nor calibrated. This can be seen as further argument for a threshold value in the -15 kV region pertaining to an effect which influences the Penning trap.

This unique background effect does not fit in with the description of the residual Penning trap at the APE at lower pressure. Furthermore, it seems to be not connected to the background component starting at higher magnetic fields of $\sim$2 T, which is discussed in section 5.3. This can be seen at t=4250 s, where the magnetic field is ramped up (fig. 5.16) and reaches 1.9 T. At this point the rate abruptly increases and stabilises on a higher level which is characteristic for this specific new background component with its characteristic threshold value of $\sim$2 T.

Further investigations of the Penning trap characteristics have not been performed due to temporary problems with the remote control of the power supplies. Accordingly, it cannot be ruled out that this background behaviour is caused by the ignition of the APE Penning trap triggered by a higher pressure instead of a potential heating process of FUG3 and FUG4 combined, an alternative hypothesis which is discussed in the following section. The fact that the event rate which is initiated from the Penning trap decreases at -18 kV with rising pressure (see above) can be a similar effect as the one experienced in this set of measurements. It would have been interesting to test the Penning trap pressure dependence for an electrostatic potential in the range of -10 kV to -15 kV. However, the potential dependence can

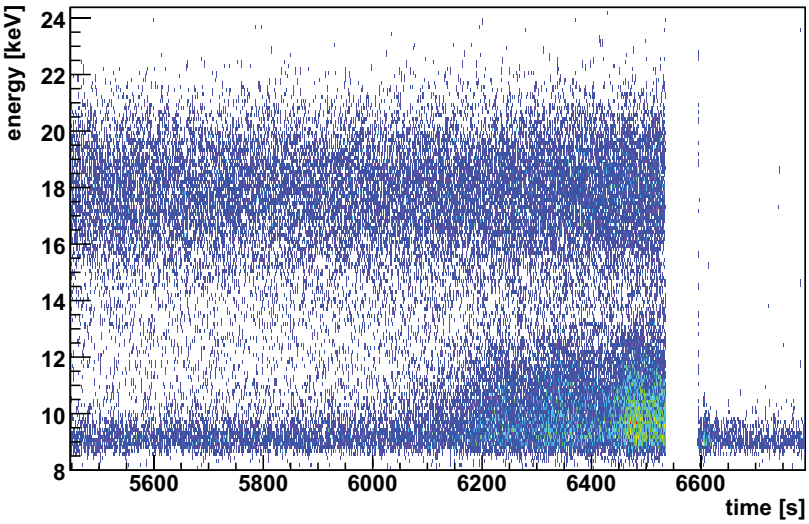

Figure 5.17: Increase of low-energy events at magnetic fields smaller 0.8 T (Run 450). During the ramp-down of the magnet, the rate increases when the magnetic field drops below 0.8 T. The increase can be ascribed mainly to low-energy events made up of negative ions. Parameters: B=1.72 T, detector position (x,y,z)=(-1.3,-0.5,-270) cm.

also be an indication for yet an additional background component not experienced before.

Complementary information is gained from the rate-increase for t>6000 s. At this time, the magnetic field drops below 0.8 T which has been found to positively influence the negative ion production, as can be seen by the increase of mostly low energetic events starting at t=6100 s, see fig. 5.17. At t=6500 s, the detector is

Table 5.5: Event rates as a function of the potential distribution at high pressures of $4.5 \cdot 10^{-8}$ mbar (Run 449f). Parameters: B=1.72 T, p=$4.5 \cdot 10^{-8}$ mbar, detector position (x,y,z)=(-1.3,-0.5,-270) cm.

U_0 [kV]	R_{all} [Hz]	U_0 [kV]	R_{all} [Hz]
-12	714 ± 2	-16	320 ± 1
-12	663 ± 2	-17	181 ± 1
-13	802 ± 2	-18	250 ± 1
-13	834 ± 2	-18	236 ± 1
-15	802 ± 2	-18	201 ± 1
-15	137 ± 1	-21	216 ± 1
-15	710 ± 2		

shut-down although the rate is only 120 Hz, see also the discussion in section 5.1.4.1.

5.2.6 Investigation of the activation mechanism

Previously it has been stated that using more than one power supply to elevate vessel and inner electrode potential changes the stability of the set-up with regard to Penning trap ignition. When using only the FUG4 device no Penning discharge or increase in rate can be detected, regardless of the absolute potential value. As soon as two different power supplies are used, one for supplying the pre-spectrometer vessel, and a second for the inner electrode system, the rate increases after a short period of time t_{ig}. The increase of the rate can be attributed to a residual Penning trap at the Anti-Penning electrode. The exact location of this trap was determined with the help of simulations taking into account the specific potential distributions. The reason for the different behaviour could not be identified completely. However, it is plausible that it is connected to a phase difference in the voltage output which can possibly lead to a 'heating' of the Penning trap process.

In a first test, the pre-spectrometer vessel and inner electrode HV supply lines are both shortcut using a capacitor with C=17.6 nF. The introduction of a capacitor suppresses high frequency differences superimposed onto the voltage output. In several measurements no differences with and without capacitor were detectable thus excluding high frequency noise as a possible activation mechanism.

A second test was aimed to investigate the influence of low frequency noise. Further objectives were to reduce the 50 Hz noise, visible as a sine wave with a frequency of 50 Hz and 3.5 V pp, which overlies the high voltage. The source for this noise stems from the insulating transformer supplying all electrical devices attached to the pre-spectrometer vessel with AC voltage. Switching it and thus all other electric devices off causes the 50 Hz noise to drop into the mV range. A so-called 'ripple probe' is measuring the low-frequency changes of the voltage. With the help of a regulator a triode is operated, which actively counteracts the voltage changes and thus stabilises the DC high voltage applied to the pre-spectrometer vessel [Wüs09]. The first results of a prototype are very promising. The ripple of the high voltage is successfully reduced to 70 mV pp [Wüs08b]. A second ripple probe is currently being built to allow a monitoring of the high voltage at both ends of the pre-spectrometer simultaneously. The ripple probe as well as the active regulator and triode have been designed and built by S. Wüstling, IPE. Although the stability of the voltage has been improved by a factor 50, no effect with regard to the heating process of the Penning trap has been discovered, leaving only the medium frequencies as a possible source.

A final test of the intermediate frequency range is still pending. The Mainz experiment used a frequency generator capable of inducing a wide range of frequencies to destabilise the storage condition of a Penning trap located at one of the inner electrode parts [Ott09]. This generator is at present on loan for an experiment carried out at CERN. As soon as this experiment is finished, it will be shipped to Karlsruhe.

Scanning through the medium frequencies and checking for possible correlations may reveal the source for the FUG3/4 heating as well as creating the possibility to eliminate the Penning trap ignition by periodically emptying the trap. Additionally, an online monitoring of the superimposed frequencies on the high voltage potential is planned, possibly revealing more information with regard to the heating process.

5.2.7 Discussion of the production and transport mechanisms

In the previous sections it has been shown that the events created as a result of an ignited Penning trap depend on many parameters: the potential distribution U, the magnetic field strength B and the residual pressure p. The question which has to be answered is wether these parameters influence the production mechanism responsible for the primary particles or if they change the transport mechanisms of the primary particles leading them to the place of production of the secondary electrons, which are finally counted by the detector system.

A close inspection of the shift of the energy allows to locate the place of production for the secondary electrons. This place has to be inside the flux tube, as electrons from the outside are generally not able to enter the flux tube due to magnetic shielding and, depending on the actual potential distribution, due to the electrostatic shielding by the inner electrode system. This z-coordinate of the production place coincides with the end of the Anti-Penning electrode, where a Penning trap of 200 V depth has been identified by simulations. Therefore, in addition to the production mechanism of the Penning trap, a viable transport mechanism is needed to bring the primary electrons created inside the trap to the place where the secondaries have to be produced. With the help of the measurements it has been proven that a pressure increase negatively affects in particular the production mechanism, as the pressure inside the pre-spectrometer is even in this regime too low so that particle interaction is still greatly suppressed.

On the other hand, a change in the B-field only affects the rate. It does not activate or deactivate the trap completely, provided that the field strength does not fall below the minimum threshold value for Penning trap ignition. This could mean that the higher B-field better confines the primary electrons inside the trap and thus negatively affects the secondaries' production rate. The spatial distribution of the rate supports this conclusion by showing a larger diameter of the low-event region at higher magnetic fields which is moving the production place closer to the Penning trap and thus towards the place of primaries production.

The potential distribution allows to ignite and quench a trap as well as to choose the primaries' production rate by adjusting the trap depth. Possible effects on the transport mechanism are therefore hard to assess. A more negative inner electrode causes a rise in rate with a spatial distribution of the rate which is rather untypical for the known Penning trap. This might be an effect on a transport mechanism, but it could also represent a new production mechanism, too.

5.2.8 Conclusion

The residual Penning trap located at the APE has been found to ignite under certain circumstances:

1. different power supplies are used for vessel and inner electrode HV supply,
2. the difference in electrostatic potential ΔU between vessel and inner electrode is required to be $|\Delta U| \leq 0.2\,\mathrm{keV}$.

If the potential distribution is chosen accordingly, the Penning trap can be activated and deactivated as desired. The Penning trap has been investigated with regard to many different parameters such as potential, magnetic field and pressure. The ignition requirements yielded some unexpected results: potential dependence at high pressure, Penning trap rate during pressure increase, and a power supply dependence with regard to Penning trap ignition.

The distinctive shift of the energy peak as well as the pixel distribution which shows an inner low-event region, a ring with an elevated rate and an outer region with a rate ranging in-between are the experimental cornerstones that allow to ascertain that the APE Penning trap is the cause for the rate increase as predicted in corresponding simulations.

While the production mechanisms are understood on a quantitative level, this is not true for the transport mechanisms. The exact process causing the primary electrons to reach the place of secondary production has still to be elucidated.

Independent from the Penning trap, the background rate is elevated to approx. 1 Hz, when magnetic and electric fields are applied as compared to a level of 20 mHz with only magnetic field active. This increase in rate is caused by a peak created by electrons at energies corresponding to vessel potential $\mathrm{U_0}$. A possible production mechanism are UV light photons from a vacuum gauge, ionising residual gas molecules inside the flux tube or low-energy secondary electrons entering the flux tube due to a magnetron drift with a radial component as the result of non-axisymmetrical magnetic and electric fields. Switching off the vacuum gauge reduces the background by a factor 3, but even then the rate does show an increase as compared to the intrinsic detector background alone.

5.3 Characterisation of background generating processes at magnetic fields larger than 2 T

After having studied the effects of the Penning trap at low magnetic fields, the investigation has been commenced at higher values. Exceeding a specific limit of magnetic field strength, the background behaviour changes fundamentally when high voltage is applied to the electrodes. After a time t_{ig} the background rate $\mathrm{R_0}$ as measured

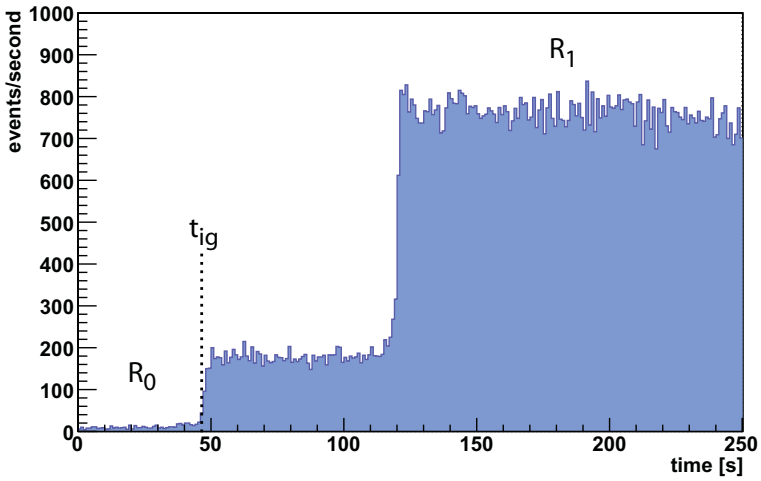

Figure 5.18: High B-field background ignition (Run 233). With a symmetric magnetic field higher than B_{lim} = 2 T and after a time t_{ig} the rate R_0 increases in a two-step function to the new value R_1 where it keeps stable. Parameters: U_0=-15 kV, B=3.44 T, detector position (x,y,z)=(-1.1,-0.35,-228) cm.

by the SPD increases abruptly with a nearly vertical slope, stabilises on an intermediate level for about one minute and subsequently rises to a final value R_1, see fig. 5.18. While the different background characteristics like, t_{ig} and R_1, depend on other parameters, the basic development as just described does not change. These correlations are investigated in the coming sections. Following this, a detailed investigation of the so-called 'high B-field background' (HBB), are presented. In a final assessment, possible explanations regarding the production mechanisms and different sources of the background are discussed which were motivating a second change of the inner electrode system.

5.3.1 Event rate dependence on magnetic field strength

Once the system is operating in a high B-field regime the detection rate R_1 of background events from the HBB modus keeps on a stable level, and longtime measurements of more than 16 h show no significant change in rate. In the beginning of the measurement campaign, periodic recurring instabilities of the event rate were observed. However, these have not been caused by the HBB itself but have been the result of small pressure increases. These effects are discussed in section 5.3.5. Table 5.6 lists values for the rate R_1 after HBB ignition for different magnetic field strengths and two potential values. As can be seen, the rate is increasing non-linearly (a polynomial function of second order fits the data best). However, the curvature of the rate-increase for -14 kV is negative, the rate reaches a maximum at ∼3.7 T and then decreases slightly when the maximum B-field is approached. For a poten-

tial of -18 kV, however, the curvature is positive and the rate is still increasing at $B_{max} = 4.5$ T. The HBB therefore depends both on the absolute value of the magnetic field strength and the electrode potential likewise – the stronger the magnetic field and the lower the negative potential, the higher the background rate.

To determine the value of the magnetic field when the HBB begins to ignite, the magnetic field is ramped down slowly with the HBB process being in action. These data, which show the rate as a function of time together with the drop in magnetic field strength, is presented in fig. 5.19. There, the exact parameters of the measurement set-up are listed as well. Starting from 4.5 T, the rate is ramped down with 10 mA/s starting at 900 s. The rate keeps stable until the magnetic field reaches 3.8 T. From then on, the rate decreases in accordance with the magnetic field, which is in good agreement with the data of table 5.6. Reaching the intermediate value of 3.44 T, the rate once again stabilises. Further ramping down the magnetic field again causes a decrease in rate. At 5400 s, the rate suddenly drops to the usual background level. This coincides with a magnetic field of 2 T which thus can be identified as threshold value B_{lim}.

The longtime behaviour of the HBB has been subject to several measurements. For different B-field values measurements over a time span of 16 h and more provide detailed information on ignition time, stability in rate and possible details of the ignition behaviour. For these measurements, a potential distribution with an inner electrode set to a more negative potential as the vessel potential was chosen. Moreover, the high voltage stabilisation introduced in section 5.2.6 was activated, which reduced the potential fluctuations' amplitude to 70 mV pp. The results for this set-up are listed in table 5.7. The rates R_0 before HBB activation are listed for the measurements with B$\leq$ 2.58 T.

The background rate R_0 is fluctuating on a small scale, but the changes observed are much larger than the statistical error limits, for B= 2.58 T the increase in R_0 is even larger. It is of particular importance to note that the background rate without electric potential and magnetic field has increased considerably as compared to earlier measurements, see table 5.1. An analysis of the spectra reveals the events to be

Table 5.6: Magnetic field dependence of the background rate for B>2 T for two different potential settings. Parameter:(x,y,z)=(-1.3,0,-228) cm.

Run #	B [T]	U_0 [kV]	R [Hz]	Run #	B [T]	U_0 [kV]	R [Hz]
441	2.01	-14	9.5 ± 0.1	327	2.15	-18	15.1 ± 0.1
440	2.58	-14	169.3 ± 0.8	151	2.58	-18	161.4 ± 0.3
439	3.15	-14	287.0 ± 1.1	336	3.44	-18	582.8 ± 0.6
438	3.73	-14	365.7 ± 1.3	246	4.50	-18	1987.0 ± 2.6
437	4.30	-14	341.5 ± 1.3				
436	4.50	-14	330.0 ± 0.8				

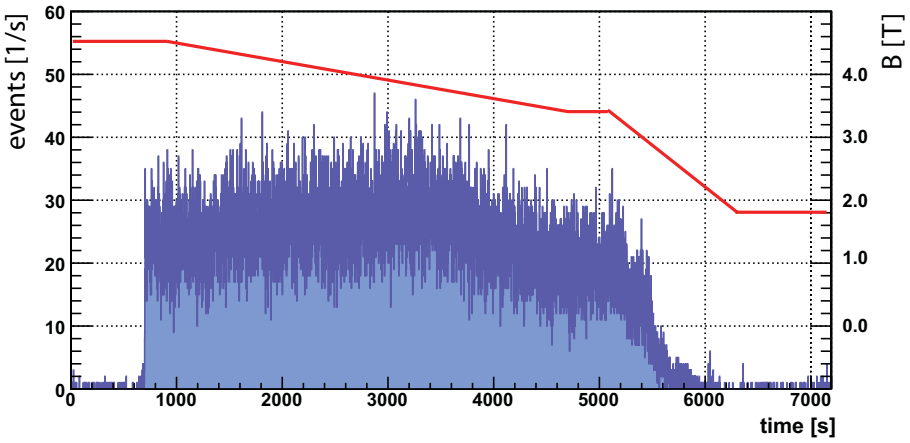

Figure 5.19: Background rate as function of monotonically decreasing B-field (Run 887). An asymmetric B-field with the detector magnet at B_{det}=4.5 T is slowly ramped down while the e-gun magnet is kept at zero magnetic field. The rate keeps stable until B=3.8 T is reached. Starting from that position, B-field and rate decrease simultaneously. For B≈2 T the rate drops sharply to background level. Parameters: U_{vessel}=-18 kV, U_{ie}=-18.5 kV, detector position (x,y,z)=(-1.1,0.5,-267) cm.

uniformly distributed in the energy-over-time histogram, with no other deviations visible when compared to spectra taken at lower magnetic field values. However, in the meantime the DAQ electronics had been changed. A reevaluation and comparison of old and new DAQ-electronics should give an answer to the question of possible electronics-induced differences. Apart from this fact, the rates below B_{lim} are stable over the whole measurement time. Above 2 T, the rate increases after some time and stabilises with R_1 clearly correlated with the magnetic field strength – the stronger the B-field, the higher the resulting background rate.

5.3.2 Ignition characteristics

A more detailed investigation of the ignition process reveals some interesting characteristics of the ignition behaviour of the low-energy tail of negative ions distributed over the entire flux tube. This can be compared to electron U_0-events, which are concentrated in a ring-like structure. In fig. 5.20(b), the time development of the ignition process is shown as a function of the energy. The plot allows to distinguish two different regions and three distinct time intervals, corresponding to a normal background regime, an intermediate HBB and active HBB process region. In the background region, events with energies close to U_0 are dominant. When the HBB starts at 50 s, events of both energy levels start to increase in number with U_0-events still outweighing the low-energy ones. This changes as soon as the HBB process is fully active. At this point, a substantial increase in low-energy events is observed, which are caused by negative ions. One can thus postulate a positive feedback

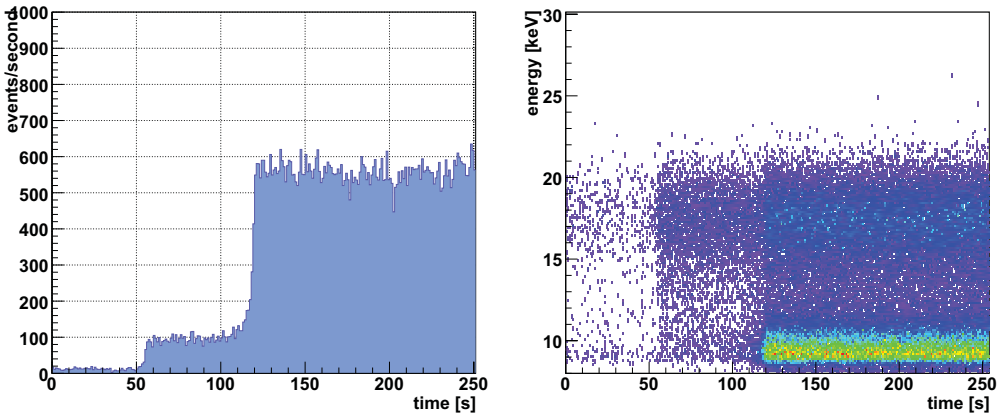

(a) Two-step HBB rate increase (b) Energy-over-time scatter plot

Figure 5.20: HBB ignition characteristics for symmetric magnetic fields (Run 324). The HBB increases for symmetric magnetic fields following a two-step function, reaching first an intermediate level and after approximately one minute a second step increases the rate to the final value which is stable. The first step leads to an increase mainly in the U_0 region, the second step results from a strong population of the low-energy events caused by negative ions. Parameters: U_0=-18 kV, B=3.44 T, detector position (x,y,z)=(-1.1,-0.35,-228) cm.

mechanism, which activates as soon as the background process is fully active and stable.

The ignition process for an asymmetric magnetic field distribution with one magnet kept below the threshold value B_{lim} shows a one step behaviour (fig. 5.21(a)). The

Table 5.7: Longtime stability of the high B-field background and background rates in the ROI of [-15,-22] keV. Several longtime measurements over a period of 16 h allowed to measure the ignition time t_{ig} as well as the background rates R_0 and R_1. An elevated detector background for zero potential is found as compared to previous measurements, potentially resulting from the changes in the DAQ hardware. Measurements with non-zero potential show a decrease in rate by a factor 3 as compared to earlier measurements, which is the result of the deactivated hot cathode vacuum gauge.

Run #	t [h]	B [T]	U_{ie}/U_{vessel} [kV]	t_{ig}	R_0 [mHz]	R_1 [Hz]
700ff	20	0	0/0	-	28.4 ± 0.02	-
797ff	16	1.72	-18.3/-18.0	-	32.47 ± 0.02	-
809ff	16	2.15	-18.3/-18.0	2:15	30.43 ± 0.02	1.12 ± 0.00
824ff	16	2.58	-18.3/-18.0	3:20	38.43 ± 0.03	7.2 ± 0.01
866ff	16	3.44	-18.3/-18.0	0	-	28.92 ± 0.02

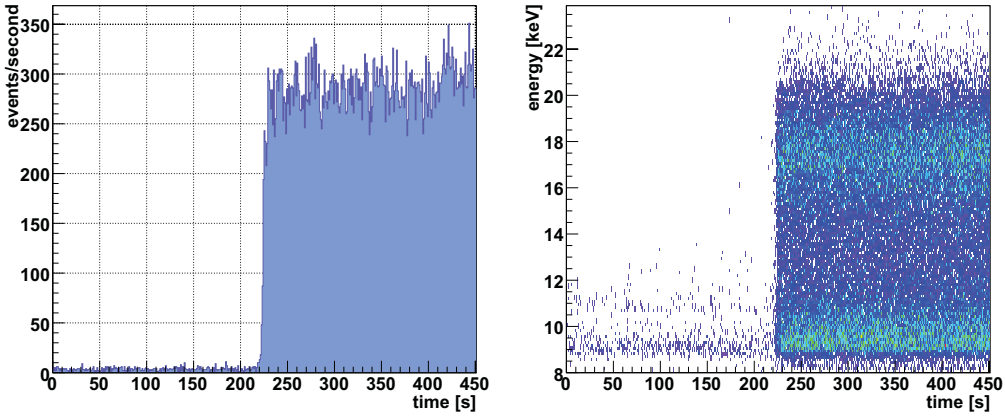

(a) One-step HBB rate increase

(b) Energy-over-time scatter plot

Figure 5.21: HBB ignition characteristics for asymmetric magnetic fields (Run 351). In contrast to symmetric magnetic fields, the HBB ignition is marked by a one-step function for asymmetric fields, which is an indication that the activation of the two traps at the east and west side are achieved independently from each other. In this case the rates of low-energy and U_0-events are about equal. Parameters: U_0=-18 kV, U_{wire}=-18.5 kV, B=3.44 T, detector position (x,y,z)=(-1.1,-0.35,-228) cm.

energy-over-time scatter plot is different, as well (fig. 5.21(b)). Here, both energy intervals feature a similar increase in rate.

The asymmetric B-field measurements give a strong indication that the HBB production is not connected to particle storage in the middle of the vessel. In this case, positive ions would be stored due to magnetic confinement in radial and potential confinement in axial direction.[11]. Instead, the area adjacent to the ground and Anti-Penning electrode and full metal coni of the inner electrode is the likely place of the production mechanism of this background. In this context it should be emphasised that the two step rate-increase is caused by two separate traps located at the entrance and exit region. A change of the magnetic field for one side does not influence the start of the trap at the other side. However, it seems that two traps might be more effective as one trap alone, which can be explained by a positive feedback in the form of positive ions and photons reaching the other side where they create more secondary electrons. In the case of low magnetic fields, the effect of the ion peak is probably increased by the influence of the hot ionisation vacuum gauge already discussed in section 5.1.3.

In contrast to earlier experiences, the ignition times t_{ig} for B-field values just above the threshold value are much longer with an activated HV stabilisation, see table 5.7. In earlier measurements, the high B-field background started already after ∼30 min

[11] For a more detailed discussion of the measurements with asymmetric magnetic fields see section 5.3.4.1.

at 2.58 T, with stabilisation ignition typically occurs after three hours. This might be an indication that the HV stabilisation has some positive effect in delaying the ignition, at least for magnetic fields near B_{lim}. On the other hand it has to be stated that the ignition time strongly depends on the previous measurement history, in some cases ignition times of only a few minutes for an identical field strength have also been observed.

5.3.3 Electrode potential dependencies

A change of the absolute potential or the potential differences between the spectrometer vessel and inner electrode parts has a big influence on the detected background rate. In this section, the influence of the applied potential is investigated with regard to the event rate, the spatial distribution of the rate and the energy spectra. With this information, a better understanding of the background processes is achieved, which allows to localise the place of production and thus to restrict the potential sources of the HBB effect.

At first, the overall influence of the absolute potential is tested for two different magnetic field strengths. Tables 5.8 and 5.9 list the event rates for the whole energy range as well as the region of interest of [-15,-22] keV for different potential values at B=3.44 T and B=4.5 T. The results show that for potentials with more negative values the rate does increase. It has to be noted that the measurements at B=4.5 T depend on the run sequence. As outlined above, there is a significant difference in rate if the high voltage is increased or decreased when going from one measurement point to the next (this corresponds to a typical hysteresis-like effect). However, apart from the hysteresis, the general trend as expressed above stays the same, see also fig. 5.22. One measurement point at -18 kV is a yet unexplained exception from the rule. Contrary to the measurements at high pressure, as discussed in section 5.2.5.1, no discrepancy between potential values lower or higher than -15 kV is observed.

Table 5.8: The background rate as a function of the potential at B=3.44 T. An increase of the potential U_0 results in a rise in rate. The background rate is investigated for the whole energy range of 0-100 keV and in the ROI of [U_0-3,U_0+4] keV. Parameters: U_0=-18 kV, B=3.44 T, detector position (x,y,z)=(-1.1,-0.35,-228) cm.

Run #	U_0 [kV]	R_{all} [Hz]	R_{ROI} [Hz]
234	-16	901 ± 2	495 ± 1
235	-17	1078 ± 2	507 ± 1
236	-18	1359 ± 2	530 ± 1
237	-19	1565 ± 2	584 ± 1
238	-20	1568 ± 2	607 ± 1
239	-21	1518 ± 2	625 ± 1
240	-22	1764 ± 2	745 ± 2

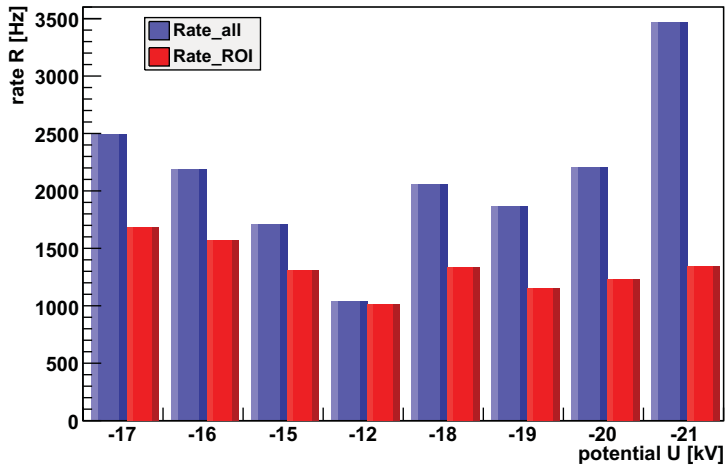

Figure 5.22: The background rate as a function of the potential at B=4.5 T (Run 242ff). For more information see text and table 5.9. Parameters: B=4.5 T, detector position (x,y,z)=(-1.1,-0.35,-228) cm.

5.3.3.1 Dipole mode test

The inner electrode system is subdivided into three sections, east and west cones and the central wire electrode, forming altogether six parts, as every section is split in two halves. This division into different sub-parts makes it possible to generate

Table 5.9: The background rate as a function of the potential at B=4.5 T. A decrease of the potential U_0 results in a rise in rate, an increase of the potential lowers the rate. However, the order in which the potential is chosen influences the absolute value of the detected rate. Therefore, only the general trend is in line with the conclusion. The background rate is investigated for the whole energy range of 0-100 keV and in the ROI of [U_0-3,U_0+4] keV. Parameters: B=4.5 T, detector position (x,y,z)=(-1.1,-0.35,-228) cm.

Run #	U_0 [kV]	R_{all} [Hz]	R_{ROI} [Hz]
242	-17	2491 ± 4	1684 ± 3
243	-16	2189 ± 3	1575 ± 3
244	-15	1708 ± 3	1313 ± 3
245	-12	1041 ± 2	1015 ± 2
246	-18	2063 ± 3	1335 ± 2
247	-19	1864 ± 3	1156 ± 3
248	-20	2210 ± 3	1234 ± 3
249	-21	3466 ± 4	1341 ± 3

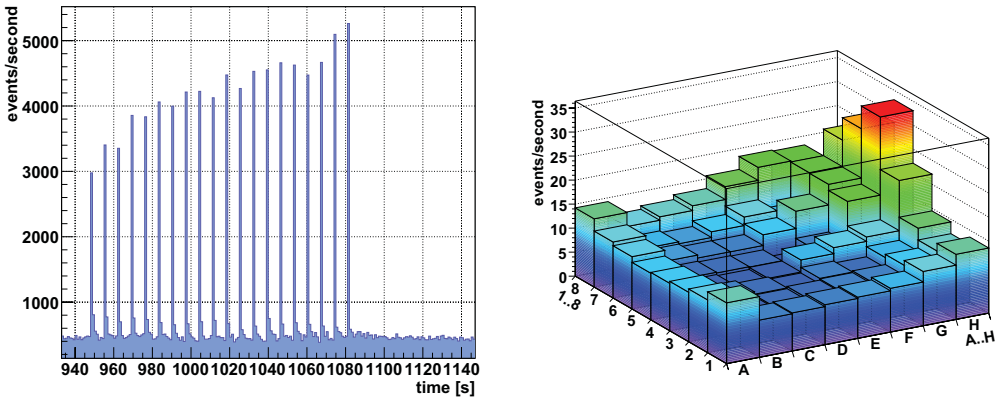

(a) dipole modulation of the rate

(b) dipole distribution of the rate

Figure 5.23: Dipole activation to test influence on background rate (Run 194). The six individual parts of the inner electrode can be supplied with two different potentials thus causing a dipole field. (a) After an activation of the dipole causes an increase in rate by approx. a factor 5 to 25 is observed depending on the time setting. (b) The inner electrode set-up is mirrored by the rate in a specific area of the pixel chessboard. Parameters: U_{vessel}=-16 kV, U_{ie}=-18.5+2 kV, dipole activation time 0.3/0.3 s, cycle time 6 s, B_{det}=4.5 T, detector position (x,y,z)=(-1.1,-0.35,-270) cm.

a dipole field by applying different high voltages to the opposing halves. In doing so, charged particles experience a transversal electric field component. Together with the magnetic field an E×B drift affects the charged particles by bestowing a radial movement component. The dipole field mechanism is a central feature not only of the pre-spectrometer but also the main spectrometer inner electrode system. This technique is essential to remove stored particles in the middle volume of the spectrometers.

Several test measurements were carried out to test the influence of this dipole mechanism. The tests comprised the variation of all available parameters such as, high voltage, polarity, geometrical direction (north, south), duration, cycles or single mode, and different geometries by varying the sub-part combinations. For example, the three halves of the north side are interconnected and supplied by the FUG1 device, the south halves are supplied by FUG2. In an initial measurement a positive offset of 2 kV was applied first to the north halves and then to the south halves for a duration of 0.3 s, and after a pause of 6 s the cycle started anew. The results are documented in figs. 5.23(a),(b). The pixel chessboard of the detector registered a strong increase, first on one side and then a weaker one on the opposing side leading to an asymmetric distribution of the rate. Before and after the dipole activation, the rate stayed on a stable level, and no lasting influence of the dipole field operation on the high B-field background could be detected. If indeed stored particles in the spectrometer volume would be the cause for the HBB effect, the dipole field should have a positive effect, even if this would be visible only for a short time after activation.

However, no decrease in rate at the beginning of the dipole modus is detected. This leads to the conclusion that the HBB process is not started or maintained in the inner volume, but has to originate in the vicinity of the ground and Anti-Penning electrode.

5.3.4 Variation of potential distribution

As outlined above, the pre-spectrometer electrode system with the vessel and the three sections of the inner electrode offers many configurations to choose from. In the following, the individual settings are characterised with regard to their influence on the background processes.

Equal potentials at vessel and inner electrode When both vessel and inner electrodes are supplied by only one power supply, the spatial distribution of the rate shows a ring structure for z=-2.28 m where the outer pixels are elevated while the inner pixels detect a lower event rate. The energy spectra registered show a peak at full energy e·U_0 and an increase of low-energy events, which is cut-off by the discriminator threshold, the so-called 'low-energy tail'. Previous investigations show (section 5.1.4) that the increase described as low-energy tail is the first indication for a second peak at lower energies which emerges from the background noise starting at U_0=-24 kV. This peak is most likely created by negative ions hitting the detector[12].

The pixels which are part of the ring structure count the majority of the U_0-electron events, whereas in the inner pixels the negative ion count rate is dominating. Therefore, the more pronounced the ring structure is, the higher will be the fraction of U_0-events as compared to lower energy events. This can be tested by retracting the detector into the maintenance position: the detector flux tube contracts accordingly so that only a small area around the centre axis is imaged. Consequently, the ring structure is washed out together with the dominance of the U_0-events.

Changes in the absolute potential can have an influence on the fraction of U_0-peak events versus the low-energy tail. At maximum magnetic field of B=4.5 T, the differences in the spatial distribution of the rate are negligible. At B=3.44 T the ring structure gets more pronounced for more negative voltage values, which implies that the U_0-events are increasing in rate. This is in agreement with the findings connected with the Penning trap: the ring diameter increases with higher magnetic field strengths. Hence, the differences as displayed by the pixel chessboard are considerably reduced at maximum magnetic field.

The U_0-peak position in the energy spectra can be determined for different potential values and two magnetic field strengths, the results are listed in table 5.10. The energy peaks are shifted to lower energies as compared to e·U_0. However, a peak

[12] This is supported by the energy difference which is in good agreement with dead layer losses in the SPD's 110 nm silicon dead layer and further investigations carried out by the Mainz experiment, see section 5.1.4

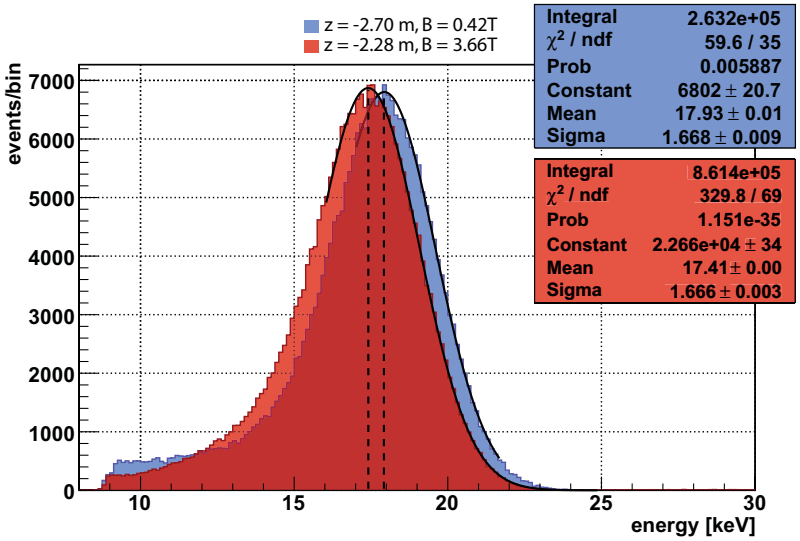

Figure 5.24: Energy peak shift for e-gun electrons at different z-positions (Runs 191&272) The transversal energy component depends on the magnetic field value at the detector position. At higher magnetic fields the transversal energy component is larger and thus also the angle with which the electrons are hitting the detector which leads to higher energy losses in the silicon dead layer. Parameters: U_{egun}=-18 kV, B=4.5 T, detector position (x,y)=(-1.1,-0.35) cm.

shift for electrons measured in high magnetic fields is expected as the impact angle at which the electrons hit the detector wafer is larger due to an increased transversal energy component. The electrons' transversal energy is increased when they are accelerated in direction of the magnet according to the MAC-E filter principle, see section 2.2.3.1. After passing the B-field maximum the transversal energy is reduced again and with it the angle of the total velocity vector with which the electrons are gyrating around the magnetic field lines. The farther the detector is retracted from the magnets, the lower the angle and thus the energy loss in the dead layer. The energy loss increases with the impact angle α by the factor f_{loss}=1/cosα.

A comparison of e-gun runs at z=-2.28 m and z=-2.7 m reveals an energy difference, visible as a peak shift, of several hundred eV, see fig. 5.24. A change in peak location is also distinguishable for smaller differences in magnetic field strength:

Run #	B [T]	B_{det}(z=-2.28 m) [T]	U_{egun} [kV]	peak location [keV]
319	3.44	2.80	-18	17.54 ± 0.01
272	4.5	3.66	-18	17.42 ± 0.01

When comparing the energy of the e-gun electrons with the energy peak location of the HBB background component for B=3.44 T, one can see that the energy of the ring pixels and thus the U_0-events is shifted to lower energies. In contrast, the U_0-peak of the inner pixels shows that here the energy loss is minimal and increases slightly for more negative potential values, causing the ring to be more

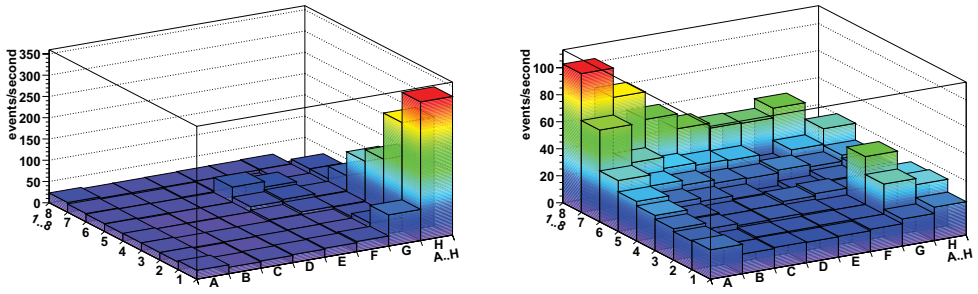

(a) Asymmetric structure (x=-2 cm) (b) ...as part of a ring (x=-0.1 cm)

Figure 5.25: Translation of detector with Δx=1.9 cm (Run 216&217). Moving the detector in x and y reveals structures which otherwise are too large geometrically for the given spatial resolution of the detector. Parameters: U_{vessel}=-18 kV, U_{ie}=-18.3 kV, B=4.5 T, detector position (y,z)=(-0.35,-228) cm.

pronounced. A different picture is observed for B=4.5 T, now the ring is rather flat without prominent ring structure, hence the energy of the U_0-peak cannot be subdivided into a ring or inner pixel group, as the energy difference is negligible. Furthermore, taking into account the energy loss due to the detector magnet field, it can be deduced that for higher electrode potentials in particular the detected energy matches those of electrons accelerated by U_0. Corresponding simulations to confirm this observation are in progress. Their aim is to determine the angle distribution of the electrons emitted from the e-gun as well as the vessel.

Table 5.10: U_0-peak location as a function of the potential for two different magnetic field strengths. Parameters: B_{233ff}=3.44 T, B_{245ff}=4.5 T, detector position (x,y,z)=(-1.1,-0.35,-228) cm.

Run #	U_0 [kV]	U_0-peak [keV] ring pixel	U_0-peak [keV] inner pixel	Run #	U_0 [kV]	U_0-peak [keV]
233	-15	14.50 ± 0.00	14.33 ± 0.02	245	-12	11.43 ± 0.02
234	-16	15.51 ± 0.02	15.30 ± 0.02	244	-15	14.45 ± 0.01
235	-17	16.42 ± 0.02	16.22 ± 0.02	243	-16	15.44 ± 0.01
236	-18	17.44 ± 0.02	17.09 ± 0.02	242	-17	16.40 ± 0.00
237	-19	18.38 ± 0.02	18.01 ± 0.02	246	-18	17.45 ± 0.01
238	-20	19.35 ± 0.02	18.91 ± 0.02	247	-19	18.33 ± 0.01
239	-21	20.31 ± 0.02	19.85 ± 0.02	248	-20	19.31 ± 0.01
240	-22	21.36 ± 0.02	20.89 ± 0.02	249	-21	20.35 ± 0.01

Inner electrode more negative than vessel If the spectrometer vessel and the inner electrode are connected to two different power supplies and if the inner electrode is elevated to a more negative potential the spatial distribution of the background rate is changed fundamentally. The ring structure disappears and only a few pixels at one edge of the wafer detect a huge increase in count rate. Moving the detector in x and y direction, see figs. 5.25(a),(b), reveals a large ring structure of approx. 5.7 cm in diameter at z=-2.28 m which is too large to be resolved completely by the limited detector area. The energy of the U_0-peak is higher for ring pixels as compared to the remaining pixels. The discrepancy in energy increases with ΔU accordingly:

Run #	B [T]	U_{vessel} [kV]	U_{ie} [kV]	inner circle [keV]	ring [keV]
216	4.5	-18	-18.3	17.71 ± 0.01	17.87 ± 0.01
267	4.5	-18	-20.0	18.77 ± 0.02	19.05 ± 0.01

The results also show that the peak energy is connected to the inner electrode settings as it increases well beyond the constant -18 kV value of the vessel potential. With increasing ΔU the rate in the ring pixels rises and the difference in count rates relative to the inner pixels gets even larger. For ΔU=0.3 kV this difference in rate is approximately a factor 10, for ΔU=2 kV it increases up to two orders of magnitude, see figs. 5.26(a),(b).

This effect can be switched off by equalising the east cone potential with that of the vessel, while the west cone and the inner electrodes are kept on a more negative potential (fig. 5.26(c)). In this configuration the rate drops and the spatial distribution gets more homogeneous. The decrease in rate is unexpected, as for a configuration with equal potentials on the east cone and the vessel supplied by different power supplies, the residual Penning trap at the APE end is supposed to ignite. However, the rate stays stable which could mean that the Penning trap is already ignited and thus part of the HBB process.

Inner electrode more positive than vessel If a more positive potential is applied to the inner electrode as compared to the spectrometer vessel, the rate increases strongly. For ΔU=0.5 kV (U_{vessel}=-18 kV, U_{ie}=-17.5 kV) at maximum magnetic field and z=2.28 m, the SPD detects a rate of 5.7 kHz. The middle pixels feature a lower rate, which is increasing monotonically but moderately to the border pixels. The energy spectrum is dominated by U_0-events, no difference between inner and outer pixels is observed. With an energy of 17.15 keV, it cannot be discriminated if these electrons originate from the vessel or the inner electrode. However, due to the more positive potential of the wire electrode, electrons from the vessel walls are not blocked and therefore can reach the flux tube in substantially larger numbers.

East cone electrode more negative The influence of the east cone alone is tested by applying a more negative potential as compared to the remaining electrodes. A strong influence of the potential difference on the rates is registered.

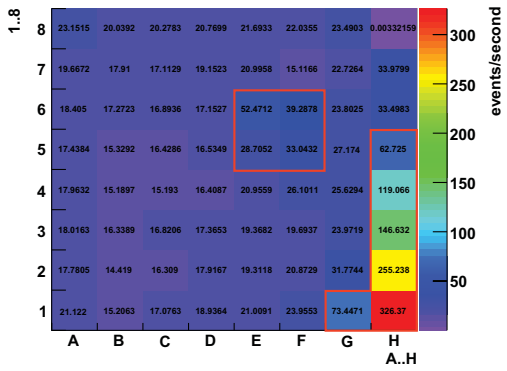

(a) ΔU=0.3 kV (Run 216)

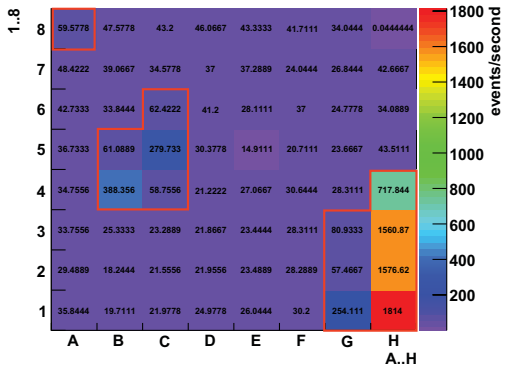

(b) ΔU=2 kV (Run 267)

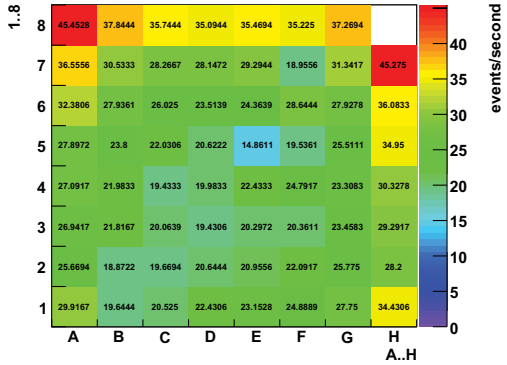

(c) U_{vessel}=U_{ec} (Run 267)

Figure 5.26: Spatial distribution of the background for a configuration with a more negative inner electrode (Run 216&267). (a) With more negative inner electrode the spatial distribution of the rate displays a very distinctive ring structure with a large diameter exceeding the detector area. (b) The difference in rate between ring pixels and inner circle pixels is increasing analogue to ΔU. The marked pixel groups of the A-F rows are discussed in section 5.3.6.1(c) Elevating the east cone potential to the vessel value, the distinctive ring structure flattens considerably. Parameters: U_{vessel}=-18 kV, B_{det}=4.5 T, detector position z=-2.28 m.

Run #	B [T]	z [m]	U_0 [kV]	U_{ec} [kV]	R [kHz]
276				-15.1	1.8
276				-15.1	2.8
276	4.5	2.28	-15	-15.2	3.2
276				-15.3	3.4
277				-15.6	4.4

This fact, together with the information gained by the configuration with the inner electrode being more negative, leads to the conclusion that a large number of charged particles which are able to enter the detector flux tube is generated by the east cone. If these charged particles are not blocked by a more negative wire electrode or west cone potential, a steep increase in rate is the result.

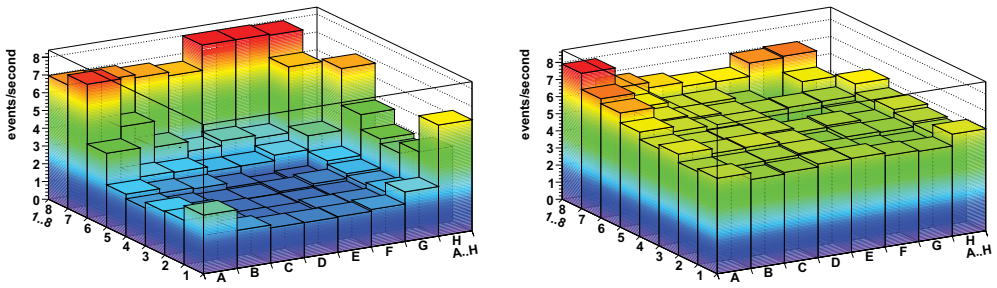

(a) ΔU=0.4 kV (b) ΔU=4 kV

Figure 5.27: Spatial distribution of the rate for a configuration with a more negative wire electrode (Run 154). Increasing the potential difference between wire electrode and remaining electrodes homogenises the spatial distribution of the rate as the events in the inner circle increase. Parameters: U_{vessel}=-19 kV, B_{det}=2.15 T, detector position (x,y,z)=(-1.1,-0.35,-228) cm.

Wire electrode more negative Elevating the wire electrode to a more negative potential, while the cones and vessel are on equal potential, has subtle effects. If, for example, the potential difference is increased to ΔU=0.4 kV, the prominence of the ring structure is strengthened slightly while the rate keeps stable, see table 5.11. If one applies a more negative potential without changing the potential difference of wire electrode and remaining electrodes, the rate is getting larger than expected. A further increase of ΔU also leads to an increase in rate, however, in this case the spatial distribution of the rate is changing in the opposite direction. Instead of showing an even more pronounced ring-like structure, the distribution flattens noticeably, see figs. 5.27(a),(b). The U_0-peak shifts to lower energies with growing ΔU[13], although the wire potential is kept constant. This can be attributed to the influence of the west cone. Electrons emitted from this area are also entering the flux and when detected by the SPD are broadening the U_0-peak, and thus cause a small shift in the peak-location.

Another generic effect of a more negative wire electrode is the emergence of pile-up peaks. Electrons reaching the detector with short time differences $\Delta t < 10^{-9}$ s are registered as a single event with n times the energy when n is the number of electrons arriving at the same time. Consequently, higher order peaks with an energy $n \times U_0$ are observed in the spectra. In case of the wire electrode being more negative, a minimum of ΔU=0.4 kV is required to start this effect. Furthermore, the intensity of these peaks decreases slightly for larger ΔU. This can be explained by the fact that the pile-up peaks constitute mainly U_0-events. Their numbers have been found to be reduced as the distribution of the rate turns more homogeneous. A possible

[13]Instead of listing the absolute peak energies, table 5.11 provides the relative peak-shift in keV, as no reliable absolute energy calibration was available. During this time the e-gun was dismounted and changes in the DAQ electronics influenced the energy calibration.

explanation for the pile-up peaks can be an asymmetry in the geometry of the wire electrode [Glü09b] creating an electric dipole which allows electrons to enter the flux tube and provides them with a radial motion component perpendicular to the magnetic field lines.

West cone more negative In a configuration where the west cone is on a more negative potential, electrons coming from the wire electrode or the east side are blocked. This hypothesis is supported by the measurements summarised in table 5.12. If the potential of the west cone is set to more negative values, the rate decreases. At ΔU=0.5 kV a limit is reached, as for higher ΔU no further significant changes in rate are observed.

The corresponding shift in the location of the U_0-peak is only small. For ΔU=2 kV the peak shift is much more pronounced. The reason for this behaviour can be explained with the influence of the Anti-Penning electrode which is connected to the tank potential on the west cone potential. The secondary electrons are created in the area of the west cone and the APE and, judging from the peak location, are mainly influenced by the APE potential. Only for large values of ΔU the influence of the west cone potential gets stronger, shifting the peak energies beyond e·U_{APE}, but still clearly shifted away from e·U_{wc}.

The rate as viewed in the spatial distribution slightly moves to the outer lying pixels with a ratio of minimum to maximum event rate of 1:3. This geometric distribution does not change, even for ΔU=2 kV.

Table 5.11: Rate dependence with the wire electrode being elevated to a more negative potential in the ROI [-15,-23] keV. The rate increases analogue to ΔU while the spatial distribution of the rate flattens. Parameters: B=2.15 T, detector position (x,y,z)=(-1.1,-0.35,-228) cm.

Run #	U_{wire} [kV]	U_0 [kV]	U_0-peak shift [keV]	R_{ROI} [Hz]
154	-18	-18	0.08	107.1 ± 0.4
	-18.2	-18	0.17	101.6 ± 0.6
	-18.4	-18	0.30	108.1 ± 0.5
	-19	-18.6	0.29	126.0 ± 0.6
	-19	-18	0.44	133.5 ± 0.6
	-19	-17	0.57	170.2 ± 0.7
	-19	-16	0.63	179.4 ± 0.9
	-19	-15	0.68	211.0 ± 0.6

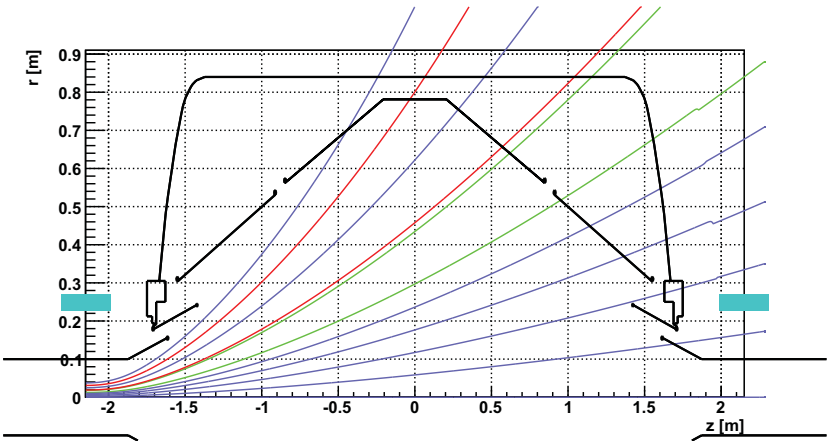

(a) Magnetic field lines for asymmetric field

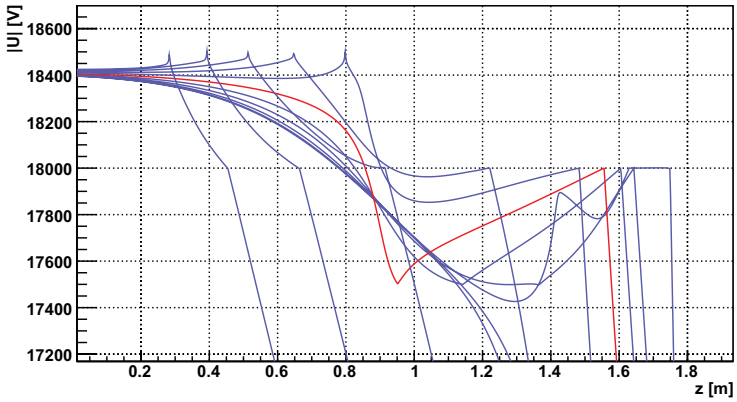

(b) Potential along magnetic field lines for asymmetric magnetic field

Figure 5.28: Electrostatic potential along the magnetic field lines revealing Penning traps in the case of asymmetric magnetic fields. (a) The magnetic field lines for B_{egun}=0 connect the detector with the vessel and electrode walls. Red lines: largest possible detector flux tube radius for pixel H8 (3.5 cm) and field line connecting ring-pixels (2.0 cm) at z=-2.28 m. Green line: the same for z=-2.43 m.
(b) Potential values around the magnetic field lines for $U_{wc,vessel}$=-18 kV, U_{wire}=-18.5 kV, U_{ec}=-17.5 kV. Deep Penning traps are to be found in the region between APE and east cone.

5.3.4.1 Investigation of potential variations at asymmetric magnetic fields

The information gained through ion tracking simulations confirms a scenario, where low-energy ions are stored in the middle of the spectrometer volume for energies below 2.5 keV [Frä08]. The confinement is due to magnetic mirror effects and negative electrode potentials in axial direction, while the radial containment is a result of the rather large magnetic fields in the analysing plane of the pre-spectrometer as compared to the predecessor experiments. These simulations do not take into account interactions with other particles, e.g. charge transfer reactions, inelastic scattering or ionisation. This simulation thus puts credit to the hypothesis that positive ions stored in the body of the spectrometer are the source for the HBB.

To thoroughly test this hypothesis, measurements with asymmetric magnetic fields were carried out[14], with the aim to eliminate the storage requirements in the middle of the spectrometer.

At first the magnetic field on the detector side was ramped up to B=3.44 T while the magnet on the e-gun side was kept at zero field strength. The layout of the magnetic field lines is plotted in fig. 5.28(a). Most of the field lines originating from the detector wafer are directly connected to the inner electrode and the vessel on negative potential. The two red lines denote the maximum radius of 3.4 cm for the pixel H8 and the radius as determined from the ring's structure (r=2 cm) for a detector position at z=2.28 m, the green lines represent once again the radius of the detector flux tube and the ring-like structure detected at z=-2.43 m.

In a first set of runs, inner electrode and vessel were elevated to an equal negative potential with the exception of the west cone to which a more negative potential value was applied to shield the detector from electrons emanating from the vessel and electrode surfaces. With a west cone potential of U_{wc}=-18.5 kV versus a potential of

[14] Elog 387, runs 351ff

Table 5.12: Rate dependence on the west cone electrode potential in the entire energy range and in the ROI [-15,-22] keV. The west cone potential blocks electrons from the wire and east cone electrodes which is visible in a decreasing rate for larger ΔU. For ΔU>0.5 keV no further decrease is observed. The detected electrons are then generated completely in the area of the west cone potential. Parameters: U_0=-18 kV, B=3.44 T, detector position (x,y,z)=(-1.1,-0.35,-228) cm.

Run #	U_{wc} [kV]	U_0 [kV]	U_0-peak [keV]	R_{all} [kHz]	R_{ROI} [kHz]
264	-17.5		17.45 ± 0.01	3.25	2.20
260	-18		17.52 ± 0.01	2.49	1.62
261	-18.5	-18	17.34 ± 0.02	1.15	0.52
262	-19		17.59 ± 0.01	1.09	0.51
263	-20		18.32 ± 0.02	1.10	0.61

the vessel and remaining electrode parts of U_0=-18 kV, an event rate of ∼280 Hz was detected. The previously observed one-step rise in the rate due to an asymmetric magnetic field is recorded which indicates the ignition of the HBB at the start of the measurement. This proves that the HBB effect is independent of the B-field asymmetry. If the west cone potential is decreased to U_{wc}=-19 kV, the rate minimally decreases to approx. 260 Hz but the energy peak shifts from 17.49 keV to 17.84 keV. This indicates that the excess rate is caused by secondary electrons created in the region between the APE and the west cone. This region is influenced by both the potentials of APE and west cone. Electrons from the wire electrode and east side do not reach the detector due to the potential wall at the west cone. As there are no magnetic field lines connecting the detector with the west cone, either an unknown transport mechanism must be present, which enables the electrons to enter the flux tube, or, as described earlier, the electrons are created inside the flux tube. In the latter case a production mechanism is required which explains the secondary electron creation there. By comparing the peak energies with the west cone potential, the second hypothesis of electrons created inside the vacuum of the flux tube is favoured. The peak energy of electrons directly coming from either the west cone electrode or the Anti-Penning electrode does not fit the observed peak energy. Electrons which are created in the vacuum, however, can in principal feature any value in-between.

As long as the west cone potential is more negative than the other electrode parts by more than 300 V, no Penning trap in the west region is created. The east region with the inner electrode cone and the APE elevated to equal potential features a Penning trap of 800 V [Hug08b]. With a magnetic field at the location of the APE end as low as B=1.3 mT, the storage conditions are not expected to be stable, however.

Once the west cone potential is increased to U_{wc}=-18.1 kV, the rate rises to over 4.2 kHz and a Penning trap of ∼100 V [Hug08b] depth is generated at the west side. The change in rate is most likely not caused by the Penning trap but by electrons emanating from the east side electrode parts which are on negative potential. These particles are now able to cross the potential barrier due to a lower potential penetration of the west cone. These secondary electrons are generated by positive ions which in turn are a product of either the Penning trap or the HBB process at the west side. This is supported by the existence of pile-up peaks which are observed in this case, but not for a potential distribution of $\Delta U \geq 0.5$ kV. Only ions and fast neutral molecules can produce several electrons at once[15] [Her65] on impact, which is the cause for the pile-up peaks up to third order [Sch66, Bla71].

The full-energy peak of 17.71 keV is higher as for the electrons created at the west cone with U_{wc}=-18.5 kV. This is another indication for the electrons to originate from the vessel and electrode walls, as electrons created by Penning traps exhibit a larger shift to lower energies.

The spatial distribution of the rate exhibits again a ring structure with an inner circle of pixels detecting a low count rate (fig. 5.29(a)). The ring diameter is reduced from

[15] The emission time is expected to be $<10^{-11}$ s [Kol64]

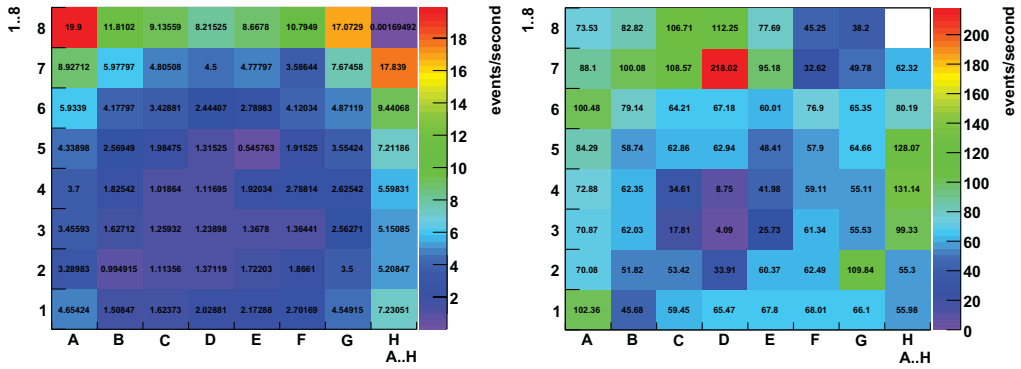

(a) Ring structure: ΔU=0.5 kV (b) Interrupted ring structure: ΔU=0.1 kV

Figure 5.29: Spatial distribution of the rate for a configuration with asymmetric magnetic fields (Run 351). Decreasing the potential difference between west cone and the remaining electrodes results in a weaker shielding effect and electrons released from the vessel walls and electrodes on negative potential are guided to the detector. For more information see text. Parameters: U_0=-18 kV, U_{wc}=-18.5 kV, B_{det}=3.44 T, B_{egun}=0 T, detector position (x,y,z)=(-1.1,-0.35,-228) cm.

2 cm for ΔU=0.5 kV to only one pixel aligned with the centre axis for ΔU=0.1 kV (fig. 5.29(b)). One can observe an above average illumination of pixel D7, which also features stronger pile-up effects in the energy spectrum. Furthermore, the ring structure now seems to be interrupted which is explained with the spatial distribution imaging the right and left halve of the east cone, the interspace can be seen running from pixels B1 to G8.

Ramping down the magnetic field from 3.44 T to 2.58 T causes the rate to drop. A further decrease of the field below the threshold value B_{lim}=2 T again switches off the HBB background altogether.

For a second set of runs (Run 354ff), the potential distribution of the electrodes was changed so that the west cone and the vessel were interconnected while the wire electrode as well as the east cone were supplied independently[16]. With this distribution, a higher count rate is expected as the west cone does not shield the detector any further from the excessive count rate originating from the electrodes. Hence, the detector is relocated to z=-2.43 m for count rate reasons, restricting the monitored area close to the centre axis, which exhibits a smaller count rate as the magnetic field lines connect most of the detector pixels with parts on ground potential.

The potential values are chosen to ensure that the wire electrode is more negative than the east cone potential, with the west cone and the vessel being elevated to a

[16]Supplying more than two independent electrode parts with high voltage can be achieved by using the dipole power supplies which allow to superimpose a positive offset voltage onto FUG3's negative output voltage. Due to safety reasons, the maximum potential difference is |ΔU|=5 kV. More information with regard to the high voltage supply is given in section 3.1.2.

value in-between. For the potential values $U_{wc,vessel}$=-12.0 kV, U_{wire}=-12.5 kV and U_{ec}=-11.5 kV a rate of ∼90 Hz is detected. Decreasing the potential to $U_{wc,vessel}$=-18.0 kV while keeping the potential difference to the electrode parts unchanged, leads to a rise in rate to 17.6 kHz. Corresponding simulations predict an increase in Penning trap depth for the east side from 1.25 kV to 1.8 kV whereas for the west side the depth changes from 100 V to 150 V[17] [Hug08b]. After increasing the potential back to the original value, the rate decreases but stabilises on a much higher level as before, namely 4.8 kHz. A further change of the potential values as well as of the potential difference between east cone and wire electrode involves distinct changes in the background rate, which depend on the Penning trap depth as well as on the potential difference between east cone and wire electrode. As a first principle it can be stated that the deeper the Penning trap, the more positive ions are produced. These then create more secondary electrons on the east side electrodes. Secondly, the more positive the east cone potential is, the less electrons are crossing the potential barrier and vice versa. The fact that the event rate does not drop to the original value of ∼90 Hz implies that the trap in the region of the east cone and APE, which has been deemed unstable due to the low magnetic field, has indeed been fed by the process of applying low potential values, resulting in the activation of a stable trap.

The count rate increase is again observed in the detector segments as a ring-like structure, see fig. 5.30(a), which can be identified as the image of the east cone end next to the wire electrode. The outer pixels beyond this ring are also elevated in rate, but on a lower level as the ring pixels. In contrast, the inner pixels are not affected at all. The pixel A8 and E8 also feature very high count rates hinting at the existence of a second ring-like area beyond the gap of intermediate levels of rate. This may be an indication for a second outer ring, now imaging the beginning of the wire electrode. These effects highlight the importance of a complete coverage of the entire flux tube with a large diameter detector.

The energy spectra of the pixels in the ring and beyond feature pile-up peaks up to fourth order. For the inner pixels, in contrast, only a peak at $e \cdot U_0$ is observed. Again, the existence of pile-up peaks leads to the conclusion of positive ions being created at the west side which subsequently hit the east side electrodes and there release large numbers of secondary electrons.

The measurements were usually finished by ramping the magnetic field down to a lower value of B=2.58 T. The observed decrease in rate is again an indication that the background mechanisms of this measurement exhibit the same characteristics as observed with the high B-field background. The conclusion that a Penning trap like background process in addition to the HBB mechanism is started, is strongly supported by the fact that below B_{lim}=2 T the background rate is still elevated and only the stop of the HBB component is registered. The magnetic field dependence also rules out field emission as the source process, as field emission does not scale with the magnetic field. [Hug08b].

[17] No contribution of the west Penning trap is expected, as the west cone and vessel are connected to the same power supply.

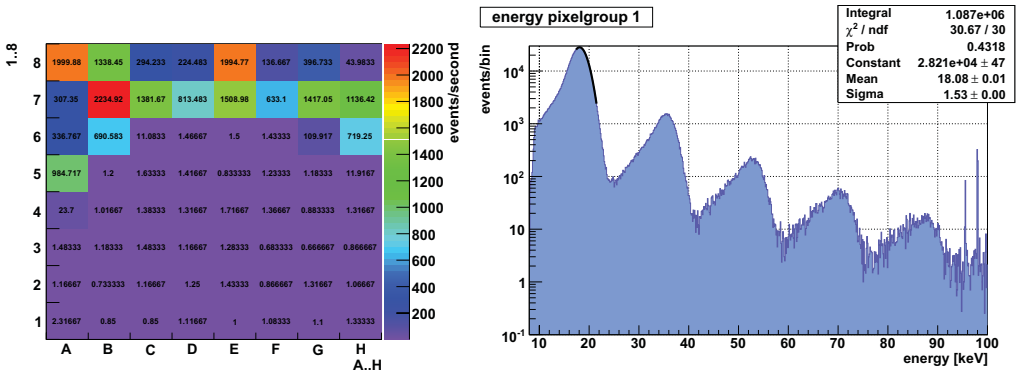

(a) Ring structure at east cone

(b) Energy spectrum for ring and outer pixel

Figure 5.30: Ignited Penning trap in an asymmetric magnetic field set-up (Run 354). With increasing Penning trap depth at the east cone and APE, the rate increases, too. Furthermore, the rate depends on the absolute potential value. This is verified when the potential is decreased to more negative values without changing the potential difference of the different electrode parts.
(a) Ring structure of ignited trap at the east cone/APE region.
(b) Ring and outer pixels feature pile-up peaks up to fourth order, the inner pixels with magnetic field lines connected to parts on ground potential are not affected.
Parameter: $U_{wc,vessel}$=-18 kV, U_{wire}=-18.5 kV, U_{ec}=-17.5 kV B_{det}=3.44 T, B_{egun}=0 T, detector position (x,y,z)=(-1.1,-0.35,-228) cm.

Conclusion The start of the HBB during asymmetric B-field measurements refutes the hypothesis of poitive charged ion storage inside the pre-spectrometer middle volume as the source for the high B-field background. Furthermore, the source process's place of production must be located in the vicinity of the inner electrode cones, Anti-Penning and earth electrode in the pre-spectrometer's entrance and exit region which is supported by the electric dipole field tests of section 5.3.3.1. The investigation of the potential dependence with asymmetric magnetic fields shows that in addition to the HBB effects a Penning trap located at the end of the APE can be brought to ignition.

5.3.5 Pressure dependence

In the course of the Penning trap discussion it could be demonstrated that an increase in pressure exerts a strong influence on the Penning trap production mechanism. The same scenario was tested with the high B-field background. Once again the rise in pressure was achieved by an increased outgassing rate due to shutting off the pumping system, instead of injecting in an inert gas like argon into the vessel.

Contrary to the Penning trap case, the rate increased in parallel to the pressure as shown in fig. 5.31. Also shown is the start of the HBB ignition at a time t=50 s, which was not reproduced in the pressure reading. Only after closing the valves, the pressure increased and simultaneously the detector rate. When the valves were

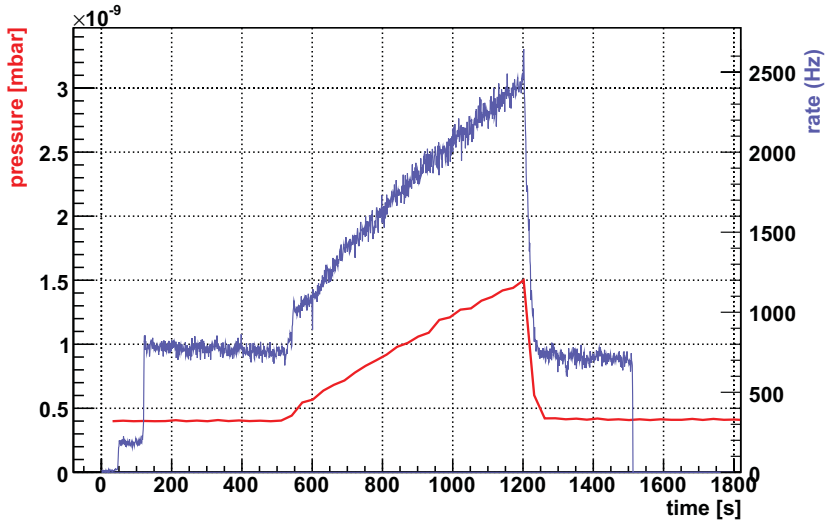

Figure 5.31: Event rates and pressure as a function of time for a pressure rise test (Run 233). Initiating a pressure rise by closing off the pumping system at t∼550 s causes a simultaneous increase in rate. On the other hand, the activation of the HBB at t=40 s is not registered by the Extraktor vacuum gauge. Parameters: U_0=-15 kV, B=3.44 T, detector position (x,y,z)=(-1.1,-0.35,-228) cm.

opened, a fast decrease in pressure restored the initial pressure values after approximately 1 min. The background rate was recovering faster and falls to an even lower value as before the pressure rise. The HBB rate, as shown in fig. 5.31, was slightly decreasing over time, and approached a stable value. This underlying process was unaffected by the pressure increase.

The energy spectra as well as the spatial distribution of the rate do not change significantly before and during the pressure rise. In the energy region above 12 keV, the ratio of the rates of the inner pixels to the ring pixels drops from 3:1 to 2:1, slightly washing out the ring structure. Otherwise the spatial distribution stays exactly the same.

If one searches for a possible correlation of the high pressure regime and the HBB ignition, no such connection is found. The measurements already discussed in section 5.2.5.1 reveal no discrepancy in B_{lim}, even for pressures as high as $4.5{\cdot}10^{-8}$ mbar.

5.3.6 Special effects of the high B-field background

Two unique effects have been observed which are connected to the high B-field background. They are discussed separately in this section.

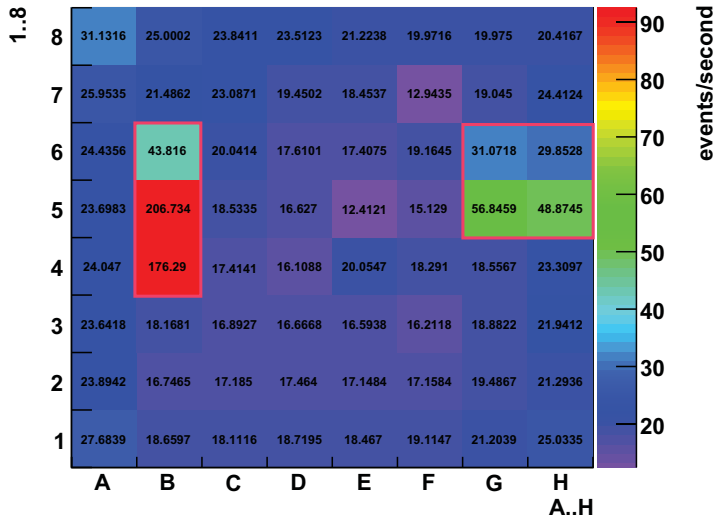

Figure 5.32: Spot-like increase in rate (Run 430). For specific measurement parameters (maximum B-field, east cone more negative) two spot-like increases in rate are observed in the pixel chessboard. Moving the detector reveals this to be a physics effect coming from the spectrometer, as the pixel islands stay fixed in space. The two islands are behaving differently but can be switched on and off by changing the potential distribution or lowering the magnetic field strength. Parameters: U_{vessel}=-18 kV, U_{cones}=-18.61 kV, U_{wire}=-18.71 kV, B=4.5 T, detector position (x,y,z)=(-1.3,0,-228) cm.

5.3.6.1 Pixel islands

The background effects observed so far in the spatial distribution of the rate have been showing a symmetrical distribution around the centre axis of the spectrometer. In particular, electrons emanating from the cone or wire electrodes were detected as discrete ring structures. In connection with the dipole field measurements this pattern changes and low magnetic field measurements also have shown some bias to the upper side of the detector. A new phenomenon, resulting in a spot-like background effect, where only one or a few pixels are illuminated, can be experienced in connection to e-gun measurements. In this section an effect featuring such a spot-like distribution (see fig. 5.32) is discussed.

Two pixel spots, here B4-6 and GH5-6, called 'pixel islands' with a rate considerably higher than the immediate surrounding pixels, are observed under certain circumstances. The configuration comprises a full magnetic field strength (B=4.5 T), necessitating the detector to be moved into the magnet at z=-2.28 m, and a special potential distribution of spectrometer vessel and inner electrode. The excess rate is not caused by an electronics effect. This can be demonstrated by moving the detector in the x-y plane, which also shifts the islands into the neighbouring pixels, see fig. 5.25. Therefore, this is a new physics effect coming from the spectrometer properties.

An investigation of the influence of the potential distribution reveals that the two islands behave differently and are not directly connected to each other. Due to their distinctive shape they are referred to as 'line-spot' and 'quad-spot', e.g. (B4-6) and (GH56) respectively. Both have in common that a potential distribution previously discussed as 'east cone electrode more negative' is required. This also comprises the potential distribution with all inner electrode parts on a more negative potential. Here, the inner pixels monitored by the SPD detect small event rates, while some border pixels are revealed as part of a ring-like structure with large diameter featuring a much higher rate. This gives the impression of a strongly asymmetric spatial distribution of the rate in the pixel chessboard. Additionally, an activation of the quad-spot requires a potential difference $\Delta U \leq 0.4\,kV$, while the line-spot favours $\Delta U \geq 1\,kV$. Both pixel islands can be switched off by choosing a potential difference of $\Delta U = 0.5\,kV$. While this pattern is usually observed for a combined inner electrode potential, one example explicitly establishes a connection to the east cone potential. If one decreases ΔU of the east cone to 0.5 kV, but keeps the value of 1 kV for the remaining inner electrode parts, the increase in rate of the corresponding pixels of the line-spot is switched off. According to this, both islands should not be observed at one time. However, this is not the case. During measurements with the inner wire electrode being 100 V more negative than the inner electrode cones, and 500 V more negative than the vessel, both pixel islands appear simultaneously. Moreover, by decreasing the potential of the inner electrode set-up in 10 V steps, the event rate in the pixel islands is significantly increased further, as compared to the surrounding pixels. One also notices a change in the substructure of the quad-spot for $\Delta U_{cone/vessel} \geq 0.57\,kV$. For lower values ΔU the pixels H56 detect the highest rate, and for higher ΔU these are the pixels GH5.

During the operation of the segmented PIN diode a strong increase in current consumption can be recognised at times. A safety-off circuit, which controls the power supply, switches the diodes off if predefined threshold values are exceeded. A specific measurement was made when the safety-off was not activated. The corresponding data show a higher event rate only in the line-spot pixels. The energy spectra contain unphysical effects, as a result of the pre-amplifiers not operating within the specified working limits. This might be a hint that the pixel islands are generated by the same effect, which also causes the shut-downs of the detector at 0.29 T. Both observations point to an unknown physics effect coming from the spectrometer and not to a malfunction of the electronics, as has already been established above. In the case of the shut-down at low magnetic fields, evidence has been found which supports the theory of ions being the origin. With energies below the energy detection threshold they are likely the cause of the effect, see section 5.1.4.1. A connection between the two effects would lead to the conclusion that negative ions are also generating the pixel islands. The investigation of the energy spectra, however, does not confirm this assumption, as no excess in low-energy events can be observed so far.

Another explanation for the pixel islands, would be a scenario with a broken wire of the inner electrode, which reaches down into the flux tube. Such a configuration could exhibit spot-like features, where electrons created inside the flux tube

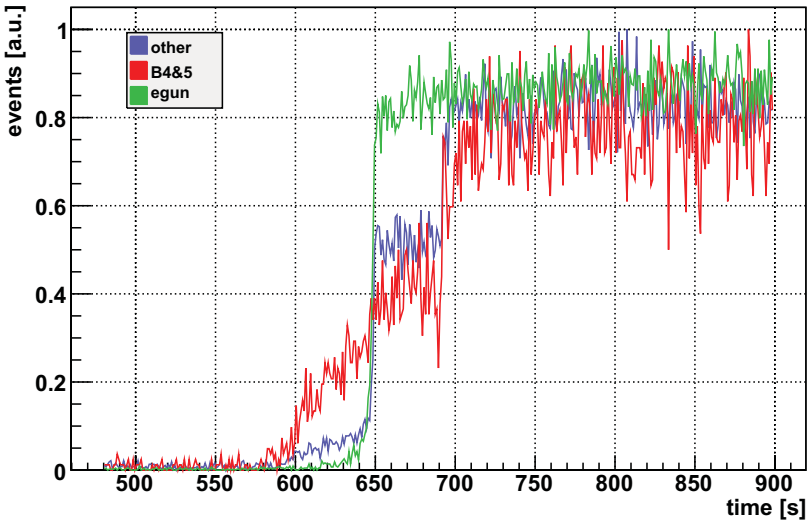

(a) Comparison of normalised rates

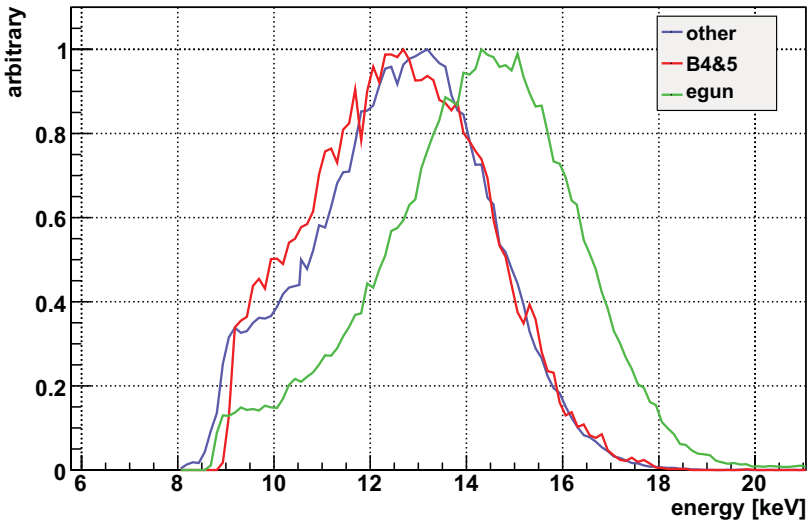

(b) Comparison of energy U_0-peaks

Figure 5.33: Comparison of HBB ignition characteristics for the pixel island configuration, for the e-gun pixel and the remaining pixels (Run 435). Comparing the increase in rate for the island pixels (red) with the other pixels (e-gun: green, other pixels: blue) allows to detect a different HBB ignition behaviour. The other pixels show the characteristic two-step increase in rate, the island pixels' rate increases continuously at the onset of the HBB to the intermediate level and also starts ∼10 s earlier. Parameters: U_{vessel}=-13 kV, U_{cones}=-13.4 kV, U_{wire}=-13.5 kV, B=4.5 T, detector position (x,y,z)=(-1.3,0,-228) cm.

would propagate along the magnetic field lines in direction of the detector. As the magnetron motion would be small, the electrons should impact on the detector in a well-defined area. To exclude a scenario with a defective wire to be the cause for the pixel islands, the inner electrode has been visually inspected via the DN160 side-port and the three chimneys' DN40 view ports. No damages or suspicious discolorations hinting at severe discharge effects have been detected. An endoscopic inspection of the eastern cone, the Anti-Penning and ground electrode has been carried out, but due to the limited resolution and maneuverability no additional information could be revealed. However, during a maintenance period, the western APE and ground electrode have been dismounted and visually inspected, showing no change in the surface condition.

The high B-field background ignition has also been investigated with regard to the time dependence of the e-gun pixel and pixel islands, see fig. 5.33(a). During activation of the HBB the e-gun pixel together with the remaining pixels exhibits the same ignition characteristics: a small continuous increase in rate leads to the typical two step rate-increase. The pixel island's event rate shows a different time behaviour. The rate starts to increase approximately 10 s before the other pixels and the increase to an intermediate level is not abrupt but continuous. Comparing the U_0-peak energies (fig. 5.33(b)) for the three different groups, a higher energy of the e-gun background is detected, while the difference between pixel island and remaining pixels is not significant.

Conclusion The mechanism creating this spot-like increase in rate has not been discovered. Assuming a connection to the high B-field background seems likely, however, the activation requirements are very specific and even more restrictive as for the HBB. Furthermore, the two observed pixel islands exhibit a different dependence on the potential distribution. Both can be activated and inactivated by choosing a specific potential distribution. Ignition times at full magnetic fields have been found to be very small in the order of seconds. The measurements have proven that the pixel islands are a physics effect and not a malfunction of the detector, further conclusions cannot be drawn at the present moment without additional information.

5.3.6.2 High-energy tail

During the time period of the investigations of pressure induced effects (see sections 5.3.5) a new effect did show up when the magnetic field was applied and the electrodes were elevated to a negative potential. Instead of an energy spectrum with only few events in the bins beyond the U_0-peak, the spectrum continues up to the overflow bins, featuring an exponential decline in the number of events, see fig. 5.34(a). All pixels share this exponential decline at the high energy domain, except one pixel right next but not identical to the centre pixel[18], e.g. in run 194

[18]The centre pixel is defined as the pixel which is hit by the e-gun beam in $\alpha_x = \alpha_y = 0^\circ$ position. The centre pixel in itself is not well-defined with regard to a discrete pixel number, it depends not

pixel D3 and centre pixel D4 at z=-2.7 m. Interestingly, this pixel D3 features no high-energy tail at all, see fig. 5.34(c).

If the high-energy event rate (R(E>30 keV)) is compared with the low-energy event rate (R(E<30 keV)), the production rate of the former starts to increase only after a period of 10 minutes, while low-energy event rates increase simultaneously with the pressure. This leads to the conclusion that the pressure increase is vital for the production mechanism of high-energy events. This is supported by the energy-over-time scatter plot (fig. 5.34(e)): the production of high-energy events starts simultaneously with the pressure increase but is rather suppressed, as the rate for events higher than 30 keV does not increase initially. There is clear evidence that the higher the pressure rises, the more high-energy events are created and the higher the energies of these events can get. The spikes which are visible in the energy-over-time and rate histograms are not caused by one of the above discussed background mechanisms. In fact, these spikes are attributed to a pressure increase[19]. The spikes are also visible in the pressure graph and are perfectly reproduced by the gradient of the rate, as well as by the energy-over-time plot. This is a clear indication that higher pressure furthers the production of high-energy events. These spikes are thus no prerequisite for an activation of this process.

The corresponding rates are distributed homogeneously over the pixel chessboard for both high and low-energy intervals and thus gives no further information on the production process.

When the detector is retracted into maintenance position one observes only a very small flux tube around the spectrometer centre as compared to a z-position near the magnet. Even in this position only one pixel is free of this background effect. This leads to the conclusion that a disc with a small radius around the spectrometer's centre axis is not affected. Moving the detector in direction of the magnet should thus result in enlarging the area viewed by the detector and thus even Pixel D3 should detect the effect.

No dedicated measurements to investigate this effect could be carried out so far. Nevertheless, by cross-checking all measurements, the minimum requirements can be specified to the following conditions:

- high pressure ($> 5 \cdot 10^{-10}$ mbar)

only on x- and y- but also on the z-position of the detector. The detector at a position with lower magnetic field, e.g. maintenance position, will detect the e-gun electrons in a different pixel due to the influence of the earth magnetic field.

[19]The increase in pressure is most likely caused by problems in the liquid nitrogen cooling of the SPD. The insulation vacuum inside the flexible cooling pipe degenerates over time and has to be renewed. Insufficient insulation may cause a reduction in cooling power on short time scales thus not completely interrupting the laminar flow. The loss in cooling power results in an increase in detector temperature, ultimately leading to higher outgassing of the detector. More likely, however, is that the detector is unaffected by the temperature increase and only the cooling tube, which acts as a cryogen pump, desorbs frozen-on water for this short time interval, which is detected by the vacuum gauges. In measurements exceeding run number 183, these periodic pressure increases have not been observed anymore.

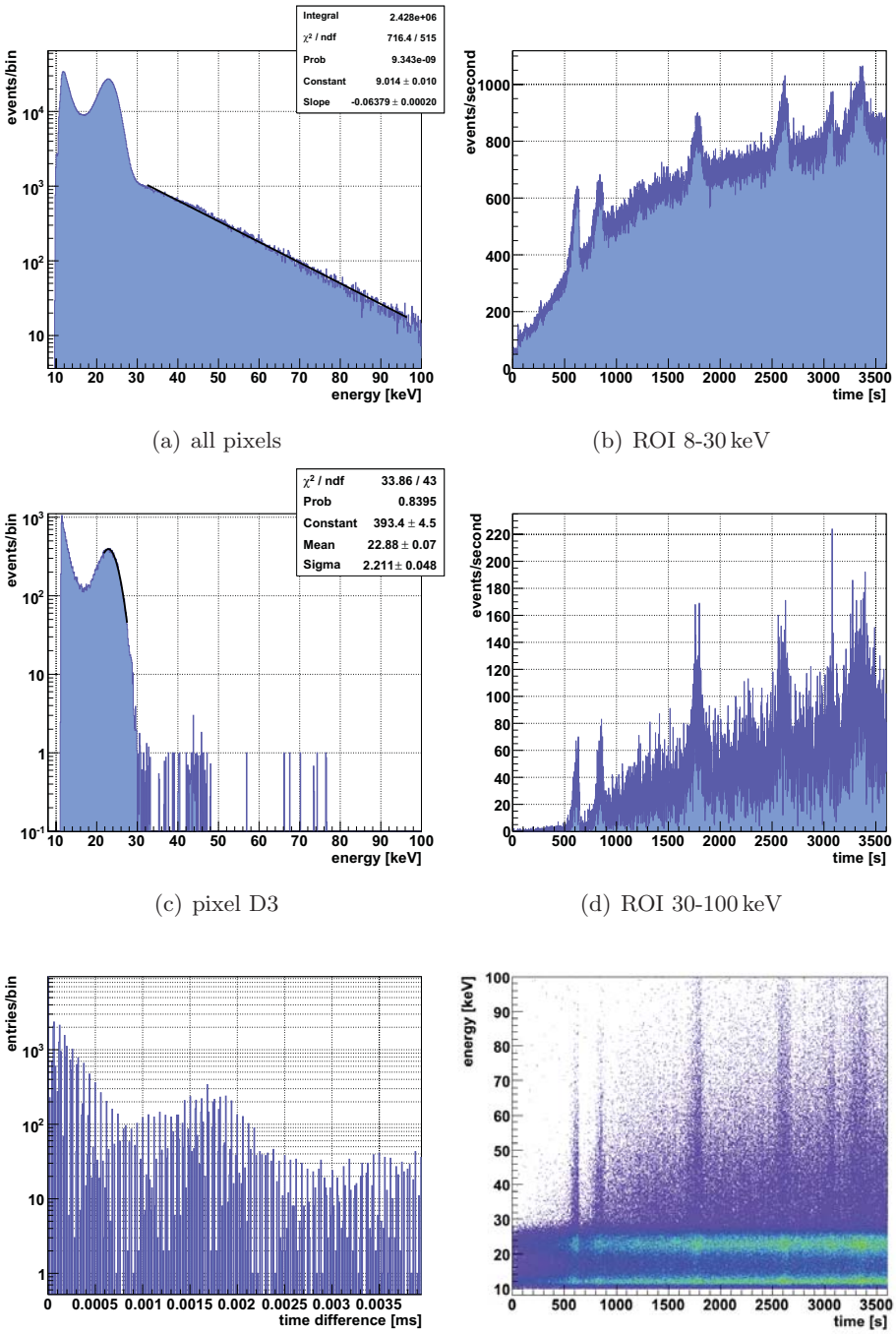

(a) all pixels (b) ROI 8-30 keV

(c) pixel D3 (d) ROI 30-100 keV

(e) all pixels (f) all pixels

Figure 5.34: High-energy tails during pressure rise measurements. The rate increases simultaneously with the pressure (b),(d). All pixels except one (D3) near the spectrometer centre show an exponential slope of the event rate up to the overflow bins (a),(c). This is caused by massive pile-up effects as is shown by the time difference structure (e). The spikes visible in the rate and energy-over-time graph are caused by periodic pressure increases not connected to the high-energy tail effect.

- active HBB
- inner electrode elevated to more negative potential than the spectrometer vessel

Additional information is gained by checking the time difference between events. For time differences of $\Delta t > 1\,\text{ms}$ only an exponential decrease in events per bin is visible, as is expected for a random process obeying the Poisson distribution. For smaller values a different picture is drawn. In fig. 5.34(e) the time differences for $\Delta t < 3.5\,\mu\text{s}$ are plotted. Now, the events exhibit a beat-like structure: a modulation of the number of entries per bin is visible with two different superimposed frequencies. With this information, one can conclude that the events in the higher bins of the energy spectrum, which are featuring an exponential decrease, are caused by pile-up of events of many different energies. Corresponding pile-up effects of the U_0-peak are observed, too, but in this case higher order peaks are created in the spectrum.

Conclusion The source creating this effect could not be identified so far, however, it is likely to be connected to the production mechanism of the HBB. More difficulties for the description of the effects taking place are added by the fact that an active HBB process in connection with high pressure does not suffice to create this effect. Once again, a difference in the potential of inner electrode versus vessel is required. An increase in pressure can positively influence the ionisation of residual gas molecules in a large area and encompass a wide spectrum of potential values. Thus secondary electrons are accelerated to different energies before hitting the detector. On the other hand, it is necessary that the electrons are created simultaneously, otherwise the pile-up effects would be lessened.

5.3.7 High B-field background conclusion

A major source of background in the measurements with the pre-spectrometer has been identified and labeled 'high B-field background'. The basic parameters are a minimum magnetic field strength of $B_{lim} \gtrsim 2\,\text{T}$ and a negative potential applied to the spectrometer electrodes. The detected background rate depends not only on the magnetic field strength but also on the absolute potential as well as on the potential distribution over the six inner electrode parts in combination with the spectrometer vessel acting as guard electrode, as well as the residual pressure inside the vessel.

Experimental investigations, in particular by employing asymmetric magnetic field configurations in conjunction with activated dipoles, and supported by simulation efforts, allow to pin down the place of HBB secondary electron production to the entrance and exit regions of the spectrometer. It has been further established that the particle traps of the exit and entrance region can be brought to ignition separately and are thus in principal independent from each other.

The primary production mechanism could not be identified. The strong pressure dependence as well as the ignition time characteristics leads however to the conclusion that charged particles are stored in a trap, possibly emitting positive ions and UV photons, which then create secondary electrons with energies close to but not identical to the electrode potential. All things considered, this strongly indicates a place of secondary electron production inside the detector flux tube.

A hypothesis details the possibility of UV light coming from a Penning trap as possible source of the HBB component [Mer09a]. Many features of the HBB can be explained, however, a main feature, the ring-like structure, of the HBB is untypical for a photon created background, for which a uniform distribution is expected.

The exact transport mechanisms are also not identified at present but are deemed to exhibit the same basic dependencies on magnetic field strength, potential and pressure as normal background processes.

Finally, it has to be stated that all attempts to deactivate the HBB component by changing the measurement parameters have so far been unsuccessful. This is to some part the result of the robust starting parameters of the HBB, in particular with regard to the starting value of the magnetic field, which remains constant even for higher pressure.

5.4 Background processes at the e-gun system

After implementing the changes described in section 3.4, the e-gun was tested in low magnetic fields and was found to work as intended. However, there was one limitation: after the activation of the ATMION^{TM} vacuum gauge installed at the e-gun chamber, background events of several kHz were created as soon as high voltage was applied to the e-gun tip and a sufficiently strong magnetic guiding field was present. This effect does not require the deuterium lamp to be switched on and therefore is not connected to the electrons which are created by the e-gun itself. The background events are likely to be created by positive ions emitted from the hot cathode vacuum gauge instead. Although the gauge has no direct line of sight to the parts elevated to negative potentials, some ions may reach the metal cap and release several electrons on impact. These electrons would be guided by the magnetic field in direction of the detector, where they would arrive in a very small time window. Thus they would create multi order pile-up peaks besides increasing the background at $e \cdot U_{egun}$ in the energy spectrum. If the vacuum gauge is turned off, the excess rate detected by the SPD is eliminated. Simulations which verify or refute this hypothesis, are planned.

A similar effect is observed as soon as the e-gun is put on high voltage: the background rate in one or more of the SPD pixels (depending on the magnetic field strength) is increasing by a factor 10-100. This background exhibits the same characteristics as the one described above. Only this pixel is affected which is connected by magnetic field lines to the e-gun tip and cap. The energy spectra reveal several

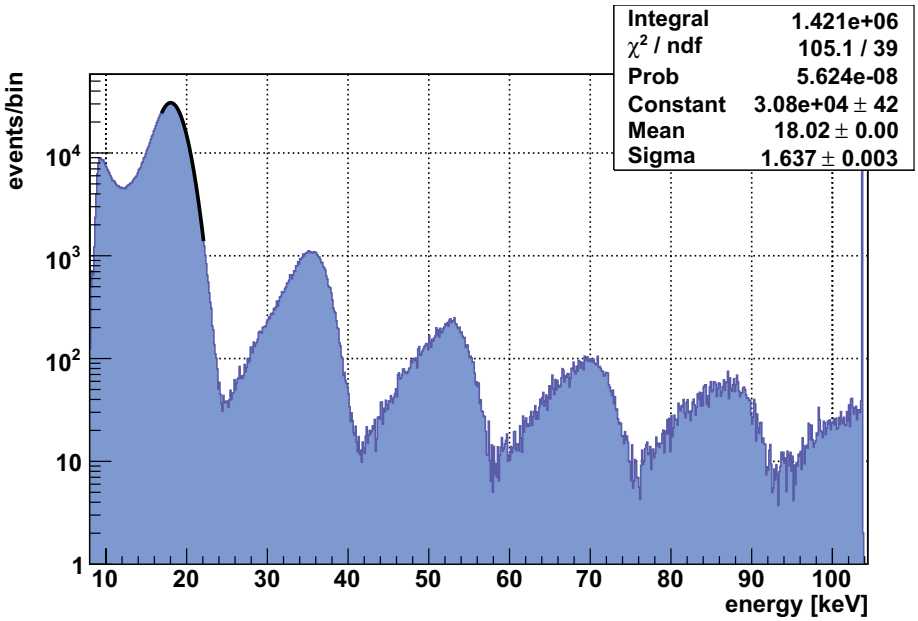

Figure 5.35: Energy spectrum of e-gun induced background (Run 420). The activation of the e-gun background requires an elevated high potential of the e-gun. A sufficiently strong magnetic field causes the background to be detected by the SPD. Either one ore more pixels (depending on the B-field strength) are illuminated, with the events clearly coming from the e-gun cap and tip. The energy spectra reveal multi order pile-up peaks up to the overflow bins. Parameters: U_{vessel}=-18 kV, U_{cones}=-18.5 kV, U_{wire}=-18.6 kV, U_{egun}=-18.6 kV, B=4.5 T, detector position (x,y,z)=(-1.3,0,-228) cm.

higher order pile-up peaks, depending on the e-gun potential. The activation of this background process is not connected to the pre-spectrometer, e.g. the increase in rate starts even if the pre-spectrometer is connected to ground. The magnetic field strength does also not change the activation in general.

If the e-gun is moved either horizontally or vertically by angles α_x and α_y, the connecting magnetic field lines are changed and thus also the pixel which detects the increase in rate. Judging from the energy information and the observed pile-up effects, the detected particles have to be electrons. Once the potential of the spectrometer is decreased below that of the e-gun, the excess events in the corresponding pixel vanish, as the background-inducing electrons are blocked by the potential barrier.

One can exclude a scenario with positive ions reaching the metal cap, in analogy to the case of the vacuum gauge. Any positive ions created by the HBB process would have to leave the spectrometer's negative potential, which is highly unlikely given the opening dimensions of the focusing lens and the distance of the e-gun to the vessel. Electrons can be equally excluded, as the e-gun tip in this scenario has to be more negative. In this case electrons coming from the pre-spectrometer vessel are repelled. This leaves fast neutral molecules with energies of up to several keV

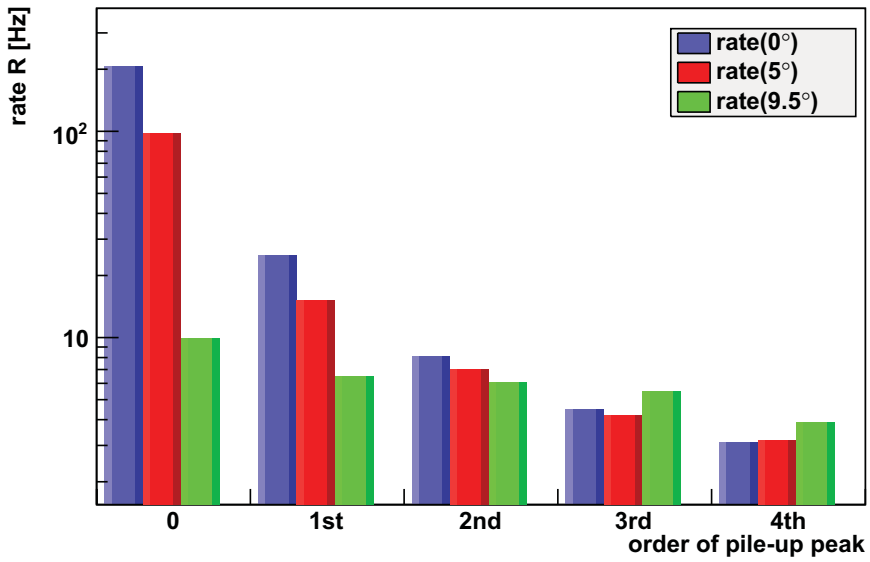

Figure 5.36: Investigation of the HBB induced e-gun background at different e-gun positions (Run 324). Moving the e-gun out of the centre axis by 5° and 9.5° changes the background rate as detected in the e-gun pixel. The decrease in rate is more pronounced in the main peak as compared to the higher order pile-up peaks. Parameters: U_0=-18 kV, U_{egun}=-18.5 kV, B=3.44 T, detector position (x,y,z)=(-1.1,-0.35,-228) cm.

as a potential origin. Positive ions created as a part of the HBB process are subject to charge transfer reactions. Once they are stripped from the positive charge, the fast neutral molecules are able to leave the spectrometer in direction of the e-gun, releasing electrons there from the metal cap or e-gun tip in the same way as positive ions would do.

This hypothesis of fast neutrals can be tested by changing the e-gun position. According to this theory, moving the high voltage parts away from the centre axis is expected to drastically decrease the rate in the detector, as the molecules with much higher mass than electrons are only weakly guided by the magnetic field. Instead of following the magnetic field lines, which are fanning out as the magnetic field strength is getting smaller, the ions are moving straight on and thus miss the e-gun cap and tip. In fig. 5.36 the rate as a function of the effective angle of the e-gun relative to the centre axis is given for the main peak and all the observed pile-up peaks in the energy range of 8-100 keV. The graph reveals that with higher angle relative to the centre axis the main peak's rate decreases most strongly, whereas for the higher order peaks a slight increase in rate for large angle positions is observed. In the light of these results, the hypothesis of fast neutral molecules as background generator can be discarded, as the rate in the pile-up peaks should be equally reduced, which is not the case. Nevertheless, if the e-gun is moved away from the

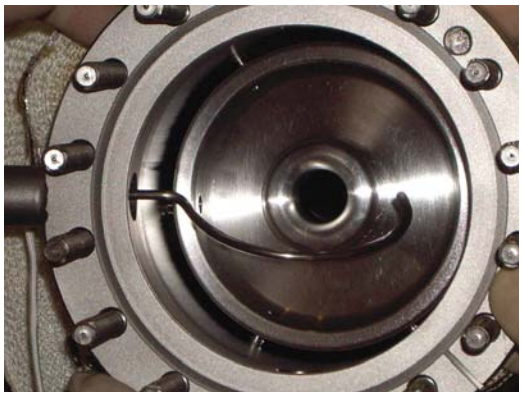

Figure 5.37: Photograph of the wire scanner in out-of-beam position. The wire scanner, a semi circular wire of 2.5 mm thickness, is built in between focussing lens and e-gun tip. It is pneumatic driven and remote controlled via SCS. By sweeping the wire through the e-gun electron flux tube stored particles are expected to be removed.

centre axis the detection rate is influenced.

An alternative explanation would be UV light photons created by the active HBB. This effect is also able to release electrons from the e-gun cap and tip by photoelectric effect. However, only one electron is generated at a time. Moving the e-gun would limit the number of photons which still reach the e-gun parts on negative potential and thus lower the background rate. The pile-up events would have to be created as a result of photon bombardment of very high intensity. For this to happen, the difference in event rate of main peak to first order peak is much too low with only one order of magnitude. X-ray photons of high energies in the keV range could also lead to multiple electron emission but a theory where or how these may be created is missing.

Further investigations aim at removing possible trapped particles in the volume of the e-gun chamber. Using the Pneumatic Blind and Shutter System, see section 3.4.2, has no positive effect on the background rate. Another attempt at removing trapped particles is discussed in the following section.

5.4.1 Investigation of removing trapped particles in the e-gun chamber using a wire scanner

The operation of two MAC-E filters in a tandem set-up automatically entails the creation of a Penning trap of large depth in-between. Stored particles will at some point affect the measurements due to an increased background rate. Corresponding simulations have determined that the background rate from a single trapped electron at starting energy E_{start}=18 keV is of the order of 10 kHz [Glü08]. Due to the rather large timescale of the electron multiplication of the order of hours, it should be possible to empty the trap without significantly reducing the running time. Investigations using a so-called 'wire scanner' to remove trapped charged particles by sweeping a wire through the trap volume have been carried out at the Mainz spectrometer and the results have proven the feasibility of this method [Val09].

In the pre-spectrometer test set-up, a similar trap is created between the spectrometer vessel and the e-gun when both are elevated to a negative potential. Another

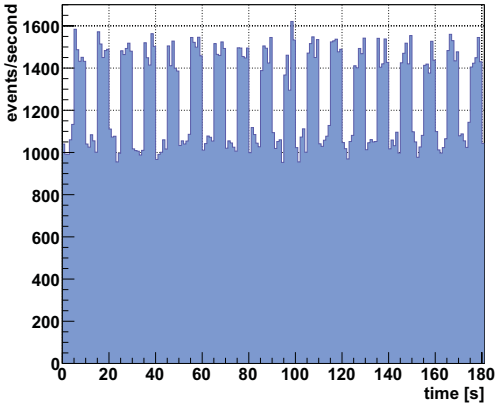

Figure 5.38: Modulation of the e-gun rate by using the wire scanner (Run 497). Using the wire scanner has no positive effect. The rate, which is reduced when the wire is passing through the electron flux, recovers instantly after the sweep through to it's original value. Parameters: U_0=0 kV, U_{egun}=-18 kV, in-beam/out-of-beam (5,5) s, B=1.72 T, detector position (x,y,z)=(-1.3,-0.5,-270) cm.

combined trapping process, coupling magnetic mirror and potential trapping, also exists at the e-gun set-up.

To test the possibility of trapped particles in the e-gun chamber, a wire scanner has been built and installed between the focusing lens and the e-gun tip, see fig. 5.37. The wire is bent in a half circle allowing to position it in and out of the e-gun electrons' flux tube. The wire is pneumatically driven and remote controlled by the SCS. A manual operation is not possible as the wire scanner is inside the dry air cabin which is locked during measurements with the vessel being on high voltage. The rotation of the trapped particles around the axis, as described by the magnetron motion, takes of the order of μs to fulfil one revolution. This is fast enough to ensure that any stored particle hits the wire and is removed from the trap within an active scan interval of merely a few seconds. Therefore, if any stored particles are present, they should be removed by the scanner. The wire scanner has been tested with different time intervals for the wire being in and out of the beam, the maximum rate by which the wire can be swept through the beam is several Hz. A faster movement is not possible due to the pneumatic operation of the movement. Unfortunately, no tested setting has had any positive effect on the e-gun background, an example is presented in fig. 5.38. If the wire is fixed inside the beam, the rate is reduced, however, when moving it out again, the rate recovers instantly to its original value. Trapped particles inside the e-gun flux tube are therefore also excluded as possible background source.

The focusing lens is connected by magnetic field lines to the metal cap of the e-gun set-up. Therefore, electrons released from the cap are guided to the blind on ground potential made of stainless steel. In close analogy to the problem with the earth electrodes of the pre-spectrometer, an electron bombardment of the blind could result in UV light emittance (see the discussion of the earth electrode material in section 3.1.2.1). However, once the stainless steel blind is exchanged with a blind made of aluminum, no effect could be detected either.

After many possibilities were ruled out only a few options remain. A remaining

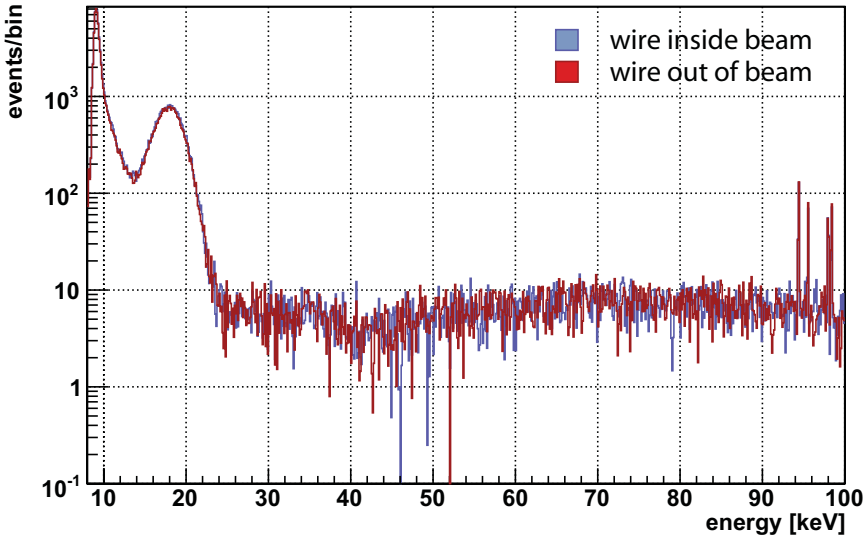

Figure 5.39: Investigation of the Penning trap between the spectrometer and the e-gun (Run 528). The Penning trap between spectrometer and e-gun is filled with e-gun electrons of energies slightly below the retarding potential value. A comparison of the rate as well as the energy spectrum does not exhibit any difference between periods with wire inserted into beam (blue) and wire outside of beam (red). Parameters: U_0=-18 kV, U_{egun}=-17.968 kV, B=1.72 T, detector position (x,y,z)=(-1.3,-0.5,-270) cm.

scenario includes positive ions stored in a corner of the e-gun chamber, where the wire scanner has no influence. Recent efforts are thus concentrating on further investigations of the possibilities of particle trapping inside the e-gun chamber with the help of dedicated simulations. It is expected that information gained thereby will help solving the problem of the e-gun background.

Additional tests are aimed at determining the possible influence of the Penning trap between the pre-spectrometer vessel and the e-gun. For this purpose, e-gun electrons are generated with a slightly more positive potential than the pre-spectrometer's retarding potential. As a result, the electrons are not transmitted but stored in-between the pre-spectrometer and the e-gun, thus potentially filling the Penning trap. Longtime measurements comparing the rate with the wire inserted and the wire outside the electron beam do not show any significant change (fig. 5.39):

Run #	wire position	duration [h]	e-gun pixel [mHz]	other pixel [mHz]
528	in-beam	8	3.9	233
528	out of beam	8	3.5	207

Considering the fact that the flux tube of the Penning trap between pre-spectrometer and e-gun is considerably smaller than the trap between pre- and main spectrometer (by a factor 2900) one can conclude that the trap is likely too small to see an effect as a result of the wire scanner operation.

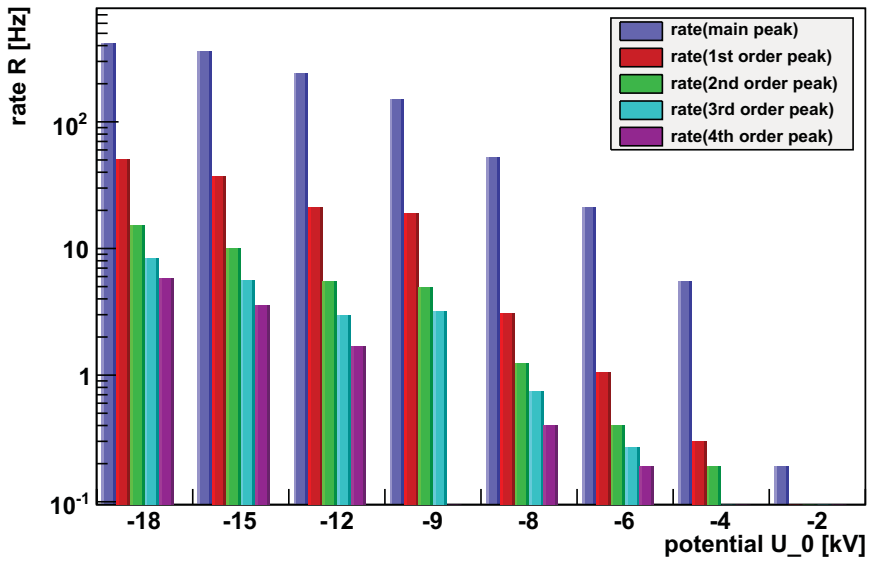

Figure 5.40: Probing the potential dependence of the high B-field background for low potential values up to -10 kV (Run 338ff). Effects of the HBB at low potentials cannot be detected by the SPD directly. Using the pile-up peaks of the e-gun background allows to probe the potential region between zero and -10 kV. The rate is continuously decreasing, showing no sign of threshold with regard to the high B-field background. Parameters: B=3.44 T, detector position (x,y,z)=(-1.1,-0.35,-228) cm. Data taken from [Hug08a]

5.4.2 Probing the potential limit of the high B-field background

In the normal mode of operation, the SPD cannot detect events with energies below ∼10 keV. This limits the gain of information of measurements with potential values which are less negative than -10 kV, in particular no information regarding the High B-field background can be gained. However, with the help of the higher order pile-up peaks from the e-gun background component, which are discernible to high energies, it is possible to probe the interesting regime between 0 kV and -10 kV indirectly[20].

In the corresponding measurements, the e-gun was elevated to a more negative potential as the spectrometer potential. The secondary electrons created by the e-gun background process were transmitted to the detector, which subsequently registered an increased rate in the corresponding e-gun pixels. The energy spectrum, for an example see fig. 5.36, features multiple pile-up peaks which are discernable up to the fifth order. When the potential of both e-gun and spectrometer are increased in steps, the U_0 and pile-up peaks are shifted in the spectrum to lower energies. Calculating the rate for the specific peak location allows to determine the decrease in rate in dependence of the spectrometer potential. The results are presented in

[20] Elog 378, 392

fig. 5.40. A continuous decrease of the rate with increasing potential is observed. Furthermore, the data shows no significant limit or threshold, at which the rate abruptly breaks down. An elevated rate is still visible at -2 kV. The HBB component leads to an additional increase in the e-gun pixel, which is discernible in the number of events of each pile-up peak. Thus it is possible, even for very low potentials, to detect an increase in rate due to the high B-field background. As the measurement suggests, the rate in the pile-up peaks decreases continuously, it can be inferred that the HBB is still active for potentials more positive than -10 kV. There seems to be no specific potential limit setting the high B-field background to stop or start working.

5.4.3 Conclusion

The elevated rate in the e-gun pixel is caused by secondary electrons created at the e-gun tip and cap which are accelerated in direction of the detector if the magnetic guiding field is sufficiently strong. The measurements feature multi order pile-up peaks and a generic rate dependence on the e-gun angle. Various trapped particle removal efforts were undertaken, albeit with limited success. A number of possible creation mechanisms have been excluded:

- positive ions and fast neutral molecules coming from the spectrometer
- UV light coming from the spectrometer or the focusing lens
- trapped particles in e-gun flux tube

Corresponding simulations, which will closely inspect the areas in the e-gun chamber outside of the electron flux tube, will allow to gain more information with regard to ion trapping. A discovery of a trapping mechanism inside the e-gun chamber could explain the secondary electron emission, which is attributed to positive ions or fast neutral molecules due to the pile-up structure of the energy spectra. This feature is not expected for photons created either by the photoelectric effect, field emission or thermionic emission [Her65, Glü09c].

5.5 Conclusion & outlook

The numerous changes which have been made to the pre-spectrometer set-up have had two major results. First, the expected Penning trap at the end of the newly installed Anti-Penning electrode has been found to ignite under specific conditions. While these conditions may interfere with dedicated measurements of the transmission properties at the pre-spectrometer test set-up, they are of no concern for the pre-spectrometer operation in the final KATRIN set-up.

Apart from the Penning trap, which can be controlled by using an optimised potential distribution in which the inner electrode is elevated to a more negative potential,

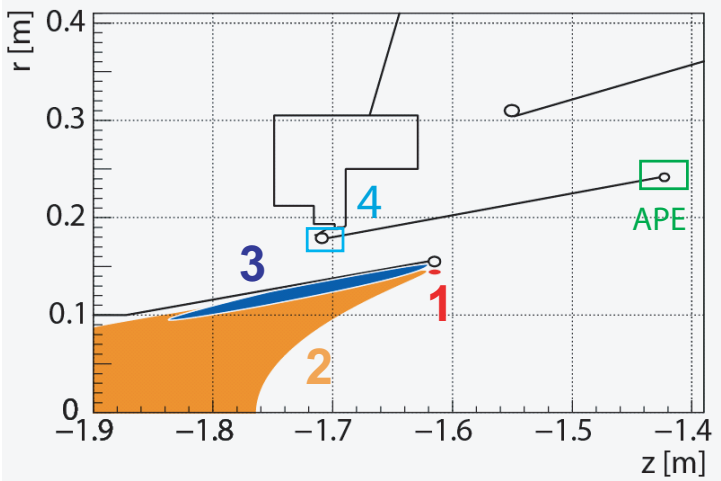

Figure 5.41: Cutout of the pre-spectrometer entrance region showing the locations of identified particle traps. Simulations revealed several locations where particles in principal can be stored. (APE) remaining Penning trap at the Anti-Penning electrode end-ring (1) Penning trap at earth electrode end-ring (2) hybrid trap resulting from magnetic bottle and potential barrier (3) positive ion trap (4) Penning trap at inner APE ring. Figure adapted from [Frä09]

a small but discernible increase in background rate has been detected when magnetic fields are active and electrodes are elevated to high potential.

The main subject of this thesis, has been the detailed investigation of a new background process which starts when the pre-spectrometer electrodes are elevated to a negative potential and the magnetic field strength exceeds a threshold value of 2 T.

A multitude of measurements have been conducted to investigate the characteristics of this background effect, which was already observed at the Mainz experiment. The experimental investigations also supported by on-going simulation efforts attribute the background rate to stored charged particles inside a trapping mechanism, which likely produces positive ions and UV light. These primary particles are then creating secondary electrons inside the detector flux tube. The complex production and transport mechanisms are not completely understood at the present moment. However, the place of production can now be attributed to the region between inner electrode cones, ground and Anti-Penning electrode.

Recent simulations concentrating on the exit and entrance region of the spectrometer yield new information. Several additional locations and mechanisms have been found [Hug08c, Zac09, Frä09], explaining that electrons and ions are stored and thus can cause an increase in background rate, see fig. 5.41. This has prompted a second change of the inner electrode set-up, foremost by changing the earth electrode of the spectrometer's west side only. The Penning trap which is located at the end-ring of the earth electrode facing the flux tube (similar to the trap of the APE) has been eliminated by moving the ring to larger diameters. In this new geometry,

no dip in the potential field in direction of the flux tube is created. The measurements following the change in set-up, now referred to as PSIII, have led to an even higher background rate. While changing the earth electrode with the aim to eliminate the trap facing the flux tube, a deeper Penning trap has been created on the electrode's outside. Due to the strong correlation of changes in the set-up and the resulting increase in background rate, the HBB effect is expected to be connected to the Penning trap at the earth electrode. All efforts are now aimed at eliminating all the identified traps by constructing an earth electrode, which features no protrusions which could be the source of additional Penning traps. In particular, it will follow in its outline the magnetic field lines thus preventing the creation of ion traps [Frä09]. In parallel, a different method of removing any trapping conditions in the entrance region is realised. This second hardware modification to remove the trapping problem will introduce an insulator on the outer surface of the earth electrode, which will feature a metallised surface facing the Anti-Penning electrode. The metallic insulator surface, vessel and APE are interconnected and thus share the same potential. This configuration eliminates possible trapping conditions by shifting potential differences between inner electrode cones and the APE, along the z-axis deeper into the spectrometer centre, where the magnetic fields are lower and the trapping possibilities are smaller.

With the implementation of the two modifications it is expected that the conditions for the high B-field background mechanism and also for the 'normal' Penning trap process are eliminated. Following these modifications, the electromagnetic measurements with the pre-spectrometer test set-up will be completed by precise transmission measurements before the pre-spectrometer is finally relocated to its final location close to the main spectrometer at the end of 2009.

The modifications performed in the framework of this thesis are of central importance for a better understanding of MAC-E filters as high resolution low background spectrometers for low-energy electrons in the keV range. In this regard, the identification and minimisation of the depth of Penning traps paves the way for the layout of the much larger main spectrometer with its much higher energy resolution. Only by completely eliminating all potential Penning traps will the KATRIN experiment be able to achieve its low level of background in the few mHz range and to measure ν-masses in the cosmologically important mass range down to 200 meV.

Appendix A

Ultra High Vacuum

To create a vacuum in a recipient a variety of vacuum pumps exists which can be ordered from different companies. The pumping concept and therefore the pump itself has to be chosen according to the medium which has to be pumped out of the recipient and on the end-pressure which has to be reached[1]. Furthermore, it has to be considered that the end-pressure constitutes an equilibrium of the molecules which are constantly removed from the recipient's inside by the pump and of the molecules getting back in, either by back-diffusion through the pump itself or by outgassing from the materials residing in the inside. To achieve hydrocarbon free UHV standards only a small list of selectable materials exists. These materials exhibit only very small outgassing rates, examples are metals like stainless steel and oxygen free copper as well as certain ceramics used for isolators. Plastics and other organic materials on the other hand, are not allowed at all due to the outgassing of hydrocarbons. Before an unknown material or a device of unknown components is used it has to be screened in a test facility. This is done by enclosing it in a test recipient which is pumped down to the designated pressure. If the outgassing is too high the end-pressure won't be reached at all. Alternatively, a residual gas analysis (RGA) can be carried out at lower pressures checking the percentage of hydrocarbons contained in the spectrum. If the contamination with hydrocarbons exceeds 1% of the total spectrum the device or material is not fit for UHV use. Nonetheless conducting an RGA even if the designated pressure is reached is standard procedure when UHV standards apply.

[1] The following vacuum regimes are differentiated: low vacuum (LV, 1000 to 1 mbar), medium vacuum (MV, 1 to 10^{-3} mbar), high vacuum (HV, 10^{-3} to 10^{-7} mbar), ultra high vacuum (UHV, $< 10^{-7}$ mbar).

A.1 Vacuum sealing techniques used at the KATRIN experiment

Depending on the vacuum range and the temperatures the material has to resist, different sealing options for joining two vacuum components together exist.

A.1.1 Dimension designation

Designation of the flange diameter differs in the North American (NA) are as compared to the European/Asien (E/A) area. NA specification lists the outer diameter in inch while E/A specifies the inner diameter in millimeter. In Europe/Asia the size designation is prefixed with either DN or NW depending on manufacturer. However, DN is commonly acknowledged. A 4-1/2" O.D. flange according to NA standards is known as DN63 or NW63 [Kur09].

A.1.2 Klein flanges and seals

The Klein flange (KF) type is used for joining small diameter vacuum components ranging from DN16 to DN50 together. The flanges on both sides are plane with a gasket placed in-between. Flanges and gasket are held in place by quick-release elements. Gaskets include a centering ring which is either inside or outside of the sealing material, which is usually made of Viton®[2]. The use of Viton® limits the pressure range to high vacuum regions due to the permeability of the elastomers and the limited heat resistance of roughly 140°C. Gaskets using silicone claim to possess higher temperature limits. However, these claims could not be verified: being exposed to temperatures above 200°C the sealing ring starts to melt and sticks to the metal.

A.1.3 ISO-K seals

The ISO-K standard is similar to the KF standard identical partners are connected by inserting a gasket ring, either made of Perbunan®[3] or Viton® [Alt08], held in place by an outer and inner centering ring. The outer ring is interrupted to allow efficient leak testing of the seal. The two flange partners are held together by a number of clamps according to the diameter or a collar ring. Bake-out temperatures and leak rates are limited by the gasket material as specified above.

[2] A fluororubber registered with DuPont Performance Elastomers [Zru09].
[3] A nitrile rubber registered with DuPont Performance Elastomers [Zru09].

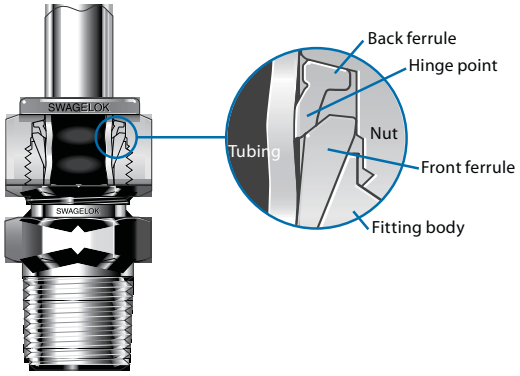

Figure A.1: Schematics explaining the Swagelok® sealing technique. The front ferrule is pressed against fitting body and tubing creating a primary seal. The back ferrule hinges inward and grips the tubing. Swagelok® connectors can be opened and closed multiple times. Figure taken from [Swa08]

A.1.4 ConFlat® flanges and seals

ConFlat® (CF) describes a sexless sealing technique: two parts to be connected together end in a flange including a sharp edge ('knife' edge). An all-metal gasket, normally copper, sometimes covered by a silver finish, is positioned in-between. While screwing the flanges together the knife edges cut into the softer copper. This is one of the few allowed UHV sealing techniques yielding vacuum tightness up to a leaking rate of 10^{-10} mbar·l/s and better with the disadvantage that the seals cannot be reused. CF seals are available for DN16 up to DN200 flange types, with custom made products even reaching DN250 and DN320.

A.1.5 Swagelok® components and seals

Swagelok® connectors employs a mechanical grip design by using two ferrules as shown in fig. A.1 to interconnect two tubes. The key feature is that Swagelok® seals can be opened and sealed again multiple times. The sealing technique uses a front ferrule which is pressed against fitting body and tubing by screwing the two connector bodies shut, thus creating a primary seal. A second back ferule hinges inward pressing into the tubing providing excellent grip.

A.1.6 O-ring sealing technique

Large diameter flanges exceeding DN320 can't be closed with conventional CF seals. The KATRIN experiment has tested a different sealing technique using two custom

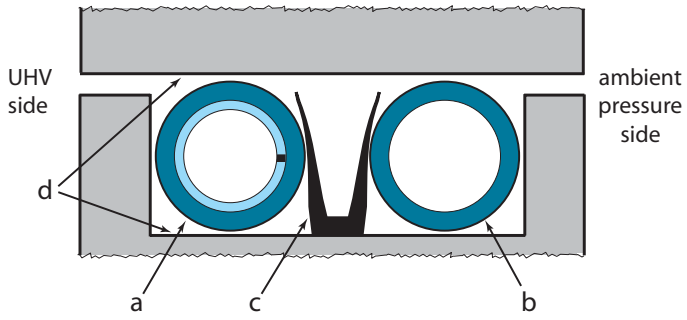

Figure A.2: Differentially pumped double O-ring sealing technique. a) spring energised metal O-ring b) metal O-ring c) spacer d) plane surface. When compressed, the metal O-rings will push against the plane surface of the flange, thus sealing off the vacuum region. This method has proven successful for DN500 and Dn1680 flanges.

made O-ring gaskets which are fitted into a groove, illustrated in fig. A.2. A placement holder also acting as a spacer keeps the rings inside the groove. The flange housing groove and O-rings is fitted onto the plane surface of the vessel flange. The surface has to be free of scratches and completely lint-free. When the flanges are pressed together the all-metal O-rings deform elastically. As a result of the deformation energy, the O-ring presses itself onto the plane but with a defined roughness surfaces on both sides and seals off the vacuum region. The O-ring on the vacuum side is spring loaded, which means a spring inside the ring increases the pressure acting onto the sealing surface when compressed. The volume in-between the two rings can be pumped if the leakage rate exceeds a critical limit. The seals are not reused to avoid the risk of a leak later during system operation, e.g. after the bake-out.

A.2 Vacuum leaks

No vacuum recipient is 100% 'tight'. This can be easily proven by pumping down a recipient and closing it with a valve. The pressure will rise instantly[4]. However, there are several reasons for the pressure rise. First, outgassing always takes place with every existing material. Second, vacuum leaks. Together, those yield a leak rate Q_L which is the ratio of pressure increase Δp for a given volume V over time span Δt:

$$Q_L = V\frac{\Delta p}{\Delta t}, \tag{A.1}$$

the unit in use is mbar·l/s. Combined with the effective pumping speed S_{eff} an equation for the end pressure p_{end}, being the equilibrium condition of pumping speed versus combined pressure increase, can be found:

$$p_{end} = \frac{Q_L}{S_{eff}} \tag{A.2}$$

[4]This can only be detected if the resolution of the pressure reading is high enough

There are different types of leaks which can be distinguished:

- Leaks from using seals: several sealing techniques for different pressure regimes exist to join two parts together but even the best techniques still yield a small leak rate. CF components are often specified with an lower limit to 10^{-10} mbar·l/s.
- Leaks in welds: only in defective components.
- Enclosures leaks, so-called virtual leaks: cavities enclosed in the material can open up into the vacuum. If the opening is very small the cavity cannot be pumped out efficiently, resulting in a continuous gas stream.
- Cold/warm leak: according to the expansion coefficient the material expands when getting warm or cold and an opening, undetectable at first, opens up. Dangerous with regard to supply lines for cryogenic fluids.
- Permeation: Some materials are permeable for certain gases. This is not a leak in general but an innate quality of the material itself.

A.2.1 Leak detection

There are several ways to determine if the vacuum system is leaky. Normally, the operator knows that a leak exists when the end pressure is not reached although the system bake-out has been carried out properly. This is much more difficult with small leaks. One way to check for leaks is the pressure rise method. All valves connecting vacuum pumps to the recipient are closed. Depending on the existence of a leak and its severity, it is possible to distinguish between three types of pressure rise curves by plotting pressure readings over time (see fig. A.3). In the case of an existing leak the pressure rises linearly and the leak rate is constant in time. If no leak is present the pressure follows the equation [Bor04]

$$p_g(t) = c_0 + c_1(1 - e^{-c_2 t}) \tag{A.3}$$

$$c_0 = p_{g_0} \tag{A.4}$$

$$c_1 = \frac{\sum\limits_i q_{g_i}}{\sum\limits_i S_{g_i}} - p_{g_0} = p_{g_e} \tag{A.5}$$

$$c_2 = \frac{1}{V} \cdot \sum_i S_{g_i} \tag{A.6}$$

Here $p_g(t)$ stands for the partial pressure of a certain gas type, p_{g_0} for the starting pressure of the measurement at time t=0, q_{g_i} for the outgassing rate of a specific source, e.g. outgassing or leaks, S_{g_i} for the pumping speed of specified gas source, p_{g_e} the pressure, when pumping, outgassing, leakage and adsorption reach a state of equilibrium. V is the volume of the recipient. The course of this equation is shown

schematically in curve (2) of fig. A.3: after a linear increase, the outgassing rate is compensated by the adsorption rate; as many particles are adsorbed on the surface as are desorbed from it. Now the curve approaches the equilibrium pressure which is ultimately dependent on the gas composition, the wall coverage and the water vapor pressure at the given temperature [Alt08]. Therefore by fitting the pressure rise curve with eq. A.6 or only the linear part with a linear fit the outgassing rate can be determined. However, when conducting an outgassing measurement the recipient is not allowed to have any leaks, otherwise the pressure rise curve is a superposition of both outgassing and leakage rate yielding a wrong value (compare curve (3) fig. A.3). On the other hand, a pressure rise curve not approaching a constant pressure value hints at a leak which has to be fixed.

The pressure rise method by itself is not able to disclose the leak's location. This can be achieved by using a dedicated leak detector. The KATRIN experiment uses a portable Alcatel ASM182 $TD_+(heliumpumpingspeed S_{He} = 4.4\,l/s)$ and a movable ASM192 $T2D_+(S_{He} = 20\,l/s)$ leak detector. Generally, leak detectors can be broken down into three major devices:

1. residual gas analyzer,
2. pumping system (fore pump and TMP),
3. Vacuum gauge.

Using an RGA as a detector is the most reliable solution for leak testing. It is possible to detect leak rates down to $10^{-12}\,mbar{\cdot}l/s$ which is sufficient for UHV purposes. The leak detectors work after the principle of helium detection, instead of being sensitive to a wide array of test gases. Helium has the clear advantage of a distinctive signature in the mass spectrum at 4 amu, chemically inert and therefore applicable in an UHV environment, neither toxic nor flammable, only to 5 ppm present in air and easily available [Umr02]. Another important point to consider is the fact that He-atoms are able to permeate materials and extremely small leaks easier than test gases of higher mass numbers. In practice, small leaks may be identified faster and more reliable by using helium compared to other test gases.

After attaching the leak detector to the vacuum recipient the pumping system evacuates the recipient. The extracted gas stream is tested with the RGA and traces of helium are detected and quantitatively analyzed, taking into account the partial pressure of helium compared to the total pressure, and calculating the leak rate according to $Q = const. \cdot Q_{He} = p_{He} \cdot S_{eff,He}$. Naturally helium has to be sprayed onto the leak on the atmospheric side. As a matter of routine, flange joints, welds and soldering joints are to be tested. Helium disperses rather fast. On the one hand, this makes it easy to test a big area on the principle existence of any leaks. On the other hand, by applying helium carelessly it can be difficult to pin-point the exact location of the leak or even worse, helium back-diffuses through the leak detector's pump and a wrong leak rate is given out. Applying helium for too short

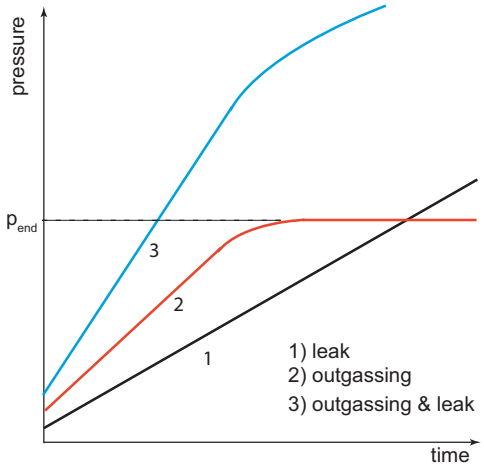

Figure A.3: Leak testing with pressure rise method: (1)leak, (2)outgassing of walls, (3) leak and outgassing combined. Picture based on [Alt08]

a time only a fraction of the leak rate will be detected. The response time constant $\tau = V/S_{He}$ [Alt08] for the pre-spectrometer with a volume of 8.5 m^3 and a leak detector featuring $S_{He} = 20$ l/s can be calculated to 425 s after which the leak rate reaches 65% of its final value. For 95% efficiency 20 minutes of waiting time have to be allowed for. At the pre-spectrometer the leak test is attached to the pumping system instead of the fore-pump. Thus, the pumping speed for helium is much higher reducing the waiting time considerably to approximately 30 s for 95% efficiency.

To prevent any contamination of the leak detector with helium, integral leak tests are carried out. Either the whole recipient or just the component which is to be tested is covered in plastic foil which is filled with helium. The advantage of this method is the high concentration of helium surrounding the component from all sides. Even if helium diffuses through the plastic foil the time constant is big enough to ensure a correct measurement.

It has to be mentioned that after activation the leak detector should be operated 'against itself', meaning without attaching it to another recipient. How long depends on the time the system hasn't been in use. In this way the detector's inherent background level decreases considerably and only then will the sensitivity be sufficient for UHV-testing. If a stand-alone RGA is attached to the recipient, it can be used instead of a dedicated leak detector.

A.3 Vacuum pumps

Vacuum pumps can be distinguished into three major categories:

1. mechanical vacuum pumps,

2. kinetic vacuum pumps,

3. gas binding vacuum pumps.

The KATRIN experiment utilises a wide range of vacuum pumps of the mechanical and gas binding categories depending on the location of operation and the restrictions this implies as well as the intended purpose. In the following only vacuum pump types used at the pre-spectrometer test experiment will be discussed.

A.3.1 Turbomolecular pumps

Turbomolecular pumps can generate vacuum of down to 10^{-10} mbar. This is the pressure regime of molecular flow of gas molecules characterised by a large mean free path length preventing the molecules to interact with each other – only contact with the recipient walls are considered. This can be described by the Knudsen coefficient K characterising the different kinds of particle flows. The mean free path length Λ for particles flowing through a cylinder with diameter d is anti-proportional to the pressure which is determined by the number of particles N inside the cylinder's volume V:

$$p = \frac{NkT}{V} \tag{A.7}$$

with T being the temperature and k the Boltzmann constant. The Knudsen constant is gained by calculating the ratio of mean free path length, and thus pressure, and diameter of the recipient through which the particles are flowing:

$$K = \frac{\Lambda}{d}. \tag{A.8}$$

Values of $K < 10^{-2}$ characterise the regime of viscous flow which can be either laminar or turbulent. Here, the interaction of particles among themselves are dominant as compared to wall-interaction which allows to treat the particle flow analogue to a fluid using the rules of continuum mechanics [Ede98]. By contrast, if $K > 0.5$ the mean free path length is large and the particle interaction is limited to the recipient walls. In the intermediate regime, which is known as Knudsen flow, interactions particle-wall and particle-particle is equally abundant.

The pumping techniques used for laminar flow are not applicable in molecular pressure regimes and vice versa. The general working principle of TMPs can be described as follows: several stages of turbine blades are positioned on top of each other. Every second stage can rotate around its axis (rotor), the other stages are static (stator). The blades are tilted to some degree in direction of the rotation in the case of the rotor (see fig. A.4) and against the rotation direction in the case of the stator. Undirected particles coming from space 1 have a chance of entering the channel between rotor blades. If the rotation velocity u equals the average thermal velocity $\bar{c}$, particles will either fall through the channel without touching or, due to the high velocity touch the lower half and desorb into the lower space 2 according to the cosine law

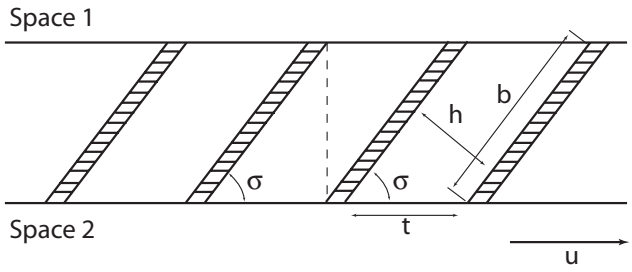

Figure A.4: Turbomolecular pump (TMP) working principle. Explanation see text. Based on [Alt08]

[Alt08]. Thus a directional flow is created. Keeping in mind that at low pressures of less than 10^{-3} mbar the mean free path lengths of molecules is larger than the gap between rotor stages (tenth of a millimeter [Alt08]), interaction only takes place with the rotor and stator blades thus increasing the pumping effect considerably. As already mentioned the velocity of the rotor blades has to be comparable to the thermal velocity of the molecules. While water with the molecular mass 18 has a speed of approximately 600 m/s, resulting in rotational frequencies of 38 kHz and up to 72 kHz depending on rotor diameter. Considering the high thermal velocities of hydrogen molecules of 1761 m/s, the comparatively low pumping speeds of TMPs for hydrogen can be explained.

With stringent UHV requirements and exceptional high speeds of pump rotors, manufacturers have to make sure that grease used for the bearings can't release hydrocarbons into the vacuum recipient. This led to the introduction of magnetic suspension of the rotor blades. Newest pump technology utilises a five-axis active regulated suspension created by permanent magnets, preventing any contact with the housing resulting in a lubrication free environment.

Turbomolecular pumps have to be operated in a molecular flow regime. Therefore a TMP can only be operated in conjunction with a fore vacuum pump compressing the gas stream against ambient pressure. Depending on the TMP the starting pressure for TMP operation varies between 10 mbar and 10^{-3} mbar. Higher starting pressures require a second stage using either the Holweck or Siegbahn principle [Umr02] for additional compression of the gas stream.

During handling of TMPs it has to be considered that maximum temperatures specified by each manufacturer are never to be exceeded (normally between 80°C and 100°C) or the rotor blades made of aluminum may get deformed. Therefore, handling of the TMP during installation has to be carried out under clean conditions because regular UHV-cleaning (see section A.4) a TMP is not possible as is cleaning by baking. Furthermore, the limits for TMP operation in magnetic fields is given by the motor and rotor temperatures which increase under the influence of eddy currents caused by the rotor movement in a static magnetic field. Dedicated

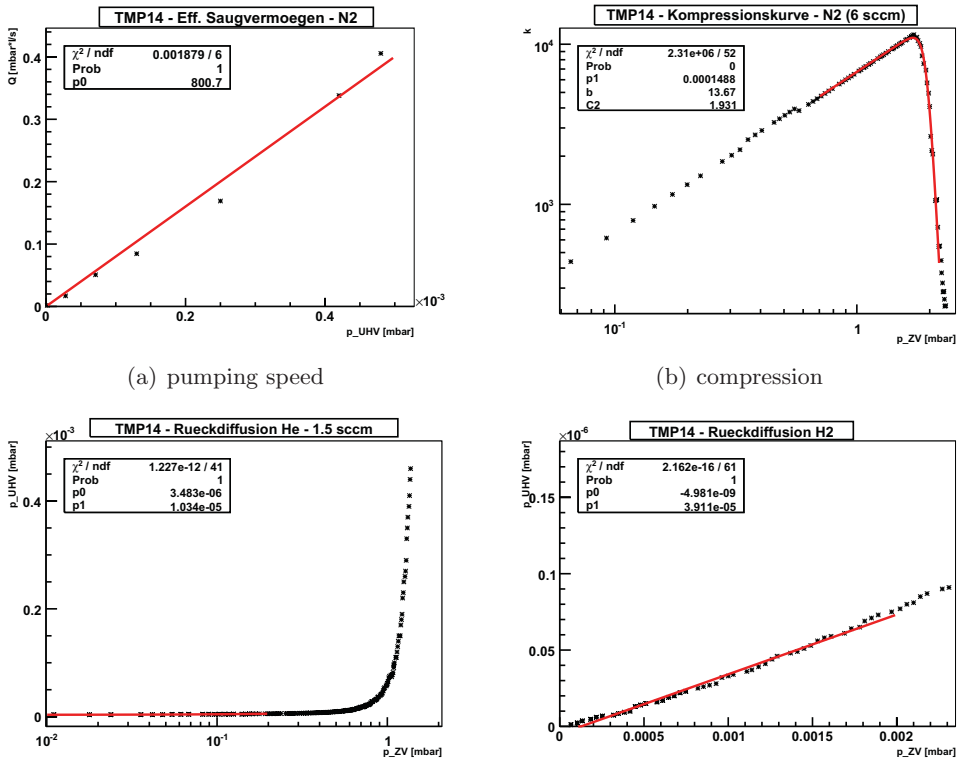

(a) pumping speed

(b) compression

(c) back diffusion He

(d) back diffusion H2

Figure A.5: Turbomolecular pump characteristics: plots for evaluating a) pumping speed b) compression c)+d) back-diffusion

measurements have been carried out to test the TMPs operated in the DPS of the KATRIN experiment. Starting at 4.4 mT the rotor temperature increased to 85°C, the limit for longtime operation is referenced by the manufacturer to 90°C. Further increasing the magnetic field causes an increase in rotor temperature to 120°C and a subsequent shutdown at 8.2 mT [Ker07].

A.3.1.1 TMP characteristics

The performance of a turbomolecular pump can be characterised with different parameters. The most important parameters will be explained. The presented plots and values are the result of test measurements of Leybold MAG W 2800 TMP, number 14. This pump type is used in the transport and main spectrometer section of the KATRIN experiment, altogether 22 TMPs.

Pumping speed The pumping speed S is the average gas throughput of a pump in a given time, the unit is usually given in l/s. The pumping speed depends not only

on the pump type, the first rotor and stator stages determine the final value, but also the gas species. The pumping speed is gained by plotting the gas throughput given in mbar·l/s over the pressure in the vacuum recipient, see fig. A.5(a).

Compression The ratio of backing pressure to the intake pressure is called compression:

$$K = K(p_{bp}) = p_{bp}/p_{UHV}(p_{bp}). \tag{A.9}$$

The compression determines the final pressure the pump can reach. Eq. A.9 shows the dependence of the UHV pressure p_{UHV} and hence the compression K of the backing pressure p_{bp}. Plotting compression over backing pressure visualises the dependence (see fig. A.5(b)). With the help of the function [Vos03]

$$K = K(p_{bp}) = p_{bp}/p_1 \cdot [exp(\beta(p_{bp} - C_2)) + 1]^{-1} \tag{A.10}$$

it is possible to fit the compression curve. The fit parameters p_1, β and C_2 are all dependent on the gas throughput Q with p_1 giving the final pressure at a certain gas throughput.

Contrary to the pumping speed, the compression is influenced by the later rotor stages.

Back diffusion Plotting p_{UHV} over p_{bp} yields a plot similar to that of the compression curve (compare fig. A.5(c) and A.5(b)). The first plot, however, makes it easier to quantise an important value, that of back-diffusion. The final pressure of a pump is reached when the ratio of molecules propelled out of the vacuum recipient by the pump turbine and the molecules diffuse back into the recipient is one. The curve in fig. A.5(d) shows that by an increase in the backing pressure the UHV pressure is influenced but keeping stable. Only after reaching a certain threshold (in the plot of fig. A.5(c) at approx. 1 mbar) the UHV pressure increases exponentially. Beyond this limit the compression of the pump is insufficient, the gas of the backing pressure streams back into the recipient. As a result the backing pump has to be chosen to always keep the backing pressure in the linear region of the curve, then the back-diffusion is kept to a minimum. A good threshold value can be gained by analysing the gradient of the linear part: as long as the gradient is less than 10^{-4} the UHV is not compromised.

A.3.2 Fore vacuum pumps

In paragraph A.3.1 it is discussed that a TMP needs to be driven in connection with a fore vacuum pump to generate the necessary vacuum with gas molecules exhibiting molecular flow characteristics. Furthermore UHV requirements call for the usage of 'dry' pumps without lubricants and therefore without outgassing hydrocarbons contaminating the vacuum. Thus fore pumps also have to have 'dry' characteristics,

otherwise hydrocarbons may diffuse backwards into the vacuum recipient. During normal operation, lubricants from the fore pump don't get into contact with the TMP. A malfunction or an operation error, however, could lead to a back flow into the TMP contaminating not only the vacuum but also the TMP which can't be cleaned sufficiently by baking and is therefore very difficult to decontaminate.

Examples for dry compressing fore vacuum pumps are pumps using the Roots, claw or scroll principle. The fore vacuum pumps used at the pre-spectrometer are Roots pumps of which the working principle will be described now, more information on other types of fore vacuum pumps can be found in references [Alt08, Umr02]. The Roots is working like a rotary positive-displacement pump: two impellers with identical shapes comparable to the shape of an 8 are set into a circular case (see fig. A.6). The special shape allows both impellers to alternately move through the same volume. Due to the distance between each other and to the casing walls of approximately $100\,\mu$m the compression rates are rather limited to 10 to 100 but on the other hand no oil or other lubricants are used and no mechanical wear takes place, although the pump is operating at high speeds. The operating principle exploits the fact that different parts of the pump walls and impellers are in contact with intake side and compression side in alternating fashion. During the compression phase the areas of rotor and casing wall in contact with the intake side are loaded with gas. The compression phase follows the suction phase. Here the loaded gas layer is released into the exhaust flange thus creating a pumping effect [Umr02]. Normally Roots pumps can't compress against ambient pressure. However, by connecting several pumping stages in serial even Roots pumps are self sufficient. Moreover, this allows to reach even high vacuum pressure regimes of 10^{-3} mbar making this type of pumps the ideal counterpart for a TMP missing a laminar flow compression stage like a Holweck stage.

A.3.3 Gas binding vacuum pumps

During the production of stainless steel hydrogen is absorbed. Creating UHV the gases still prevalent in the residual gas are water vapour, carbon monoxide, carbon dioxide and hydrogen. After a sufficient bake-out water is greatly reduced so that hydrogen is dominating the gas composition to nearly 100%. TMPs are not able to sufficiently pump the hydrogen which is continuously outgassing from the steel, the reason being the high thermal velocities of hydrogen which is higher than the TMP's rotor speed resulting in a lower pumping speed compared to heavier gases like nitrogen. To reach pressures below 10^{-10} mbar vacuum pumps binding gases, especially hydrogen, are utilised.

A.3.3.1 Sorption pumps

All pumps using some kind of sorption agent to bind gas particles are called sorption pumps. Adsorption, sublimation, ion getter and non-evaporable getter (NEG)

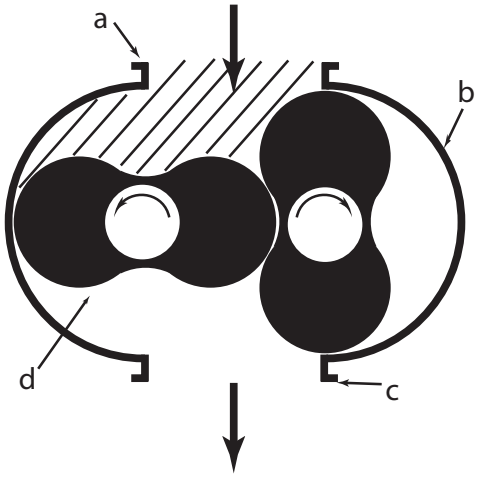

Figure A.6: Rotary positive-displacement pump. Two impellers move alternately through the same space. The distance of 100 μm between the walls and the impellers themselves allows gas compression in the range of 10-100, a more detailed explanation is given in the text. The low compression factor is compensated by the lack of lubricants making this a 'dry' pump possible for the use in connection with TMPs in UHV regimes. Picture based upon [Umr02].

pumps belong to this group. The NEG pump is presented in more detail; for more information with regard to the other pump types, see refs. [Alt08, Umr02].

NEG, also known as bulk getters, encompass solid materials which adsorb gas particles by chemical reactions from where the gas particles, depending on the gas type, are subsequently absorbed into the material by diffusion. The process of chemisorption describes the covalent linkage of the particles called adsorbate onto the surface of the getter material. By binding otherwise free-roaming particles the pressure is decreased. Unlike physisorption, chemisorption is irreversible under normal working temperature conditions, the binding energy is also ten times higher ranging between 0.8-8 eV. To be able to bind particles by covalent linkage the adsorbate has to be chemical reactive with the getter material. Noble gases and some hydrocarbons are not so, with a small chance, they can only physisorb (dipole forces and van der Waals forces) to the surface, therefore pumping speeds for these gases are several magnitudes lower.

As getter material certain porous metals like titanium and zirconium are suitable; strips covered with getter powder of the type ST707 retain a surface area of 1500 cm^2/g [SAE]. It has to be considered that the maximum gas collection of each material is different depending on the temperature of operation. As a result, special alloys of zirconium have been developed to maximise the pumping abilities.

Considering that NEGs work by adsorption of particles it is advantageous to maximise the surface of the material. One way to do this is to cover metal strips with

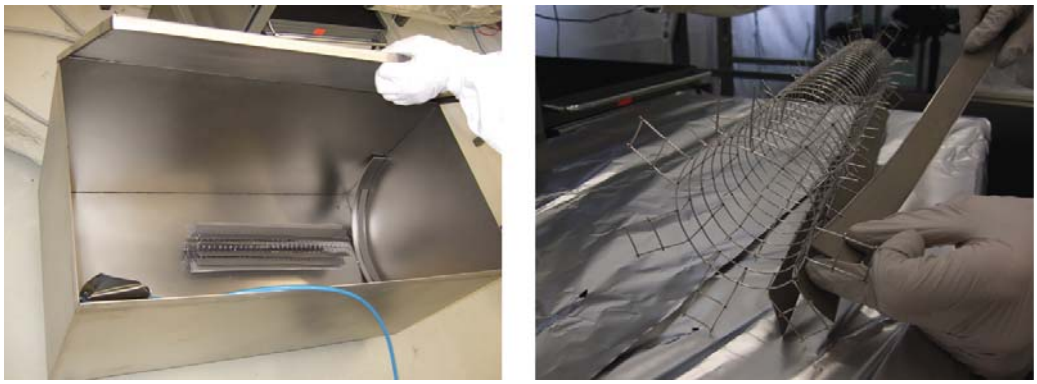

Figure A.7: Manufacturing of a getter pump. St707 strips have to be cut under an argon protective layer. This is achieved by working the material inside a container which is continually flooded with argon. The strips are placed onto a wire-mesh which can be adjusted to the appropriate diameter.

the getter material. The strips can be placed inside a customised holding structure which is placed inside the vacuum chamber. One of the prerequisites of getter material is to be chemical active, also for the constituents of air. Because of this, precaution has to be taken while working with getter material and during storage; it is mandatory to store getter material using a protective gas with argon being well suited. Argon is also suited to work as a protective gas while assembling the getter pump or cutting of the getter strips, see fig. A.7. This is done by using a basin which is flooded with argon; as long as the getter is kept inside the basin during assembly it won't get in contact with air. Getter is not inflammable by just getting in contact with air, instead a passivating layer of oxides and nitrites forms on the surface. However, friction during the reworking induces heat which can inflame the getter and even lead to a continuous reaction or even, in the case of abrasion creating sufficient getter dust to a dust explosion. Particular care has to be taken of getter powder falling off of the strips. Due to the passivating layer getter has to be activated after installation. The getter surface can be freed of bound particles by baking: the increase in temperature does not desorb the oxides and nitrites into the vacuum, the chemical bonds are too strong even at temperatures over 700°C, in fact they diffuse into the getter. This can be repeated up to 20 times and more before the pumping speed is worsening considerably. When venting the vacuum system using Argon instead of nitrogen is to be preferred. The argon also creates a passivating layer but contrary to oxygen and nitrogen doesn't bind chemically. During baking the physisorbed argon molecules break off and are released into the vacuum. Temperature and duration of the getter activation depend on the getter material used. Special getter alloys are manufactured with regard to decrease activation temperature. Temperatures range from 250-800°C and durations from second to hours and days.

The advantages of bulk getters are manifold [Umr02]:

- constant pumping speed
- high pumping speed for hydrogen and its isotopes
- NEG is self sufficient after activation
- no interference from magnetic fields
- free of vibration
- small weight

Most important is the high pumping speed for hydrogen which makes it the ideal partner for a pumping scheme using turbomolecular pumps: a standard pumping scheme can reach UHV beyond 10^{-10} mbar only by using another pumping method in connection like getter pumps.

A.3.3.2 Cryopumps

The fact that cold surfaces bind gas molecules is used to lower the pressure in vacuum recipients. With temperatures smaller than 120 K the term cryopumping is used. Three processes for particle binding are differentiated: cryocondensation, cryotrapping and cryosorption. Gases condense on cold surfaces when the temperature is lower as a given threshold which depends on the ambient pressure. The gas molecules are then bound by van der Waals forces to the adsorber. With liquid nitrogen temperatures of 77 K and vacuum pressures below 10^{-9} mbar only water, carbon dioxide and longer hydrocarbon chains freeze on. Other gases require lower temperatures to cryocondensate, in the case of hydrogen a temperature of less than 3.5 K is needed [Alt08]. Cryotrapping and cryosorption allow to bind low-boiling gases like hydrogen, neon and helium which don't bind below 20 K, at higher temperatures. This is achieved by mixing the lower boiling gas with a higher boiling gas like argon, methane or carbon dioxide. The vapour pressure of the co-condensate compared to that of the pure low boiling gas is decreased by several decades depending on the mixture rate. In cryosorption an adsorbent layer is frozen on the cold surface prior to the start of pumping which reduces low-temperature requirements in the same way as cryotrapping. Although cryotrapping and cryosorption have the big benefit to reduce the complexity of the cryopump by increasing the pumping temperature they also have the disadvantage of introducing an adsorber gas which in some systems cannot be tolerated.

The general mechanical principle of a cryopump uses a baffle, the actual cryocondensation surface and an adsorbent surface located inside the condensation area. The baffle, kept at liquid nitrogen temperatures, retains H_2O and CO_2 very effectively. After the baffle the gas passes the cryocondensation surface at approximately 10 K which suffices to bind everything except H_2, He and Ne, the latter two, however, are of no importance in UHV. To also bind H_2, a layer of argon or another adsorbent is

freezed on the opposite of the cryocondensation surface, which can be reached after several collisions with the neighboring heat shield.

Cryopumps are very effective and can reach final pressures below that of combined TMP and NEG systems. Also advantageous is the possibility to design the cryopumping surface as needed making them very adaptable to all kinds of mechanical constructions. A disadvantage of cryopumps can be the need for regeneration. After forming a monolayer on the cold surface the following gas molecules are then attaching to the condensate. With thickness increasing the temperature of the condensate rises also due to a reduced thermoconductivity between cold surface and top layer resulting in a decrease of pumping speed. Heating up of the cryopump during a maintenance cycle and deployment of a new adsorbent layer if necessary restores the pump's capabilities.

A.4 Treatment of UHV-components

Reaching UHV requires not only careful selection of the materials used but also special treatment of the components with which the vacuum system is assembled.

A.4.1 UHV pre-cleaning

In general, all UHV components have to be vacuum cleaned. The cleaning procedures vary depending on the type of material the component is made of. The standard cleaning procedure for stainless steel and comparable materials utilised in KATRIN comprises following steps:

1. coarse contamination is cleaned by using ethanol, acetone only for severe contaminations
2. cleaning of the component in an ultra-sonic bath using P3-almeco 36 dissolved in demineralised water. Characteristics: pH-value > 12 ($10\,\mathrm{g/l}$), temperature $60°\mathrm{C}$, duration $> 10\,\mathrm{min}$
3. thorough rinsing with demineralised water ($0.7\,\mu\mathrm{S}$)
4. second cleaning in ultra-sonic bath only using demineralised water
5. thorough rinsing with ultrapure water ($0.05\,\mu\mathrm{S}$)
6. dry-baking at $120°\mathrm{C}$
7. wrapping the component in grease-free aluminum foil and plastic foil
8. labeling with component type and date of cleaning

Components made entirely of ceramics can be cleaned by baking at 900°C. Critical components which are difficult to clean, e.g. silicon detectors or valves have to be treated with care preventing any severe contamination in the first place.

During assembly of UHV components protective clothing has to be used to prevent contamination: hair net (hairs and dandruff), clean room coat (lint-free), mask against perspiration and rubber gloves (fingerprints); working in a clean room also requires special footwear. Goggles can be added for special critical tasks, e.g. detector assembly. These tasks have to be carried out in a clean room or if not possible under a mobile clean room tent. The pre-spectrometer task is equipped with a ISO 8 clean room for assembly and storage of critical components. Working outside a clean room, a clean working area has to be created. This includes no storage of wooden or cardboard crates, sealed floor and walls, cleaned tools and closed doors to prevent turbulent air flow distributing any dust.

A.4.2 Baking procedure

Regardless of how strong the safety measures are, contact with the atmosphere always deposits at least a layer of water on the component. As a result, after closure of the vacuum recipient and pump down of the system the pressure won't drop below 10^{-8} mbar. A residual gas analysis (RGA) identifies water as the main fraction contained in the gas composition. The solution to get rid of the water and all other dirt intruding into the system during assembly is to bake out the whole vessel under vacuum. This includes all electrical instruments attached; all vacuum gauges attached to the pre-spectrometer are bake-able to 350°C. Depending on the circumstances, the bake-out temperature can be varied, a minimum of 100°C has to be reached, however, otherwise the vapour pressure of water is not reached and the efficiency of the baking process is very small. Furthermore the whole vessel is supposed to show a uniform temperature distribution (as in fig. A.8): water desorbed from a hot spot can condense on a colder one, particularly if it is below 100°C. It is highly recommended to increase baking temperature to more than 185°C. At this level water remnants are more efficiently desorbed considerably decreasing the water ratio in the residual gas after the bake-out. Increasing the temperature even further also increases the benefits by further reducing the outgassing rate. The best results in bake-out processes are achieved with annealing the stainless steel at temperatures of 950°C to drain the steel of as much hydrogen as possible. While in some cases vacuum annealing (annealing under vacuum conditions) is requested recent results question the necessity [Nem99]. Ref. [Par08] even goes so far to attest air baked vacuum recipients better outgassing features arguing that the oxide layer on the outside acts as an additional hydrogen barrier. Furthermore, the necessity for high temperatures of higher than 900°C is not supported. Medium temperatures (400°C) are sufficient for ultra low outgassing properties. Also important is the conclusion that after an initial treatment at medium temperatures subsequent baking cycles can be carried out at low temperatures of 150°C and still reach the same outgassing level as before.

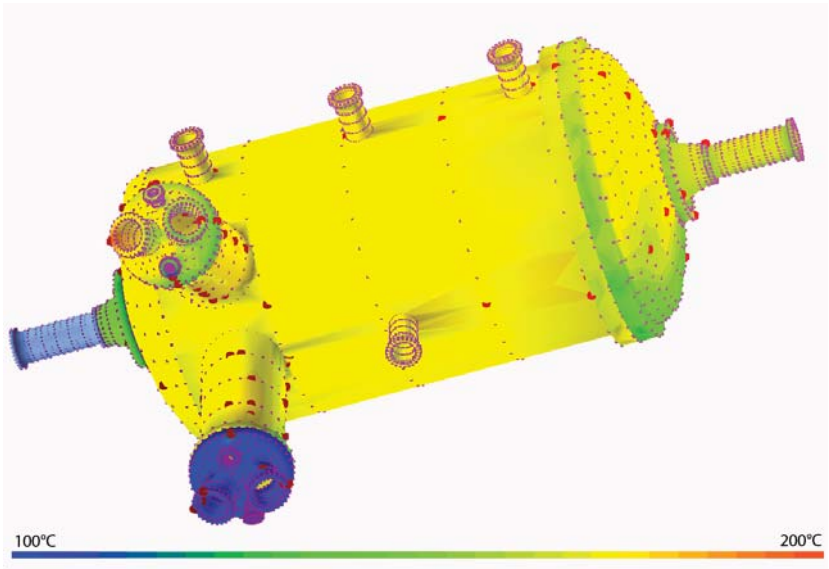

Figure A.8: Temperature distribution during baking of the pre-spectrometer. The temperature of 170°C is uniformly distributed over the main body. Colder spots can be found on the side caps due to a less effective isolation. The coldest spot can be found at the DN500 flange of the TMP pump port. Here the temperature is not allowed to surpass 100°C to prevent overheating of the TMPs.

Generally, the disadvantage of lower baking temperatures can be compensated by increasing the bake-out time. At temperatures around 200°C the baking procedure should be stretched out over several days of up to a week. A good indication that the bake-out has been successful and can be stopped is the development of the pressure: starting the baking procedure the pressure rises until it reaches a maximum some time after the highest bake-out temperature has been reached. As soon as most of the water has been desorbed from the surface and transported out by the pumps the pressure starts to decrease although the temperature is kept constant. This is the point where only an increase in temperature will have a positive effect on the outgassing rate.

A.5 Vacuum gauges

Similar to turbomolecular pumps, a single vacuum gauge principle covering the whole pressure range from 1 bar to 10^{-12} mbar does not exist. Therefore, different measurement techniques for the different pressure regimes have been developed creating a variety of gauge models to select from. The gauges can be divided into mechanical ones directly measuring a force F applied to an area A with which the pressure p can be calculated: $F = p \cdot A$ and indirectly ones, measuring a quantity which is proportional to the pressure, e.g. the particle number density. For measuring low pressures in the high and ultra high vacuum regime only indirect methods can be

applied, the difference in the exerted forces are too small to be discriminated. For UHV pressures only ionisation gauges provide a reliable reading below 10^{-10} mbar.

A.5.1 Ionisation vacuum gauges

Inside a volume, the pressure is defined by particle-collisions with the surrounding walls. Therefore, the number of particles, being proportional to the pressure, can be used to calculate the pressure. The working principle of an ionisation gauge is to accelerate electrons using an electric field. Those electrons are then sufficiently energetic to ionise the gas molecules. The positive ions are collected, and the electron current necessary to neutralise those ions is proportional to density number and thus pressure.

A disadvantage of this method is the ionisation probability which depends on the type of gas the electrons have to ionise. Ionisation gauges are calibrated for nitrogen, if the gas composition deviates from a pure nitrogen atmosphere special correction factors taking the ionisation probability into account have to be applied. Furthermore, these factors also depend on the settings used for the vacuum gauge, e.g. acceleration voltage. Therefore, gas correction factors can vary slightly depending on gauge type and brands. A table provided by the manufacturer should be consulted.

A.5.1.1 Cold cathode gauges

These gauges use a set of two electrodes which are not heated. A DC voltage between the anode and cathode causes a so-called 'cold discharge'. An overlying magnetic field oriented in such a way that the electrons are forced onto a spiral path. This increases the path length of the electrons and as a result the collision rate with the gas molecules. By creating a sufficient number of electron-ion-pairs to hold up the discharge, thus stabilising the trap even at low pressures. The much heavier positive ions escape the trap and are measured as a pressure-dependent gas-discharge current[Alt08]:

$$p = KI^m. \tag{A.11}$$

With K being the proportional factor and m a quantity depending on design varying between 1-1.4.

Cold cathode gauges use either the principles of a Penning trap or that of the magnetron and inverted magnetron type. Penning traps are discussed in more detail in section 4.1.3. An inverted magnetron gauge has a similar design: crossed magnetic fields in the range of 01.-0.2 T and electric fields created by anode and cathode. The cathode is a nearly closed cylinder with a rod-like anode positioned in the middle-axis. Field emission currents are prevented by two guard rings between cathode and anode. The magnetic field is parallel to the anode, the electric field is in the range of 2-6 kV depending on design. The advantage of the magnetron design compared to a

Penning gauge is the improved starting condition. At low pressures, starting a gas discharge does not happen immediately, newer models incorporate a weak radioactive source for discharge ignition. A disadvantage on behalf of magnetron gauges is the pressure dependence of m. At low pressures in the range of 10^{-11} mbar, errors range in the order of a magnitude. Cold cathode gauges in general, feature pumping effects which also influences the accuracy. However, the gauges are cheap, easy to use and less sensitive with regard to outside magnetic fields.

A.5.1.2 Hot cathode gauges

Hot cathode gauges use a three electrode set-up: a hot cathode for electron creation, an anode to accelerate the electrons and a collector electrode which absorbs the ions. On their way through the gas with particle number density n the electrons gather enough energy to create ΔN^+ ions [Alt08]:

$$\Delta N^+ = N^- n\sigma\Delta l \tag{A.12}$$

with the ionisation cross section σ and the typical path length Δl of electrons traversing though the gas. Dividing ΔN^+ by time yields the electrical current

$$I^+ = I_e n\sigma\Delta l, \tag{A.13}$$

which can be measured at the collector electrode which is set on a negative potential compared to the anode. With the relation $p = nkT$ eq. A.13 can be written as

$$I^+ = I_e n\frac{\sigma\Delta l}{kT}p = I_e \cdot K \cdot p, \tag{A.14}$$

with K as the proportional constant linking pressure and ion current.

Hot cathode gauges are limited at higher pressures to approximately 2 mbar, Extraktor and Magnetron gauges to 10^{-5} mbar. At higher pressures the free path lengths of ions is too short which prevents ions to reach the collector electrode. Furthermore discharges can occur. At lower pressures two effects limit the pressure reading to a specific threshold.

X-ray effect Electrons emitted from the cathode hitting the anode cause the release of X-rays. Those X-rays also hit the ion collector, photoelectrons are released in turn which are accelerated to the anode thus creating a negative electron current which is complementary to the positive ion current - the pressure increases.

In contrast to this positive X-ray effect it is possible to create a negative effect, too. Depending on the system layout it is possible for photons to strike the surrounding walls. Are the walls on equal potential as the ion collector, electrons released from the wall are accelerated to the anode and some of the electrons are passing the anode and strike the ion collector. This negative X-ray effect creates a negative current.

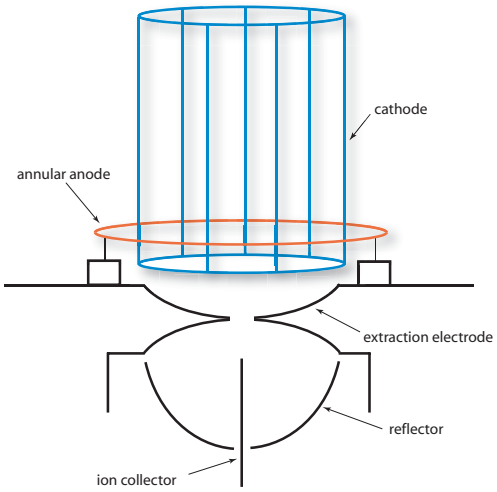

Figure A.9: Hot cathode vacuum gauge set-up using the example of an Extraktor gauge. The typical three electrode set-up is improved upon by separating the ion collector from anode and cathode. The extraction electrode on negative potential focusses ions in direction of the collector. X-rays are not focussed, thus reducing the number of X-rays reaching the collector. Schematics based upon [Bri03].

Ion desorption Gas molecules adsorbed on a surface can be desorbed by electron bombardment. In the case of a gas covered anode electrons desorb gas molecules in the form of ions. The ions travel to the ion collector. The resulting ion current is independent of the real recipient pressure but dependent on the electron current hitting the anode.

Both effects, having an influence on the correct pressure reading, can be mitigated by adjusting the design, e.g. that of extractor gauges, which have a limit of 10^{-12} mbar.

Extractor and other hot cathode vacuum gauges allow 'degassing' of the electrode surfaces either by electron bombardment or resistance heating to counteract the problems of ion desorption. The anode voltage and the emission current is increased. As a result the number of electrons released increase drastically, they hit the anode and desorb adsorbed gas molecules until an equilibrium state of adsorbing and desorbing is reached. The desorption rate increases due to the higher temperature which is a result of the increased anode voltage.

A countermeasure against the X-ray effect is to separate the ion collector from the location of X-ray and ion production (see fig. A.9). A negative Extraktor electrode with an aperture connecting both chambers accelerates and focusses ions in direction of the collector, X-rays, however, are not affected, resulting in a shielding effect resulting in an increase in accuracy.

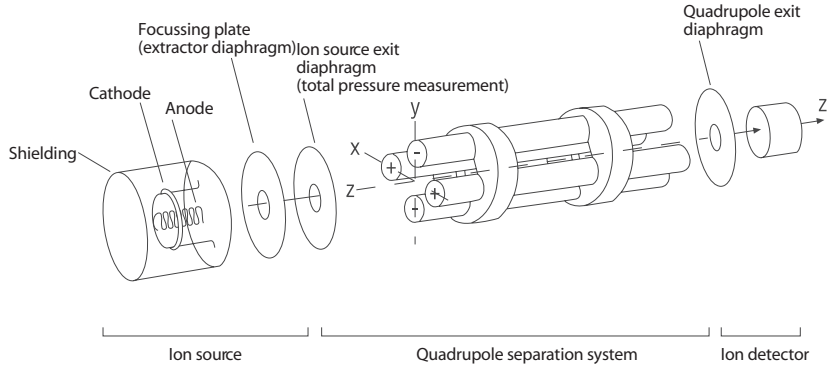

Figure A.10: Quadrupole mass spectrometer. Electrons created at the cathode are accelerated in direction of the anode. On the way residual gas molecules are ionised. Focussing lens are collimating the ion beam. In the separation unit an AC frequency is imprinted on the ions which start to oscillate. Only ions with a specific e/m fraction reach a collector and are measured. Picture taken from [Umr02]

A.6 Residual Gas Analysis

Analysing the residual gas fractions is one of the most important techniques when dealing with UHV. Foremost it allows to check for impurities and contaminations of vacuum components. Second, it's an alternative means to check for leaks e.g. in flange connections or a weld. RGAs are carried out with mass spectrometers, in KATRIN only quadrupole mass spectrometers (QMS) are used. The configuration of a QMS is shown in figure A.10. Electrons created in a cathode are accelerated in direction of an anode. On the way ionisation of residual gas molecules takes place. The resulting ion beam is extracted by a series of focussing lens and guided into the quadrupole separation unit. Here four rods are arranged in such away that the opposite rod carries the same charge and potential, furthermore a DC voltage and a superimposed high frequency AC voltage are applied. The ions guided through the centre in-between the rods start to oscillate. Before leaving the separation system all oscillations escalate; the ions get in contact with the rods and are lost. Only ions with a certain charge-mass fraction e/m make it through and are collected in an ion trap. In the case of this being a Faraday cup it can also be used as a photomultiplier, effectively increasing the measured ion current. The ion current is proportional to the pressure so, by changing the e/m-ratio, it is possible to plot the measured pressure over the respective mass unit. Tables providing the mass fractions allow to draw conclusions which gas types contribute to the residual gas composition. An example of the pre-spectrometer's gas distribution after getter activation is shown in fig. A.11.

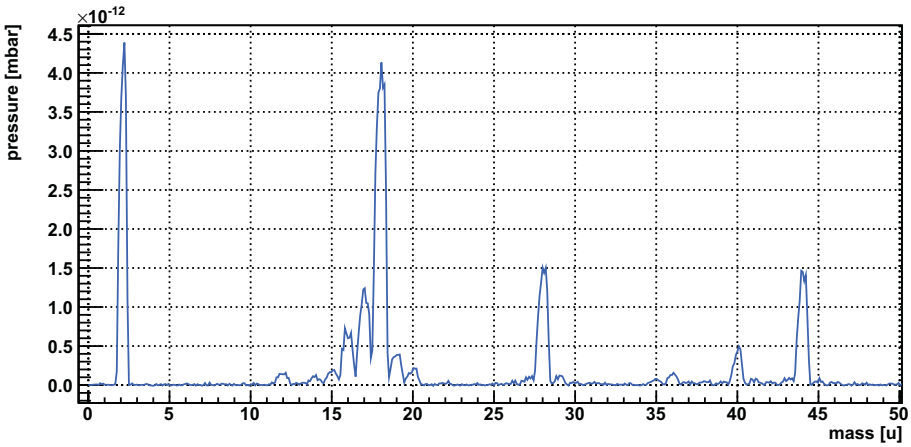

Figure A.11: Residual gas analysis after getter activation at $p_{Extraktor} = 3 \cdot 10^{-11}$ mbar. The spectrum shows the mass distribution of the pre-spectrometer after getter activation, fractions of H_2O (masses 18, 17, 16) and H_2 (mass 2) are equally big. The only other contributions are form CO_2 (mass 44) and CO (mass 28).

Appendix B

Calibration of FuG power supplies

The FuG power supplies, which are providing the retarding potential for the pre-spectrometer system, show a discrepancy between setpoint value and output value of the high voltage in the range of 100 V and more, as measured by the power supply itself. To check which value really is applied and to minimise the deviation from the designated voltage value measurement data was taken allowing to calibrate the power supplies.

For the calibration power supplies FUG3 and FUG4 are connected to a Julie Research high precision voltage divider using a RG11 cable. A Fluke 45 multimeter, equipped with an interface for personal computer access, is used to monitor the voltage output as provided by the high voltage divider. The data is stored on a personal computer reading out the Fluke voltmeter. For both power supplies six different values U_{set} are measured for a minimum time of one hour. For FUG4 the measurement values are in the range of -5 kV to -30 kV, for FUG3 from -5 kV to -20 kV. Above -20 kV, the current in the high voltage divider rises to such a level that FUG3's current limitation of 0.3 mA takes effect.

In figs. B.2,B.3 the graphs for the different voltage setpoints are plotted. Different effects are observable:

1. **The measured value does not match the set value.** The discrepancy gets larger with rising high voltage reaching a maximum of $\Delta U = 144\,\mathrm{V}$ at $U_{set} = -30\,\mathrm{kV}$.

2. **Drifting of voltage**. It is drifting, mostly in one direction depending on the value set before, but also changing the sign of the slope in-between. The drift interval for FUG4 is [0.3,4], for FUG3 [0.08,1.7] measured in V. The drift effects can be caused by the FuG power supplies, the Fluke voltmeter or the high voltage divider. However, FUG3 exhibits better stability as compared

to FUG4. Considering that FUG3 features a more precise internal measuring device one can conclude that the drift effects are dominated by the FuG power supplies.

3. **Jumps in voltage.** Several graphs show a clear step in voltage(B.2(a),(b), B.3(a),(b)). Fig. B.2(d) seems to feature a small discharge after which the voltage falls down to a lower level than before.

4. **Stabilization after ~ 1 h.** In figs. B.3(c),(d),(f) the voltage drifts for about 1 h after which the voltage value seems to stabilise.

To obtain average voltage values which can be plotted to gain a calibration curve constant values are fitted to the slopes. The fit was applied to the whole data set and not to a specific time interval, e.g. after stabilisation of the voltage value – during measurements no waiting time for voltage stabilisation is taken either.

The voltage values gained (listed in table B.1) are plotted over their respective setpoints and fitted with a straight line and in the case of FUG4 additionally with a parabola. Fig. B.1 shows that for FUG4 a parabola fit describes the measured data better, ΔU deviates less from the zero-value as compared to a straight-line fit.

The fit parameter values provide equations with which the setpoint values can be calculated:

$$U_{set}(FUG3) = (0.99780 \pm 0.00008) \cdot U - (6.2 \pm 1.2)\ [V], \tag{B.1}$$

$$U_{set}(FUG4) = (-2.22977 \pm 0.00001)10^{-7} \cdot U^2 \tag{B.2}$$

$$+ (0.9963 \pm 0.0002) \cdot U - 52.7 \pm 1.8\ [V]. \tag{B.3}$$

The fit values deviate for both power supplies by less than ± 5 V. This accuracy is comparable to the one of the high voltage stability discussed in section 3.1.3.1, see fig. 3.18(a). The calibration lowers the uncertainties of the power supplies' set value down into the range of the measurement accuracy. Further decreasing the uncertainties is not the aim of these measurements as long as the voltage stability of the pre-spectrometer vessel is not improved into the sub-V region. This is aimed at by installing a device which is measuring the voltage instabilities and actively counteracts the voltage fluctuations [Wüs08a], e.g. the 3.5 V peak-to-peak sine wave oscillation caused by the insulating transformer. As soon as this device is commissioned and in use a new calibration with higher precision is needed. In the meantime, however, higher precision would be of no benefit.

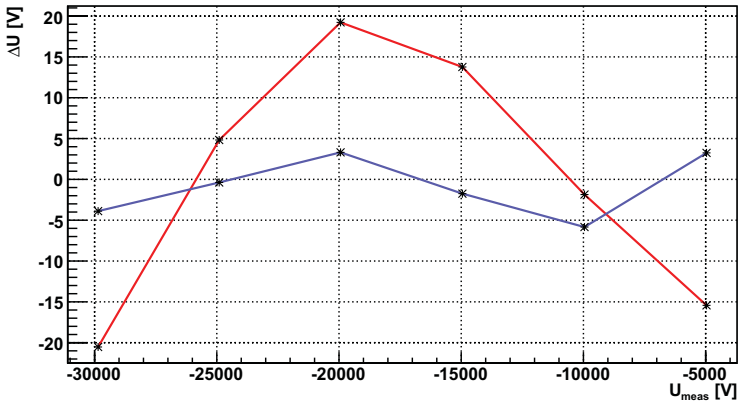

Figure B.1: Deviation of calculated and measured voltage values for two different fit functions: linear fit(red) and parabola fit(blue). The values calculated with the parabola fit coefficients deviates much less around the measured vales as compared to the ones calculated with the linear fit coefficients.

Table B.1: Fit-values for the calibration of FUG3 and FUG4. A constant value is fitted to the graphs presented in figs. B.2 and B.3.

FUG3		**FUG4**	
U_3 [V]	σ_{U_3} [V]	U_4 [V]	σ_{U_4} [V]
-5004.78	0	-4963.42	0.02
-10015.19	0.02	-9956.59	0.01
-12522.76	0.02	-14951.80	0.02
-15025.70	0.02	-19936.85	0.02
-17533.52	0.02	-24902.03	0.02
-20037.35	0.02	-29856.27	0.01

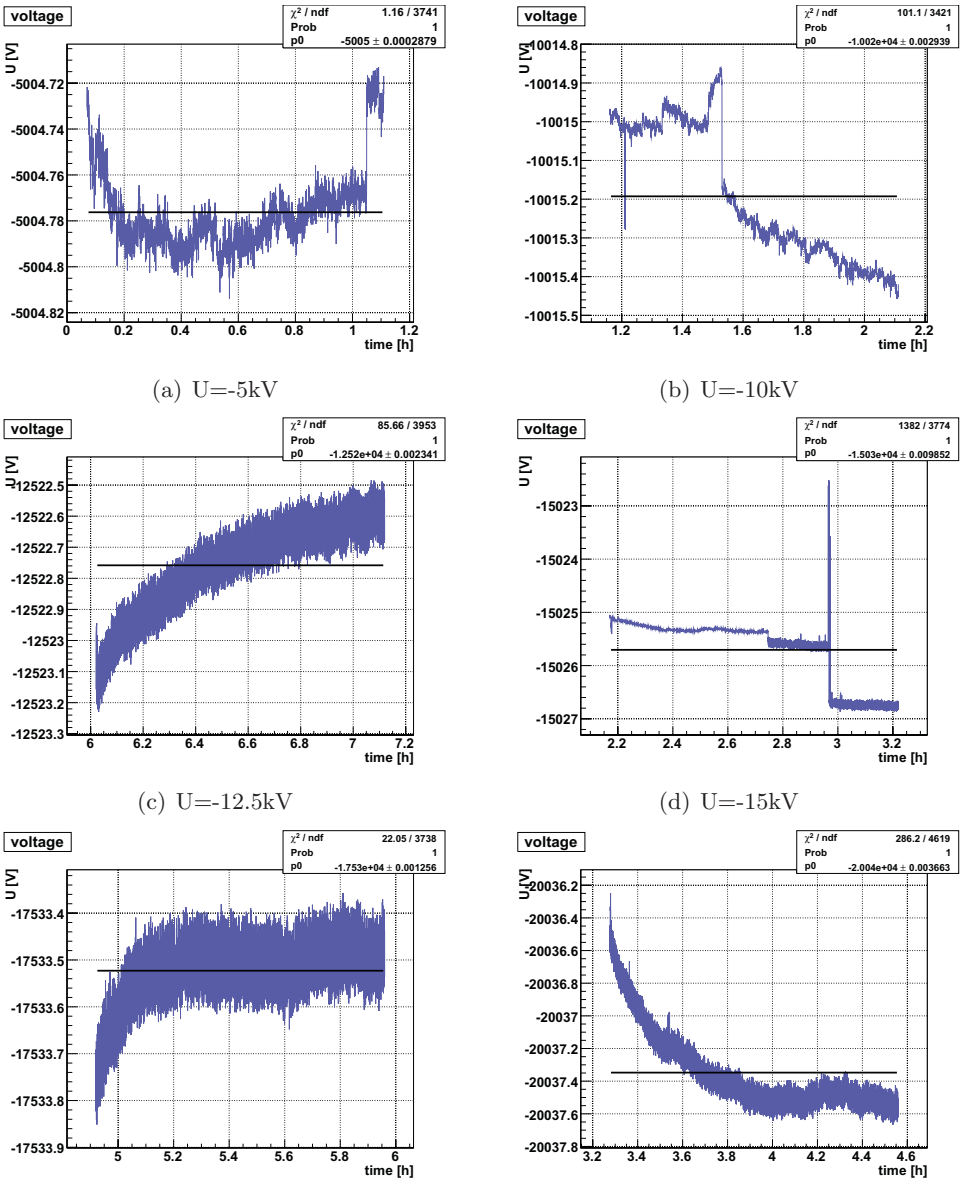

(a) U=-5kV (b) U=-10kV

(c) U=-12.5kV (d) U=-15kV

(e) U=-17.5kV (f) U=-20kV

Figure B.2: FUG3 high voltage stability. Measurements of the output voltage of FUG3 for 6 different values for a measurement time of minimum one hour.

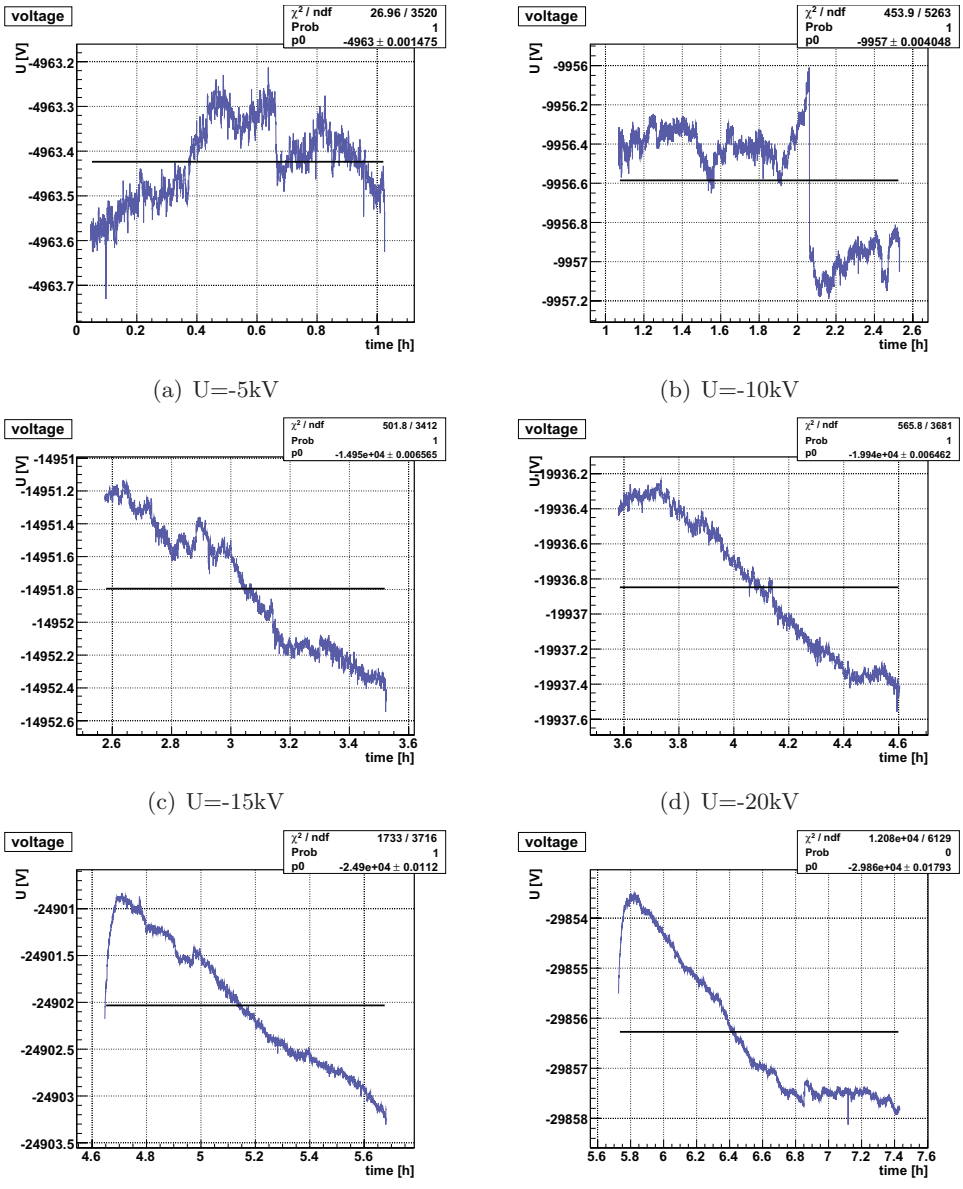

(a) U=-5kV (b) U=-10kV

(c) U=-15kV (d) U=-20kV

(e) U=-25kV (f) U=-30kV

Figure B.3: FUG4 high voltage stability. Measurements of the output voltage of FUG4 for 6 different values for a measurement time of minimum one hour.

Appendix C

Tables

This appendix contains different data in table form for reference purposes.

C.1 Americium source

The X-ray fluorescence lines for different exit windows of an americium calibration source are given [Vau01]:

element	line	I_{rel}	E [keV]	element	line	I_{rel}	E [keV]
	K_{α_1}	100	13.395		K_{α_1}	100	17.479
	K_{α_2}	52	13.335		K_{α_2}	52	17.374
^{37}Rb	K_{β_1}	14	14.961	^{42}Mo	K_{β_1}	15	19.608
	K_{β_2}	2	15.185		K_{β_2}	3	19.965
	K_{β_3}	7	14.951		K_{β_3}	8	19.590
	K_{α_1}	100	22.162		K_{α_1}	100	32.193
	K_{α_2}	53	21.990		K_{α_2}	54	31.817
^{47}Ag	K_{β_1}	16	24.942	^{56}Ba	K_{β_1}	18	36.378
	K_{β_2}	4	25.456		K_{β_2}	6	37.257
	K_{β_3}	9	24.911		K_{β_3}	10	36.304
	K_{α_1}	100	44.481				
	K_{α_2}	56	43.744				
^{65}Tb	K_{β_1}	20	50.382				
	K_{β_2}	7	51.698				
	K_{β_3}	10	50.229				

C.2 UW-DAQ threshold values

The table lists the threshold values for the UW DAQ shaper cards. Every channel has an individually determined value according to its noise rate.

	A	**B**	**C**	**D**	**E**	**F**	**G**	**H**
8	342	374	381	381	349	452	445	420
7	349	413	432	381	368	445	400	407
6	323	329	355	413	349	394	374	323
5	349	381	407	381	387	432	394	394
4	342	420	387	394	349	368	387	381
3	349	413	432	381	374	445	420	374
2	368	471	413	381	381	426	387	452
1	368	458	445	387	361	420	387	432

Appendix D

Pre-spectrometer heating/cooling system

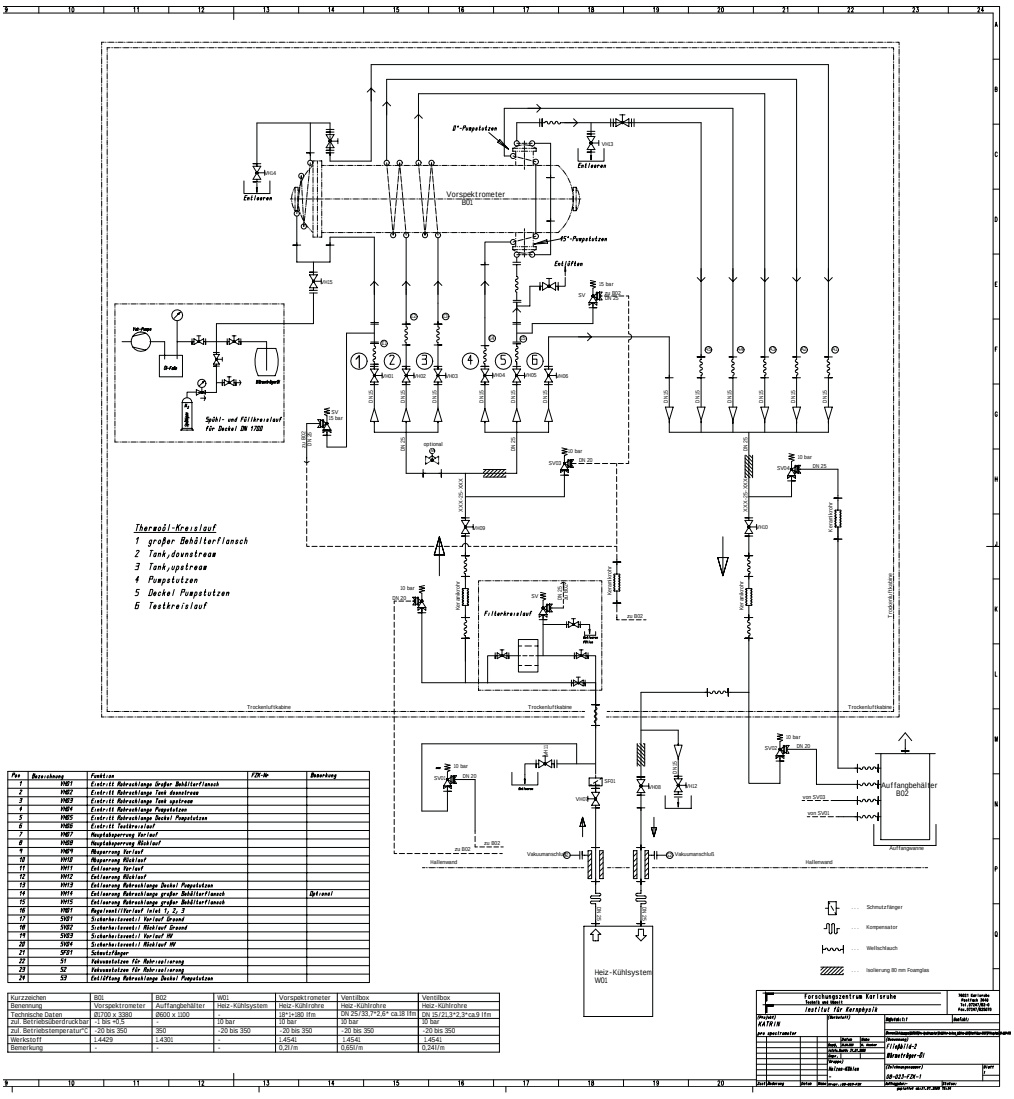

Kurzzeichen	B01	B02	W01	Vorspektrometer	Ventilbox	Ventilbox
Benennung	Vorspektrometer	Auffangbehälter	Heiz-Kühlsystem	Heiz-Kühlrohre	Heiz-Kühlrohre	Heiz-Kühlrohre
Technische Daten	ID700 x 3380	ID600 x 1200	-	18*1+180 lfm	DN 25/33,7*2,6* ca.38 lfm	DN 25/21,3*2,3*ca.9 lfm
zul. Betriebsüberdruck bar	-1 bis +0,5		10 bar	10 bar	10 bar	10 bar
zul. Betriebstemperatur°C	-20 bis 350	350	-20 bis 350	-20 bis 350	-20 bis 350	-20 bis 350
Werkstoff	1.4429	1.4301	-	1.4541	1.4541	1.4541
Bemerkung	-	-	-	0,2l/m	0,65l/m	0,24l/m

Figure D.1: Process and instrumentation diagram for the pre-spectrometer heating/cooling system.

Bibliography

[Aal04] C. Aalseth, H. Back, L. Dauwe, D. Dean, G. Drexlin, Y. Efremenko, H. Ejiri, S. Elliott, J. Engel, B. Fujikawa, R. Henning, G. W. Hoffmann, K. Lang, K. Lesko, T. Kishimoto, H. Miley, R. Norman, S. Pascoli, S. Petcov, A. Piepke, W. Rodejohann, D. Saltzberg, S. Sutton, P. Vogel, R. Warner, J. Wilkerson, and L. Wolfenstein, *Neutrinoless double beta decay and direct searches for neutrino mass*, ArXiv High Energy Physics - Phenomenology e-prints (2004), arXiv:hep-ph/0412300.

[Abd94] J. N. Abdurashitov, E. L. Faizov, V. N. Gavrin, A. O. Gusev, A. V. Kalikhov, T. V. Knodel, I. I. Knyshenko, V. N. Kornoukhov, I. N. Mirmov, A. M. Pshukov, A. M. Shalagin, A. A. Shikhin, P. V. Timofeyev, E. P. Veretenkin, V. M. Vermul, G. T. Zatsepin, T. J. Bowles, J. S. Nico, W. A. Teasdale, D. L. Wark, J. F. Wilkerson, B. T. Cleveland, T. Daily, R. Davis, K. Lande, C. K. Lee, P. W. Wildenhain, S. R. Elliott, M. L. Cherry, and R. T. Kouzes, *Results from SAGE (The Russian-American gallium solar neutrino experiment)*, Physics Letters B **328** (1994), 234–248.

[Abd96] J. N. Abdurashitov, V. N. Gavrin, S. V. Girin, V. V. Gorbatchev, A. O. Gusev, A. V. Kalikhov, T. V. Knodel, I. N. Mirmov, A. M. Pshukov, A. M. Shalagin, A. A. Shikhin, E. P. Veretenkin, V. M. Vermul, V. Yants, G. T. Zatsepin, T. J. Bowles, J. S. Nico, W. A. Teasdale, D. L. Wark, S. R. Elliott, J. F. Wilkerson, B. T. Cleveland, T. Daily, R. Davis, Jr., K. Lande, C. K. Lee, P. W. Wildenhain, and M. L. Cherry, *Results from SAGE*, Nuclear Physics B Proceedings Supplements **48** (1996), 299–303.

[Akh93] E. K. Akhmedov, S. T. Petcov, and A. Y. Smirnov, *Pontecorvo's original oscillations revisited*, Physics Letters B **309** (1993), 95–102, arXiv:hep-ph/9301247.

[Alt03] G. Altarelli, K. Winter, G. Altarelli, and K. Winter (eds.), *Neutrino Mass*, 2003.

[Alt08] F. Altenheimer et al., *Handbook of Vacuum Technology*, Wiley-VCH Verlag GmbH & Co. KGaA, Weinheim, 2008.

[Ams08] C. Amsler et al., *Particle Data Group*, Physics Letters **B667** (2008), 1.

[And07] E. Andreotti, C. Arnaboldi, P. de Bernardis, J. Beyer, C. Brofferio, M. Calvo, S. Capelli, O. Cremonesi, C. Enss, E. Fiorini, A. Fleischmann, L. Foggetta, M. Galeazzi, G. Gallinaro, L. Gastaldo, F. Gatti, A. Giuliani, P. Gorla, K. Heeger, K. D. Irwin, R. Kelley, C. A. Kilbourne, B. Margesin, R. Maruyama, S. Masi, D. McCammon, A. Monfardini, C. Nones, A. Nucciotti, M. Pavan, M. Pedretti, D. Pergolesi, G. Pessina, S. Petcov, F. S. Porter, M. Prest, E. Previtali, P. Repetto, M. Ribeiro-Gomez, S. Sangiorgio, D. Schaeffer, and M. Sisti, *MARE, Microcalorimeter Arrays for a Rhenium Experiment: A detector overview*, Nuclear Instruments and Methods in Physics Research A **572** (2007), 208–210.

[Ang04] J. Angrik et al. (KATRIN Collaboration), *KATRIN design report 2004*, FZKA Scientific Report **7090** (2004), FZKA-7090.

[Ans92] P. Anselmann, W. Hampel, G. Heusser, J. Kiko, T. Kirsten, E. Pernicka, R. Plaga, U. Rönn, M. Sann, C. Schlosser, R. Wink, M. Wójcik, R. von Ammon, K. H. Ebert, T. Fritsch, K. Hellriegel, E. Henrich, L. Stieglitz, F. Weyrich, M. Balata, E. Bellotti, N. Ferrari, H. Lalla, T. Stolarczyk, C. Cattadori, O. Cremonesi, E. Fiorini, S. Pezzoni, L. Zanotti, F. von Feilitzsch, R. Mößbauer, U. Schanda, G. Berthomieu, E. Schatzman, I. Carmi, I. Dostrovsky, C. Bacci, P. Belli, R. Bernabei, S. D'Angelo, L. Paoluzi, S. Charbit, M. Cribier, G. Dupont, L. Gosset, J. Rich, M. Spiro, C. Tao, D. Vignaud, R. L. Hahn, F. X. Hartmann, J. K. Rowley, R. W. Stoenner, and J. Weneser, *Solar neutrinos observed by GALLEX at Gran Sasso*, Physics Letters B **285** (1992), 376–389.

[APP07] APPEC Peer Review Commitee, *Status and Perspective of Astroparticle Physics in Europe*, ASPERA Roadmap Phase I (2007).

[Ard59] M. V. Ardenne, *Tabellen der Elektronenphysik Ionenphysik und Übermikroskopie. I. Band (C. Möllenstedt)*, Zeitschrift Naturforschung Teil A **14** (1959), 849–+.

[Arn03] C. Arnaboldi, C. Brofferio, O. Cremonesi, E. Fiorini, C. Lo Bianco, L. Martensson, A. Nucciotti, M. Pavan, G. Pessina, S. Pirro, E. Previtali, M. Sisti, A. Giuliani, B. Margesin, and M. Zen, *Bolometric Bounds on the Antineutrino Mass*, Phys. Rev. Lett. **91** (2003), no. 16, 161802.

[Bah04] J. N. Bahcall and C. Pena-Garay, *Solar models and solar neutrino oscillations*, New Journal of Physics **6** (2004), 63.

[Bah06] J. N. Bahcall, A. M. Serenelli, and S. Basu, *10,000 Standard Solar Models: a Monte Carlo Simulation*, The Astrophysical Journal **165** (2006), 400.

[Bas07] M. BastaniNejad, A. Elmustafa, C. Ankenbrandt, A. Moretti, M. Popovic, K. Yonehara, D. Kaplan, M. Alsharo'a, P. Hanlet, R. Johnson, M. Kuchnir, and D. Newsham, *Evidence for Fowler-Nordheim behavior in RF*

breakdown, Particle Accelerator Conference, 2007. PAC. IEEE (2007), 2499–2501.

[Bea80] G. Beamson, H. Q. Porter, and D. W. Turner, *The collimating and magnifying properties of a superconducting field photoelectron spectrometer* , Journal of Physics E Scientific Instruments **13** (1980), 64–66.

[Ben03] C. L. Bennett, M. Bay, M. Halpern, G. Hinshaw, C. Jackson, N. Jarosik, A. Kogut, M. Limon, S. S. Meyer, L. Page, D. N. Spergel, G. S. Tucker, D. T. Wilkinson, E. Wollack, and E. L. Wright, *The Microwave Anisotropy Probe Mission*, Astrophysical Journal **583** (2003), 1–23, arXiv:astro-ph/0301158.

[Ber72] K.-E. Bergkvist, *A high-luminosity, high-resolution study of the end-point behaviour of the tritium β-spectrum (I). basic experimental procedure and analysis with regard to neutrino mass and neutrino degeneracy*, Nuclear Physics B **39** (1972), 317–370.

[Bla71] E. W. Blauth, W. M. Draeger, J. Kirschner, H. Liebl, N. Müller, and E. Taglauer, *Experimental and Statistical Investigations on the Measurement of Very Low Ion Currents in Mass Spectrometers*, Journal of Vacuum Science and Technology **8** (1971), no. 1, 384–387.

[Ble63] H. A. Blevin and S. C. Haydon, *The Interpretation of Breakdown Characteristics of Electrodeless Discharges in Transverse Magnetic Fields*, Proc. Phys. Soc. **81** (1963).

[Bod08] L. Bodine, M. Leber, A. Myers, K. Tolich, B. Vandevender, and B. Wall, *Characterization of the KATRIN Focal Plane Detector*, APS Meeting Abstracts (2008), L4+.

[Bor04] L. Bornschein and J. Wolf, *Interpretation of UHV Measurements*, internal KATRIN document (2004), no. 30-ME-5002-0.

[Bri03] H. Brinkmann, *Hot Cathode Gauges for UHV Pressures*, International Workshop on Extreme High Vacuum - Application and Technology (X-VAT), 2003.

[Bru97] R. Brun and F. Rademakers, *ROOT - An object oriented data analysis framework*, Nuclear Instruments and Methods in Physics Research A **389** (1997), 81–86.

[CAN04] CANBERRA, *Detector specifications performance data certificate of conformity*, Tech. report, 2004.

[Cha32] J. Chadwick, *Possible Existence of a Neutron*, Nature **129** (1932), 312–+.

[Chi08] S. A. Chilingaryan, *Advanced Data Extraction Infrastructure*, 2008, `http://ipepdvadei.ka.fzk.de/adei/`.

[Cle95] B. T. Cleveland et al., *Update on the measurement of the solar neutrino flux with the Homestake chlorine detector*, Nucl. Phys. Proc. Suppl. **38** (1995), 47–53.

[Cou99] K. P. Coulter, T. E. Chupp, S. R. Hwang, R. C. Welsh, M. C. Browne, H. P. Mumm, R. G. H. Robertson, T. D. Steiger, J. F. Wilkerson, J. M. Anaya, T. J. Bowles, G. L. Greene, W. A. Teasdale, J. M. Adams, M. S. Dewey, G. L. Jones, J. S. Nico, A. K. Thompson, F. E. Wietfeldt, S. J. Freedman, B. K. Fujikawa, L. J. Lising, and A. Garcia, *Time Reversal in Polarized Neutron Decay - The emiT Experiment*, APS Meeting Abstracts (1999), 7–+.

[Cow56] C. L. Cowan, Jr., F. Reines, F. B. Harrison, H. W. Kruse, and A. D. McGuire, *Detection of the Free Neutrino: A Confirmation*, Science **124** (1956), 103–104.

[Cry04] Cryogenics Ltd, *Cut through of a cryogen free magnet system*, March 2004, `http://www.cryogenic.co.uk/products/cf_systems/16_tesla.asp`.

[Dav94] R. Davis, *A review of the homestake solar neutrino experiment*, Progress in Particle and Nuclear Physics **32** (1994), 13–32.

[Dav06] Y. I. Davydov, *On the first Townsend coefficient at high electric field*, IEEE Transactions on Nuclear Science **53** (2006), 2931.

[Deh90] H. Dehmelt, *Experiments with an isolated subatomic particle at rest*, Reviews of Modern Physics **62** (1990), 525–530.

[Doe08] P. Doe, *Status of the focal plane detector (FPD)*, presentation at the XVth KATRIN Collaboration Meeting, 2008.

[Dru40] M. J. Druyvesteyn and F. M. Penning, *The Mechanism of Electrical Discharges in Gases of Low Pressure*, Rev. Mod. Phys. **12** (1940), no. 2, 87.

[Dun09] J. Dunkley, E. Komatsu, M. R. Nolta, D. N. Spergel, D. Larson, G. Hinshaw, L. Page, C. L. Bennett, B. Gold, N. Jarosik, J. L. Weiland, M. Halpern, R. S. Hill, A. Kogut, M. Limon, S. S. Meyer, G. S. Tucker, E. Wollack, and E. L. Wright, *Five-Year Wilkinson Microwave Anisotropy Probe Observations: Likelihoods and Parameters from the WMAP Data*, Astrophysical Journal, Supplement **180** (2009), 306–329, 0803.0586.

[Ede98] C. Edelmann, *Vakuumphysik: Grundlagen, Vakuumerzeugung und -messung, Anwendungen*, Spektrum Akademischer Verlag, Heidelberg - Berlin - Oxford, 1998.

[Eic09] F. Eichelhardt, *Measurement of the Tritium pumping properties of a 4.2 K Argon Condensate for the Cryogenic Pumping Section of KATRIN*, Ph.D. thesis, University of Karlsruhe, 2009.

[Fla04] B. Flatt, *Voruntersuchungen zu den Spektrometern des* KATRIN *experiments*, Ph.D. thesis, Johannes Gutenberg-Universität Mainz, 2004.

[Fow28] R. H. Fowler and L. Nordheim, *Electron Emission in Intense Electric Fields*, Royal Society of London Proceedings Series A **119** (1928), 173–181.

[Frä06] F. Fränkle, *Erste Messungen der elektromagnetischen Eigenschaften des KATRIN Vorspektrometers*, Master's thesis, Universität Karlsruhe, 2006.

[Frä07a] F. Fränkle, *private communication*, 2007, `http://www-ik.fzk.de:8080/pre-spectrometer/195`.

[Frä07b] F. Fränkle, *Simulation of different e-gun geometries*, internal KATRIN document (2007).

[Frä08] F. Fränkle, *Simulation of trapped ions*, XIVth Collaboration Meeting, 2008.

[Frä09] F. Fränkle, *KATRIN pre-spectrometer*, XVIth KATRIN Colaboration Meeting, 2009.

[Fuk98] Y. Fukuda, T. Hayakawa, E. Ichihara, K. Inoue, K. Ishihara, H. Ishino, Y. Itow, T. Kajita, J. Kameda, S. Kasuga, K. Kobayashi, Y. Kobayashi, Y. Koshio, K. Martens, M. Miura, M. Nakahata, S. Nakayama, A. Okada, M. Oketa, K. Okumura, M. Ota, N. Sakurai, M. Shiozawa, Y. Suzuki, Y. Takeuchi, Y. Totsuka, S. Yamada, M. Earl, A. Habig, J. T. Hong, E. Kearns, S. B. Kim, M. Masuzawa, M. D. Messier, K. Scholberg, J. L. Stone, L. R. Sulak, C. W. Walter, M. Goldhaber, T. Barszczak, W. Gajewski, P. G. Halverson, J. Hsu, W. R. Kropp, L. R. Price, F. Reines, H. W. Sobel, M. R. Vagins, K. S. Ganezer, W. E. Keig, R. W. Ellsworth, S. Tasaka, J. W. Flanagan, A. Kibayashi, J. G. Learned, S. Matsuno, V. Stenger, D. Takemori, T. Ishii, J. Kanzaki, T. Kobayashi, K. Nakamura, K. Nishikawa, Y. Oyama, A. Sakai, M. Sakuda, O. Sasaki, S. Echigo, M. Kohama, A. T. Suzuki, T. J. Haines, E. Blaufuss, R. Sanford, R. Svoboda, M. L. Chen, Z. Conner, J. A. Goodman, G. W. Sullivan, M. Mori, J. Hill, C. K. Jung, C. Mauger, C. McGrew, E. Sharkey, B. Viren, C. Yanagisawa, W. Doki, T. Ishizuka, Y. Kitaguchi, H. Koga, K. Miyano, H. Okazawa, C. Saji, M. Takahata, A. Kusano, Y. Nagashima, M. Takita, T. Yamaguchi, M. Yoshida, M. Etoh, K. Fujita, A. Hasegawa, T. Hasegawa, S. Hatakeyama, T. Iwamoto, T. Kinebuchi, M. Koga, T. Maruyama, H. Ogawa, A. Suzuki, F. Tsushima, M. Koshiba, M. Nemoto, K. Nishijima, T. Futagami, Y. Hayato, Y. Kanaya, K. Kaneyuki, Y. Watanabe, D. Kielczewska, R. Doyle, J. George, A. Stachyra, L. Wai, J. Wilkes, and K. Young, *Measurements of the Solar Neutrino Flux from Super-Kamiokande's First 300 Days*, Physical Review Letters **81** (1998), 1158–1162, arXiv:hep-ex/9805021.

[Fuk02] S. Fukuda, Y. Fukuda, M. Ishitsuka, Y. Itow, T. Kajita, J. Kameda, K. Kaneyuki, K. Kobayashi, Y. Koshio, M. Miura, S. Moriyama, M. Nakahata, S. Nakayama, T. Namba, A. Okada, N. Sakurai, M. Shiozawa, Y. Suzuki, H. Takeuchi, Y. Takeuchi, Y. Totsuka, S. Yamada, S. Desai, M. Earl, E. Kearns, M. D. Messier, J. L. Stone, L. R. Sulak, C. W. Walter, M. Goldhaber, T. Barszczak, D. Casper, W. Gajewski, W. R. Kropp, S. Mine, D. W. Liu, M. B. Smy, H. W. Sobel, M. R. Vagins, A. Gago, K. S. Ganezer, W. E. Keig, R. W. Ellsworth, S. Tasaka, A. Kibayashi, J. G. Learned, S. Matsuno, D. Takemori, Y. Hayato, T. Ishii, T. Kobayashi, T. Maruyama, K. Nakamura, Y. Obayashi, Y. Oyama, M. Sakuda, M. Yoshida, M. Kohama, T. Iwashita, A. T. Suzuki, A. Ichikawa, T. Inagaki, I. Kato, T. Nakaya, K. Nishikawa, T. J. Haines, S. Dazeley, S. Hatakeyama, R. Svoboda, E. Blaufuss, M. L. Chen, J. A. Goodman, G. Guillian, G. W. Sullivan, K. Scholberg, A. Habig, M. Ackermann, J. Hill, C. K. Jung, M. Malek, K. Martens, C. Mauger, C. McGrew, E. Sharkey, B. Viren, C. Yanagisawa, T. Toshito, C. Mitsuda, K. Miyano, C. Saji, T. Shibata, Y. Kajiyama, Y. Nagashima, K. Nitta, M. Takita, H. I. Kim, S. B. Kim, J. Yoo, H. Okazawa, T. Ishizuka, M. Etoh, Y. Gando, T. Hasegawa, K. Inoue, K. Ishihara, J. Shirai, A. Suzuki, M. Koshiba, Y. Hatakeyama, Y. Ichikawa, M. Koike, K. Nishijima, H. Ishino, M. Morii, R. Nishimura, Y. Watanabe, D. Kielczewska, H. G. Berns, S. C. Boyd, A. L. Stachyra, and R. J. Wilkes, *Determination of solar neutrino oscillation parameters using 1496 days of Super-Kamiokande-I data*, Physics Letters B **539** (2002), 179–187, arXiv:hep-ex/0205075.

[Fur39] W. H. Furry, *On Transition Probabilities in Double Beta-Disintegration*, Physical Review **56** (1939), 1184–1193.

[GAL99] GALLEX Collaboration, W. Hampel, J. Handt, G. Heusser, J. Kiko, T. Kirsten, M. Laubenstein, E. Pernicka, W. Rau, M. Wojcik, Y. Zakharov, R. V. Ammon, K. H. Ebert, T. Fritsch, D. Heidt, E. Henrich, L. Stielglitz, F. Weirich, M. Balata, M. Sann, F. X. Hartmann, E. Bellotti, C. Cattadori, O. Cremonesi, N. Ferrari, E. Fiorini, L. Zanotti, M. Altmann, F. V. Feilitzsch, R. Mößbauer, S. Wänninger, G. Berthomieu, E. Schatzman, I. Carmi, I. Dostrovsky, C. Bacci, P. Belli, R. Bernabei, S. D'Angelo, L. Paoluzi, M. Cribier, J. Rich, M. Spiro, C. Tao, D. Vignaud, J. Boger, R. L. Hahn, J. K. Rowley, R. W. Stoenner, and J. Weneser, *GALLEX solar neutrino observations: results for GALLEX IV*, Physics Letters B **447** (1999), 127–133.

[Geh08] R. Gehring, *private communication*, 2008, persistent mode not possible for longtime.

[GER05] GERDA Collaboration, I. Abt, M. Altmann, A. M. Bakalyarov, I. Barabanov, C. Bauer, M. Bauer, E. Bellotti, S. Belogurov, S. T. Belyaev,

A. Bettini, L. Bezrukov, V. Brudanin, C. Büttner, V. P. Bolotsky, A. Caldwell, C. Cattadori, M. V. Chirchenko, O. Chkvorets, H. Clement, E. Demidova, A. di Vacri, J. Eberth, V. Egorov, E. Farnea, A. Gangapshev, G. Y. Grigoriev, V. Gurentsov, K. Gusev, W. Hampel, G. Heusser, W. Hofmann, L. V. Inzhechik, J. Jochum, M. Junker, S. Katulina, J. Kiko, I. V. Kirpichnikov, A. Klimenko, K. T. Knöpfle, O. Kochetov, V. N. Kornoukhov, R. Kotthaus, V. Kusminov, M. Laubenstein, V. I. Lebedev, X. Liu, H.-G. Moser, I. Nemchenok, L. Pandola, P. Peiffer, R. H. Richter, K. Rottler, C. Rossi Alvarez, V. Sandukovsky, S. Schönert, S. Scholl, J. Schreiner, B. Schwingenheuer, H. Simgen, A. Smolnikov, A. V. Tikhomirov, C. Tomei, C. A. Ur, A. A. Vasenko, S. Vasiliev, D. Weißhaar, M. Wojcik, E. Yanovich, J. Yurkowski, S. V. Zhukov, and G. Zuzel, *The GERMANIUM DETECTOR ARRAY (GERDA) for the search of neutrinoless $\beta\beta$ decays of ^{76}Ge at LNGS*, Nuclear Physics B Proceedings Supplements **145** (2005), 242–245.

[Glü04] F. Glück, *The 3-dimensional electric field calculation program package elcd3 3*, Tech. report, Forschungszentrum Karlsruhe, Institut für Kernphysik, 2004.

[Glü05] F. Glück, *Background theory: radial motion of electrons from spectrometer electrodes into the fluxtube*, internal KATRIN document (2005).

[Glü06] F. Glück, *Pennig traps in the pre-spectrometer*, KATRIN EMD meeting (Fulda), 2006.

[Glü07a] F. Glück, K. Hugenberg, K. Valerius, and C. Weinheimer, *Simulations of a pair of additional electrodes to shield the Penning trap at the cone regions of the KATRIN pre-spectrometer*, internal KATRIN document (2007).

[Glü07b] F. Glück, *The Penning discharge*, internal KATRIN document (2007).

[Glü07c] F. Glück, L. Bornschein, F. Fränkle, F. Habermehl, K. A. Hugenberg, M. Leber, and K. Valerius, *Penning discharge experiments with the KATRIN pre-spectrometer*, internal KATRIN document (2007).

[Glü08] F. Glück, *Background at FPD and the pre-spectrometer potential*, XVth Collaboration Meeting, 2008.

[Glü09a] F. Glück, private communication, 2009.

[Glü09b] F. Glück, *Pre-spectrometer measurements: electrode configuration and potential dependence, asymmetric magnetic fields*, presentation at the EMD Meeeting, Münster, 2009.

[Glü09c] F. Glück, *Secondary electron emission in the pre-spectrometer and in the Mainz spectrometer*, XVIth Collaboration Meeting, 2009.

[Goo06] A. Goobar, S. Hannestad, E. Mörtsell, and H. Tu, *The neutrino mass bound from WMAP 3 year data, the baryon acoustic peak, the SNLS supernovae and the Lyman-α forest*, Journal of Cosmology and Astro-Particle Physics **6** (2006), 19–+, arXiv:astro-ph/0602155.

[Gri69] V. Gribov and B. Pontecorvo, *Neutrino astronomy and lepton charge*, Physics Letters B **28** (1969), 493–496.

[Gui08] V. E. Guiseppe and for the Majorana Collaboration, *The Majorana Neutrinoless Double-Beta Decay Experiment*, ArXiv e-prints (2008), 0811.2446.

[Hae53a] R. Haefer, *Über den Mechanismus der Zündung einer elektrischen Gasentladung unter der Einwirkung eines transversalen Magnetfeldes im Druckbereich* 10^{-1} *bis* 10^{-8} *Torr*, Acta Physica Austriaca 7 **251** (1953).

[Hae53b] R. Haefer, *Die Zündspannung von Gasentladungen unter dem Einfluß eines transversalen Magnetfeldes im Druckbereich von 10 bis* 10^{-8} *Torr*, Acta Physica Austriaca 7 **52** (1953).

[Ham99] Hamamatsu Photonics, *Micro Channel Plates*, December 1999, `http://sales.hamamatsu.com/assets/pdf/catsandguides/MCP-circular.pdf`.

[Ham07] Hamamatsu Photonics, *Deuterium Lamps*, April 2007, `http://sales.hamamatsu.com/de/produkte/electron-tube-division/light-sources/deuterium-lamps/part-l6565.php`.

[Han07] S. Hannestad, A. Mirizzi, G. G. Raffelt, and Y. Y. Y. Wong, *Cosmological constraints on neutrino plus axion hot dark matter*, JCAP **0708** (2007), 015, 0706.4198.

[Han08] S. Hannestad, A. Mirizzi, G. G. Raffelt, and Y. Y. Y. Wong, *Cosmological constraints on neutrino plus axion hot dark matter: Update after WMAP-5*, 0803.1585.

[Har89] M. Hara, H. Shigematsu, S. Yano, K. Yamafuji, M. Takeo, and K. Funaki, *Influence of transverse magnetic field on breakdown characteristics of vacuum, gaseous helium at low temperature and liquid helium*, Cryogenics **29** (1989), no. 4, 448 – 456.

[Hei09] H. Hein et al., *An angular selective photo-electron gun*, XVIth KATRIN Collaboration Meeting, 2009.

[Her65] M. Herrmann, *Untersuchung verschiedener Elektronenemissionsprozesse auf Mehrfachemission*, Zeitschrift für Physik A Hadrons and Nuclei **184** (1965), 352–354.

[Hir92] K. S. Hirata, K. Inoue, T. Ishida, T. Kajita, K. Kihara, M. Nakahata, K. Nakamura, S. Ohara, A. Sakai, N. Sato, Y. Suzuki, Y. Totsuka, Y. Yaginuma, M. Mori, Y. Oyama, A. Suzuki, K. Takahashi, M. Yamada, M. Koshiba, K. Nishijima, T. Kajimura, T. Suda, T. Tajima, K. Miyano, H. Miyata, H. Takei, Y. Fukuda, E. Kodera, Y. Nagashima, M. Takita, H. Yokoyama, K. Kaneyuki, Y. Takeuchi, T. Tanimori, E. W. Beier, E. D. Frank, W. Frati, S. B. Kim, A. K. Mann, F. M. Newcomer, R. van Berg, and W. Zhang, *Observation of a small atmospheric v_μ/v_e ratio in Kamiokande*, Physics Letters B **280** (1992), 146–152.

[Hos06] J. Hosaka, K. Ishihara, J. Kameda, Y. Koshio, A. Minamino, C. Mitsuda, M. Miura, S. Moriyama, M. Nakahata, T. Namba, Y. Obayashi, N. Sakurai, A. Sarrat, M. Shiozawa, Y. Suzuki, Y. Takeuchi, S. Yamada, I. Higuchi, M. Ishitsuka, T. Kajita, K. Kaneyuki, G. Mitsuka, S. Nakayama, H. Nishino, A. Okada, K. Okumura, C. Saji, Y. Takenaga, S. Clark, S. Desai, E. Kearns, S. Likhoded, J. L. Stone, L. R. Sulak, W. Wang, M. Goldhaber, D. Casper, J. P. Cravens, W. R. Kropp, D. W. Liu, S. Mine, M. B. Smy, H. W. Sobel, C. W. Sterner, M. R. Vagins, K. S. Ganezer, J. Hill, W. E. Keig, J. S. Jang, J. Y. Kim, I. T. Lim, K. Scholberg, C. W. Walter, R. W. Ellsworth, S. Tasaka, G. Guillian, A. Kibayashi, J. G. Learned, S. Matsuno, M. D. Messier, Y. Hayato, A. K. Ichikawa, T. Ishida, T. Ishii, T. Iwashita, T. Kobayashi, T. Nakadaira, K. Nakamura, K. Nitta, Y. Oyama, Y. Totsuka, A. T. Suzuki, M. Hasegawa, I. Kato, H. Maesaka, T. Nakaya, K. Nishikawa, T. Sasaki, H. Sato, S. Yamamoto, M. Yokoyama, T. J. Haines, S. Dazeley, B. K. Kim, K. B. Lee, S. Hatakeyama, R. Svoboda, E. Blaufuss, J. A. Goodman, G. W. Sullivan, D. Turcan, J. Cooley, A. Habig, Y. Fukuda, T. Sato, Y. Itow, C. K. Jung, T. Kato, K. Kobayashi, M. Malek, K. Martens, C. Mauger, C. McGrew, E. Sharkey, C. Yanagisawa, N. Tamura, M. Sakuda, Y. Kuno, M. Yoshida, S. B. Kim, J. Yoo, H. Okazawa, T. Ishizuka, Y. Choi, H. K. Seo, Y. Gando, T. Hasegawa, K. Inoue, J. Shirai, A. Suzuki, K. Nishijima, H. Ishino, Y. Watanabe, M. Koshiba, D. Kielczewska, J. Zalipska, H. G. Berns, R. Gran, K. K. Shiraishi, A. L. Stachyra, K. Washburnand, and R. J. Wilkes, *Solar neutrino measurements in Super-Kamiokande-I*, Phys. Rev. D **73** (2006), no. 11, 112001–+, arXiv:hep-ex/0508053.

[How04] M. A. Howe, G. A. Cox, P. J. Harvey, F. McGirt, K. Rielage, J. F. Wilkerson, and J. M. Wouters, *Sudbury Neutrino Observatory Neutral Current Detector Acquisition Software Overview*, IEEE Transactions on Nuclear Science **51** (2004), 878–883.

[How08] M. Howe, *ORCA*, Tech. report, University of North Carolina, 2008, `http://orca.physics.unc.edu/~markhowe/Getting_Started/Overview.html`.

[Hug08a] K. Hugenberg, F. Fraenkle, and F. Glück, *More detailed investigation of the high B-field background at low potentials*, Elog 392, 2008.

[Hug08b] K. A. Hugenberg, F. Glück, and F. Fränkle, *Asymmetric magnetic field analysis with simulations*, KATRIN pre-spectrometer electronic logbook, entry 387, 2008.

[Hug08c] K. A. Hugenberg, *Design of the electrode system for the KATRIN main spectrometer*, Master's thesis, Westfälische Wilhelms-Universität Münster, 2008.

[KAT08] KATRIN Collaboration, *Technical Specification Cryogenic Pumping Section*, Tech. Report Annex_TA_10-DSP-4210-1, KATRIN internal document, 2008.

[Ker07] N. Kernert and A. Gotsova, *Influence of magnetic field on MAG 2800 operation*, XIIIth KATRIN Collaboration Meeting, 2007.

[KK97] H. V. Klapdor-Kleingrothaus and K. Zuber, *Teilchenastrophysik*, Teubner, Stuttgart, 1997 (ger).

[KK06] H. V. Klapdor-Kleingrothaus and I. V. Krivosheina, *The evidence for the observation $0\nu\beta\beta$ decay: the identification of $0\nu\beta\beta$ events from the full spectra*, Modern Physics Letters A **21** (2006), no. 20, 1547–1566.

[Kla01] H. V. Klapdor-Kleingrothaus, A. Dietz, L. Baudis, G. Heusser, I. V. Krivosheina, B. Majorovits, H. Paes, H. Strecker, V. Alexeev, A. Balysh, A. Bakalyarov, S. T. Belyaev, V. I. Lebedev, and S. Zhukov, *Latest results from the HEIDELBERG-MOSCOW double beta decay experiment*, European Physical Journal A **12** (2001), 147–154, arXiv:hep-ph/0103062.

[Kli86] G. Klingelhoefer, H. Wiacker, and E. Kankeleit, *Measurement of the detection efficiency of microchannel plates for 1-15 keV electrons*, Nuclear Instruments and Methods in Physics Research A **247** (1986), 379–384.

[Kod08] K. Kodama, N. Ushida, C. Andreopoulos, N. Saoulidou, G. Tzanakos, P. Yager, B. Baller, D. Boehnlein, W. Freeman, B. Lundberg, J. Morfin, R. Rameika, S. H. Chung, J. S. Song, C. S. Yoon, P. Berghaus, M. Kubantsev, N. W. Reay, R. Sidwell, N. Stanton, S. Yoshida, S. Aoki, T. Hara, J. T. Rhee, D. Ciampa, C. Erickson, M. Graham, E. Maher, K. Heller, R. Rusack, R. Schwienhorst, J. Sielaff, J. Trammell, J. Wilcox, T. Furukawa, K. Hoshino, H. Jiko, M. Komatsu, M. Nakamura, T. Nakano, K. Niwa, N. Nonaka, K. Okada, B. D. Park, O. Sato, S. Takahashi, V. Paolone, C. Rosenfeld, A. Kulik, T. Kafka, W. Oliver, T. Patzak, and J. Schneps, *Final tau-neutrino results from the DONuT experiment*, Phys. Rev. D **78** (2008), no. 5, 052002–+.

[Kol64] R. Kollath and K.-H. Simon, *Bemerkung zur Mehrfach-Emission von Sekundärelektronen*, June 1964, pp. 274–275.

[Kra05] C. Kraus, B. Bornschein, L. Bornschein, J. Bonn, B. Flatt, A. Kovalik, B. Ostrick, E. W. Otten, J. P. Schall, T. Thümmler, and C. Weinheimer, *Final results from phase II of the Mainz neutrino mass searchin tritium {β} decay*, European Physical Journal C **40** (2005), 447–468, arXiv:hep-ex/0412056.

[Kur09] Kurt J. Lesker Company, *CF Flanges Technical Notes*, 2009, `http://www.lesker.com/newweb/flanges/flanges_technicalnotes_conflat_1.cfm?pgid=0`.

[Leb09] M. L. Leber, *Determining Backgrounds for the KATRIN Experiment, in preparation*, Ph.D. thesis, University of Washington, 2009.

[Lob01] V. M. Lobashev, V. N. Aseev, A. I. Belesev, A. I. Berlev, E. V. Geraskin, A. A. Golubev, O. V. Kazachenko, Y. E. Kuznetsov, R. P. Ostroumov, L. A. Rivkis, B. E. Stern, N. A. Titov, C. V. Zadoroghny, and Y. I. Zakharov, *Direct Search for Neutrino Mass and Anomaly in the Tritium Beta-Spectrum: Status of "Troitsk Neutrino Mass" Experiment*, Nuclear Physics B Proceedings Supplements **91** (2001), 280–286.

[Luo07] X. Luo, L. Bornschein, C. Day, and J. Wolf, *KATRIN NEG pumping concept investigation*, Vacuum **81** (2007), no. 6, 777 – 781, Proceedings of the European Vacuum Conference (EVC-9).

[Mer09a] S. Mertens, *Pre-spectrometer simulations: the Zacher trap as source for the high B-field background?*, EMD meeting Münster, 2009.

[Mer09b] S. Mertens, F. Glück, A. Osipowicz, P. Plischke, J. Reich, and N. Wandkowsky, *Design Document: Air Coil System & Magnetic Field Sensor System*, Tech. report, Forschungszentrum Karlsruhe, University of Applied Sciences Fulda, 2009.

[Mon06] A. Monfardini, C. Arnaboldi, C. Brofferio, S. Capelli, F. Capozzi, O. Cremonesi, C. Enss, E. Fiorini, A. Fleischmann, L. Foggetta, G. Gallinaro, L. Gastaldo, F. Gatti, A. Giuliani, P. Gorla, R. Kelley, C. A. Kilbourne, B. Margesin, D. McCammon, C. Nones, A. Nucciotti, M. Pavan, M. Pedretti, D. Pergolesi, G. Pessina, F. S. Porter, M. Prest, E. Previtali, P. Repetto, M. Ribeiro-Gomez, S. Sangiorgio, and M. Sisti, *The microcalorimeter arrays for a rhenium experiment (MARE): A next-generation calorimetric neutrino mass experiment*, Nuclear Instruments and Methods in Physics Research A **559** (2006), 346–348, arXiv:hep-ex/0509038.

[Nem99] V. Nemanic and J. Setina, *A study of thermal treatment procedures to reduce hydrogen outgassing rate in thin wall stainless steel cells*, Vacuum **53** (1999), no. 1-2, 277 – 280.

[Osi01] A. Osipowicz et al. (KATRIN Collaboration), *KATRIN: A next generation tritium beta decay experiment with sub-eV sensitivity for the electron neutrino mass*, hep-ex/0109033.

[Ott08] E. W. Otten and C. Weinheimer, *Neutrino mass limit from tritium β decay*, Reports on Progress in Physics **71** (2008), no. 8, 086201–+.

[Ott09] E. Otten and C. Weinheimer, *Summary on background studies at Mainz: Ionisation of the residual gas, Penning plasmas*, EMD Meeting, Münster (2009).

[Par08] C. D. Park, S. M. Chung, X. Liu, and Y. Li, *Reduction in hydrogen outgassing from stainless steels by a medium-temperature heat treatment*, Journal of Vacuum Science & Technology A: Vacuum, Surfaces, and Films **26** (2008), no. 5, 1166–1171.

[Pen36] F. M. Penning, Physica **3** (1936), 873.

[Pic90] T. Picard, Ph.D. thesis, Johannes Gutenberg Universität Mainz, 1990.

[Rei56] F. Reines and C. L. Cowan, *The Neutrino*, Nature **178** (1956), 446–449.

[Ren07] P. Renschler, *Inbetriebnahme und Charakterisierung von Detektrosystemen für elektromagnetische Tests von Spektrometern*, Master's thesis, Universität Karlsruhe, 2007.

[Riv66] J. C. Rivière, *The Work Function of Gold*, Aplied Physics Letters **8** (1966).

[SAE] SAES company, *Getter alloy ST707*, `http://www.saesgetters.com/default.aspx?idpage=212`.

[Sch66] P. Schackert, *Zur Sekundärelektronenemission durch Argonionen und Argonatome im Energiebereich von 1 bis 20 keV*, Zeitschrift für Physik A Hadrons and Nuclei **197** (1966), 32–40.

[Sch97] N. Schmitz, *Neutrinophysik*, Teubner, Stuttgart, 1997.

[Sch04] F. Schwamm, *Background studies for the KATRIN experiment. (In German)*, FZKA Scientific Report **7067** (2004), 1+, FZKA-7067.

[Sch06] P. Schneider, *Extragalactic astronomy and cosmology: an introduction*, XIV, 459 S. (eng), Literaturverz. S. 433 - 435; tocsubgoe.

[Sch08] U. Schmitt, *Forward Monitor detector*, Ph.D. thesis, Forschunsgzentrum Karlsruhe, University of Karlsruhe, 2008.

[Sis04] M. Sisti, C. Arnaboldi, C. Brofferio, G. Ceruti, O. Cremonesi, E. Fiorini, A. Giuliani, B. Margesin, L. Martensson, A. Nucciotti, M. Pavan, G. Pessina, S. Pirro, E. Previtali, L. Soma, and M. Zen, *New limits from*

the Milano neutrino mass experiment with thermal microcalorimeters, Nuclear Instruments and Methods in Physics Research A **520** (2004), 125–131.

[Sis07] M. Sisti, *MARE: 187Re beta spectrum analysis with bolometric techniques*, Nuclear Physics B - Proceedings Supplements **168** (2007), 48 – 50, Proceedings of the Neutrino Oscillation Workshop.

[SNO01] SNO Collaboration, *Solar Neutrino Results from the Sudbury Neutrino Observatory*, ArXiv High Energy Physics - Experiment e-prints (2001), arXiv:hep-ex/0111040.

[SNO05a] SNO Collaboration, *Electron Energy Spectra, Fluxes, and Day-Night Asymmetries of $\{\hat{8}\}$B Solar Neutrinos from the 391-Day Salt Phase SNO Data Set*, Physical Review C **72** (2005), 055502.

[SNO05b] SNO Collaboration, *The Sudbury Neutrino Observatory*, Nuclear Physics B Proceedings Supplements **149** (2005), 128–130.

[Som] Sommerschmied GmbH, `http://www.glas-rohr.de/de/impressum.html`.

[Ste05] M. Steidl, *Comparison of Segmented PIN Diodes versus Silicon Drift Detectors for the KATRIN Focal Plane Detector*, Tech. report, Forschunsgzentrum Karlsruhe, Institut für Kernphysik, 2005.

[Ste09] M. Steidl, *private communication*, 2009.

[Swa08] Swagelok Company, *Gaugeable Tube Fit tings and Adapter Fit tings*, Tech. report, 2008, `http://www.swagelok.com/downloads/webcatalogs/en/ms-01-140.pdf`.

[Tow10] J. Townsend, *The theory of ionization of gases by collision*, Constable & Company Ltd., London, 1910.

[Umr02] W. Umrath, *Fundamentals of Vacuum Technology*, Leybold Vacuum, 2002.

[Val04] K. Valerius, *Elektromagnetisches Design für das Hauptspektrometer des KATRIN Experiments*, Master's thesis, Rheinische Friedrich-Wilhelms-Universität, 2004.

[Val09] K. Valerius, *Spectrometer-related background processes and their suppression in the KATRIN experiment*, Ph.D. thesis, Westfälische Wilhelms-Universität Münster, 2009.

[Vau01] D. Vaughan and A. Thompson, *X-ray data booklet, 2nd edition*, Tech. report, January 2001, `http://xdb.lbl.gov/`.

[Vöc08] S. Vöcking, Master's thesis, Westfälische Wilhelms-Universität Münster, Institut für Kernphysik, 2008.

[Vos03] G. Voss, *Compression and Ultimate Pressure of Turbomolecular Pumps*, International Workshop on Extreme High Vacuum - Application and Technology (X-VAT), 2003.

[Wal06] B. Wall, T. Burritt, P. Doe, C. Fredericks, H. Gemmeke, G. Harper, M. Howe, M. Leber, A. Myers, R. Robertson, M. Steidl, B. VanDevender, T. Van Wechel, S. Wustling, and J. Wilkerson, *Dead layer measurements for KATRIN prototype PIN diode array*, vol. 1, 29 2006-Nov. 1 2006, pp. 204–207.

[Wer] G. Werth, *The Penning trap*, `http://www.physik.uni-mainz.de/Werth/g_fak/penning.htm`.

[Wil87] J. F. Wilkerson, T. J. Bowles, J. C. Browne, M. P. Maley, R. G. H. Robertson, J. S. Cohen, R. L. Martin, D. A. Knapp, and J. A. Helffrich, *Limit on $\overline{\nu_e}$ mass from free-molecular-tritium beta decay*, Physical Review Letters **58** (1987), 2023–2026.

[Wil07] C. Wilhelm, *Ergebnisse der gammspektrometrischen Analyse*, Tech. report, Forschungszentrum Karlsruhe, Institut für Strahlenforschung, 2007.

[Wil09] J. Wilkerson, *KATRIN DAQ*, XVIth KATRIN Collaboration Meeting, March 2009.

[Wol06] J. Wolf, L. Bornschein, C. Day, F. Habermehl, and X. Luo, *Outgassing measurements with a prototype for a large UHV spectrometer*, Hydrogen in Matter (G. Rao Myneni and B. Hjörvarsson, eds.), American Institute of Physics Conference Series, vol. 837, May 2006, pp. 200–209.

[Wüs06] S. Wüstling, T. Armbrust, M. Steidl, and S. Zadorozhny, *A large, 64-pixel PIN-diode detector for low-energy beta-electrons*, Nuclear Instruments and Methods in Physics Research A **568** (2006), 382–387.

[Wüs08a] S. Wüstling, *private communication*, 2008.

[Wüs08b] S. Wüstling, T. Thümmler, and F. Fränkle, *HV stabilization working*, Elog entry 410, 2008.

[Wüs09] S. Wüstling, *Active HV stabilization for the pre-spectrometer*, private communication, 2009.

[Yao06] W.-M. Yao, C. Amsler, D. Asner, R. Barnett, J. Beringer, P. Burchat, C. Carone, C. Caso, O. Dahl, G. D'Ambrosio, A. DeGouvea, M. Doser, S. Eidelman, J. Feng, T. Gherghetta, M. Goodman, C. Grab, D. Groom, A. Gurtu, K. Hagiwara, K. Hayes, J. Hernández-Rey, K. Hikasa, H. Jawahery, C. Kolda, K. Y., M. Mangano, A. Manohar, A. Masoni, R. Miquel,

K. Mönig, H. Murayama, K. Nakamura, S. Navas, K. Olive, L. Pape, C. Patrignani, A. Piepke, G. Punzi, G. Raffelt, J. Smith, M. Tanabashi, J. Terning, N. Törnqvist, T. Trippe, P. Vogel, T. Watari, C. Wohl, R. Workman, P. Zyla, B. Armstrong, G. Harper, V. Lugovsky, P. Schaffner, M. Artuso, K. Babu, H. Band, E. Barberio, M. Battaglia, H. Bichsel, O. Biebel, P. Bloch, E. Blucher, R. Cahn, D. Casper, A. Cattai, A. Ceccucci, D. Chakraborty, R. Chivukula, G. Cowan, T. Damour, T. DeGrand, K. Desler, M. Dobbs, M. Drees, A. Edwards, D. Edwards, V. Elvira, J. Erler, V. Ezhela, W. Fetscher, B. Fields, B. Foster, D. Froidevaux, T. Gaisser, L. Garren, H.-J. Gerber, G. Gerbier, L. Gibbons, F. Gilman, G. Giudice, A. Gritsan, M. Grünewald, H. Haber, C. Hagmann, I. Hinchliffe, A. Höcker, P. Igo-Kemenes, J. Jackson, K. Johnson, D. Karlen, B. Kayser, D. Kirkby, S. Klein, K. Kleinknecht, I. Knowles, R. Kowalewski, P. Kreitz, B. Krusche, Y. Kuyanov, O. Lahav, P. Langacker, A. Liddle, Z. Ligeti, T. Liss, L. Littenberg, L. Liu, K. Lugovsky, S. Lugovsky, T. Mannel, D. Manley, W. Marciano, A. Martin, D. Milstead, M. Narain, P. Nason, Y. Nir, J. Peacock, S. Prell, A. Quadt, S. Raby, B. Ratcliff, E. Razuvaev, B. Renk, P. Richardson, S. Roesler, G. Rolandi, M. Ronan, L. Rosenberg, C. Sachrajda, S. Sarkar, M. Schmitt, O. Schneider, D. Scott, T. Sjöstrand, G. Smoot, P. Sokolsky, S. Spanier, H. Spieler, A. Stahl, T. Stanev, R. Streitmatter, T. Sumiyoshi, N. Tkachenko, G. Trilling, G. Valencia, K. van Bibber, M. Vincter, D. Ward, B. Webber, J. Wells, M. Whalley, L. Wolfenstein, J. Womersley, C. Woody, A. Yamamoto, O. Zenin, J. Zhang, and R.-Y. Zhu, *Review of Particle Physics*, Journal of Physics G **33** (2006), 1+.

[Zac09] M. Zacher, private communication, 2009.

[Zie08] J. F. Ziegler, *SRIM - The Stopping and Range of Ions in Matter, ver2008*, 2008,
`http://www.srim.org/index.htm`.

[Zru09] Zrunek Gummiwaren GmbH, *FAQ*, 2009,
`http://www.zrunek.at/fpmviton.htm`.

[Zwi09] D. Zwick, *3 dimensional drawing of the detector chamber*, private communication, 2009.